HAL
open science

Surface recovery and reconstruction after deformation

Joseph Lejeune

To cite this version:

Joseph Lejeune. Surface recovery and reconstruction after deformation. Other [cond-mat.other]. Université de Strasbourg; Albert-Ludwigs-Universität (Freiburg im Breisgau, Allemagne), 2014. English. NNT : 2014STRAE031 . tel-02399585v2

HAL Id: tel-02399585

https://theses.hal.science/tel-02399585v2

Submitted on 9 Dec 2019

HAL is a multi-disciplinary open access archive for the deposit and dissemination of scientific research documents, whether they are published or not. The documents may come from teaching and research institutions in France or abroad, or from public or private research centers.

L'archive ouverte pluridisciplinaire **HAL**, est destinée au dépôt et à la diffusion de documents scientifiques de niveau recherche, publiés ou non, émanant des établissements d'enseignement et de recherche français ou étrangers, des laboratoires publics ou privés.

UNIVERSITÉ DE STRASBOURG

ALBERT-LUDWIGS-UNIVERSITÄT FREIBURG

École doctorale de Physique et Chimie Physique (ED 182)

Fakultät für Chemie, Pharmazie und Geowissenschaften

Institut Charles Sadron UPR22

Freiburger Materialforschungzentrum

PhD thesis by

Joseph LEJEUNE

Defended on **June 3rd 2014**

To obtain the title of **Doctor of the universities of Strasbourg and Freiburg**

Specialty: Chemistry and Tribology

Surface recovery and reconstruction after deformation

PhD thesis directors:

M. PELLETIER Hervé	Professeur des Universités, université de Strasbourg
M. MÜLHAUPT Rolf	Professor für Makromolekular Chemie, Universität Freiburg

Reviewers:

M. REITER Günter	Professor für experimentelle Polymerphysik, Universität Freiburg
M. EL MANSORI Mohamed	Professeur des Universités, Arts et métiers Paris tech

---

Other Jury members:

M. BARLETTA Massimiliano	assistant Professor, University of Rome Tor Vergata
M. MISCHLER Stephano	Maître d'enseignement et de recherche, EPFL Lausanne

SURFACE RECOVERY AND RECONSTRUCTION AFTER DEFORMATION

Dành cho em,

ACKNOWLEDGMENT

Pour leurs jugements, leurs avis et leurs questions avisés, je tiens à remercier les membres de mon jury de thèse : les Professeurs Reiter et El Mansori, les docteurs Barletta et Mischler. J'ai apprécié la pluridisciplinarité tant scientifique que linguistique de l'épreuve.

La région Alsace a financé ce projet de thèse dans le cadre de l'International Research Training Group, je les remercie de m'avoir fait confiance.

Je tiens à exprimer ma reconnaissance envers mes directeurs de thèse : les professeurs Hervé Pelletier et Rolf Mülhaupt.

Mes remerciements vont aussi à Christian Gauthier de m'avoir accueilli dans son équipe. Jean-François Legrand et Jean-Michel Guenet ont dirigé le laboratoire pendant le temps de ma thèse.

J'exprime ma reconnaissance envers les membres de l'équipe mécanique, particulièrement Leandro, Damien et Vincent.

À mes collègues de bureau, je souhaite exprimer de vifs remerciements pour tous les moments passés ensemble, Athmane, Larisa, Nicolas.

Les autres amis, qui m'ont supporté et aidé pendant ces trois années, sont entre autre Tristan, Rémi, Andru, Laure Biniek, Magali, Jean-Baptiste, Patricja, …

An die jenigen, die mir in Deutschland Ihre Freundschaft gegeben haben, ich möchte mich bedanken Jens, Beni, Hannes, Michael, Stas, ...

Doctorants, j'ai eu grand plaisir à être votre représentant au Bureau des Jeunes Chercheurs, particulièrement dans la commission enseignement recherche. Je tiens à vous remercier pour le temps passé ensemble. Arnaud, Laure Hermann, Emmanuelle, Diana, Rebecca, Johanna, Rémi, Georges, Andru et les autres, j'ai tout particulièrement apprécié nos soirées.

Rugbymen and women, je vous remercie de m'avoir accepté parmi vous malgré mon faible niveau. Lorchat, Lorchat frêre, Charitat, et toute l'équipe.

Kiko, Tobi, Iaro, Alhama, Andru, Gladys, Zum wohl, Na Zdarovie, Salute, Norok, …

À ma famille (Laurence, Yves, Ismaël, Jean-Guillaume, Anne-Fleur), que j'aime et qui me soutient, je dis merci.

Cảm ơn em yêu.

PREFACE

Surfaces are neither remarked nor seen unless they are deteriorated. The observation of the nonetheless very common surfaces damages and therefore the loss of their intrinsic properties (such as brightness, transparency, opto-electronic, protection, adhesion …) made us wonder on the capacity of certain surfaces to heal. In this thesis we will focus on the spontaneous recovery of the polymeric surfaces. The more recent subject, named "self-healing", occurs when new material is created. The understanding of this subject is outside of these thesis objectives.

On the contrary this thesis will focus on the recovery that polymers present when slightly solicited (No permanent damages are done.). To understand these recoveries, two model amorphous polymers are studied thoroughly from the macro to the nano scale. The macro scale is characterized by compression experiments whereas the micro and nano scale tests are done by contact experiments. To better understand the polymers and in particular their recovery, Finite Element Modeling experiments were conducted. Moreover this study was completed by the fabrication and testing of diverse filled polymers.

Finally, I had the chance to be part of the IRTG soft matter science. It enabled me to have a joint PhD thesis supervision.

The chapter division of the manuscript answers to these miscellaneous requirements. Firstly extended summaries of the thesis in English, French and German are proposed. Each of them presents, in the three languages, a stand-alone version of the thesis. Then, the Bibliography shows the state of the art and the void in it. The materials and methods part present the used material and methods. Afterwards the experimental and numerical results obtained during this thesis are displayed

CONTENTS

CHAPTER I. SUMMARY 2

I.1. INTRODUCTION 3
I.2. EXPERIMENTAL METHODS AND TECHNIQUES 3
I.3. BULK MECHANICAL PROPERTIES 5
I.3.1. Relaxation 5
I.3.2. Relaxation modulus and master curves 6
I.3.3. Conclusion 8
I.4. CONTACT ANALYSIS 8
I.4.1. Indentation Creep 8
I.4.1.1 Room temperature 8
I.4.1.2 Influence of temperature 9
I.4.2. Indentation Recovery 10
I.4.3. Master curves comparison 11
I.4.4. Scratch recovery analysis 13
I.4.4.1 General Information 13
I.4.4.2 Influence of distance toward end of scratch 14
I.4.4.3 Influence of load 14
I.4.4.4 Partial conclusion 15
I.4.5. Conclusion 15
I.5. FINITE ELEMENT MODELING 16
I.5.1. Constitutive laws 16
I.5.2. Uni-axial Relaxation 18
I.5.2.1 Relaxation at 4.88% 18
I.5.2.2 Relaxation at 17.69% 19
I.5.2.3 Partial conclusion 20
I.5.3. Indentation 20
I.5.3.1 Indentation creep 21
I.5.3.2 Indentation recovery 21
I.5.4. Conclusion 22
I.6. GENERAL CONCLUSION 22
I.7. BIBLIOGRAPHY 24

CHAPTER II. RÉSUMÉ 28

II.1. INTRODUCTION 29
II.2. MÉTHODES EXPÉRIMENTALES ET TECHNIQUES 29
II.3. PROPRIÉTÉS MÉCANIQUES EN VOLUME 32
II.3.1. Relaxation 32
II.3.2. Modules de relaxation et courbes maîtresses 33
II.3.3. Conclusion 35
II.4. ANALYSE DU CONTACT 35

II.4.1. Fluage d'indentation 35
II.4.1.1 Température ambiante 35
II.4.1.2 Influence de la température 36
II.4.2. Recouvrance d'indentation 37
II.4.3. Comparaison de Courbes maîtresses 38
II.4.4. Analyse de la recouvrance de la rayure 40
II.4.4.1 Informations générales 40
II.4.4.2 Influence de la distance depuis la fin de la rayure 41
II.4.4.3 Influence de la charge 42
II.4.4.4 Conclusion partielle 43
II.4.5. Conclusion 43
II.5. SIMULATION PAR ÉLÉMENTS FINIS 44
II.5.1. Lois de comportement 44
II.5.2. Relaxation uni-axiale 46
II.5.2.1 Relaxation à 4.88 % 46
II.5.2.2 Relaxation à 17.69 % 47
II.5.2.3 Conclusion partielle 48
II.5.3. Indentation 48
II.5.3.1 Fluage d'indentation 48
II.5.3.2 Recouvrance d'indentation 49
II.6. CONCLUSION GÉNÉRALE 50
II.7. BIBLIOGRAPHIE 52

CHAPTER III. ZUSAMMENFASSUNG 56

III.1. EINLEITUNG 57
III.2. EXPERIMENTALTEIL 57
III.3. VOLUMEN MECHANISCHEN EIGENSCHAFTEN VON CR39 60
III.3.1. Relaxation 60
III.3.2. Relaxationmoduln und Masterkurven 61
III.3.3. Fazit 63
III.4. KONTAKTANALYSE 63
III.4.1. Indentations-Kriechversuche 63
III.4.1.1 Raumtemperatur 63
III.4.1.2 Einfluss der Temperatur 64
III.4.2. Indentations-Heilung 65
III.4.3. Masterkurve 66
III.4.4. Kratzer Heilung 68
III.4.4.1 Generelle Information 68
III.4.4.2 Einfluss von der Kratzerendedistanz 69
III.4.4.3 Einfluss von Belastung 69
III.4.4.4 Fazit 70
III.4.5. Fazit 71
III.5. FINITE ELEMENT MODELLIERUNG 71

III.5.1. Materialmodelle 71
III.5.2. Bulk-Relaxationsexperiment 73
III.5.2.1 Relaxationsexperiment 4.88 % 73
III.5.2.2 Relaxationsexperiment 17.69 % 74
III.5.2.3 Fazit 75
III.5.3. Indentation 75
III.5.3.1 Indentations-Kriechen 75
III.5.3.2 Indentations-Heilung 76
III.5.4. Fazit 77
III.6. FAZIT 77
III.7. BIBLIOGRAPHIE 79

CHAPTER IV. BIBLIOGRAPHY 82

IV.1. INTRODUCTION 83
IV.2. POLYMERIC MATERIALS 83
IV.2.1. Polymer fabrication 83
IV.2.2. Polymer applications 83
IV.3. GENERAL MECHANICS 83
IV.3.1. Boltzmann superposition principle 84
IV.4. CONTACT MECHANIC 88
IV.4.1. Indentation 88
IV.4.1.1 Principle 88
IV.4.1.2 Deformation shape below the indenter 89
IV.4.1.3 Load-depth curves 89
IV.4.1.4 Indentation master curves 90
IV.4.1.5 Indentation recovery 91
IV.4.1.6 Recent improvement in indentation 91
IV.4.2. Scratch 92
IV.4.2.1 Scratching method 92
IV.4.2.2 Microvisioscratch master curves 92
IV.4.2.3 Recovery observation generality 93
IV.4.2.4 Recent scratch recovery observation 94
IV.4.3. Conclusion 95
IV.5. ANALYTICAL MODELING 95
IV.5.1. Simple rheological model 95
IV.5.1.1 Maxwell model 95
IV.5.1.2 Kelvin-Voigt model 96
IV.5.2. Generalized model 97
IV.5.3. Indentation 98
IV.6. FINITE ELEMENT MODELING 99
IV.6.1. Model 99
IV.6.2. Constitutive law 100
IV.6.2.1 G'Sell Jonas law 100

IV.6.2.2 Norton's law 101
IV.6.2.3 Generalized Maxwell 101
IV.6.2.4 Master curves 101
IV.6.2.5 Strain rate dependent plasticity 102
IV.7. CONCLUSION 102
IV.8. BIBLIOGRAPHY 104

CHAPTER V. MATERIALS & METHODS 110

V.1. INTRODUCTION 111
V.2. POLYMERS ORIGIN 111
V.2.1. Industry product 111
V.2.1.1 PMMA 111
V.2.1.2 CR39 essilor 112
V.2.2. Lab made product 113
V.2.2.1 Process 113
V.2.2.2 Fillers 114
V.2.2.2.1 AlO(OH) 114
V.2.2.2.2 SiO_2 114
V.2.2.2.3 Nanopox® A 410 114
V.2.2.2.4 Aerosil 115
V.2.2.2.5 Functionalized Stöber particles 115
V.2.3. Summary of available samples 115
V.3. SURFACE TEXTURE 116
V.3.1. Clean surfaces and no texture 116
V.3.2. Glass 116
V.3.3. Teflon spray 116
V.3.4. Kapton film 116
V.4. MECHANICAL CHARACTERIZATION 117
V.4.1. Bulk characterization 117
V.4.1.1 Instron® machine 117
V.4.1.2 Uniaxial measurement generality 118
V.4.1.3 Dynamic Mechanical Temperature Analysis (DMTA) 119
V.4.1.4 Relaxation 120
V.4.1.5 Creep 121
V.4.2. Indentation 122
V.4.2.1 Indentation generality 122
V.4.2.2 Nano indentation 124
V.4.2.2.1 Nano indentation principle 124
V.4.2.2.2 Nano Indenter XP®MTS 124
V.4.2.2.3 Nano Indenter CSM 125
V.4.2.3 Micro and macro Indentation 126
V.4.2.3.1 Lab made apparatus the Microvisioscratch 126
V.4.2.3.2 Macro Indenter 130
V.4.2.4 Principle validation 131
V.4.3. Scratch 132

V.4.3.1 Micro scratch 132
V.4.3.1.1 Groove fabrication in situ observation 132
V.4.3.1.2 Groove recovery in situ observation 133
V.5. OTHER CHARACTERIZATIONS 134
V.5.1. Optical microscope....134
V.5.2. Differential scanning calorimeter 134
V.5.3. Transmission Electron Microscopy (TEM) 135
V.6. CONCLUSION 136
V.7. BIBLIOGRAPHY....137

CHAPTER VI. EXPERIMENTAL RESULTS 138

VI.1. INTRODUCTION 139
VI.2. COMPARISON BETWEEN BULK MECHANICAL PROPERTIES OF CR39, PMMA CN AND PMMA 10 ALO(OH) 139
VI.2.1. DMTA 139
VI.2.2. Relaxation....141
VI.2.3. Relaxation modulus and master curves....143
VI.2.4. Influence of environmental atmosphere....147
VI.2.5. Conclusion 148
VI.3. CONTACT ANALYSIS 148
VI.3.1. Indentation Creep 148
VI.3.1.1 Room temperature 149
VI.3.1.2 Influence of temperature....149
VI.3.1.2.1 Mean contact pressure 149
VI.3.1.2.2 Normalized Tabor deformation 151
VI.3.2. Indentation Recovery 152
VI.3.2.1 Room temperature 152
VI.3.2.2 Influence of temperature....153
VI.3.2.3 Influence of creep time....155
VI.3.2.4 Partial conclusion 155
VI.3.3. Master curves comparison 156
VI.3.4. Scratch recovery analysis....157
VI.3.4.1 Scratch Generality 158
VI.3.4.2 Influence of the scratch deformation 160
VI.3.4.3 Influence of the scratch speed....161
VI.3.4.4 Partial conclusion 161
VI.3.5. Conclusion 162
VI.4. INFLUENCE OF FILLERS ADDITION 162
VI.4.1. SiO_2 and AlO(OH) addition....162
VI.4.1.1 General observation....162
VI.4.1.2 Bulk analysis 164
VI.4.1.3 Indentation analysis....164
VI.4.2. Comparison between other SiO_2 fillers with different end groups 165
VI.4.2.1 General Observation....165

VI.4.2.2 Bulk analysis 166
VI.4.2.3 Indentation analysis 167
VI.4.3. Conclusion 168
VI.5. CHAPTER CONCLUSION 168
VI.6. BIBLIOGRAPHY 170

CHAPTER VII. NUMERICAL RESULTS 172

VII.1. MODEL PRESENTATION 173
VII.1.1. Uni-axial 173
VII.1.2. Indentation 174
VII.2. CONSTITUTIVE LAWS 177
VII.2.1. Young's moduli and Poisson coefficients 177
VII.2.2. Elasto Plastic G'sell Jonas 177
VII.2.3. Viscoelastic Generalized Maxwell model 179
VII.2.4. Viscoplastic Norton's law 183
VII.3. UNI-AXIAL RELAXATION 186
VII.3.1. Relaxation at 4.88% 186
VII.3.2. Relaxation at 17.69% 187
VII.3.3. Conclusion 188
VII.4. INDENTATION CREEP 188
VII.4.1. CR39 188
VII.4.2. PMMA CN 189
VII.4.3. PMMA 10 AlO(OH) 190
VII.4.4. Law comparison 191
VII.4.5. Conclusion 191
VII.5. INDENTATION RECOVERY 191
VII.5.1. CR39 192
VII.5.2. PMMA CN 192
VII.5.3. Law comparison 193
VII.5.4. Conclusion 194
VII.6. CHAPTER CONCLUSION 194
VII.7. BIBLIOGRAPHY 195

THESIS CONCLUSION 198

TABLE OF ILLUSTRATIONS

FIGURE I-1 CREEP OBSERVATION A) VISION THROUGH THE TIP B) VISION THROUGH THE SAMPLE. RECOVERY OBSERVATION C) VISION THROUGH THE SAMPLE D) AFM OBSERVATION 4
FIGURE I-2 SCRATCH RECOVERY WITH TIME B) 3D GROOVE REPRESENTATION C) LONGITUDINAL PROFILES AT THREE DIFFERENT TIMES 5
FIGURE I-3 3D REPRESENTATION OF A RELAXATION SERIES ON CR39 AT 30°C 6
FIGURE I-4 A) RELAXATION MODULUS FOR CR39 AT 30°C, B) RELAXATION MODULUS MASTER CURVE FOR CR39 AT 30°C WITH 0.75% DEFORMATION AS REFERENCE 7
FIGURE I-5 SHIFT FACTORS FOR THE DIFFERENT MATERIALS VERSUS TRUE STRAIN 8
FIGURE I-6 MEAN CONTACT PRESSURE (A) AND NORMALIZED INDENTATION CREEP DEFORMATION (B) VERSUS CREEP TIME FOR CR39 AND PMMA CN AT 30°C 9
FIGURE I-7 MEAN CONTACT PRESSURE VERSUS TIME AT DIFFERENT TEMPERATURES (STARTING TABOR DEFORMATION EQUAL TO 4%) FOR CR39 (A) NORMAL TIME(B) MASTER CURVE 10
FIGURE I-8 NORMALIZED INDENTATION RECOVERY DEFORMATION VERSUS RECOVERY TIME FOR PMMA CN AND CR39 AT 30°C 11
FIGURE I-9 COMPARISON OF NORMALIZED MASTER CURVES OUT OF RELAXATION AND CONTACT EXPERIMENTS FOR A) CR39 AFTER 1.2S OF SOLICITATION, AT 30°C FOR A DEFORMATION OF 4% AND B) PMMA CN AFTER 10S OF SOLICITATION, AT 30°C FOR A DEFORMATION OF 4% 12
FIGURE I-10 COMPARISON OF NORMALIZED MASTER CURVES OUT OF DMTA, RELAXATION AND CONTACT EXPERIMENTS FOR A) CR39 AFTER 1.2S OF SOLICITATION, AT 30°C FOR A DEFORMATION OF 4% AND B) PMMA CN AFTER 10S OF SOLICITATION, AT 30°C FOR A DEFORMATION OF 4% 13
FIGURE I-11 A) SCHEME SHOWING THE POSITION OF THE DIFFERENT PROFILES B) THREE PROFILES TAKEN AT DIFFERENT TIMES AT A $4A_C$ DISTANCE FROM END OF SCRATCH 13
FIGURE I-12 SCRATCH RECOVERY DEPTH OF CR39 AT 30°C VERSUS TIME AT DIFFERENT DISTANCE OF THE END OF SCRATCH 14
FIGURE I-13A) INFLUENCE OF THE SCRATCHING TABOR DEFORMATION ON THE RECOVERY DEPTH AT A 4 A_C DISTANCE FROM END OF SCRATCH VERSUS TIME ELAPSED SINCE TIP REMOVAL ON CR39 AT 30°C B) SAME EXPERIENCE NORMED BY THE FIRST MEASURED RECOVERY DEPTH 15
FIGURE I-14 NORTON'S LAW FITTED ON RELAXATION EXPERIMENT 16
FIGURE I-15 CR39 MASTER CURVES SHIFTED TO 4.88% DEFORMATION, FITTED WITH A GENERALIZED MAXWELL EQUATION 17
FIGURE I-16 STRESS VERSUS TIME FOR CR39 4.88% DEFORMATION RELAXATION EXPERIMENT AT 30°C FOR EXPERIMENT AND SIMULATIONS A) VE LAWS IDENTIFIED AT 4.88% B) VE LAWS IDENTIFIED AT 17.69% C) EP AND VP LAWS 19
FIGURE I-17 STRESS VERSUS TIME FOR CR39 17.64% DEFORMATION RELAXATION EXPERIMENT AT 30°C FOR EXPERIMENT AND SIMULATIONS A) VE LAWS IDENTIFIED AT 4.88% B) VE LAWS IDENTIFIED AT 17.69% C) EP AND VP LAWS 20
FIGURE I-18 A) MEAN CONTACT PRESSURE AND B) NORMALIZED TABOR INDENTATION CREEP DURING INDENTATION CREEP EXPERIMENT AT 30°C FOR EXPERIENCE AND SIMULATION ON CR39 21
FIGURE I-19 CR39 EXPERIMENTAL AND SIMULATION INDENTATION CREEP RECOVERY 22
FIGURE II-1 OBSERVATION DU FLUAGE A) VISION A TRAVERS LA POINTE B) VISION A TRAVERS L'ECHANTILLON. OBSERVATION DE LA RECOUVRANCE C) VISION A TRAVERS L'ECHANTILLON D) OBSERVATION AFM 31
FIGURE II-2 RECOUVRANCE DE RAYURE AVEC LE TEMPS A) IMAGE INITIALE B) REPRESENTATION 3D DU SILLON C) PROFILES LONGITUDINAUX A TROIS TEMPS DIFFERENTS 32
FIGURE II-3 REPRESENTATION 3D DE LA SERIE D'EXPERIENCE SUR LE CR39 A 30°C 33
FIGURE II-4 A) MODULE DE RELAXATION POUR DU CR39 A 30°C, B) COURBE MAITRESSE DU MODULES DE RELAXATION POUR LE CR39 A 30°C AVEC L'EXPERIENCE A 0.75 % DE DEFORMATION COMME REFERENCE 34
FIGURE II-5 COEFFICIENTS MULTIPLICATEURS POUR LES DIFFERENTS MATERIAUX EN FONCTION DE LA DEFORMATION VRAIE 34

FIGURE II-6 A) PRESSION MOYENNE DE CONTACT ET B) DEFORMATION DE FLUAGE D'INDENTATION NORMEE EN FONCTION DU TEMPS DE FLUAGE POUR DU CR39 ET DU PMMA CN A 30°C 36
FIGURE II-7 PRESSION MOYENNE DE CONTACT EN FONCTION DU TEMPS A DIFFERENTE TEMPERATURE (DEFORMATION INITIALE DE TABOR EGALE A 4 %) POUR LE CR39 A) TEMPS NORMAL B) COURBE MAITRESSE 37
FIGURE II-8 DEFORMATION NORMEE DE RECOUVRANCE D'INDENTATION EN FONCTION DU TEMPS POUR LE PMMA CN ET LE CR39 A 30°C 38
FIGURE II-9 COMPARAISON DE COURBES MAITRESSES NORMALISEES A PARTIR DE FLUAGE DE CONTACT ET DE RELAXATION POUR DU A) CR39 CENTRE APRES UNE SOLLICITATION DE 1.2 S, A UNE TEMPERATURE DE 30°C ET UNE DEFORMATION DE 4 % ET DU B) PMMA CN CENTRE APRES UNE SOLLICITATION DE 10 S, A UNE TEMPERATURE DE 30°C ET UNE DEFORMATION DE 4% 39
FIGURE II-10 COMPARAISON DE COURBES MAITRESSES NORMALISEES A PARTIR DE DMTA, FLUAGE DE CONTACT ET DE RELAXATION POUR DU A) CR39 CENTRE APRES UNE SOLLICITATION DE 1.2 S, A UNE TEMPERATURE DE 30°C ET UNE DEFORMATION DE 4 % ET DU B) PMMA CN CENTRE APRES UNE SOLLICITATION DE 10 S, A UNE TEMPERATURE DE 30°C ET UNE DEFORMATION DE 4% 40
FIGURE II-11 A) SCHEMA REPRESENTANT LES POSITIONS DES DIFFERENTS PROFILS B) TROIS PROFILS A DIFFERENTS INSTANTS A UNE DISTANCE DE 4AC DE LA FIN DE LA RAYURE 41
FIGURE II-12 LA PROFONDEUR DES RAINURES LORS DE LA RECOUVRANCE DU CR39 A 30°C EN FONCTION DU TEMPS A PLUSIEURS DISTANCES DE LA FIN DE LA RAYURE 42
FIGURE II-13 A) INFLUENCE DE LA DEFORMATION DE TABOR EN RAYURE SUR LA PROFONDEUR DE RECOUVRANCE A 4AC DE LA FIN DE LA RAYURE EN FONCTION DU TEMPS ECOULE DEPUIS LE RETRAIT DE LA POINTE DE LA SURFACE DE CR39 A 30°C B) MEME EXPERIENCE DONT LES DONNEES ONT ETE NORMEES PAR LA PREMIERE PROFONDEUR DE RECOUVRANCE MESUREE 43
FIGURE II-14 FIT DE LA LOI DE NORTON SUR DES EXPERIENCES DE RELAXATION 44
FIGURE II-15 COURBE MAITRESSE DU CR39 DECALEE POUR AVOIR L'EXPERIENCE A 4.88 % DE DEFORMATION, AJUSTE AVEC UNE EQUATION DE MAXWELL GENERALISEE 45
FIGURE II-16 LA CONTRAINTE EN FONCTION DU TEMPS POUR DES EXPERIENCES DE RELAXATION FAITE SUR DU CR39 A 30°C A) LOIS VE 4.88 % B) LOIS VE 17.69 % C) LOIS EP ET VP 47
FIGURE II-17 CONTRAINTE EN FONCTION DU TEMPS POUR UN ESSAI DE RELAXATION A 17.69 % DE DEFORMATION ET 30°C A) LOIS VE (E = 4.88 %) ET CM VE (E = 4.88 %) B) LOIS VE (E = 17.69 %) ET CM VE (E = 17.69 %) C) LOIS EP ET VP 48
FIGURE II-18 A) LA PRESSION MOYENNE DE CONTACT ET B) LA DEFORMATION NORMEE DE TABOR EN INDENTATION PENDANT UN ESSAI DE FLUAGE D'INDENTATION SUR DU CR39 EN SIMULATION ET EN EXPERIMENTALE 49
FIGURE II-19 DEFORMATION NORMEE EN RECOUVRANCE DU CR39 POUR DES ESSAIS EXPERIMENTAUX ET EN SIMULATIONS 50
ABBILDUNG III-1 KRIECHBEOBACHTUNG A) DURCH DIE SPITZE B) DURCH DIE PROBE. BEOBACHTUNG DER HEILUNG C) DURCH DIE PROBE D) AFM-AUFNAHME 59
ABBILDUNG III-2 A) KRATZERHEILUNG IM LAUFE DER ZEIT B) 3D-DARSTELLUNG DES RISSES C) LÄNGENPROFILE ZU DREI VERSCHIEDENEN ZEITEN 60
ABBILDUNG III-3 CR39 RELAXATION EXPERIMENT UM 30°C 61
ABBILDUNG III-4 A) RELAXATIONSMODULN VON CR39 BEI 30°C B) RELAXATIONSMODUL-MASTERKURVE FÜR CR39 MIT 0.75 % DEHNUNG ALS REFERENZ 62
ABBILDUNG III-5 VERSCHIEBUNGSFAKTOREN FÜR DIE DREI VERSCHIEDENEN MATERIALIEN GEGEN WAHRE DEHNUNG 62
ABBILDUNG III-6 VERGLEICH ZWISCHEN DEM INDENTATIONS-KRIECHEN VON CR39 UND PMMA BEI 30°C A) DURCHSCHNITTLICHE KONTAKTSPANNUNG GEGEN DIE KRIECHZEIT B) NORMIERTE TABOR-DEHNUNG GEGEN ZEIT 64
ABBILDUNG III-7 DURCHSCHNITTLICHE KONTAKTSPANNUNG GEGEN DIE ZEIT BEI VERSCHIEDENEN TEMPERATUREN (ANFANGS-TABOR DEHNUNG VON 4 %) FÜR CR39 A) NORMAL B) MASTERKURVE 65
ABBILDUNG III-8 NORMIERTE MASTERKURVE FÜR CR39 A) UND PMMA CN B) 67

ABBILDUNG III-9 NORMIERTE INDENTATIONS-HEILUNGSDEHNUNG GEGEN HEILUNGSZEIT VON CR39 UND PMMA BEI 30°C 66
ABBILDUNG III-10 SCHEMATISCHE DARSTELLUNG DER ENTNAHMESTELLEN VERSCHIEDENER PROFILE B) DREI PROFILE, ENTNOMMEN ZU VERSCHIEDENEN ZEITEN BEI EINEM ABSTAND VON $4A_C$ KRATZERENDE 68
ABBILDUNG III-11 KRATZERHEILUNG FÜR CR39 BEI 30°C IM LAUFE DER ZEIT ZU VERSCHIEDENEN ABSTÄNDEN VOM KRATZERENDE 69
ABBILDUNG III-12 A) KRATZERHEILUNG FÜR VERSCHIEDENEN DEHNUNGEN IM LAUFE DER ZEIT FÜR EINEN $4A_C$-ABSTAND VOM KRATZERENDE B) GLEICHES EXPERIMENT NORMIERT AUF DIE ERSTE GEMESSENE TIEFE 70
ABBILDUNG III-13 NORTON GLEICHUNG UND ANGEPASSTE KOEFFIZIENTEN 72
ABBILDUNG III-14 CR39 MASTERKURVE MIT REFERENZ BEI 4,88 % DEHNUNG, ANGEPASST AN DIE MAXWELL GLEICHUNG 72
ABBILDUNG III-15 EXPERIMENTELLE UND SIMULIERTE SPANNUNG GEGEN DIE ZEIT FÜR DAS DEHNUNGSRELAXATIONSEXPERIMENT AN CR39 BEI 4,88 % UND 30°C A) VISKOELASTISCHES MODELL BEI 4,88 % B) VISKOELASTISCHES MODELL BEI 17,69 % C) ELASTOPLASTISCHES UND VISKOPLASTISCHES MODELL 74
ABBILDUNG III-16 EXPERIMENTELLE UND SIMULIERTE SPANNUNG GEGEN DIE ZEIT DES 17,69 %-DEHNUNGSRELAXATIONSEXPERIMENTES MIT CR39 BEI 30°C A) VISKOELASTISCHES MODELL BEI 4,88 % B) VISKOELASTISCHES MODELL BEI 17,69 % C) ELASTOPLASTISCHES UND VISKOPLASTISCHES MODELL 75
ABBILDUNG III-17 A) DURCHSCHNITTLICHE KONTAKTSPANNUNG UND B) NORMIERTE TABOR-DEHNUNG BEI 30°C VON EXPERIMENT UND SIMULATION FÜR CR39 76
ABBILDUNG III-18 EXPERIMENTELLE UND SIMULIERTE HEILUNG IM INDENTATIONS-KRIECHVERSUCH FÜR CR39 77
FIGURE IV-1 STORAGE COMPLIANCE OF POLY(N-OCTYL METHACRYLATE) IN THE TRANSITION ZONE BETWEEN GLASSLIKE AND RUBBERLIKE CONSISTENCY, PLOTTED LOGARITHMICALLY AGAINST FREQUENCY AT 24 TEMPERATURES AS INDICATED [22] B)COMPOSITE CURVE OBTAINED BY PLOTTING THE DATA OF A) WITH REDUCED VARIABLES, REPRESENTING THE BEHAVIOR OVER AN EXTENDED FREQUENCY SCALE AT TEMPERATURE T0=100°C [23] 85
FIGURE IV-2 TEMPERATURE DEPENDENCE OF THE SHIFT FACTOR A_T USED IN PLOTTING FIGURE I 1 B). POINTS, CHOSEN EMPIRICALLY; CURVE FROM EQUATION I 5 [22] 86
FIGURE IV-3 APPARITION OF FREE VOLUME IN A POLYMER AROUND THE GLASS TRANSITION 87
FIGURE IV-4 A) STRESS DISTRIBUTIONS AT THE SURFACE AND ALONG THE AXIS OF SYMMETRY CAUSED BY (LEFT) UNIFORM PRESSURE AND (RIGHT) HERTZ PRESSURE ACTING ON A CIRCULAR AREA RADIUS A [51] B) VON MISES STRESS IN SPHERICAL INDENTATION SIMULATED WITH MSC MARC 89
FIGURE IV-5 A) LOAD VERSUS DISPLACEMENT CURVES OF PP AT DIFFERENT UNLOADING RATES. ALL THREE EXPERIMENTS HAD THE SAME LOADING RATE TO THE SAME PEAK LOAD AND THE SAME HOLDING TIME BEFORE UNLOAD [57] B) ELASTIC MODULUS AS A FUNCTION OF HOLD TIME (PMMA $\boldsymbol{L/L}$ = 0.05 S-1). [58] 90
FIGURE IV-6 A) VISCOELASTIC CHARACTERISTICS EVALUATED BY INDENTATION TEST. MASTER CURVE OF CREEP COMPLIANCE AT A REFERENCE TEMPERATURE OF 313 K [61] B) SUPERPOSITION OF THE MASTER CURVES OF INDENTATION CREEP COMPLIANCES [62] 91
FIGURE IV-7 A) TIME VARIATIONS OF MAXIMUM DEPTH OF IMPRESSION [61] B) AFM CROSS SECTION OF A SHALLOW INDENT RIGHT AFTER THE INDENTATION AND BEFORE ANY THERMAL TREATMENT ABOVE T_G (T = 0) [63] 91
FIGURE IV-8) CREEP PHASE-EVOLUTION OF THE REPRESENTATIVE STRAIN AS A FUNCTION OF THE CREEP TIME FOR DIFFERENT INITIAL RATIOS $<E_0>$- COMPARISON OF EXPERIMENTAL RESULTS WITH THE VISCOELASTIC CONTACT MODEL OF LEE AND RADOK (R = 400 μM, T=30°C, $<E_0>$ FIXED AT T_C = 0.5 S [66] B) RECOVERY PHASE- EVOLUTION OF THE REPRESENTATIVE STRAIN AS A FUNCTION OF THE RECOVERY TIME FOR DIFFERENT INITIAL MEAN CONTACT STRAINS (T=30°C, $T_0=10^5$ S, $<E_0>$ FIXED AT T_C DURING THE CREEP PHASE [66] 92
FIGURE IV-9 A) SCISSION SHEAR STRESS AT THE INTERFACE VERSUS STRAIN RATE B) MASTERCURVES FOR THE SCISSION SHEAR STRESS VERSUS STRAIN RATE AT 20°C. THERE ARE TWO REGIMSES OF SCISSION STRES, BELOW AND ABOVE 10^{-1} S^{-1} [75] 93
FIGURE IV-10 A) A PROFILE OF A SCRATCH TRACE ON A PTFE SURFACE FOR THE APPLIED LOAD OF 15.0 N. THE PROFILE IS PERPENDICULAR TO THE SIDE AND GOES THROUGH THE CENTER OF THE GROOVE [72]. B) TIME-

TEMPERATURE SUPERPOSITION CURVE OF SCRATCH DEPTH VS. TIME FOR CLEARCOAT A. THE REFERENCE TEMPERATURE IS 30°C. A FIRST PLATEAU IS FOLLOWED BY A DECREASE OF THE SCRATCH DEPTH AND THEN BY A SECOND PLATEAU. THE DECREASE OF THE SCRATCH DEPTH OCCURS AT "HEALING TEMPERATURE" [68]. 93
FIGURE IV-11 A) SEM OF FISH-SCALE DAMAGE FOR THERMOPLASTIC OLEFINS [74] B) SEM MICROGRAPH OF SCRATCH PROPERTIES OF EPOXIES WITH DIFFERENT CROSSLINK DENSITIES, POLISHED WITH 3 μM PARTICLE SIZE DIAMOND PASTE, BEING SCRATCHED BY INDENTER WITH RADIUS = 80 NM SHOWING THE SCRATCH MORPHOLOGIES. THE INSET SHOWS THE SCRATCH IN LARGER MAGNIFICATION [79]. 94
FIGURE IV-12 EXPERIMENTAL PICTURE - VISUALIZATION OF RESIDUAL GROOVE FOR DIFFERENT EXPERIMENTAL CONDITION [65] 94
FIGURE IV-13 RHEOLOGICAL MAXWELL MODEL 95
FIGURE IV-14 RHEOLOGICAL KELVIN VOIGT MODEL 96
FIGURE IV-15 A) GENERALIZED MAXWELL MODEL B) GENERALIZED KELVIN-VOIGT MODEL 97
FIGURE IV-16 A) CREEP RESPONSE FOR HOLD PERIOD OF 20 S AT 10MN ON A 1 μM AL FILM ON SILICON WITH A SPHERICAL INDENTER 20 μM NOMINAL RADIUS (36 μM ACTUAL RADIUS). DATA POINTS SHOW EXPERIMENTAL RESULTS. THE SOLID LINE SHOWS THE FITTED RESPONSE ACCORDING TO EQUATION IV-32 (THREE-ELEMENT VOIGT MODEL). THE DOTTED LINE SHOWS THE RESPONSE ACCORDING TO EQUATION IV-31 (TWO-ELEMENT MAXWELL MODEL). [54] B) URETHANE INDENTATION RAMP-AND-HOLD CREEP EXPERIMENTAL DATA (OPEN SYMBOLS) FOR THREE DIFFERENT LOADING PROTOCOLS: P_{MAX} = 10 MN, T_R = 20 AND 200 S; P_{MAX} = 1 MN, T_R = 20 S. THE CREEP PORTION OF THE 10 MN, 20 S DATA WERE FIT TO OBTAIN CREEP FUNCTION PARAMETERS. PREDICTIONS (SOLID LINES) WERE MADE FOR THE FULL RAMP-HOLD RESPONSES FOR EACH LOAD–RISE TIME COMBINATION USING THE PARAMETERS OBTAINED IN THE SINGLE CREEP FIT AND THE TWO-TIME CONSTANT RELAXATION FUNCTION [80] 99
FIGURE IV-17 A) EXAMPLE AXISYMMETRIC (RIGID) HEMISPHERE AND FINITE ELEMENT MESH [82]. B) FINITE ELEMENT MESH, WITH MESH REFINEMENT [34] 100
FIGURE IV-18 FORCE-PENETRATION CURVES DURING LOADING FOR A POLYCARBONATE. COMPARISON BETWEEN THE EXPERIMENTAL CURVES (BERKOVICH INDENTER) AND THE NUMERICAL CURVES (μ = 0, P = 0 NM AND P = 455 NM). FOR MORE LEGIBILITY THE CURVES FOR THE INTERMEDIATE LOADING RATE (C = 0.01 S-1) ARE NOT PLOTTED. (A) P = 0 NM. (B) P = 455 NM. [83] 101
FIGURE IV-19 A) FLAT-TIP INDENTATION SYMBOLS ARE EXPERIMENTS ; LINES ARE RESULT OF MODELING USING THE MULTI-MODE EGP-MODEL B) LOAD VERSUS DISPLACEMENT CURVE FOR A NOTCHED TENSILE BAR; SYMBOLS ARE EXPERIMENTS; LINE IS COMPUTATIONAL RESULT WITHOUT FAILURE CRITERION. 102
FIGURE IV-20 TRUE STRESS VS TRUE STRAIN IN UNIAXIAL COMPRESSION, MODEL PREDICTION (SOLID LINES) COMPARED TO EXPERIMENTAL RESULTS (SYMBOLS) A) FOR DIFFERENT STRAIN RATES B) FOR DIFFERENT INITIAL STATES AT A STRAIN RATE OF 10-4 S^{-1}. [91] 102
FIGURE V-1 SCHEME OF A) METHYL METHACRYLATE MONOMER AND B) POLY (METHYL METHACRYLATE) 112
FIGURE V-2 EXAMPLE OF PMMA UTILIZATION A PLASTIC WINDOW FOR HOUSES 112
FIGURE V-3 CR39 UTILIZATION EXAMPLE [1] 113
FIGURE V-4 A) SCHEME OF ALLYL DIGLYCOL B) SCHEME OF CR39 NETWORK 113
FIGURE V-5 EXAMPLE OF SURFACE DIRTINESS AND RUGOSITY AFTER USE OF A TEFLON SPRAY 116
FIGURE V-6 KAPTON FILM AS IT LOOKS BEFORE USE 117
FIGURE V-7 A) UNIAXIAL TENSILE MACHINE B)UNIAXIAL SAMPLE POSITIONED IN THE MACHINE WITH LONGITUDINAL AND AXIAL EXTENSOMETERS C)UNIAXIAL SAMPLE (TRANSPARENT POLYMER) WITH LONGITUDINAL EXTENSOMETER 117
FIGURE V-8 UNIAXIAL SAMPLES SCHEMES WITH GEOMETRICAL INFORMATION 118
FIGURE V-9 RELAXATION EXPERIMENT PRESENTED WITH ENGINEERING STRESS AND STRAIN 119
FIGURE V-10 A) STRESS VERSUS STRAIN FOR DMTA EXPERIMENT AT 30°C AND 0.5HZ B) CR39 YOUNG'S MODULUS AND MECHANICAL LOSS IN FUNCTION OF TEMPERATURE AT 0.05HZ 119
FIGURE V-11 TRUE STRESS AND STRAIN VERSUS TIME FOR A RELAXATION TEST ON CR39 AT 30°C 121
FIGURE V-12 A) STRESS AND DEFORMATION VERSUS TIME FOR A CREEP TEST ON CR39 AT 30°C B) STRESS AND STRAIN VERSUS TIME FOR CREEP RECOVERY ON CR39 AT 30°C 121
FIGURE V-13 SCHEMATIC REPRESENTATION OF CONTACT BETWEEN TWO SOLID MATERIALS 122

FIGURE V-14 A) SCHEMATIC REPRESENTATION OF THE HARD SPHERE-SOFT PLANE CONTACT AND SIZE DEFINITION B) DEFINITION OF THE RECOVERY RADIUS AND IMPRINT CURVATURE 123
FIGURE V-15 A) FORCE AND DEPTH VERSUS TIME FOR AN INDENTATION CREEP ON CR39 AT ROOM TEMPERATURE B) LOAD-DEPTH INDENTATION CURVE ON CR39 AT 30°C 124
FIGURE V-16 AFM RECOVERY OBSERVATION AFTER NANO-INDENTATION ON CR39 AT 30°C 125
FIGURE V-17 NANO-INDENTER PHOTOGRAPHY AND LEGEND 125
FIGURE V-18 NANO-INDENTATION CREEP OBSERVATION OF CR39 AT 30°C WITH CSM NANO-INDENTER IN SITU OPTICAL SYSTEM 126
FIGURE V-19 MICRO VISIO SCRATCH SCHEMATIC REPRESENTATION 127
FIGURE V-20 FORCE AND CONTACT RADIUS WITH TIME FOR A MICRO INDENTATION 127
FIGURE V-21 MICRO-INDENTATION IN SITU OBSERVATION ON CR39 AT 30°C 128
FIGURE V-22 IN SITU RECOVERY OBSERVATION AFTER MICRO-INDENTATION ON CR39 AT 30°C "CONTACT" RADIUS MEASUREMENT 128
FIGURE V-23 IN SITU RECOVERY OBSERVATION AFTER MICRO-INDENTATION ON CR39 MEASUREMENT OF R(T) . 129
FIGURE V-24 A) MEASURED "CONTACT" RECOVERY RADIUS AND FITTED RADIUS OF RECOVERY IMPRINT B) COMPARISON BETWEEN DIFFERENT METHOD FOR MEASURING DEFORMATION RECOVERY 129
FIGURE V-25 INDENTER ENABLING VISION THROUGH THE TIP R=3300μM 130
FIGURE V-26 MACRO-INDENTER WITH VISION THROUGH THE TIP PRINCIPLE 131
FIGURE V-27 CREEP IMPRINT OBSERVATION IN MACRO INDENTATION 131
FIGURE V-28 A) 29 COMPARISON BETWEEN TWO INDENTATION SYSTEM MICROVISIOSCRATCH AND INSTRON, WITH TWO DIFFERENT VISION METHODS B) COMPARISON BETWEEN TWO INDENTATION SYSTEMS: NANO INDENTER AND MICROVISIOSCRATCH 132
FIGURE V-30 IN SITU GROOVE FORMATION FOR THREE SCRATCHING VELOCITY DECADES 132
FIGURE V-31 A) GROOVE RECOVERY PICTURE B) 3D REPRESENTATION OF THE SURFACE 133
FIGURE V-32 FROM THE 3D SURFACE THE PRESENTED RED PROFILE ARE EXTRACTED 133
FIGURE V-33 PROFILE ANALYSIS TO RECOVER DEPTH AND GROOVE WIDTH 134
FIGURE V-34 SAMPLE MICROSCOPE OBSERVATION 134
FIGURE V-35 TYPICAL RESULTS PRESENTING PMMA CN VITREOUS TRANSITION 135
FIGURE V-36 FILLED POLYMER TEM PICTURE OF SIO2 FILLED PMMA 136
FIGURE VI-1 COMPARISON OF DYNAMIC MECHANICAL THERMAL ANALYSIS EXPERIMENT FOR CR39, PMMA CN AND PMMA 10 ALO(OH) AT 0.05 HZ 140
FIGURE VI-2 A) DMTA EXPERIMENT ON CR39 AT DIFFERENT TEMPERATURE AND FREQUENCY B) FREQUENCY TEMPERATURE MASTER CURVES FROM THE PREVIOUS DATA 140
FIGURE VI-3 TIME-TEMPERATURE MASTER CURVES FOR CR39, PMMA CN AND PMMA 10 ALO(OH) 141
FIGURE VI-4 3D REPRESENTATION OF A RELAXATION SERIES ON CR39 AT 30°C (REPRODUCTION OF FIGURE I-3) 142
FIGURE VI-5 3D REPRESENTATION OF RELAXATION SERIES ON PMMA CN AT 30°C 142
FIGURE VI-6 3D REPRESENTATION OF RELAXATION SERIES ON PMMA 10 ALO(OH) AT 30°C 143
FIGURE VI-7 A) RELAXATION MODULUS FOR CR39 AT 30°C, B) RELAXATION MODULUS MASTER CURVE FOR CR39 AT 30°C WITH 0.75% DEFORMATION AS REFERENCE (REPRODUCTION OF FIGURE I-4) 144
FIGURE VI-8 A) RELAXATION MODULUS FOR PMMA AT 30°C B) RELAXATION MODULUS MASTER CURVE FOR PMMA AT 30°C WITH 0.75% DEFORMATION AS REFERENCE 144
FIGURE VI-9 A) RELAXATION MODULUS FOR PMMA 10ALO(OH) AT 30°C B) RELAXATION MODULUS MASTER CURVE FOR PMMA 10 ALO(OH) AT 30°C WITH 0.75% DEFORMATION AS REFERENCE 145
FIGURE VI-10 SHIFT FACTORS FOR THE DIFFERENT MATERIALS VERSUS TRUE STRAIN (REPRODUCTION OF FIGURE I-5) 146
FIGURE VI-11 COMBINATION OF THE TIME TEMPERATURE AND THE TIME-DEFORMATION FOR A) CR39, B) PMMA CN AND C) PMMA 10 ALO(OH) 147
FIGURE VI-12 INFLUENCE ON THE EXPERIMENTAL RELAXATION MODULUS OF CR39 DEPENDING ON AMBIENT ATMOSPHERE 148

FIGURE VI-13 MEAN CONTACT PRESSURE (A) AND NORMALIZED INDENTATION CREEP DEFORMATION (B) VERSUS CREEP TIME FOR CR39 AND PMMA AT 30°C (REPRODUCTION OF FIGURE I-6) 149
FIGURE VI-14 MEAN CONTACT PRESSURE VERSUS TIME AT DIFFERENT TEMPERATURES (STARTING TABOR DEFORMATION EQUAL TO 4%) FOR CR39 (A) AND PMMA CN (B) 150
FIGURE VI-15 MEAN CONTACT PRESSURE MASTER CURVE OF CR39 (A) AND PMMA CN, CHOSEN TEMPERATURE REFERENCE IS 30°C 150
FIGURE VI-16 NORMALIZED CREEP TABOR DEFORMATION VERSUS TIME BELOW (A) AND ABOVE (B) THE GLASS TEMPERATURE OF CR39 151
FIGURE VI-17 NORMALIZED INDENTATION CREEP DEFORMATION VERSUS CREEP TIME FOR PMMA CN AT DIFFERENT TEMPERATURE 152
FIGURE VI-18 NORMALIZED INDENTATION RECOVERY DEFORMATION VERSUS RECOVERY TIME FOR PMMA AND CR39 AT 30°C (REPRODUCTION OF FIGURE I-8) 153
FIGURE VI-19 NORMALIZED INDENTATION RECOVERY DEFORMATION VERSUS RECOVERY TIME FOR CR39 AT TEMPERATURE BELOW (A) AND ABOVE GLASS TEMPERATURE 154
FIGURE VI-20 NORMALIZED INDENTATION RECOVERY DEFORMATION VERSUS RECOVERY TIME FOR PMMA CN AT DIFFERENT TEMPERATURES 154
FIGURE VI-21 CR39 (A) AND PMMA CN (B) NORMALIZED INDENTATION RECOVERY DEFORMATION VERSUS TIME AT 30°C AFTER DIFFERENT CREEP HOLDING TIME 155
FIGURE VI-22 COMPARISON OF NORMALIZED MASTER CURVES OUT OF RELAXATION AND CONTACT EXPERIMENTS FOR A) CR39 CENTERED AFTER 1.2 S OF SOLICITATION, AT 30°C FOR A DEFORMATION OF 4% AND B) PMMA CN CENTERED AFTER 10 S OF SOLICITATION, AT 30°C FOR A DEFORMATION OF 4% 157
FIGURE VI-23 COMPARISON OF NORMALIZED MASTER CURVES OUT OF DMTA, RELAXATION AND CONTACT EXPERIMENTS FOR A) CR39 CENTERED AFTER 1.2S OF SOLICITATION, AT 30°C FOR A DEFORMATION OF 4% AND B) PMMA CN CENTERED AFTER 10S OF SOLICITATION, AT 30°C FOR A DEFORMATION OF 4% 157
FIGURE VI-24 THREE PROFILES TAKEN AT DIFFERENT TIMES AT A 4AC DISTANCE FROM END OF SCRATCH 158
FIGURE VI-25 SCRATCH RECOVERY DEPTH OF CR39 AT 30°C VERSUS TIME AT DIFFERENT DISTANCES OF THE END OF SCRATCH (REPRODUCTION OF FIGURE I-12) 159
FIGURE VI-26 RECOVERY WIDTH AT A 4AC DISTANCE FROM END OF SCRATCH VERSUS TIME SINCE TIP REMOVAL ON CR39 ON AN EXPERIMENT WITH SLOW TIP SPEED (1 μM/S, 2.5 N) 159
FIGURE VI-27 A) DEPTH RECOVERY, AT END AND IN FRONT OF SCRATCH, VERSUS RECOVERY TIME AFTER A SCRATCH AT P_M = 100 MPA AND 10 μM/S B) RECOVERY CONTACT DEPTH AFTER INDENTATION AT P_M = 125 MPA ON CR39 IN BOTH CASES 160
FIGURE VI-28 A) INFLUENCE OF THE SCRATCHING TABOR DEFORMATION ON THE RECOVERY DEPTH AT A 4 A_C DISTANCE FROM END OF SCRATCH VERSUS TIME ELAPSED SINCE TIP REMOVAL ON CR39 AT 30°C B) SAME EXPERIENCE NORMED BY THE FIRST MEASURED RECOVERY DEPTH (REPRODUCTION OF FIGURE I-13) 161
FIGURE VI-29 A) INFLUENCE OF THE SCRATCHING SPEED ON THE RECOVERY DEPTH AT A 4 A_C DISTANCE FROM THE END OF SCRATCH VERSUS TIME SINCE TIP REMOVAL ON CR39 AT 30°C B) MASTER CURVE OBTAINED BY LATERALLY SHIFTING THE PREVIOUS DATA 161
FIGURE VI-30 TEM PICTURE PMMA FILLED WITH A) 10% OF NANOPOX B) 20% NANOPOX C) 10%ALO(OH) 163
FIGURE VI-31 COMPARISON OF DMTA EXPERIMENT FOR DIFFERENT FILLERS (A) OR DIFFERENT FILLERS QUANTITY (B) AT 0.05HZ 164
FIGURE VI-32 A) MEAN CONTACT PRESSURE OVER TIME AND B) NORMALIZED INDENTATION CREEP AT 30°C FOR PMMA FILLED WITH ALO(OH) AND NANOPOX 165
FIGURE VI-33 PREDICTION OF THE MEAN CONTACT PRESSURE VERSUS TIME THROUGH RELAXATION AND DMTA EXPERIMENT 165
FIGURE VI-34 TEM PICTURES OF PMMA 2.5 STA(A) PMMA 2.5STT (B) AND PMMA 2.5 NANOPOL (C) 166
FIGURE VI-35 COMPARISON OF DMTA EXPERIMENT FOR PMMA CHARGED WITH DIFFERENT STÖBER PARTICLES AT 0.05HZ 167
FIGURE VI-36 MEAN CONTACT PRESSURE (A) AND NORMALIZED INDENTATION CREEP DEFORMATION (B) VERSUS CREEP TIME FOR PMMA FILLED WITH STOBER ACRYLATE, STOBER THIOL OR NANOPOL PARTICLES AT 30°C 168
FIGURE VII-1 USED UNI AXIAL MODEL, LEFT WITHOUT LOAD, RIGHT LOADED (VON MISES STRESS) 173

FIGURE VII-2 THE EXPERIMENTAL BEAM DISPLACEMENT AND THE CALCULATED, BY FEM, STRESS VERSUS TIME INPUT AND OUTPUT RESPECTIVELY OF THE UNI AXIAL SIMULATION 174
FIGURE VII-3 A) SHEMATIC REPRESENTATION OF THE INDENTATION MODEL B) INDENTATION MODEL USED IN MSC MARC C) ZOOM ON THE VOLUME BELOW THE CONTACT DURING EXPERIMENT 175
FIGURE VII-4 LOAD AND CONTACT RADII VERSUS EXPERIMENTAL TIME, RESPECTIVELY INPUT AND OUTPUT OF THE FEM INDENTATION MODEL 176
FIGURE VII-5 A) INDENTATION RECOVERY HALF PROFILE AND ITS DRIFT VERSUS DISTANCE FROM SYMMETRY AXIS B) RECOVERY CONTACT RADIUS AND RECOVERY CURVATURE RADIUS VERSUS RECOVERY TIME 176
FIGURE VII-6 YOUNG'S MODULI AND POISSON COEFFICIENT FOR CR39 PMMA AND PMMA 10 ALO(OH) VERSUS TEMPERATURE 177
FIGURE VII-7 INTRODUCED G'SELL JONAS LAW IN MARC MENTAT FOR CR39 AND PMMA CN 178
FIGURE VII-8 GENERALIZED MAXWELL MODEL WITH 8 TIME CONSTANTS 179
FIGURE VII-9 CR39 4.88% RELAXATION SHEAR MODULUS VERSUS TIME AT 30°C, FIT WITH GENERALIZED MAXWELL FORMULA AND FIT ERROR 180
FIGURE VII-10 CR39 MASTER CURVES SHIFTED TO 4.88% DEFORMATION, FITTED WITH A GENERALIZED MAXWELL EQUATION (REPRODUCTION OF FIGURE I-15) 181
FIGURE VII-11 A) CR39, B) PMMA CN C) PMMA 10 ALO(OH) RELAXATION EXPERIMENTAL SET AT 30°C (DOTS) AND THE FITTED NORTON'S LAW SURFACE 185
FIGURE VII-12 STRESS VERSUS TIME FOR CR39 4.88% DEFORMATION RELAXATION EXPERIMENT AT 30°C FOR EXPERIMENT AND SIMULATIONS A) VE LAWS IDENTIFIED AT 4.88% B) VE LAWS IDENTIFIED AT 17.69% C) EP AND VP LAWS (REPRODUCTION OF FIGURE I-16) 187
FIGURE VII-13 STRESS VERSUS TIME FOR CR39 17.64% DEFORMATION RELAXATION EXPERIMENT AT 30°C FOR EXPERIMENT AND SIMULATIONS A) VE LAWS IDENTIFIED AT 4.88% B) VE LAWS IDENTIFIED AT 17.69% C) EP AND VP LAWS (REPRODUCTION OF FIGURE I-17) 188
FIGURE VII-14 A) MEAN CONTACT PRESSURE AND B) NORMALIZED TABOR INDENTATION CREEP DURING INDENTATION CREEP EXPERIMENT AT 30°C FOR EXPERIENCE AND SIMULATION ON CR39 (REPRODUCTION OF FIGURE I-18) 189
FIGURE VII-15) MEAN CONTACT PRESSURE AND B) NORMALIZED TABOR INDENTATION CREEP DURING INDENTATION CREEP EXPERIMENT AT 30°C FOR EXPERIENCE AND SIMULATION ON PMMA CN 190
FIGURE VII-16) MEAN CONTACT PRESSURE AND B) NORMALIZED TABOR INDENTATION CREEP DURING INDENTATION CREEP EXPERIMENT AT 30°C FOR EXPERIENCE AND SIMULATION ON PMMA 10 ALO(OH) 190
FIGURE VII-17 COMPARISON BETWEEN THE SIMULATION RESULTING FROM THE DIFFERENT LAWS 191
FIGURE VII-18 CR39 EXPERIMENTAL AND SIMULATION INDENTATION CREEP RECOVERY (REPRODUCTION OF FIGURE I-19) 192
FIGURE VII-19 PMMA EXPERIMENTAL AND SIMULATION INDENTATION CREEP RECOVERY 193
FIGURE VII-20 CR39, PMMA CN AND PMMA 10 ALO(OH) SIMULATION INDENTATION CREEP RECOVERY 194

CHAPTER I. SUMMARY

CHAPTER I. SUMMARY 2
I.1. INTRODUCTION 3
I.2. EXPERIMENTAL METHODS AND TECHNIQUES 3
I.3. BULK MECHANICAL PROPERTIES 5
I.3.1. Relaxation 5
I.3.2. Relaxation modulus and master curves 6
I.3.3. Conclusion 8
I.4. CONTACT ANALYSIS 8
I.4.1. Indentation Creep 8
I.4.2. Indentation Recovery 10
I.4.3. Master curves comparison 11
I.4.4. Scratch recovery analysis 13
I.4.5. Conclusion 15
I.5. FINITE ELEMENT MODELING 16
I.5.1. Constitutive laws 16
I.5.2. Uni-axial Relaxation 18
I.5.3. Indentation 20
I.5.4. Conclusion 22
I.6. GENERAL CONCLUSION 22
I.7. BIBLIOGRAPHY 24

I.1. INTRODUCTION

Due to their low weight, polymer materials have nowadays lots of applications [1]. Moreover, polymers generally have a good resistance to atmospherics conditions. Therefore they are used as layer to protect surfaces (paint, smartphones …) or in composites as the matrix (tire, boat shell). Unfortunately polymers also present a poor resistance to mechanical damages in particular scratches. Scratches and mar [2] can lead to a strong decrease of other optical, esthetical properties [3, 4]. To avoid this loss, materials must either be non scratching or curing materials. On the contrary curing materials exist and have multiples applications: lenses, nail polish, tactile screen or paints [5]. There are two major ways to improve the curing: either protect the bulk material with a thin layer or improve the bulk resistance by modifying the material by introducing fillers (nano-charges) in the matrix in order to create a composite. During this PhD thesis, the main objective deals with a better understanding of the relationship between mechanical properties of charged polymers and their scratch resistance and more generally their contact behavior. In particular, two aspects of these behaviors are the polymer long time behavior and the recovery. This thesis is part of the International Research Training Group (IRTG Soft Matter).

Charged polymers samples were realized at the Freiburg Institut for Advanced studies. In particular reinforced Poly Methyl MethAcrylate (PMMA) with various form of SiO_2 particles were prepared to serve as model for composite materials. The mechanical characterization was held in Institut Charles Sadron in Strasbourg.

I.2. EXPERIMENTAL METHODS AND TECHNIQUES

The classical characterization of polymers is performed by uni-axial tests. These experiments consist in applying a constant strain or a constant stress and measuring the other one. A perfect material (purely elastic, elasto plastic) reacts instantly to the imposed mechanical constraints. This is generally the case for ceramics and metals at room temperature. On the contrary, viscous phenomena are observed for polymers. To characterize viscoelastic and/or viscoplastic properties, relaxation and creep tests are performed. Stress and strain evolutions at constant strain or stress can thus, respectively, be measured as a function of time. Nevertheless as polymers are used as protective layers, bulk measurements are not appropriated and not always possible. The standard hardness measurements are done by applying a dead weight on a surface and then observe the residual imprint. In this case only the residual plasticity can be measured. In order to have a better understanding, more recent instruments record the load and depth during indentation. Then the elastic material properties are determined through the Hertz equation [6]. For the elasto-plastic materials the analysis of the load depth curves during unloading phase (assumed to be elastic) leads with Oliver & Pharr model to the Young's modulus and the material hardness [7, 8]. But for polymers [9] and bones [10] the Oliver & Pharr model is not accurate. Indeed these materials present viscous properties (not taken into account in the model) and the analysis results are test dependent ("nose-problem") [11]. Furthermore the penetration depth is the combination of the deflection, more important in case of polymers than for metals, and

contact depth. Deflection is mainly elastic whereas contact penetration is a combination of elastic, viscoelastic, viscoplastic and plastic properties.

For instance, no analytical model is available to separate all contributions and then estimate with sufficient accuracy the true contact depth during indentation in case of polymeric surfaces. One way to avoid the use of analytical model consists in observing directly the contact through the sample (transparent material) [4, 12] or through the tip (using spherical glass indenter). We have developed a specific system Microvisioscratch to this aim [4].

However, when using spherical indenter for constant load creep, the contact area will increase thus the Tabor's [13] strain increases whereas the average pressure decreases during experiment. Due to this effect, the indentation creep test appears as a complex experiment, but close to real polymer degradation during static contact between two functionalized surfaces. Typical creep observations obtained by our Microvisioscratch system are presented in Figure I-1 a) and b). This specific apparatus enables to see, as a function of time, both the contact between the tip and the deformed surface during indentation phase at constant applied load (Figure I-1 b) and the recovery phase (Figure I-1 c) immediately after withdrawal of the tip [14]. Unfortunately, non transparent materials cannot be characterized using our Microvisioscratch system. Instead of looking through (when samples are transparent), the observation was done through the indenter tip. In order to be able to observe an image with sufficient accuracy to estimate contact radius, a high indenter tip radius is needed (at least 3.3 mm). With such indenters very important loads are imposed to obtain a non-purely elastic deformation [14]. Figure I-1 a) shows in situ observation obtained by a homemade macro indentation machine built in an Instron tensile machine developed during this PhD. These characterizations were conducted over the temperature range [-40°C; +95°C], which corresponds to the utilization temperature of polymers in general.

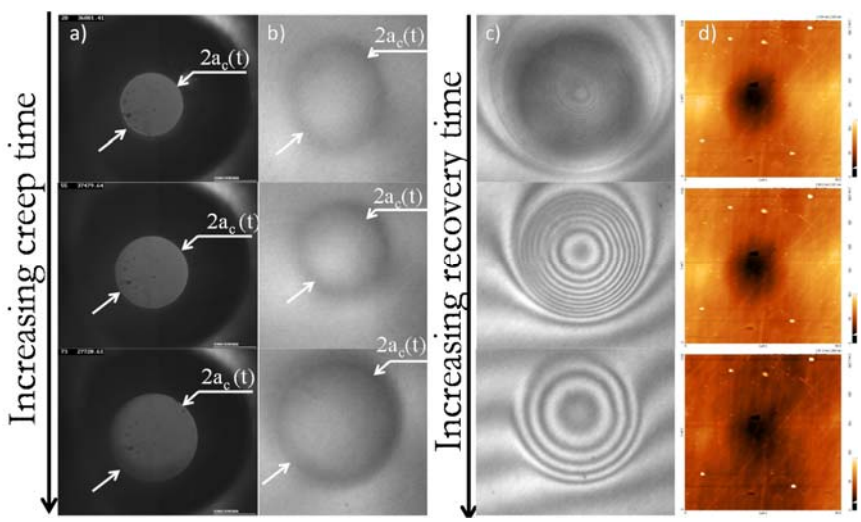

Figure I-1 Creep observation a) vision through the tip b) vision through the sample. Recovery observation c) vision through the sample d) AFM observation

In a degradation process, due to contact, there are two distinct phases: the contact phase and the healing phase. Contrary to metals and ceramics, which do not recover, the recovery phenomenon is an important step to characterize polymer resistance to contact load bearing. Generally, the residual imprint or scratching, respectively after indentation or groove, are measured post-

mortem by AFM (see example in Figure I-1 d)) or profilometry [15, 16]. The difficulty is the delay between end of contact and the end of imaging process. Unfortunately the major changes or evolutions of the residual imprint or groove, related to viscoelastic behavior, are observed during this corresponding time [17]. Thanks to the Microvisioscratch system [14] first images are taken after 0.5 s, that is to say, just after the complete withdrawal of the tip. Furthermore in our case the creep and recovery are observed for a long period of time (generally more than 24 hours each). As observed in Figure I-1, a multi-tools approach can be now conducted from the macro-contact to micro-contact.

Mechanical characterization of polymeric surfaces is also done by scratch experiments too [18]. First descriptions of the groove recovery were given by several authors [18-20]. Nevertheless, no information was given before 15 minutes. In our case the recovery phase is observed (Figure I-2 a)) with the Microvisioscratch system. Then the images is computed into a 3D representation (Figure I-2 b)) of the sample. Finally some profiles are extracted. Figure I-2 c) presents the longitudinal profile with time. Moreover some cross profile at a given distance of the end of scratch are also extracted. The distance to the end of the scratch is chosen relatively to the contact radius (a_c) during scratch. Thus the chosen distances are multiples of a_c, the more extensively studied are 4 a_c and 9 a_c. For many of them the groove width and depth are measured and analyzed.

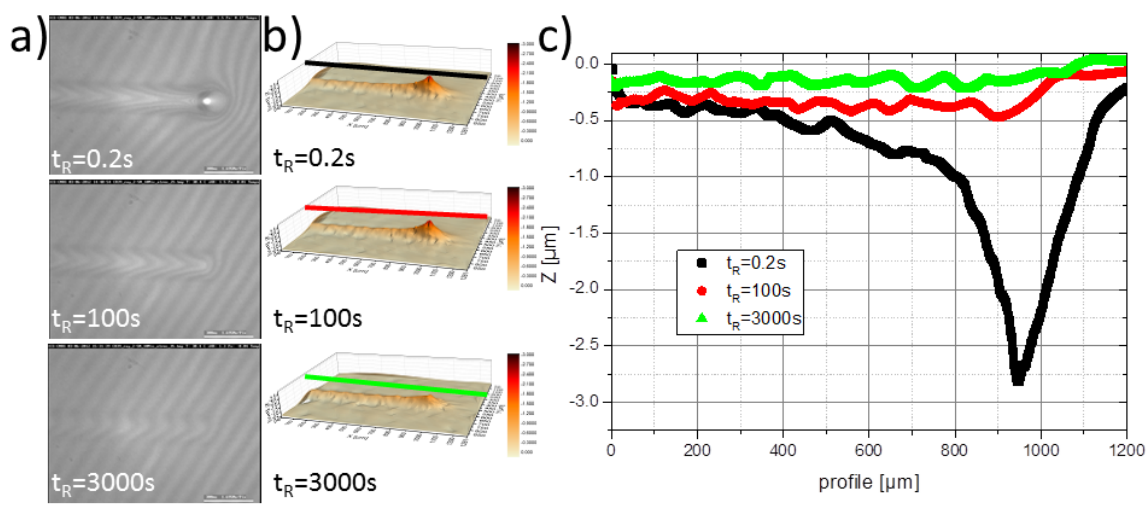

Figure I-2 scratch recovery with time b) 3D groove representation c) longitudinal profiles at three different times

I.3. BULK MECHANICAL PROPERTIES

In this chapter part, the bulk mechanical properties of the CR39, PMMA CN and PMMA 10 AlO(OH) are observed. First, DMTA experiment results were done. Secondly relaxation experiments are presented. Thirdly the relaxation experiments are used to construct master curves.

I.3.1. Relaxation

The instantaneous elasticity does not reflect all the possibility of the polymeric material. Indeed, Struick [21] and other authors [22, 23] observed polymeric time dependency by creep or

relaxation experiments. We chose to do compression relaxation. The compression was chosen because it is closer to indentation. The relaxation experiments were chosen because MSC Marc viscoelasticity relates to relaxation formalism [24].

Figure I-3 presents the true stress versus true deformation and time for CR39 at 30°C. For all the curves, 10 times the loading time are removed to prevent the observation from loading effects. The darkening gradient is used for an increasing deformation level [0.75-22%]. For each experiment the stress gradually declines over time. Furthermore, for CR39 (Figure I-3), the starting stresses grow up over deformation until 4% deformation (black dotted line). Then the starting stress drops by 10% and finally increases again (black dashed line). The material elasticity is responsible for the experimental starting stress at low deformation. Then when time and/or deformation increase CR39 time dependent elasticity evolves. At very high deformation the cross-linking blocks the material flow and thus increase the stress again. CR39 is elastic then viscoelastic. Some other experiments (temperature dependence) are available in VI.2.2.

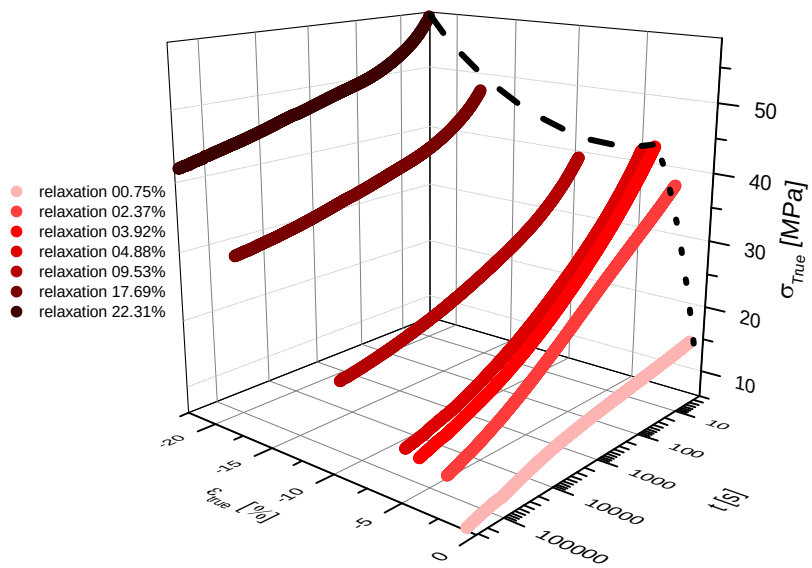

Figure I-3 3D representation of a relaxation series on CR39 at 30°C

I.3.2. Relaxation modulus and master curves

These experimental sets are used to calculate the relaxation modulus over time (see Equation V-11). Figure I-4 represents the CR39 elastic moduli versus time. For each curve the relaxation modulus is decreasing. The higher deformation leads to smaller relaxation modulus. Finally the 0.75% deformation relaxation is convex whereas all higher deformation relaxations are concave. Master curves versus strain and temperature, were already proposed by several authors on high density Poly-ethylene (HDPE) [25], Polypropylene [23, 26], polycarbonate (PC) [27, 28] or Poly(vinyl acetate) [29]. By translating (horizontally uniquely) Figure I-4 a) curves, one can construct a master curve of the relaxation modulus. To do so a reference is chosen: the relaxation at 0.75% deformation. Then the experimental time is multiplied by a shift factor called a_T. The obtained curve is shown in Figure I-4 b). The strong decrease of relaxation modulus over

deformation is now present over time. Indeed the relaxation modulus dramatically drops to 10% of its initial value after 30 million centuries. At this point the relaxation modulus seems to reach a plateau. This is probably due to the CR39 cross-linking that blocks the flow. Finally the truncated and inverted "S-like" observed shape can be related to three different regime of relaxation: elastic (not presented in the figure and related to instantaneous response), short time viscoelasticity, long time viscoelasticity.

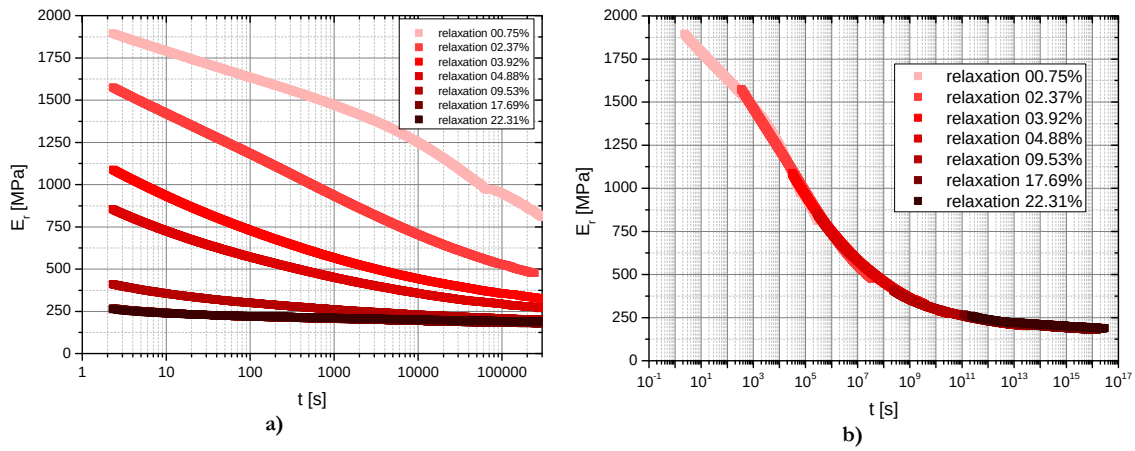

Figure I-4 a) Relaxation modulus for CR39 at 30°C, b) relaxation modulus master curve for CR39 at 30°C with 0.75% deformation as reference

The shift factors, used for the relaxation moduli, are plotted versus the true deformation in Figure I-5 for all the available materials. As all the master curves were taken relative to the smaller deformations, in all cases the first point is [0.75%, 1]. CR39 (red square) shift factors steadily increase up to 5% true deformation. Then between 5 and 25 % true deformation there is a gradual increase. PMMA CN (blue circles) and PMMA 10 AlO(OH) (green triangles) have very similar behaviors. The shift factors increase linearly versus deformation up to 5%. The CR39 shift factors increase slow down whereas above 5% true deformation, the shift factors for PMMA CN and PMMA 10 AlO(OH) continue to increase almost linearly. CR39 shift factors stagnation suggests that above 5% the cross-linking slows down the material flow. On the contrary PMMA CN and PMMA 10 AlO(OH), the flow is almost proportional to the imposed deformation. As both PMMA have the same flow behavior, let us conclude that the fillers do not block the creep process into the material.

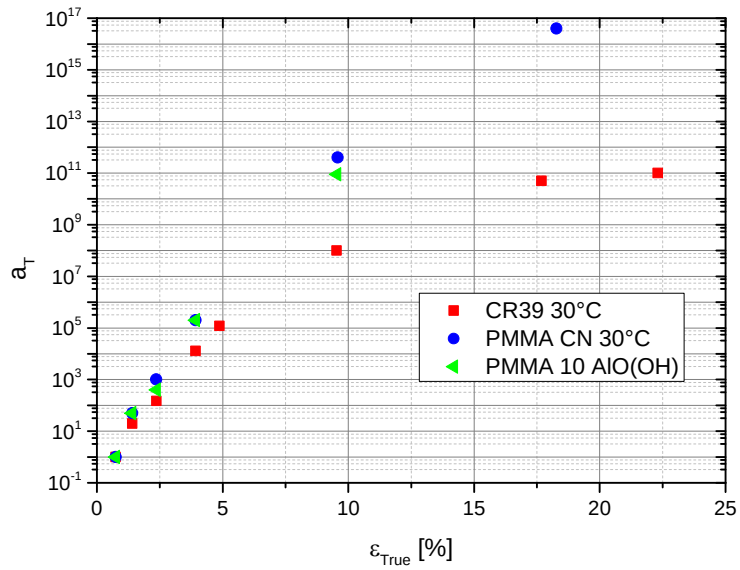

Figure I-5 Shift factors for the different materials versus true strain

I.3.3. Conclusion

The bulk mechanical properties of CR39, PMMA CN and PMMA 10 AlO(OH) were analyzed by DMTA and relaxation experiment over long times. The construction of master curves at the glance of 0.75% enables the prediction of the material viscoelastic behavior over centuries.

I.4. CONTACT ANALYSIS

I.4.1. Indentation Creep

Indentation creep of CR39 and PMMA CN polymers is first conducted at room temperature. Very long indentation creep times are used. Then a set of temperatures is chosen to cover the utilization temperature of polymers in general.

I.4.1.1 Room temperature

The creep comparison of CR39 and PMMA CN is presented in Figure I-6. The mean contact pressure (left) is displayed versus indentation time. All the creep loads are chosen so that the initial Tabor deformations are equal to 0.2 [13]. Nonetheless the starting mean contact pressure of CR39 and PMMA CN follow the observed ratio in DMTA. CR39 mean contact pressure decreases linearly versus logarithm of time. On the contrary PMMA CN mean contact pressure decrease seems to have two distinct slopes. The first is below 100 s, the second is above 1000 s. Although the initial deformation is the same, the path of the normalized deformation is different for each material (Figure I-6 b)). PMMA CN deformation increases quickly and then seems to reach a maximum then the creep speed decelerates. On the contrary the CR39 has an initial slower creep speed and it accelerates afterwards. Finally similar deformations are obtained at the end of experiment. Thus the recoveries are comparable. The slowdown in PMMA CN creep can

be attributed to the apparition of plasticity or a change in the viscoelasticity phenomenon, whereas the creep acceleration in CR39 is associated with an evolution of the viscoelasticity.

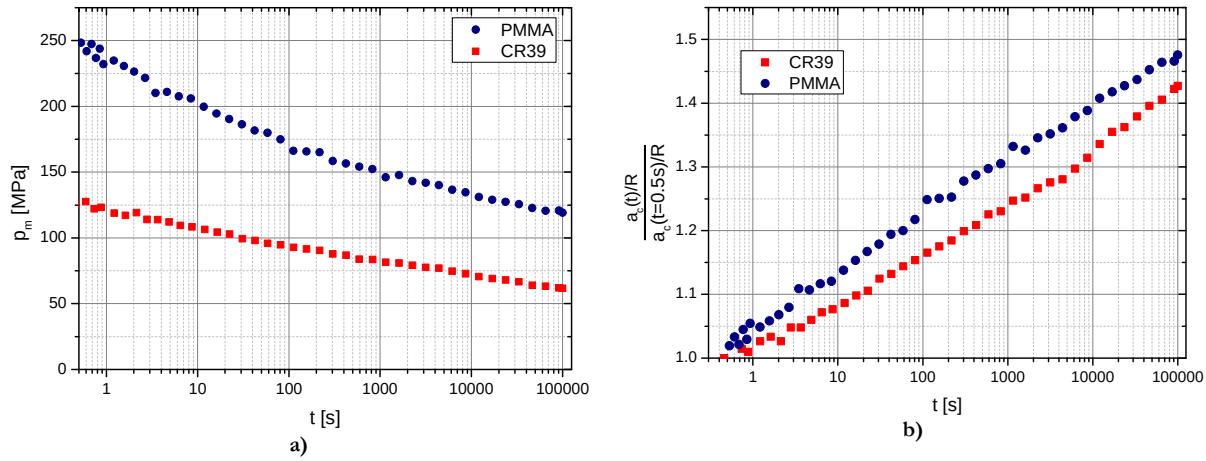

Figure I-6 Mean contact pressure (a) and Normalized indentation creep deformation (b) versus creep time for CR39 and PMMA CN at 30°C

I.4.1.2 Influence of temperature

Polymers are very strongly temperature dependent, thus their contact behavior can also be explored over temperature [2, 30, 31]. Moreover all the information concerning PMMA CN and PMMA 10 AlO(OH) are not displayed and can be found in VI.3.1.2.

Indentation creep experiments were conducted at different temperatures on CR39. The mean contact pressure versus time and temperature are presented in Figure I-7. In all cases the mean contact pressure decreases slowly as a function of the logarithm of time but the decreasing slopes are temperature dependent. The slope is almost the same for the two lower temperatures, and then it is strongly increasing over temperature (the mean contact pressure decreases slower for high temperature than for low temperature). Furthermore the ratio of the mean contact pressure at the beginning of the experiment for one material at two different temperatures is equal to the ratio of the Young's modulus of the same material at the same temperatures. For example CR39 Young's modulus at -20°C is roughly 80% higher than CR39 Young's modulus at 20°C. The CR39 mean contact pressure at -20°C is also 80% higher than the CR39 mean contact pressure at 20°C. These data, slopes and initial mean contact pressure, suggest as expected that the instantaneous mean contact pressure is mostly dependent on the Young's modulus whereas the creep is not.

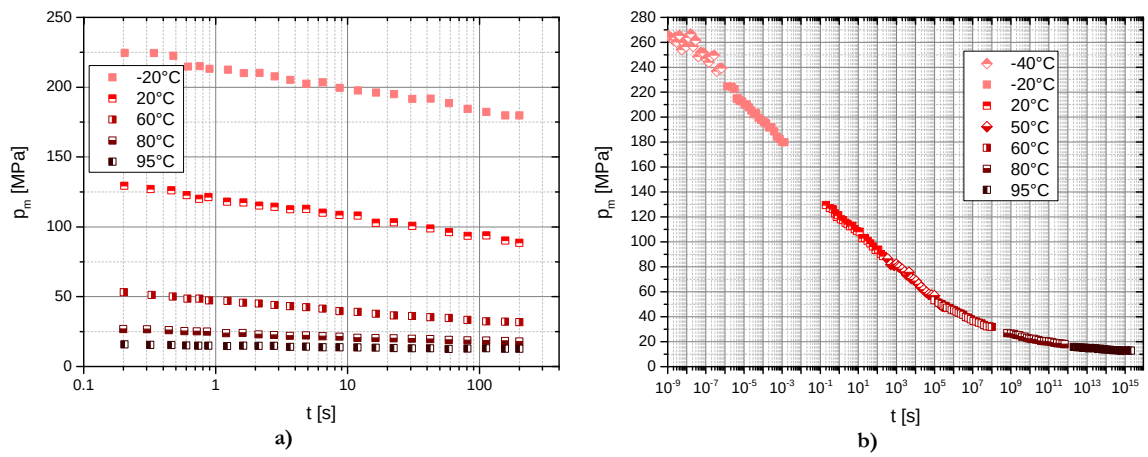

Figure I-7 Mean contact pressure versus time at different temperatures (starting Tabor deformation equal to 4%) for CR39 (a) normal time(b) master curve

Subsequently, the curves in Figure I-7 a) can be shifted laterally to form master curves. Figure I-7 b) presents the mean contact pressure versus time at all available temperatures. The chosen reference temperature is 30°C. The CR39 curves strongly decrease as a function of time until it reaches 10^7 s. The bending occurs for a temperature of 60°C. This is explained by the glass transition of CR39. After this transition temperature/time, the material is retained by the cross-linking and the measured mean contact pressure is stable. Some other authors already presented indentation master curves but they used the creep compliance [25, 32]. The available data, Figure I-6, are in accordance with the so constructed master curve.

I.4.2. Indentation Recovery

The indentation recovery observation is done through the normalized indentation recovery deformation. As it is normalized by the Tabor deformation at the end of the previous creep experiment the values are between 1 and 0. Nonetheless the phenomenon understanding is complex: a difference in recovery can be due to the parameter difference (material, temperature, indentation creep time …) or to the end of indentation state (already discussed in previous part). It would be ideal to end the creep at the same Tabor deformation for all experiments. As it would require a very large number of experiments (trial and error process), the start Tabor deformation (a/R = 0.2 at 0.5 s) is used. Moreover during the recovery two phenomena occur: the deflection around the indenter (elastic and viscoelastic) and the imprint (combination of elastic viscoelastic and plastic properties) recover. The major changes occur during the first seconds of recovery, thus the optical focus is hard to obtain and the image quality is poor. The larger the imprint, the more difficult it is to obtain reliable data. Hence a gray shaded triangle is drawn on the unreliable data.

In Figure I-8, the normalized recovery deformation is observed versus the recovery time for CR39 and PMMA CN. It presents the recovery after the indentation presented in Figure I-6. Both curves seem to drop to ¾ of the initial imprint deformation then PMMA CN recovery deformation decreases to 25% of its initial value whereas CR39 recovery Tabor deformation decreases down to less than 5% of the initial imprint deformation (the imprint is no longer measurable). Furthermore the decreasing slopes are different for PMMA CN and CR39. PMMA CN recovery seems to slow down at 100 s and almost stop after 10 000 s. On the contrary CR39

recovery has 2 slopes: one between 10 and 1000 s and the second one between 1000 s and 1 000 000 s. The immediate recovery of 25% can be associated in both cases to the material Elastic recovery. The delayed recovery is the sign of a viscoelastic behavior. The CR39 two slopes can be associated with two different viscoelastic behaviors. The PMMA CN recovery is associated with two phenomena. First the PMMA CN viscoelasticity enables the beginning of the recovery. Then the recovery progressively enters in the plastically deformed material, thus the recovery speed gradually slows down until it stops. The recovery analysis illustrates then in which case the material is plastically deformed and in which case it is not, information that we could not determine simply by the indentation creep analysis.

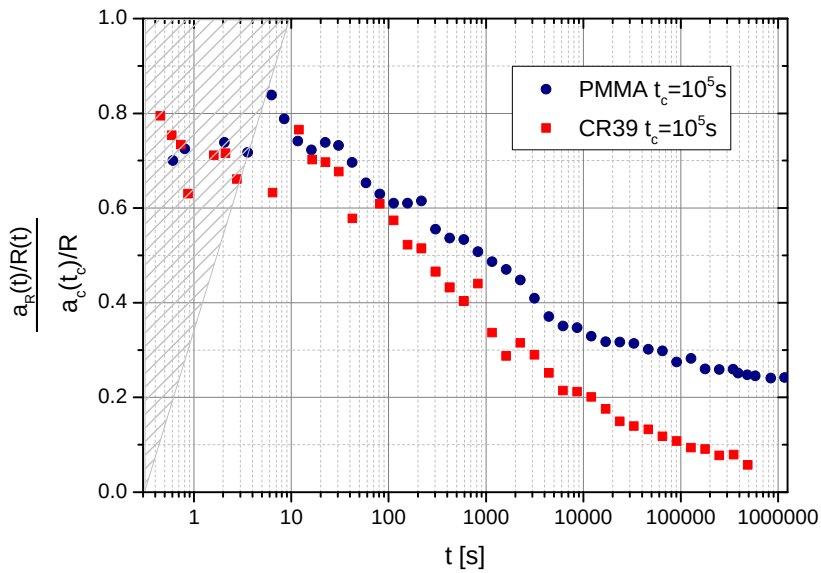

Figure I-8 Normalized indentation recovery deformation versus recovery time for PMMA CN and CR39 at 30°C

I.4.3. Master curves comparison

Thereafter, we acquired two different types of master curves: time-deformation and time-temperature. The deformation dependent master curves were done uni-axially with relaxation experiments. It is presented in Figure I-4 b) for CR39. As the bulk master curves present the relaxation modulus (measured in 1000 of MPa) and the contact master curves present the mean contact pressure (measured in 100 of MPa), they can not be compared directly. Thus we choose to normalize using a data point that both master curves have in common. All the CR39 values will be divided by the value of the data point [1.2 s: 30°C: 4% strain]. For the bulk master curve this corresponds to the relaxation modulus at the end of loading for the 3.92% deformation relaxation (E_r = 1140 MPa). For the contact master curves this corresponds to the mean contact pressure after 1.2 s of indentation at 30°C (p_m = 125 MPa). With these references points chosen, one has to shift horizontally the master curves to adjust these reference points to [1.2s: 1]. Similar procedure is done for PMMA CN. The obtained master curves are shown for CR39 and PMMA CN in Figure I-9 a) and b) respectively. Bulk and contact master curves are very close for CR39 and PMMA CN. Thus time, temperature and deformation affect the same mechanism. However their respective influences over it are different. Another major observation is the fact that contact and bulk experiments can lead to the same master curves. Thus if the contact temperature dependence is not known (PMMA 10 AlO(OH) for example), it can be estimated with the whole

bulk experimental set and one contact experiment. The reverse is also true: knowing the contact master curve and one Young's modulus the bulk master curve could be determined (this would be helpful in the case of thin layer). Moreover the influence of the plasticity can also be deduced from these curves. There is no plasticity in CR39 contact (see part I.4.2). On the contrary, there is plasticity in PMMA CN contact curves for the higher deformation and temperature and for the longer time. If there is plasticity in relaxation experiment, this occurs during loading and not during the stress relaxation which is purely viscoelastic. As the loading part was removed from the data, the bulk experiments display only viscoelastic behavior. As the curves shapes for CR39 and PMMA CN are similar with or without plasticity, the plasticity does not affect the viscoelasticity of polymers. Similarly if there was viscoplasticity, it should affect the time dependence. So there is no viscoplasticity in the tested polymers.

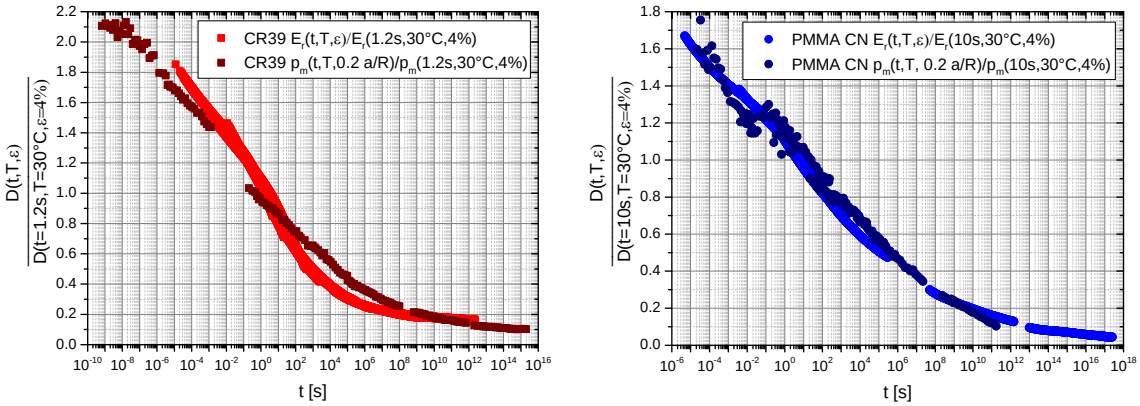

a) b)

Figure I-9 Comparison of normalized Master curves out of relaxation and contact experiments for a) CR39 after 1.2s of solicitation, at 30°C for a deformation of 4% and b) PMMA CN after 10s of solicitation, at 30°C for a deformation of 4%

Moreover the Figure I-9 can be completed by master curves obtained from DMTA experiments. More information on these curves can be found in part VI.3.3. Thus one obtains three differently produced master curves. The DMTA (time-temperature master curve), relaxation (time-deformation master curve) and the indentation (time-temperature-deformation master curve) are coherent with each other. This ad equation is observed for both materials CR39 and PMMA CN in Figure I-10. As a conclusion the phenomena occurring in the materials for the three experiments are similar whatever the temperature, deformation or time of solicitation.

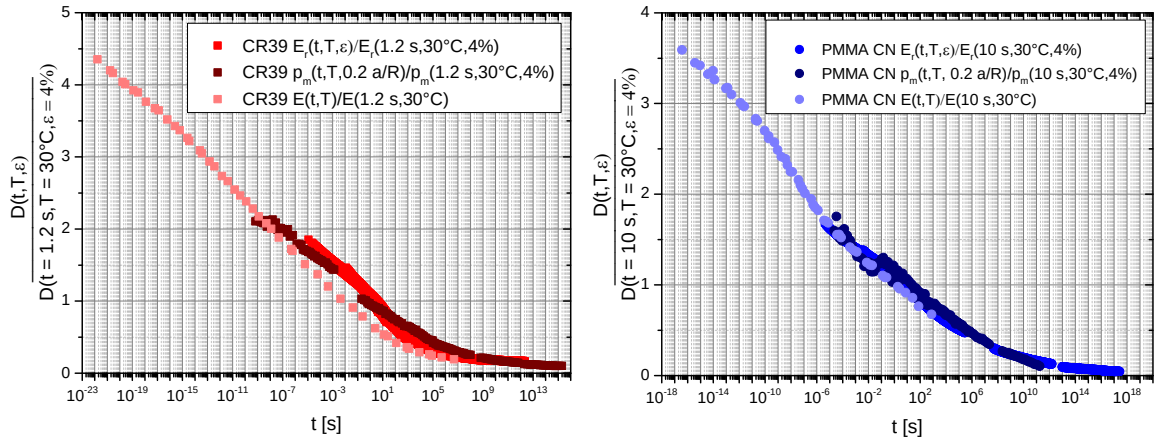

a) b)

Figure I-10 Comparison of normalized master curves out of DMTA, relaxation and contact experiments for a) CR39 after 1.2s of solicitation, at 30°C for a deformation of 4% and b) PMMA CN after 10s of solicitation, at 30°C for a deformation of 4%

I.4.4. Scratch recovery analysis

As we have observed and concluded from the previous part, the spherical indentation creep and recovery is a complex experiment. The scratch is even closer to polymer degradation due to everyday life. Thus in order to understand these degradations, mechanical characterizations of polymeric surfaces is also done by scratch experiments [18].

I.4.4.1 General Information

In the performed scratch neither cracking nor crazing were observed but only ductile behavior on CR39. The position of the different cross profile is explained in Figure I-11 a). One example of a cross profile at a 4 a_c distance from end of scratch is presented in Figure I-11 b). The graphs scales are not orthonormal; the y axis is 350 more zoomed than the x axis. So the groove appears sharper than it really is. The groove depth decreases over time. Furthermore on both sides of the groove, pile ups can be observed, they seem to decrease over time too. Then a shouldering is observed on the left side of the groove. This is due to the interpolation method.

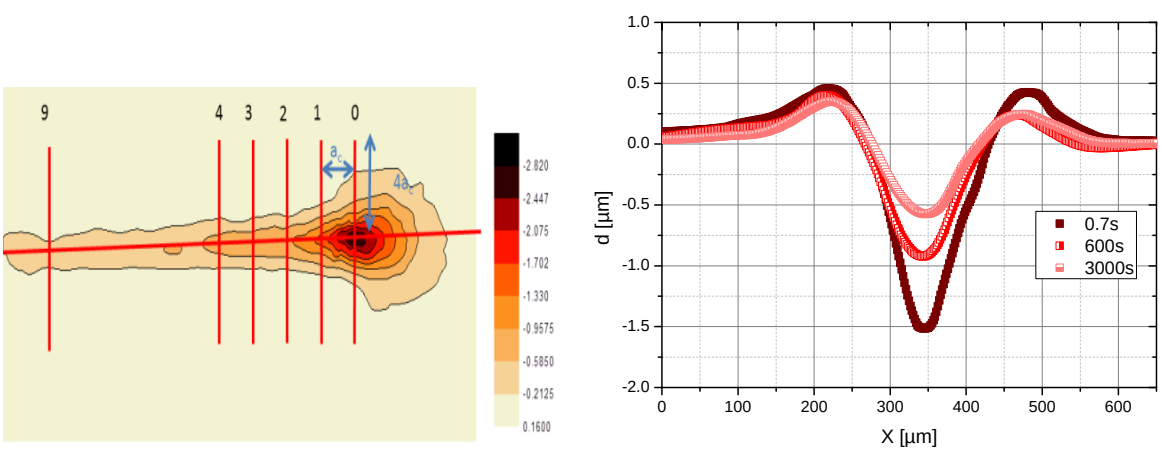

a) b)

Figure I-11 a) Scheme showing the position of the different profiles b) Three profiles taken at different times at a 4a_c distance from end of scratch

I.4.4.2 Influence of distance toward end of scratch

The scratch depth recovery is observed versus recovery time at different distances from the end of scratch in Figure I-12. The elapsed time displayed is the time since the tip removal from surface is achieved. This is not the same as the time since the tip passed over the material. Thus all the cross-profiles do not reflect the same recovery time. An additional complexity comes from the fact that all the material did not have the same mechanical history. Indeed in front and below the tip, the material is compressed and sheared, and then behind the tip the material is tensed. Furthermore on the scratch sides combinations of shear, compression and tensile deformation are observed. Thus the cross-profile at 0 a_c, image material which was submitted to less tensile stress than the material at 1 a_c which underwent even less than the one at 2 a_c. Nonetheless Figure I-12 demonstrates that, the depth decreases as a function of time for all distances. All the curves join at the point [200 s; -0.4 µm]. Furthermore the scratch as up to a distance of 3 a_c seems to follow a different path even if we try to shift them laterally to take into account the different recovery time. The difference probably comes from different mechanical history. We can then assume that at 4 a_c distance from end of scratch the material was submitted to almost all the mechanical solicitation. Therefore the following studies will mostly be conducted at this distance.

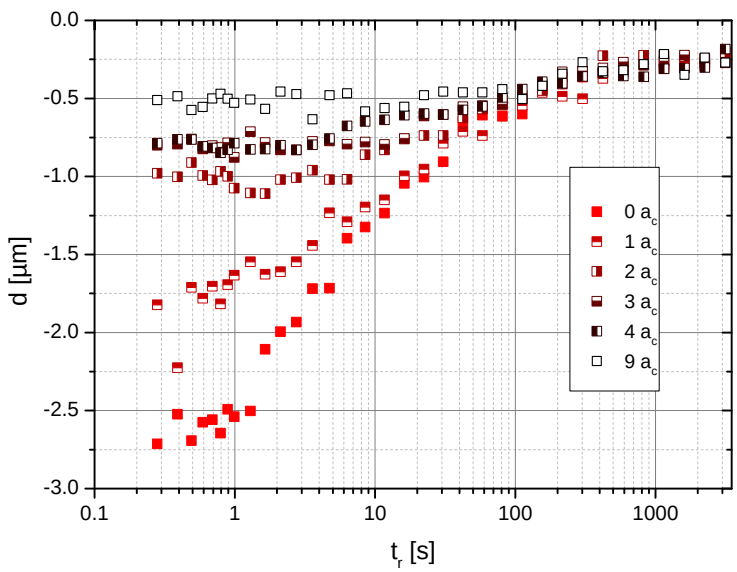

Figure I-12 Scratch recovery depth of CR39 at 30°C versus time at different distance of the end of scratch

I.4.4.3 Influence of load

As we have seen before, the material at 4 a_c was submitted to the whole mechanical history. Therefore all the following graphs concern the recovery observed for the cross profile at 4 a_c. Figure I-13 a) shows the recovery depth over time and deformation. The chosen time origin is the time elapsed since the tip removal from surface is achieved. The different deformations are obtained through different load on the tip (from the smaller to the higher deformation 1, 2.5, 5 N). The contact depths measure respectively 3.6, 9.5 and 14 µm. In all cases there is a plateau value for the first 2-3 seconds of the measure. Then the depth decrease over time for all deformations. The final depths are very small compared to the contact depth. The plateau comes

from the chosen time origin, the elapsed time since the tip center passed (or since the major strain took place) is about 30 s. Thus three more seconds of recovery do not influence strongly the recovery. The curves shape can give the impression of two different behaviors for different deformations. In order to compare the proportional recovery speed, the Figure I-13 b) presents the same data but normalized by the first measured depth. The plateau value is still observed and the decrease speeds are identical. The curves are shifted. One possible explanation is again the time origin, as the deformations are different; the 4 a_c distance is different thus the time since the tip center passed is different. Therefore a small shift in time can occur.

In conclusion doubling the deformation increases the time to obtain a full recovery. Nonetheless the recovering mechanisms are similar because the normalized recovery is the same for all deformations. In all cases no measurable permanent deformation was observed.

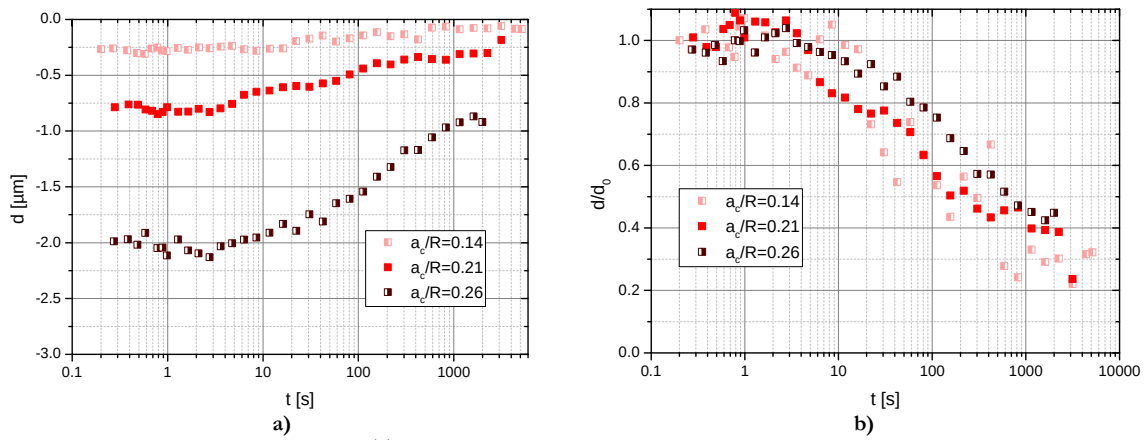

Figure I-13a) Influence of the scratching Tabor deformation on the recovery depth at a 4 a_c distance from end of scratch versus time elapsed since tip removal on CR39 at 30°C b) same experience normed by the first measured recovery depth

I.4.4.4 Partial conclusion

The scratch recovery of CR39 was examined in this section. We observed that the computed surfaces enable us to follow the recovery as a function of time. Then the depths were plotted as a function of time and distance to the end of scratch (the distances were chosen as multiple of the contact radius). The 4 a_c distance corresponds to the shorter distance, thus the shorter elapsed time, where the whole mechanical history occurred. The recovery is then only studied at this distance. In the manuscript, the load and scratch speed influences are studied. The higher the load, or the slower the scratch speed, the higher the beginning residual depth. Nonetheless the recovery was demonstrated to be proportional to each other in all cases, thus no plasticity was observed. Only long time (see master curve VI.3.4.3) viscoelastic behavior was observed.

I.4.5. Conclusion

This part was dedicated to the understanding of polymer mechanical behavior. In particular we studied the viscoelasticity. Deformation-time master curves were constructed out of compression relaxation experiments. The indentation creep and recovery analysis permitted us to observe the apparition of plasticity in PMMA CN for long indentation time or high temperature. CR39 presented, like PMMA CN, thermoplastic behavior below its glass transition and elastomeric

behavior above. In the whole tested range CR39 showed only viscoelastic behavior. Furthermore the mean contact pressure enabled the creation of deformation-time-temperature master curves in almost perfect adequacy with the previous ones, thus demonstrating a non-influence of plasticity on viscoelasticity and an absence of viscoplasticity in polymer behavior. The immediate scratch recovery was presented in this chapter for the first time.

I.5. FINITE ELEMENT MODELING

I.5.1. Constitutive laws

Finally Finite Element Modeling was conducted to better understand the recovery phase. In order to characterize the viscous properties of the material, several uni-axial relaxation experiments were conducted. The applied strains were in the range [0.5-20%]. A 3D representation of this experimental set is presented in Figure I-3. From these experiments two different laws can be identified. The first law type is viscoplastic. The equation is based on a Norton's law (see part VII.2.4 for details). This law gives the stress in function of the true plastic strain and true plastic strain rate. Figure I-14 presents the plane that was fitted on the experimental data. The Norton's law [33] and its obtained coefficient are also written on the graph.

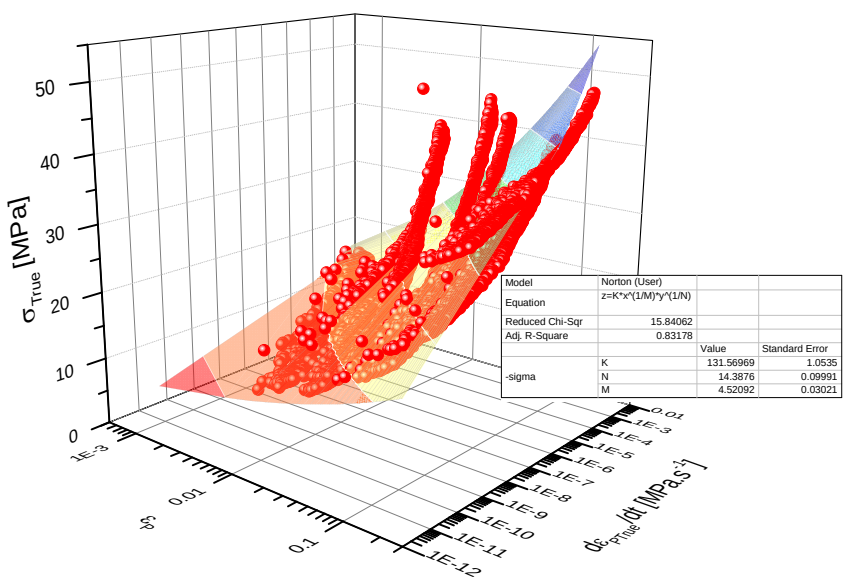

Figure I-14 Norton's law fitted on relaxation experiment

The viscoelastic law consists in a generalized Maxwell model (in our case 8 or more spring-dashpot couple are used in parallel). The Maxwell shear and bulk modulus formulae are then fitted on one relaxation experiment. Thus for each relaxation experiment a set of VE [34] coefficient is extracted. In this summary the parameters sets corresponding to the 4.88% strain and the 17.69% strain are used and respectively named VE (ε = 4.88%) and VE (ε = 17.69%).

Furthermore we observed previously (Figure I-4b)) that it was possible to build master curves with the relaxation experiments. Thus one can fit a generalized Maxwell model on the master

curve (MC VE) [35]. In this case the master curve is centered on the chosen relaxation. This means that, in Figure I-15, which presents a master curve of shear modulus on CR39 centered at the 4.88% deformation relaxation, the value for this experiment (4.88%) are not shifted. The shear moduli coming from smaller deformation are shifted horizontally to the left whereas those coming from higher deformation are shifted to the right. The presented fit on this graph is a generalized Maxwell model with 18 time constants to cover the whole available time. The fit quality is lower than previously; this is probably due to the large amount of discrepancy between experimental data and the non-perfect shifting of the experimental curves.

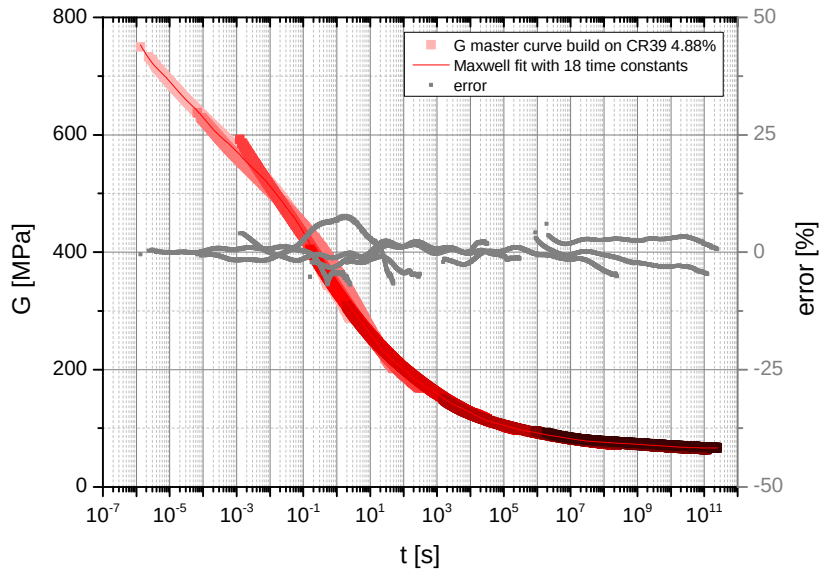

Figure I-15 CR39 master curves shifted to 4.88% deformation, fitted with a generalized Maxwell equation

As explained before each relaxation experiment enables a set of viscoelastic parameters and so does each master curve. The study on the viscoelastic parameter will be done with the most studied material, CR39. The generalized Maxwell model is a mathematical operator which fits well on viscous phenomena due to its high parameterization [36].

For comparison, four Maxwell based viscoelastic laws were analyzed. They were identified as previously shown at different strains. The chosen strains were 4.88% and 17.69%. These strains correspond to the true strain of relaxation experiment conducted at 5% and 19.4% engineering strain. For both relaxations master curves were constructed. Thus one has two named "simple" viscoelastic constitutive laws and two viscoelastic constitutive laws master curves.

Finally a literature available constitutive law, the G'Sell Jonas elasto plastic law was used [37-39]. It will be further related to EP. The coefficients are calculated through indentation experiments with differently shaped indenters.

In order to improve simulation reality, the experimental loadings are used in the numerical code. It means that numerical relaxation experiments are piloted by the experimental beam displacement and the numerical indentation are piloted by the experimental load.

I.5.2. Uni-axial Relaxation

The different constitutive laws are tested on a simple relaxation test. The relaxation test advantage is that the strain is almost uniformed in the material. Thus the quality of a constitutive law at a given deformation can be evaluated.

I.5.2.1 Relaxation at 4.88%

Figure I-16 presents the stress as a function of time for a relaxation test at 4.88%. The graph a) shows in addition the results of the numerical tests done with the viscoelastic laws identified at 4.88% deformation (VE and MC VE). Then the graph b) displays the results obtained with the viscoelastic laws identified at 17.69% relaxation (VE and MC VE). The last graph, c), presents the results obtained by numerical test with the viscoplastic and elasto-plastic law. It is remarkable that both VE laws identified at 4.88% are very accurate. The start of the simple VE is nonetheless of very poor quality (see Figure I-16). It is observable that the Master curve VE 4.88% fit is clearly better for shorter time. For longer time the fit is equal to the simple VE. This was expected as the coefficients are close for these time constants. The VE laws identified at 17.69% are very far from the experiment. The material described by this law is too stiff for this experiment (the stress is much smaller than the reality). The objective of this graph is to demonstrate the non-accuracy of a VE law identified on another deformation. The laws were not fitted for this strain but for a higher strain where the proportionality between stress and strain is different. Finally, the VP law gives a rough approximation of the obtained value whereas the EP law gives a good approximation of the instantaneous response but then do not evolve over time.

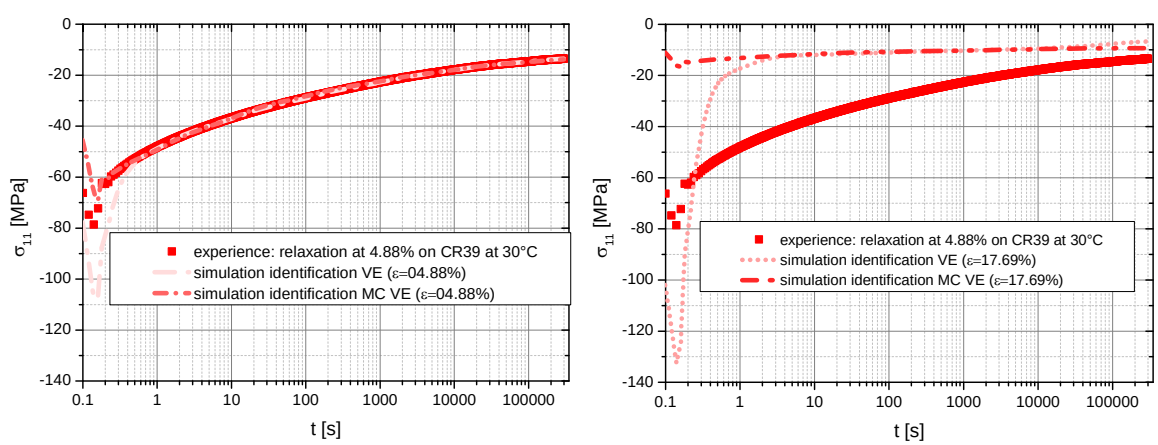

a) b)

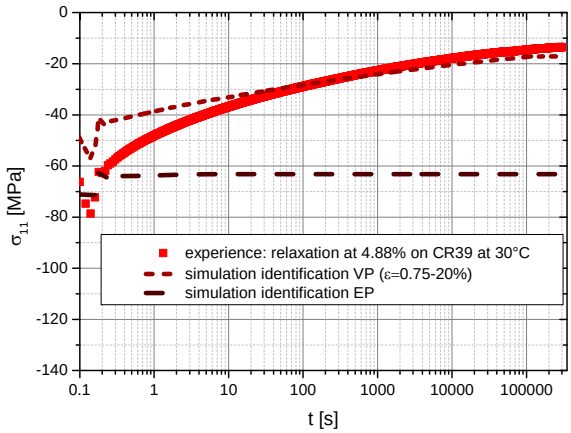

c)

Figure I-16 Stress versus time for CR39 4.88% deformation relaxation experiment at 30°C for experiment and simulations a) VE laws identified at 4.88% b) VE laws identified at 17.69% c) EP and VP laws

I.5.2.2 Relaxation at 17.69%

In Figure I-17 the stress versus time for a relaxation test at 17.69% is presented. As before the graph a) shows the experimental, VE 4.88% and MC VE 4.88% results, then the graph b) the experimental, VE 17.69% and MC VE 17.69% results, finally the graph c) the experimental, the EP and the VP results. The VE 4.88% laws stresses are much higher than those of the experiment thus the laws are too soft. And again the wrongly identified law is not adequate. The VE 17.69% laws demonstrate a very good accuracy after the loading, but the simple VE law show a material that is too soft during loading whereas the MC VE is too stiff. Utterly the EP law gives a good approximation of the loading and the VP law presents a material that is a little too stiff.

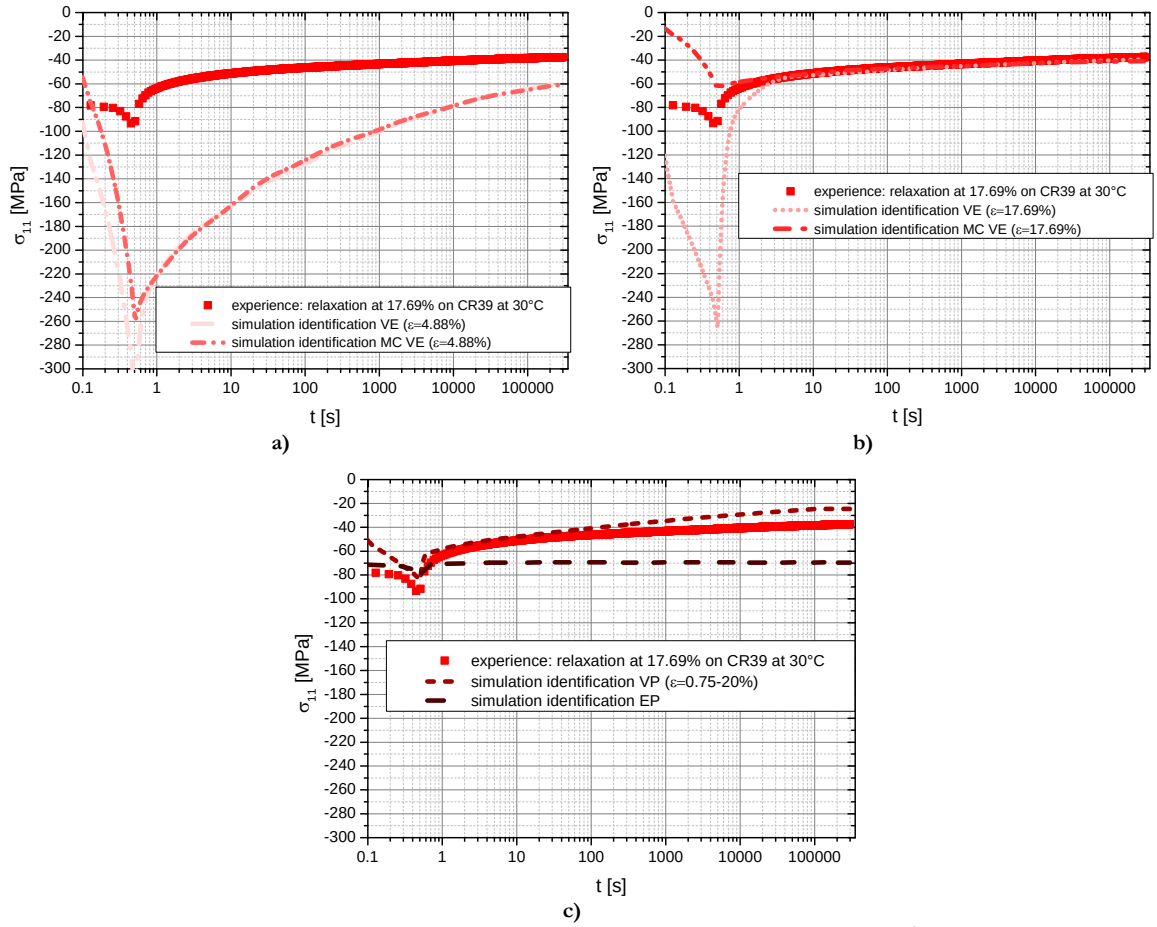

Figure I-17 Stress versus time for CR39 17.64% deformation relaxation experiment at 30°C for experiment and simulations a) VE laws identified at 4.88% b) VE laws identified at 17.69% c) EP and VP laws

I.5.2.3 Partial conclusion

The VE laws are very accurate when the strain is close to the strain for which they were identified. Furthermore the use of master curves improves the quality of the loading simulation. Indeed the MC VE improve the fit on the short times which corresponds to the loading time thus the non-fitted time on the simple VE. The master curve laws are fitted for shorter and longer times. Moreover the EP law simulation gives an instantaneous accurate stress but no viscous phenomenon, crucial for accurate material description. In the end the VP law gives a rough, time evolving, approximation in all the cases. As our indentations have a mean contact Tabor deformation between 4 and 6% (begin and end of indentation on CR39 and PMMA CN Figure I-6) [13, 40], the viscoelastic constitutive law at 4.88% and the master curve viscoelastic law at 4.88% are used.

I.5.3. Indentation

Indentation creep simulation has become of great interest for numerous applications in the recent years [41-43]. The indentation creep and recovery of CR39 are presented below.

I.5.3.1 Indentation creep

The mean contact pressure versus time is drawn in Figure I-18 a). The experimental data decreases versus log(t). The G'Sell Jonas law does not decrease at all, it was to be expected as the law is not strain rate dependent. The start value is nonetheless adequate. On the contrary the start value of the simple VE law is far too high thus it stays too high throughout the experiment. The VE master curve and the VP law are slightly below but decrease like the experiment over time. The non evolution of the plastic law was to be expected as the time is not taken into account in the equation. The high value of the VE law can be explained by the fact that the first milliseconds of the relaxation experiment are not taken into account thus inducing an error that is present during the whole experiment. The master curve corrects this shortcoming; indeed the start value is much closer to the experiment. The relative accuracy of the VP law comes from a wide deformation domain. Therefore all stressed material has an averaged appropriate deformation. The Figure I-18 b) presents the normalized Tabor creep deformation for the experiment and the numerical tests versus time. As previously observed, the EP law does not evolve thus proving the absence of modification after loading. The master curve deformation is slightly above the experimental values. On the contrary, the VE and VP laws are below the experimental values. The VP law is the closest to the experiment. Indeed the average response for each deformation seems to produce a good compromise.

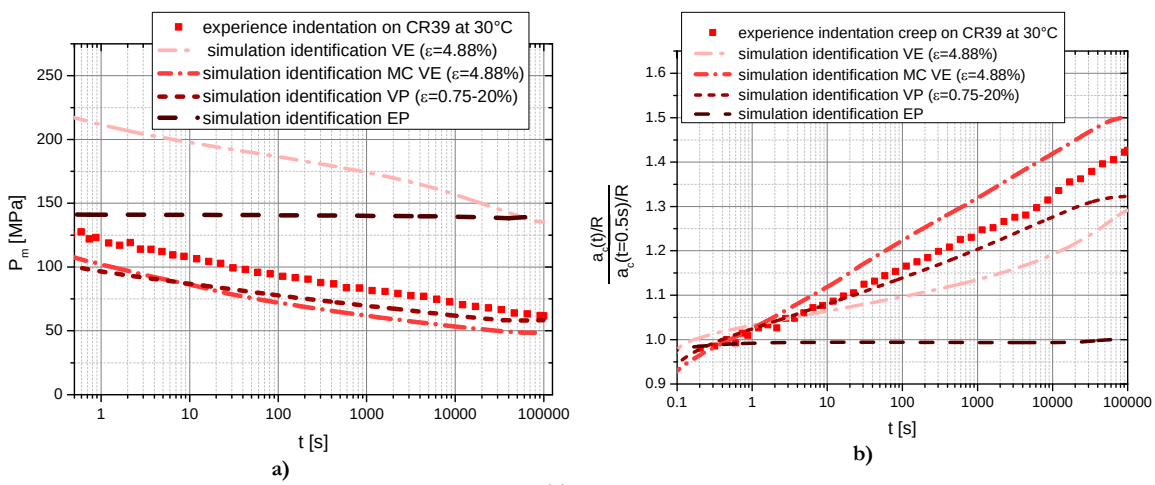

Figure I-18 a) Mean contact pressure and b) normalized Tabor indentation creep during indentation creep experiment at 30°C for experience and simulation on CR39

As a conclusion the CR39 indentation creep, at 4-6% Tabor average strain, behavior can be simulated with the more accuracy either by a Master Curve viscoelastic 4.88% law or by a viscoplastic law. The both laws show a mean contact pressure slightly lower than the experiment but the numerical deformations frame the experimental deformation.

I.5.3.2 Indentation recovery

The results of the experimental and numerical test recovery are presented in Figure I-19. The normalized deformation in these graphics is equal to 1 at the end of indentation and to 0 for a full recovery. The EP and VP law curves are horizontal as expected. They respectively recovered 45% and 20% of the indentation imprints. In both cases, they recover immediately from the

elastic part of the imprint and then no more. The EP law led to a smaller imprint (see Figure I-18 b)) therefore the part of elastically deformed material is higher and so is the percentage of recovered material. The two other laws fully recover. The immediate recovery of the VE 4.88% law is roughly 45%, 20% more than the experiment. This higher immediate recovery comes from the smaller final indentation deformation. On the contrary the final deformation observed with MC VE 4.88% law is 5% higher than the experiment. The immediate recovery of the simulation with the MC VE 4.88% is therefore much closer to the experiment. The MC VE 4.88% presents a very accurate representation of the experiment thus supporting our experimental observation that CR39 is viscoelastic on the whole tested range (see part VI.3.2).

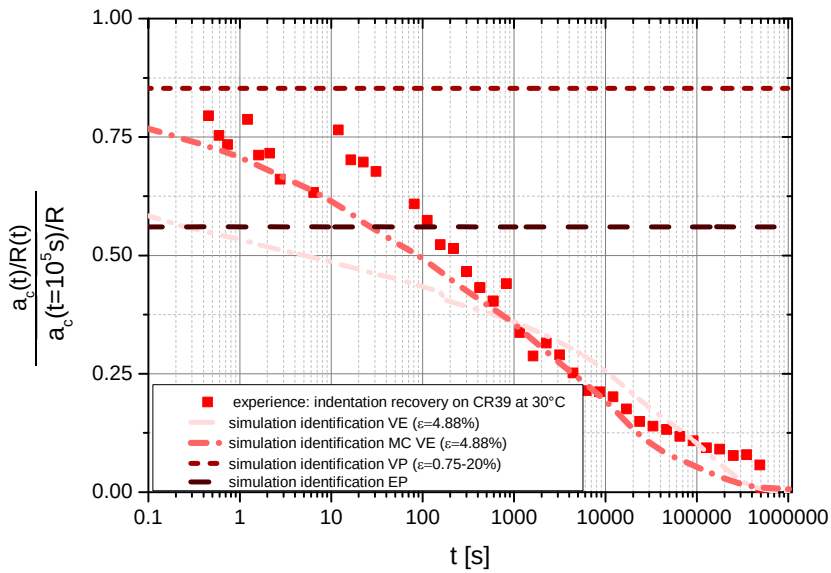

Figure I-19 CR39 experimental and simulation indentation creep recovery

I.5.4. Conclusion

Three types of constitutive laws were introduced in MSC Marc software. The EP law enables a good prediction of the immediate stress-strain relationship on the tested polymers. There is no evolution due to creeping effects. The VP law gives a relatively good representation of the mean contact pressure evolution, but it does not reflect the recovery well. Finally the master curve law demonstrates a very good precision if it is used for the deformation on which it was fitted. In the case of indentation creep, it gives an accurate idea of the normalized creep deformation. The recovery of the master curves is appropriate and accurate as long as there is no plasticity involved in the deformation (see in VII.5.3 for more details).

In order to improve the simulation quality, one should use the VE law on which a plasticity threshold is added. The next step toward constitutive law improvement would be to differentiate the compression, the pulling and the shear response

I.6. GENERAL CONCLUSION

This thesis presents time dependent mechanical behavior of polymeric materials. In particular we studied the viscoelasticity in the bulk. Deformation-time master curves were constructed out of

compression relaxation experiments. The indentation creep and recovery analysis permitted us to observe the apparition of plasticity in PMMA CN for long indentation time. CR39 presented, like PMMA CN, thermoplastic behavior below its glass transition and elastomeric behavior above. In the whole tested range CR39 showed only viscoelastic behavior. We determined whether a material is viscoelastic or elastic plastic by the analysis of the material recovery. Furthermore, through creep under indentation experiments, the mean contact pressure enabled the creation of deformation-time-temperature master curved in almost perfect adequacy with the classical time-temperature, thus demonstrating a non-influence of plasticity on viscoelasticity and an absence of viscoplasticity in polymer behavior. We demonstrated the equivalence of the contact and bulk master curves thus proving that one can predict the one master curve knowing the other. The immediate scratch recovery analysis is presented in this thesis for the first time.

Then the polymeric mechanical behavior is simulated by three types of constitutive laws in MSC Marc software. The elasto-plastic law enables a good prediction of the immediate stress-strain relation on the tested polymers. There is no evolution due to creeping effects. The viscoplastic law gives a relatively good representation of the mean contact pressure evolution. The viscoelastic master curve law demonstrates a very good precision if it is used for the deformation on which it was fitted. In the case of indentation creep, it gives an accurate idea of the normalized creep deformation. The recovery of the master curves is appropriate and accurate as long as there is no plasticity involved in the deformation.

To improve, the simulation quality, the master curve viscoelastic law could receive a plasticity threshold. Indeed CR39 and PMMA CN can undergo plasticity that is absolutely not taken into account in actual model. More improvement would be obtained by differentiating compression, traction and shear in particular for scratch simulation. In fact the compression and traction comportment of polymers is different thus differentiating it in the simulation of scratch is one of the next steps toward a better constitutive law. There is place for improvement in the simulation of the indentation recovery. The combination of a plastically, a viscoelastically and an elastically deformed material remains to be done.

In order to improve the understanding of polymeric material, one should improve the time-temperature-deformation observed relationship by adding a molecular dynamic and a fracture mechanics understanding.

I.7. BIBLIOGRAPHY

[1] S.C. Tjong, Structural and mechanical properties of polymer nanocomposites, Materials Science and Engineering R: Reports, 53 (2006) 73-197.

[2] P. Bertrand-Lambotte, J.L. Loubet, C. Verpy, S. Pavan, Nano-indentation, scratching and atomic force microscopy for evaluating the mar resistance of automotive clearcoats: Study of the ductile scratches, Thin Solid Films, 398-399 (2001) 306-312.

[3] M. Mansha, C. Gauthier, P. Gerard, R. Schirrer, The effect of plasticization by fatty acid amides on the scratch resistance of PMMA, Wear, 271 (2011) 671-679.

[4] C. Gauthier, R. Schirrer, Time and temperature dependence of the scratch properties of poly(methylmethacrylate) surfaces, Journal of Materials Science, 35 (2000) 2121-2130.

[5] K. Yasui, Curable material containing photopolymerizable polymer and cured object, in: L. Nissan Chemical Industries (Ed.) USPTO, Nissan Chemical Industries , Ltd., united states of america, 2007.

[6] H. Hertz, Über die Berürhung fester elasticher Körper, Journal für die reine und angewandte Mathematik, 92 (1882) 156-171.

[7] W.C. Oliver, G.M. Pharr, Improved technique for determining hardness and elastic modulus using load and displacement sensing indentation experiments, J. Mater. Res., 7 (1992) 1564-1580.

[8] W.C. Oliver, G.M. Pharr, Measurement of hardness and elastic modulus by instrumented indentation: Advances in understanding and refinements to methodology, J. Mater. Res., 19 (2004) 3-20.

[9] A.C. Fischer-Cripps, A simple phenomenological approach to nanoindentation creep, Materials Science and Engineering A, 385 (2004) 74-82.

[10] S.E. Olesiak, M.L. Oyen, V.L. Ferguson, Viscous-elastic-plastic behavior of bone using Berkovich nanoindentation, Mech. Time-Depend. Mater., 14 (2010) 111-124.

[11] B.J. Briscoe, L. Fiori, E. Pelillo, Nano-indentation of polymeric surfaces, Journal of Physics D: Applied Physics, 31 (1998) 2395-2405.

[12] A. Rubin, C. Gauthier, R. Schirrer, The friction coefficient on polycarbonate as a function of the contact pressure and nanoscale roughness, Journal of Polymer Science, Part B: Polymer Physics, 50 (2012) 580-588.

[13] D. Tabor, The hardness of solids, Review of Physics in Technology, 1 (1970) 145.

[14] T. Chatel, C. Gauthier, H. Pelletier, V. Le Houerou, D. Favier, R. Schirrer, Creep of the contact with a spherical tip and recovery of the imprint on amorphous polymer surfaces, Journal of Physics D-Applied Physics, 44 (2011).

[15] I. Karapanagiotis, D.F. Evans, W.W. Gerberich, Dynamics of the leveling process of nanoindentation induced defects on thin polystyrene films, Polymer, 43 (2002) 1343-1348.

[16] Z.Y. Zhang, H.N. Dhakal, S.N. Surip, I. Popov, N. Bennett, Characterisation of roof tile coating degradation using nano-indentation test and surface profilometry, Polymer Degradation and Stability, 96 (2011) 833-838.

[17] T. Chatel, Fluage et recouvrance d'empreintes et de sillons sur suface de polymère, in, Université de Strasbourg, Strasbourg, 2010.

[18] J.S.S. Wong, H.J. Sue, K.Y. Zeng, R.K.Y. Li, Y.W. Mai, Scratch damage of polymers in nanoscale, Acta Materialia, 52 (2004) 431-443.

[19] W. Shen, S.M. Smith, H. Ye, F. Jones, P.B. Jacobs, Real time observation of viscoelastic creep of a polymer coating by scanning probe microscope, Tribology Letters, 5 (1998) 75-79.

[20] M. Wong, G.T. Lim, A. Moyse, J.N. Reddy, H.J. Sue, A new test methodology for evaluating scratch resistance of polymers, Wear, 256 (2004) 1214-1227.

[21] L.C.E. Struick, Physical Aging in Amorphous Polymers and Other Materials, Elsevier, Amsterdam, , 1978.

[22] J.J. Martinez-Vega, H. Trumel, J.L. Gacougnolle, Plastic deformation and physical ageing in PMMA, Polymer, 43 (2002) 4979-4987.

[23] J. Kolařík, Tensile creep of thermoplastics: Time-strain superposition of non-iso free-volume data, Journal of Polymer Science, Part B: Polymer Physics, 41 (2003) 736-748.

[24] M. Software, Volume A: Theory and User Information, in, 2012, pp. 813.

[25] F. Quadrini, E.A. Squeo, A. Guglielmotti, Indentation creep of polymers. I. Experimental, Polymer Engineering and Science, 50 (2010) 2431-2439.

[26] J. Kolařík, A. Pegoretti, Non-linear tensile creep of polypropylene: Time-strain superposition and creep prediction, Polymer, 47 (2006) 346-356.

[27] S. Jazouli, W. Luo, F. Bremand, T. Vu-Khanh, Application of time-stress equivalence to nonlinear creep of polycarbonate, Polym. Test, 24 (2005) 463-467.

[28] P.A. O'Connell, G.B. McKenna, Large deformation response of polycarbonate: Time-temperature, time-aging time, and time-strain superposition, Polymer Engineering and Science, 37 (1997) 1485-1495.

[29] J. Zhao, G.B. McKenna, Temperature divergence of the dynamics of a poly(vinyl acetate) glass: Dielectric vs. mechanical behaviors, Journal of Chemical Physics, 136 (2012).

[30] B.J. Briscoe, E. Pelillo, S.K. Sinha, Scratch hardness and deformation maps for polycarbonate and polyethylene, Polymer Engineering and Science, 36 (1996) 2996-3005.

[31] I.C. Choi, B.G. Yoo, Y.J. Kim, J.I. Jang, Indentation creep revisited, J. Mater. Res., 27 (2012) 3-11.

[32] K. Sakaue, S. Okazaki, T. Ogawa, Indentation technique for evaluation of master curve of creep compliance, Experimental Techniques, 35 (2011) 16-22.

[33] J. Lemaitre, J.-L. Chaboche, Mécanique des matériaux solides, Bordas, 1988.

[34] T. Chatel, V. Le Houérou, H. Pelletier, C. Gauthier, Numerical analysis of the creep of the contact and recovery of the imprint on amorphous polymer surfaces, Mech. Time-Depend. Mater., (2012) 1-15.

[35] L.C.A. Van Breemen, E.T.J. Klompen, L.E. Govaert, H.E.H. Meijer, Extending the EGP constitutive model for polymer glasses to multiple relaxation times, Journal of the Mechanics and Physics of Solids, 59 (2011) 2191-2207.

[36] P.E. Combette, Isabelle Physique des polymères propriété mécaniques, 6 rue de la sorbonne, paris, 2005.

[37] M.C. Baietto Dubourg, J. Rannou, A. Gravouil, H. Pelletier, C. Gauthier, R. Schirrer, 3D crack network during the scratching of a polymer: Comparison between experimental results and localized multigrid X-FEM, in, Ottawa, ON, 2009, pp. 3827-3836.

[38] C. G'Sell, J.J. Jonas, Determination of the plastic behaviour of solid polymers at constant true strain rate, Journal of Materials Science, 14 (1979) 583-591.

[39] J.L. Bucaille, E. Felder, G. Hochstetter, Mechanical analysis of the scratch test on elastic perfectly plastic materials with the three-dimensional finite element modeling, Wear, 249 (2001) 422-432.

[40] H. Pelletier, C. Gauthier, R. Schirrer, Experimental measurement and numerical simulation of the plastic strain during indentation and scratch tests on polymeric surfaces, J. Mater. Res., 24 (2009) 1184-1196.

[41] J. Krier, J. Breuils, L. Jacomine, H. Pelletier, Introduction of the real tip defect of Berkovich indenter to reproduce with FEM nanoindentation test at shallow penetration depth, J. Mater. Res., 27 (2012) 28-38.

[42] H. Jiang, R. Browning, H.J. Sue, Understanding of scratch-induced damage mechanisms in polymers, Polymer, 50 (2009) 4056-4065.

[43] F.L. Li, F.L. Peng, Y. Tan, W. Kongkitkul, M.S.A. Siddiquee, FE simulation of viscous behavior of geogrid-reinforced sand under laboratory-scale plane-strain-compression testing, Geotextiles and Geomembranes, 31 (2012) 72-80.

CHAPTER II. RÉSUMÉ

II.1. INTRODUCTION 29
II.2. MÉTHODES EXPÉRIMENTALES ET TECHNIQUES 29
II.3. PROPRIÉTÉS MÉCANIQUES EN VOLUME 32
II.3.1. Relaxation 32
II.3.2. Modules de relaxation et courbes maîtresses 33
II.3.3. Conclusion 35
II.4. ANALYSE DU CONTACT 35
II.4.1. Fluage d'indentation 35
II.4.2. Recouvrance d'indentation 37
II.4.3. Analyse de la recouvrance de la rayure 40
II.4.4. Conclusion 43
II.5. SIMULATION PAR ÉLÉMENTS FINIS 44
II.5.1. Lois de comportement 44
II.5.2. Relaxation uni-axiale 46
II.5.3. Indentation 48
II.6. CONCLUSION GÉNÉRALE 50
II.7. BIBLIOGRAPHIE 52

II.1. INTRODUCTION

L'industrie des polymères est en constante recherche d'innovation et de nouvelles applications [1]. Les polymères ont en effet des avantages : une masse volumique faible par rapport aux métaux et une bonne résistance aux conditions atmosphériques. C'est pourquoi les polymères sont choisis pour servir de protection de surface (peintures, Smartphones,…) ou dans les matrices des composites (pneus, coques de bateau,…). Malheureusement les polymères sont peu résistants face à des sollicitations mécaniques [2] en particulier les rayures. Les rayures peuvent conduire à une forte dégradation des propriétés esthétiques [3, 4]. Deux solutions sont alors possible : fabriquer des matériaux inrayables d'une part ou bien fabriquer des matériaux pour lesquels la rayure cicatrise. Les matériaux organiques vitreux inrayables n'existent pas. Les matériaux cicatrisants ont de nombreuses applications industrielles : les lunettes, les peintures de voitures, les vernis à ongle devraient rester brillant plus longtemps, et les écrans tactiles télé, ordinateurs, téléphones portables, tablettes[5]. Il existe deux méthodes pour améliorer la recouvrance : soit protéger les matériaux avec une couche mince, soit augmenter la résistance du volume en y ajoutant des nano-charges et ainsi créer un matériau composite. Durant cette thèse, l'objectif était de mieux comprendre la relation entre les propriétés mécaniques volumiques des matériaux chargés et leur résistance à la rayure et au contact en général. En particulier, deux aspects ont été étudiés : la recouvrance et le comportement des polymères après des temps de sollicitations longs. Cette thèse a été réalisée dans le cadre de l'International Research Training Group soft matter (IRTG).

Les matériaux chargés ont été réalisés au Freiburg Institute for Advanced Studies. En particulier des PMMA renforcés avec des charges de SiO_2 ont été préparés pour servir de modèle comme matériaux composites. Par la suite les caractérisations mécaniques ont été faites à l'Institut Charles Sadron à Strasbourg.

II.2. MÉTHODES EXPÉRIMENTALES ET TECHNIQUES

Les caractérisations mécaniques classiques des polymères se font par tests uni-axiaux. Ces expériences consistent à appliquer une déformation constante ou une contrainte constante et d'observer l'autre. Un matériau parfait (élastique, élasto-plastique) réagit instantanément à la sollicitation mécanique. C'est généralement le cas du verre et des métaux à température ambiante. Au contraire, des phénomènes visqueux sont observés dans les polymères. Pour caractériser les propriétés viscoélastiques et/ou viscoplastiques, des tests de relaxation et de fluage ont été effectués. L'évolution de la contrainte et de la déformation sont ainsi mesurées en fonction du temps. Néanmoins comme les polymères sont souvent utilisés en couche mince, les mesures volumiques ne sont pas toujours appropriées ni possibles. C'est pourquoi des mesures de contact sont utilisées. En particulier la mesure de la dureté se fait par l'application d'un poids mort sur une surface suivie d'une observation du contact résiduel. Dans ce cas uniquement la plasticité résiduelle peut être mesurée. Pour mieux comprendre ces phénomènes, des instruments plus récents enregistrent la force et la profondeur pendant l'indentation. Ensuite les propriétés élastiques sont déterminées par l'équation d'Hertz [6]. Pour les matériaux élasto-platiques,

l'analyse de la décharge de la courbe force-enfoncement (supposée élastique) conduit grâce au modèle d'Oliver&Pharr au module et à la dureté du matériau [7, 8]. Mais pour les polymères [9] et les os [10], le modèle d'Oliver & Pharr n'est pas juste. En effet ces matériaux présentent des propriétés visqueuses (non prise en compte dans le modèle) or les résultats de l'analyse sont dépendants du test réalisé (« nose-problem ») [11]. De plus, l'enfoncement est la combinaison de la déflection, plus importante pour les polymères que pour les métaux, et de la profondeur de contact. La déflection est majoritairement élastique alors que la profondeur de contact est due à une combinaison de propriétés élastiques, visco-élastiques, viscoplastiques et plastiques.

À l'heure actuelle, aucun modèle analytique ne permet de séparer toutes les contributions et d'estimer avec précision la véritable profondeur de contact pendant l'indentation sur des surfaces de polymères. Un moyen pour éviter l'utilisation de modèles analytiques consiste à observer directement le contact à travers l'échantillon (matériaux transparents) [4, 12], ou à travers la pointe (en utilisant une pointe en verre). Nous avons développé un système spécifique : le Microvisioscratch [4].

Cependant, en utilisant un indenteur sphérique pour le fluage d'indentation à charge constante, l'aire de contact va augmenter. Donc la déformation selon Tabor [13] va augmenter alors que la pression moyenne de contact diminue au cours de l'essai. Le fluage d'indentation est donc un essai complexe, mais proche de conditions réelles de sollicitation des polymères dans le cas d'un contact statique entre deux surfaces fonctionnalisées. Les Figure II-1 a) et b) décrivent les observations classiques obtenues par le Microvisioscratch. Notre appareil permet de voir, au cours du temps, à la fois le contact entre la pointe et la surface déformée pendant un fluage d'indentation (Figure II-1 b)) mais aussi la recouvrance du matériau juste après retrait de la pointe [14] (Figure II-1 c)). Malheureusement, les matériaux non transparents ne peuvent pas être caractérisés en utilisant le Microvisioscratch. Au lieu de regarder à travers l'échantillon (quand les échantillons sont transparents), l'observation a été faite à travers la pointe. Pour pouvoir observer une image avec suffisamment de précision pour estimer un rayon de contact, une pointe sphérique à faible rayon de courbure est nécessaire (au moins 3.3 mm). Avec de tels indenteurs, de très fortes charges sont nécessaires pour ne pas avoir une déformation purement élastique [14]. Figure II-1 a) présente un appareil de macro-indentation maison construit et développé pendant cette thèse dans une machine de traction. Ces caractérisations ont été effectuées sur la gamme de température [-40°C : 95°C], ce qui correspond aux températures d'utilisation des polymères en général.

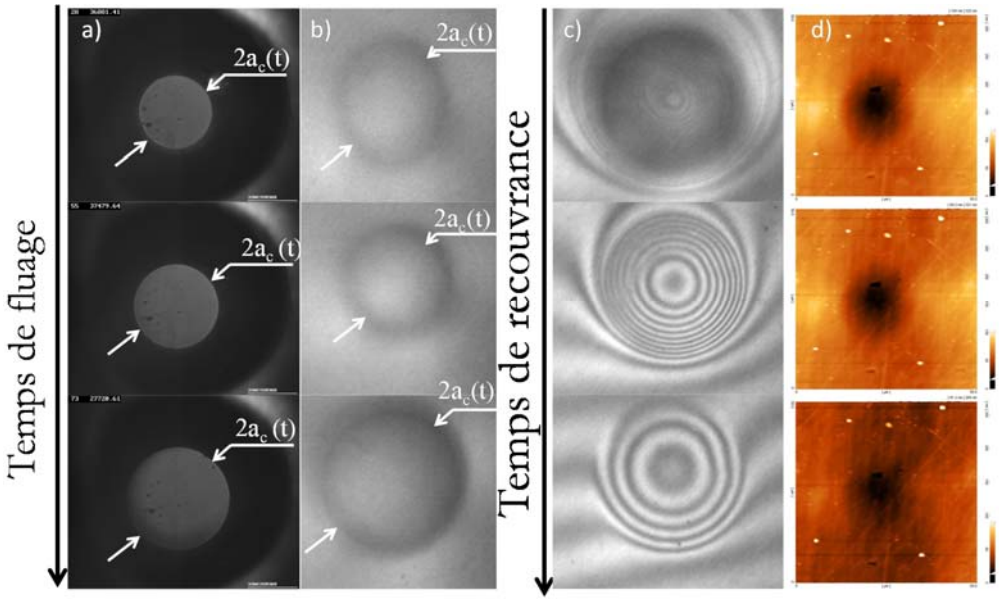

Figure II-1 Observation du fluage a) vision à travers la pointe b) vision à travers l'échantillon. Observation de la recouvrance c) vision à travers l'échantillon d) observation AFM

Lors d'un contact macroscopique entre deux surfaces, il existe deux phases distinctes : le contact, à proprement parler, et la recouvrance. Par rapport aux matériaux métalliques et céramiques, qui ne recouvrent pas, le phénomène de recouvrance est une phase importante pour les matériaux polymères, et doit être prise en compte pour caractériser leur résistance globale. En général, l'empreinte résiduelle ou le sillon, après indentation ou rayure, sont mesurés par profilométrie ou AFM [15, 16]. La difficulté réside dans le délai entre la fin du contact et la fin de la procédure d'imagerie. Malheureusement, la majorité des changements et des évolutions des empreintes résiduelles ou des sillons sont observés durant ces premiers temps à cause des comportements viscoélastiques [17]. Grâce au Microvisioscratch [14], les premières images de la recouvrance sont prises après 0.5s. De plus dans notre cas le fluage et la recouvrance d'indentation sont observés sur de très longues périodes de temps (en général plus de 24 heures). En utilisant différent instruments, une approche multi technique a pu être conduite du macro au nano-contact. Dans ce travail, nous nous intéresserons principalement aux macro et micro contacts.

La caractérisation mécanique des surfaces de polymères est aussi faite par des expériences de rayures [18]. Les premières descriptions de la recouvrance des sillons ont été données par plusieurs auteurs [18-20]. Néanmoins, aucune information n'a été donnée avant 15 minutes. Dans notre cas la phase de recouvrance a été observée avec le Microvisioscratch (Figure II-2 a)). Puis les images ont été transformées en une représentation 3D de l'échantillon (Figure II-2 b)). La Figure II-2 c) présente trois profils transversaux au cour du temps. Finalement, certain profils, compris entre le début et la fin de la rayure, à des distances de la fin de la rayure choisies, ont été extraits.

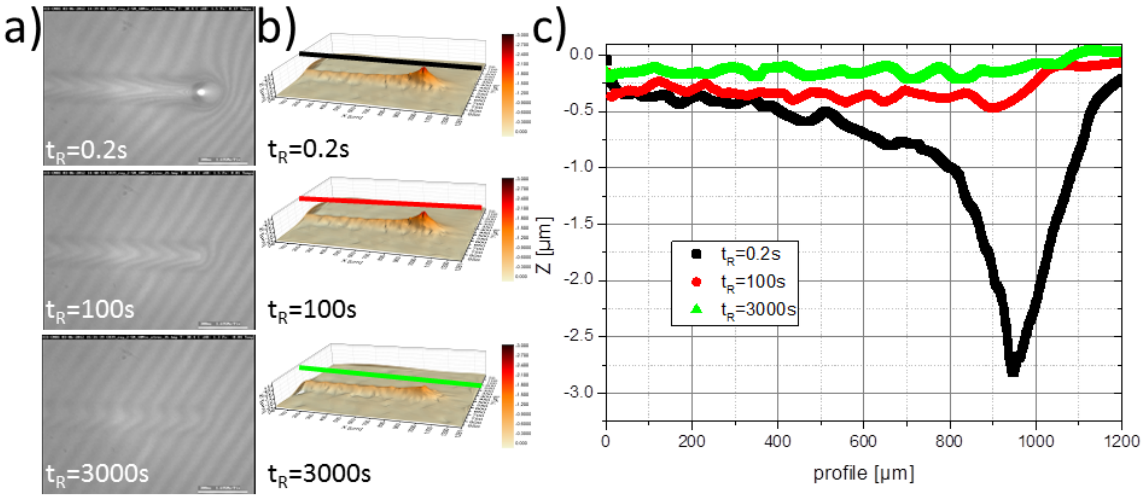

Figure II-2 Recouvrance de rayure avec le temps a) image initiale b) représentation 3D du sillon c) profils longitudinaux à trois temps différents

II.3. PROPRIÉTÉS MÉCANIQUES EN VOLUME

Dans cette partie, les propriétés mécaniques du CR39, du PMMA CN et du PMMA 10 AlO(OH) sont observées. Tout d'abord des mesures en DMTA ont été effectuées. Puis des expériences de relaxation sont présentées. Enfin les expériences de relaxation sont utilisées pour construire des courbes maîtresses.

II.3.1. Relaxation

L'élasticité instantanée ne reflète pas toutes les possibilités des matériaux polymères. En effet, Struick [21] et d'autres auteurs [22, 23] ont observé la dépendance au temps des matériaux polymères par des essais de relaxation ou de fluage. Nous avons choisi de faire des essais de relaxation en compression. La compression a été choisie parce qu'elle constitue la sollicitation majoritaire de l'indentation. Par ailleurs, les essais de relaxation ont été choisis car la viscoélasticité est introduite dans le logiciel MSC Marc par des essais de relaxation [24].

La Figure II-3 représente la contrainte vraie et le temps en fonction de la déformation vraie et du temps pour le CR39 à 30°C. Pour toutes les courbes, le début des données enregistrées correspondant à 10 fois le temps de chargement a été enlevé pour ne pas observer le chargement et ses effets. Le gradient de couleur s'assombrit pour les hauts niveaux de déformations [0.75 %-22 %]. Pour toutes les expériences la contrainte diminue au cours du temps. En outre, pour le CR39 (Figure II-3), la contrainte initiale augmente avec la déformation jusqu'à une valeur de 4 % (ligne pointillé noir). Puis la contrainte initiale chute jusqu'à une valeur de 10 % de déformation et finalement augmente de nouveau (ligne en tiret noir). L'élasticité du matériau est responsable de la contrainte initiale à faible déformation. Ensuite, avec l'augmentation du temps et/ou de la déformation, la dépendance du CR39 évolue. À très haute déformation, la réticulation du CR39 empêche le matériau de couler et ainsi la contrainte augmente de nouveau. Le CR39 est donc

élastique puis viscoélastique. D'autres expériences (dépendance à la température, autres matériaux) sont disponibles dans la partie VI.2.2.

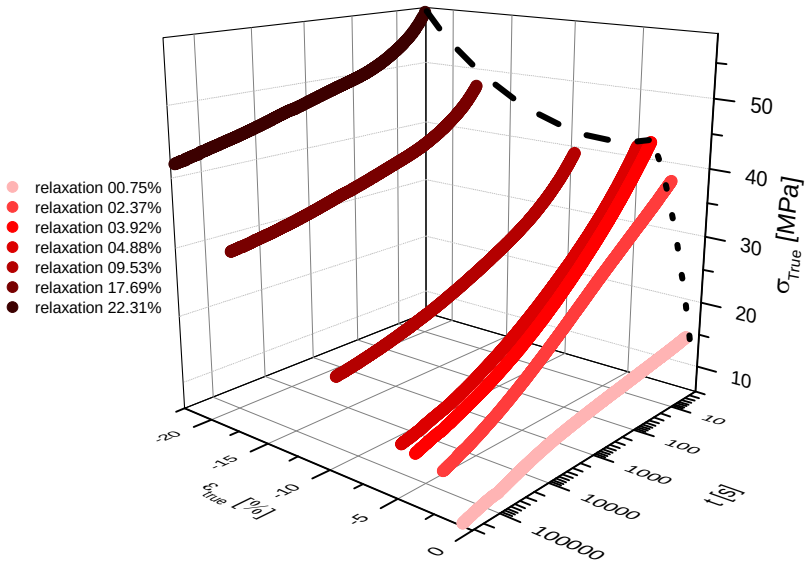

Figure II-3 Représentation 3D de la série d'expérience sur le CR39 à 30°C

II.3.2. Modules de relaxation et courbes maîtresses

Le groupe d'expérience précédent est utilisé pour calculer (voir Equation V-11) le module de relaxation en fonction du temps. Pour chaque courbe le module de relaxation diminue. Les plus grandes déformations conduisent aux plus petits modules de relaxation. Enfin, la courbe de l'expérience réalisée à 0.75 % de déformation est convexe alors que les autres sont concaves. Des courbes maîtresses en fonction de la température et de la déformation ont déjà été proposées par plusieurs auteurs sur du HDPE [25], Polypropylène [23, 26], PC [27, 28] ou Poly(vinyle acétate) [29]. En décalant (latéralement uniquement) les courbes de la Figure II-4 a), il est possible de construire une courbe maîtresse de module de relaxation. Pour ce faire nous avons choisi comme courbe de référence (non décalée) la courbe de la relaxation à 0.75 % de déformation. Pour translater les courbes, le temps expérimental a simplement été multiplié par un coefficient appelé a_T. La courbe ainsi obtenue est présentée dans la Figure II-4 b). On observe une forte décroissance du module de relaxation en fonction du temps. En effet, le module de relaxation chute de manière importante jusque 10 % de sa valeur initiale après 30 millions de siècles. À ce point le module de relaxation semble atteindre un plateau. Cela est probablement dû à la réticulation du CR39 qui bloque le fluage. Enfin, la forme de « S », tronquée et inversée, observée sur la courbe maîtresse peut être associée aux propriétés élastique, viscoélastique à temps court et viscoélastique à temps long.

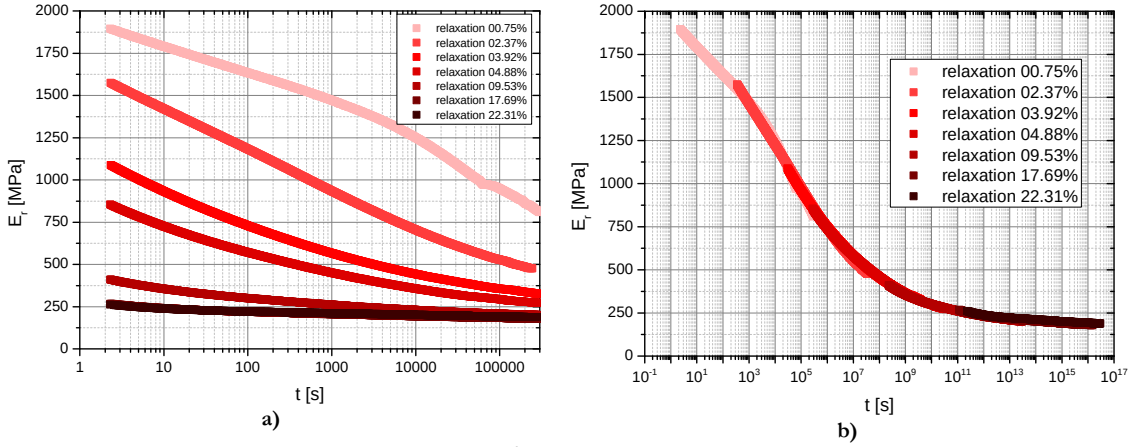

Figure II-4 a) Module de relaxation pour du CR39 à 30°C, b) Courbe maîtresse du module de relaxation pour le CR39 à 30°C avec l'expérience à 0.75 % de déformation comme référence

Les coefficients multiplicateurs, utilisés pour les modules de relaxation, sont tracés sur la Figure II-5 pour tous les matériaux disponibles. Ainsi, toutes les courbes maîtresses ont comme référence un essai réalisé à 0.75 % de déformation, le premier point de chaque courbe est donc [0.75 % : 1]. Les coefficients multiplicateurs pour le CR39 (carré rouge) augmente linéairement jusque 5 % de déformation. Ensuite entre 5 et 25 % de déformation il y a un faible accroissement. PMMA CN (cercle bleu) et PMMA 10 AlO(OH) (triangle vert) ont des comportements très similaires. Les coefficients multiplicateurs augmentent linéairement jusque 5 %. Après 5 % de déformation vraie, les coefficients multiplicateurs du PMMA CN et du PMMA 10 Al(OH) continuent d'augmenter presque linéairement. La stagnation des coefficients multiplicateurs du CR39 suggère que la réticulation ralentit le fluage du matériau au-delà de 5 %. Au contraire l'écoulement du PMMA CN et le PMMA 10 AlO(OH) est presque proportionnel à la déformation imposée. Comme les deux matrices de PMMA ont le même écoulement, nous pouvons conclure que les charges ne bloquent pas l'écoulement du matériau.

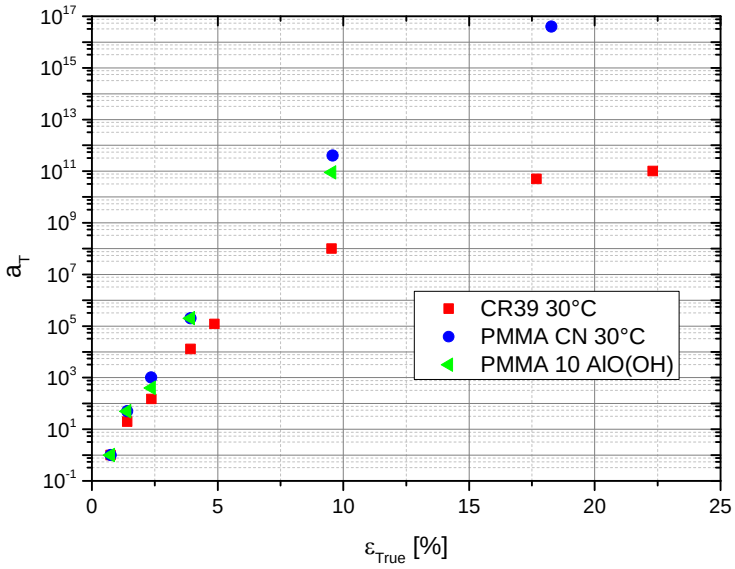

Figure II-5 Coefficients multiplicateurs pour les différents matériaux en fonction de la déformation vraie

II.3.3. Conclusion

Les propriétés mécaniques du CR39, du PMMA CN et du PMMA 10 AlO(OH) ont été analysées par des expériences de DMTA et de relaxation. La relaxation de ces matériaux a été observée sur de longues périodes de temps. La construction de courbes maîtresses à 0.75 % de déformation permet la prédiction du comportement viscoélastique des matériaux sur des siècles.

II.4. ANALYSE DU CONTACT

II.4.1. Fluage d'indentation

Le fluage d'indentation du PMMA CN et du CR39 est d'abord conduit à température ambiante. De très longs temps de maintien sont utilisés. Puis un ensemble de température est choisi pour couvrir les températures d'utilisation des polymères en général.

II.4.1.1 Température ambiante

La comparaison du fluage d'indentation du CR39 et du PMMA CN est présentée sur la Figure II-6. La pression moyenne de contact (gauche) est affichée en fonction du temps d'indentation. Toutes les forces (auquel les essais de fluages sont effectués) sont choisies de telle sorte que les déformations initiales de Tabor soient égales à 4 % [13]. Les pressions moyennes de contact du CR39 et du PMMA CN suivent les ratios observés en DMTA. La pression moyenne de contact du CR39 décroit linéairement avec le logarithme du temps. Au contraire la pression moyenne de contact du PMMA CN semble avoir deux pentes distinctes. La première est observée en dessous de 100s, la deuxième au-delà de 1000s. Bien que la déformation initiale de contact soit la même, les chemins des déformations normées sont différents pour chaque matériau (Figure II-6 b)). La déformation du PMMA CN augmente rapidement puis semble atteindre un maximum puis la vitesse de fluage diminue. Au contraire le CR39 a une vitesse de fluage plus lente qui augmente au cours du temps. À la fin des expériences des déformations similaires sont obtenues. Ainsi, les recouvrances sont comparables. Le ralentissement dans la vitesse de fluage du PMMA CN peut être imputé à l'apparition de la plasticité ou à un changement dans le phénomène viscoélastique. L'accélération du fluage du CR39 est, quant à elle, associée à une évolution de la viscoélasticité.

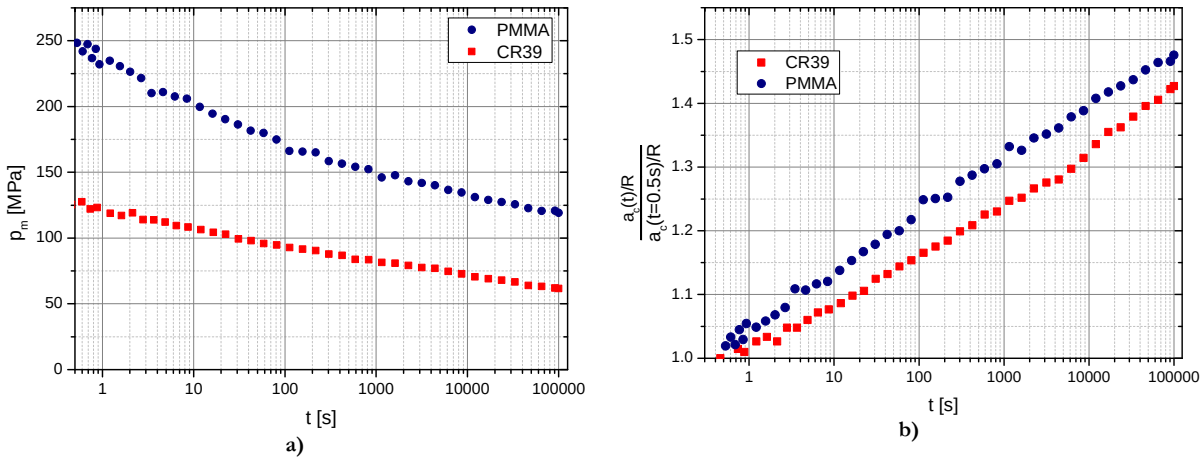

Figure II-6 a) Pression moyenne de contact et b) déformation de fluage d'indentation normée en fonction du temps de fluage pour du CR39 et du PMMA CN à 30°C

II.4.1.2 Influence de la température

Les polymères sont très sensibles à la température, donc leurs propriétés de contact le sont aussi [2, 30, 31]. Par ailleurs toutes les informations concernant le PMMA CN et le PMMA 10 AlO(OH) ne sont pas affichées ici, elles peuvent être trouvées dans la partie VI.3.1.2.

Les expériences de fluage d'indentation ont été conduites à différente température sur le CR39. La pression moyenne de contact en fonction du temps et de la température est présentée sur la Figure II-7. Dans tous les cas la pression moyenne de contact diminue lentement avec le logarithme du temps mais l'inclinaison des pentes est dépendante de la température. La pente est presque la même pour les deux températures les plus basses, puis les pentes augmentent avec la température (la pression moyenne de contact diminue plus lentement à haute température qu'à basse température). De plus le ratio de la pression moyenne de contact initiale sur son module d'Young à la même température est égal d'un matériau à l'autre et d'une température à l'autre. Par exemple, le module d'Young du CR39 à -20°C est environ 80 % plus grand que le module de Young du CR39 à 20°C. La pression moyenne de contact à -20°C est aussi 80 % plus grande que la pression moyenne de contact du CR39 à 20°C. Ces données, pentes et pression moyenne de contact initiale, suggèrent que la pression moyenne de contact instantanée est principalement dépendante du module d'Young alors que le fluage ne l'est pas comme cela était attendu.

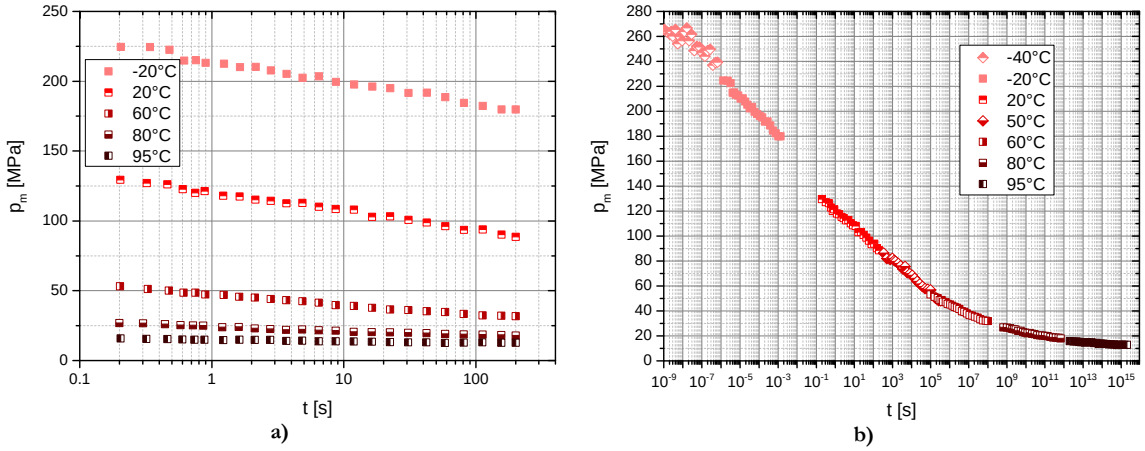

Figure II-7 Pression moyenne de contact en fonction du temps à différente température (déformation initiale de Tabor égale à 4 %) pour le CR39 a) temps normal b) courbe maîtresse

Par la suite, les courbes sur la Figure II-7 a) peuvent être décalées latéralement pour former une courbe maîtresse. La Figure II-7 b) présente l'évolution de la pression moyenne de contact en fonction du temps pour toutes les températures accessibles. La température de référence choisie est 30°C. La courbe maîtresse du CR39 décroit fortement en fonction du temps jusqu'à atteindre un point d'inflexion pour 10^7 s et correspond à une température de 60°C. Ainsi, l'effet de la température de transition vitreuse est observé. Pour un temps supérieur à 10^7 s ou une température supérieure à 60°C, l'écoulement du matériau est bloqué par la réticulation et la pression moyenne de contact mesurée est stable. D'autres auteurs ont déjà présenté des courbes maîtresses en indentation, en utilisant la grandeur mécanique de souplesse en indentation [25, 32]. Les données accessibles (Figure II-6) sont en accord avec la courbe maîtresse ainsi construite.

II.4.2. Recouvrance d'indentation

L'observation de la recouvrance d'indentation est faite à travers la mesure de la déformation normée de recouvrance d'indentation. Comme elle est normée par la déformation selon Tabor à la fin de l'expérience de fluage précédente, la valeur varie entre 1 et 0. Néanmoins, la compréhension du phénomène reste complexe : une différence de recouvrance peut être attribuée à une différence de propriétés rhéologiques (matériaux), de conditions (températures, temps de maintien, …) ou à l'état en fin d'indentation (cf. II.4.1). L'idéal serait de terminer toutes les expériences au même niveau de déformation. Toutefois, une telle démarche expérimentale demanderait un important nombre d'essais préliminaires (procédures d'essais et d'erreur). C'est pourquoi la déformation initiale de Tabor est utilisée (a/R=0.2 à 0.5 s) dans ce travail. De plus, durant la recouvrance, on observe le recouvrement à la fois de la déflection de la surface autour de l'indenteur (élastique et viscoélastique) et de l'empreinte (combinaison de propriétés élastique, viscoélastique et plastique). Les changements principaux surviennent pendant les premières secondes de recouvrance. Durant ces quelques secondes, il est difficile de réaliser une image optique nette. Ce problème est d'autant plus marqué que l'empreinte est importante. Par conséquent, un triangle hachuré gris est placé sur les données les moins fiables.

La Figure II-8 présente la déformation normée de recouvrance d'indentation en fonction du temps de recouvrance pour le CR39 et le PMMA CN. Il s'agit des recouvrances après 100 000s d'indentation (Figure II-6). Les deux courbes semblent chuter à ¾ de leur déformation finale

d'indentation. Ensuite la recouvrance du PMMA CN décroit jusque 25 % de sa valeur initiale alors que la déformation de recouvrance du CR39 diminue jusqu'à une valeur inférieure à 5 % de la valeur de déformation initiale (l'empreinte n'est plus mesurable). Par ailleurs les pentes ne sont pas les même pour le PMMA CN et le CR39. La recouvrance du PMMA CN semble ralentir autour de 100 s et presque s'arrêter autour de 10 000 s. Au contraire la courbe du CR39 présente deux pentes de recouvrance l'une entre 10 et 1000 s et la deuxième entre 1000 et 1 000 000 s. La recouvrance immédiate de 25 % peut être imputée dans les deux cas à la recouvrance élastique des matériaux. La recouvrance retardée est le signe du comportement viscoélastique. Les deux pentes observées sur le CR39 peuvent être associées à deux comportements viscoélastiques différents. Il y a deux phénomènes dans la recouvrance du PMMA CN : la viscoélasticité et la plasticité. Tout d'abord la viscoélasticité du PMMA CN permet le début de la recouvrance. Puis la recouvrance entre dans le matériau déformé plastiquement, ainsi la vitesse de recouvrance diminue rapidement jusqu'à s'arrêter. La recouvrance illustre donc dans quel cas le matériau est déformé plastiquement et dans quel cas il ne l'est pas, information que nous ne pouvons pas déterminer simplement par une analyse du fluage en indentation.

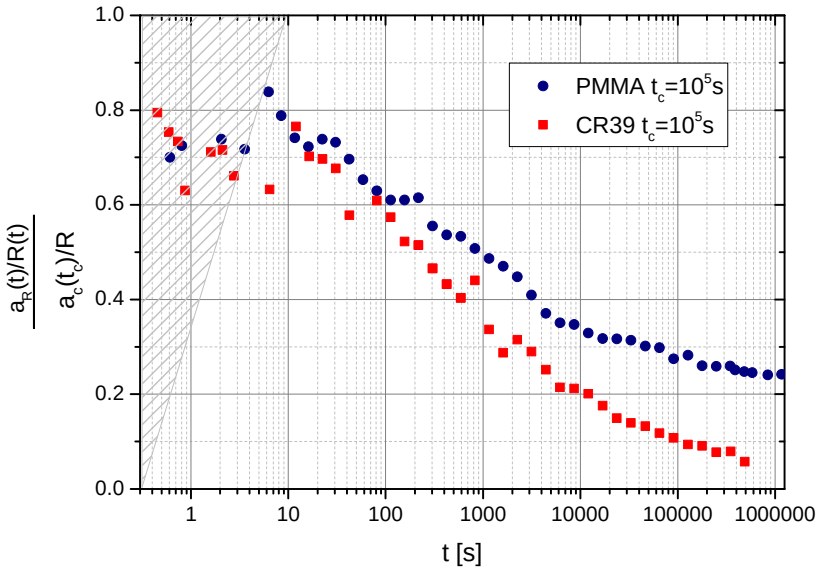

Figure II-8 Déformation normée de recouvrance d'indentation en fonction du temps pour le PMMA CN et le CR39 à 30°C

II.4.3. Comparaison de Courbes maîtresses

Ainsi, nous avons acquis deux types de courbes maîtresses : temps-déformation et temps-température. Les courbes maîtresses en déformation ont été faites en volume sur des essais de relaxation. L'une d'entre elle est représentée sur la Figure II-4 b) pour le CR39. Les courbes maîtresses temps-température ont été faites en indentation par exemple sur la Figure II-7 b). Les courbes maîtresses en volume montrent le module de relaxation alors que les courbes maîtresses montrent la pression moyenne de contact. Il n'est pas possible de les comparer directement. C'est pourquoi nous avons choisi de les normer par une valeur que les deux courbes ont en commun. Toutes les courbes concernant le CR39 vont être divisées par la valeur du point [1.2 s : 30°C : 4 %]. Pour la courbe maîtresse en volume, cela correspond au module de relaxation à la fin du

chargement de la relaxation à 3.92 % de déformation (E_R=1140 MPa). Pour la courbe maîtresse de contact, cela correspond à la pression moyenne de contact après 1.2 s d'indentation à 30°C (p_m=125 MPa). Une fois ces points de références choisis, les points doivent être placés à la valeur [1.2s : 1]. Une procédure similaire est effectuée sur le PMMA CN. Les courbes maîtresses obtenues sont présentées sur la Figure II-9 a) et b). Les courbes maîtresses en volume et en contact sont très proches l'une de l'autre pour le CR39 et le PMMA CN. Ainsi le temps, la température et la déformation affectent les mêmes mécanismes. Leur influence respective est différente. Les expériences en contact et en volume conduisent à la même courbe maîtresse. C'est pourquoi si la dépendance en contact n'est pas connue (dans le cas de PMMA 10 AlO(OH) par exemple), elle peut être estimée à partir de la courbe maîtresse de volume. L'inverse est aussi vrai : si la courbe maîtresse en contact et un module d'Young sont connus, la courbe maîtresse en volume pourra être déduite. L'application directe correspond au cas d'un revêtement ou d'une couche mince. De plus, l'influence de la plasticité peut aussi être déduite de ces courbes. La plasticité apparaît uniquement pendant la phase de chargement. Durant la phase de relaxation, le comportement est supposé purement viscoélastique. Les observations indiquent que des phénomènes de plasticité apparaissent dans les contacts des matériaux polymères non réticulés (voir II.4.2). Les courbes montrent que la plasticité n'affecte pas la viscoélasticité des polymères. Pour les matériaux testés, nous n'observons pas de phénomènes de viscoplasticité, car, dans le cas contraire, les courbes décrivant la dépendance au temps ne seraient pas identiques.

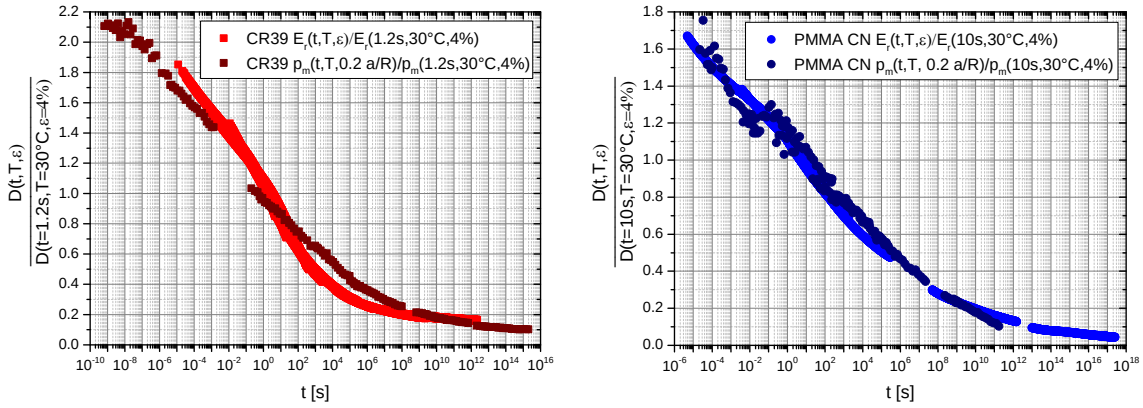

a) b)

Figure II-9 Comparaison de Courbes maîtresses normalisées à partir de fluage de contact et de relaxation pour du a) CR39 centré après une sollicitation de 1.2 s, à une température de 30°C et une déformation de 4 % et du b) PMMA CN centré après une sollicitation de 10 s, à une température de 30°C et une déformation de 4%

Par ailleurs la Figure II-9 peut être complétée par des courbes maîtresses obtenue d'expérience de DMTA. Plus d'informations sur ces courbes peuvent être trouvées dans la partie VI.3.3. Ainsi nous pouvons obtenir trois courbes maîtresses par différentes méthodes. Les courbes maîtresses de DMTA (temps-température), de relaxation (temps-déformation) et d'indentation (temps-déformation-température) sont cohérentes les unes avec les autres. Cette adéquation est observée pour les deux matériaux étudié le CR39 et le PMMA CN dans la Figure II-10. En conclusion, les phénomènes visqueux sont similaires quelque soit la température, la déformation ou le temps de sollicitation.

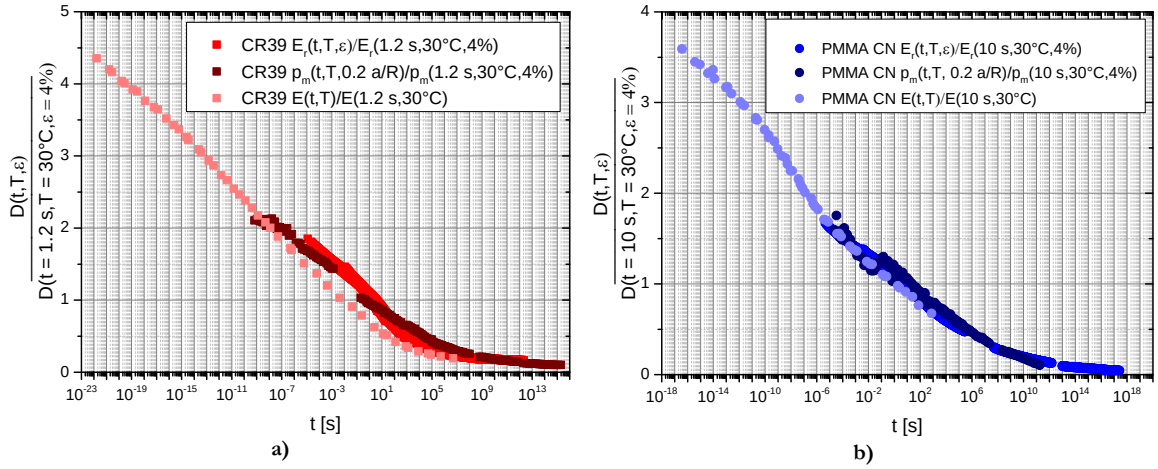

Figure II-10 Comparaison de Courbes maîtresses normalisées à partir de DMTA, fluage de contact et de relaxation pour du a) CR39 centré après une sollicitation de 1.2 s, à une température de 30°C et une déformation de 4 % et du b) PMMA CN centré après une sollicitation de 10 s, à une température de 30°C et une déformation de 4%

II.4.4. Analyse de la recouvrance de la rayure

Nous avons conclu de la partie précédente, que le fluage sous indentation sphérique et sa recouvrance sont des expériences complexes. La rayure est un test encore plus proche de la dégradation des polymères dans la vie courante. Ainsi pour mieux comprendre ces dégradations, les caractérisations mécaniques des polymères sont souvent réalisées par des essais de rayures [18].

II.4.4.1 Informations générales

Dans les rayures réalisées dans ce travail, aucun phénomène irréversible (craquelures, fissures) n'a été observé. Seul le comportement ductile du CR39 est étudié. La Figure II-11 a) est une représentation en fausse couleur d'un sillon résiduel de rayure, déduite des observations optiques après retrait de l'indenteur. La position des différentes coupes est expliquée sur la Figure II-11 a). Un exemple de profil en coupe à une distance de 4 a_c est présenté sur la Figure II-11 b). En fonction du temps la profondeur de rainure décroît. Par ailleurs sur chaque côté de l'empreinte des bourrelets latéraux « pile-up » peuvent être observés. Ces derniers semblent eux aussi diminuer avec le temps. Les profils mesurés ne sont pas tout à fait symétriques. Cela est dû à la méthode d'interpolation.

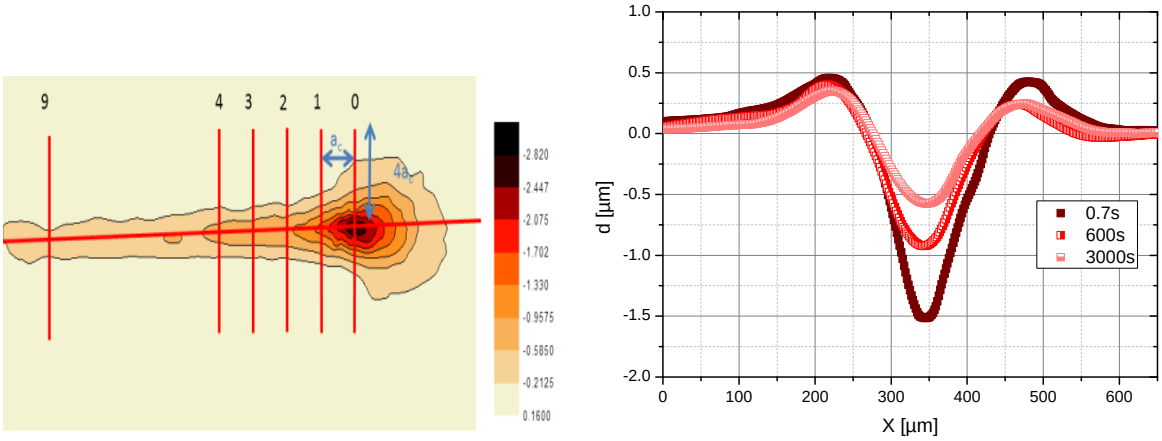

a) b)

Figure II-11 a) schéma représentant les positions des différents profils b) trois profils à différents instants à une distance de 4ac de la fin de la rayure

II.4.4.2 Influence de la distance depuis la fin de la rayure

La profondeur de recouvrance de rainure est observée en fonction du temps à des distances différentes de la fin de rayure sur la Figure II-12. Le temps de recouvrance présenté est le temps depuis le retrait de la pointe de la surface, qui est différent du temps écoulé depuis le passage de l'indenteur sur cette partie du matériau. Ainsi tous les profils ne reflètent pas le même temps de recouvrance. Une difficulté supplémentaire vient du fait que tous les profils ne reflètent pas la même histoire mécanique. En effet devant et sous la pointe, le matériau est compressé et cisaillé, puis derrière la pointe le matériau est tiré. Par ailleurs sur les bords de la rayure une combinaison de compression et de traction est observée. Ainsi la coupe à 0 a_c, représente un matériau qui a subi moins de traction que le matériau à 1 a_c qui lui-même a subi encore moins que celui à 2 a_c. Néanmoins la Figure II-12 démontre que la profondeur diminue en fonction du temps, et ce pour toutes les distances. Toutes les courbes se rejoignent au point [200 s : -0.4 µm]. Pour une distance supérieure à 4 a_c, les profils de recouvrance du fond du sillon sont identiques, indiquant que le matériau a subi la sollicitation mécanique totale et que l'indenteur s'est suffisamment éloigné pour ne plus affecter le phénomène de recouvrance. Pour des distances inférieures à 4 a_c, les différents volumes de matière n'ont pas subi la même histoire mécanique. Ainsi, les études suivantes présentées dans la partie 0 seront principalement conduite à la distance charnière de 4 a_c.

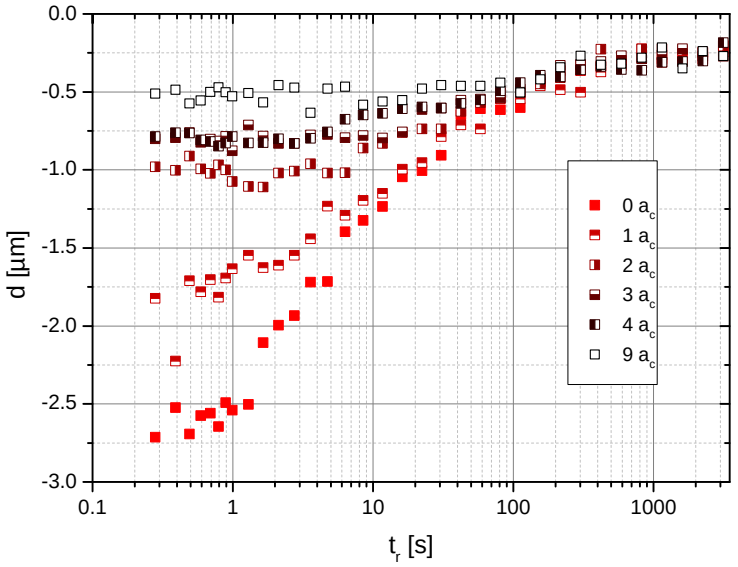

Figure II-12 La profondeur des rainures lors de la recouvrance du CR39 à 30°C en fonction du temps à plusieurs distances de la fin de la rayure

II.4.4.3 Influence de la charge

Comme vu précédemment, la matière à 4 a_c a été soumise à toute l'histoire mécanique. C'est pourquoi tous les graphiques présentés ci-après concerne la recouvrance observée pour les profils transversaux à 4 a_c. La Figure II-13 a) présente la profondeur de recouvrance en fonction du temps et de la déformation. L'origine des temps choisie est le moment où la pointe est enlevée de la surface. Les différentes déformations sont obtenues pour différentes forces appliquées sur l'indenteur (de la plus basse à la plus haute déformation les forces sont 1, 2.5, 5 N). Les profondeurs de contact sont respectivement 3.6, 9.5 et 14 µm. Dans tous les cas, une valeur plateau est observée pour les 2-3 premières secondes de mesures. Ensuite la profondeur de recouvrance diminue en fonction du temps pour toutes les déformations. Les profondeurs finales sont très petites en comparaison avec les profondeurs de contact. Le choix de l'origine des temps induit la présence du plateau. En effet le temps écoulé depuis le passage du centre de la pointe (ou depuis que la contrainte la plus importante a eu lieu) est d'environ 30 s. Ainsi trois secondes de plus ou de moins de recouvrance n'ont pas une influence importante sur la recouvrance du sillon. Les formes des courbes peuvent donner l'impression de deux comportements différents pour les différentes déformations. De manière à comparer la proportionnalité de la vitesse de recouvrance, la Figure II-13 b) présente les mêmes données mais normées par leur première valeur de profondeur de recouvrance. Le plateau est toujours observé mais les vitesses de recouvrance sont identiques. Les courbes sont légèrement décalées en temps. Une explication possible est de nouveau l'origine des temps, comme les déformations sont différentes, alors les distances de 4 a_c sont différentes, ainsi le temps écoulé depuis le passage du centre de la pointe est différent. C'est pourquoi un léger décalage en temps peut apparaître.

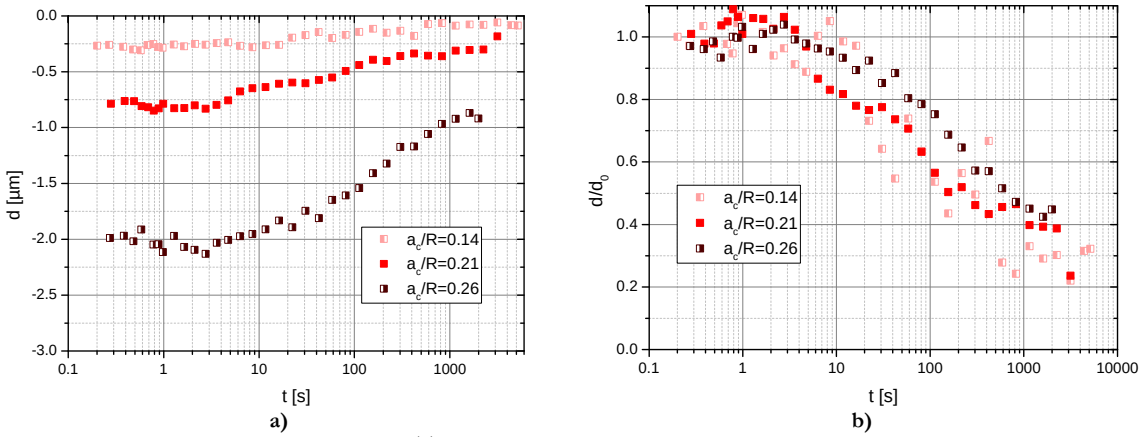

Figure II-13 a) Influence de la déformation de Tabor en rayure sur la profondeur de recouvrance à 4ac de la fin de la rayure en fonction du temps écoulé depuis le retrait de la pointe de la surface de CR39 à 30°C b) Même expérience dont les données ont été normées par la première profondeur de recouvrance mesurée

II.4.4.4 Conclusion partielle

Ensuite les profondeurs de recouvrance ont été présentées en fonction du temps de recouvrance et de leur distance à la fin de la rayure (les distances choisies sont des multiples du rayon de contact). La distance de 4 a_c correspond à la plus courte distance pour laquelle toute l'histoire mécanique a été réalisée. La recouvrance est étudiée par la suite à cette distance. Dans le manuscrit, l'influence de la charge et de la vitesse de la pointe sont étudiées. Plus la charge est importante, ou plus la vitesse de rayure est lente, plus la profondeur de recouvrance initiale est importante. Néanmoins la recouvrance est démontrée proportionnelle les unes aux autres dans tous les cas, il n'y a donc pas de plasticité d'observée dans ces rayures, seul de la viscoélasticité à temps long (voir la courbe maîtresse VI.3.4.3).

II.4.5. Conclusion

Dans cette section, des courbes maîtresses temps-déformation en compression ont été construites. L'analyse du fluage et de l'indentation nous ont permis d'observer l'apparition de la plasticité pour le PMMA CN pour des temps de maintien longs lors d'essais de fluage en indentation ou à haute température. Le CR39 présente, comme le PMMA CN, un comportement thermoplastique en dessous de sa température de transition vitreuse et élastomérique au-dessus. Dans tout le domaine de température testé, le CR39 présente uniquement un comportement viscoélastique.

Par ailleurs la pression moyenne de contact permet la création de courbes maîtresses en déformation-temps-température. Ces courbes sont en adéquation presque parfaite avec les courbes maîtresse obtenues en compression, ce qui démontre l'absence d'influence de la plasticité sur la viscoélasticité et l'absence de viscoplasticité dans le comportement des polymères. La recouvrance instantanée de la rayure a été présentée pour la première fois dans ce chapitre.

II.5. SIMULATION PAR ÉLÉMENTS FINIS

II.5.1. Lois de comportement

Finalement des simulations par éléments finis ont été conduites pour mieux comprendre la phase de recouvrance. De manière à caractériser les propriétés visqueuses du matériau plusieurs essais uni-axiaux de relaxation ont été réalisés. Les déformations appliquées sont dans le domaine [0.5-22 %]. Une représentation 3D de cette série d'expérience peut être observée sur la Figure II-3. De ces expériences deux types de lois de comportement peuvent être identifiées : viscoplastique et viscoélastique. La loi de comportement viscoplastique introduite est fondée sur une équation de Norton (voir partie VII.2.4). Cette loi donne la contrainte en fonction de la déformation vraie et de la vitesse de déformation vraie. La Figure II-14 présente le plan ajusté sur les données. La loi de Norton [33] et les coefficients obtenus sont aussi indiqués sur le graphique.

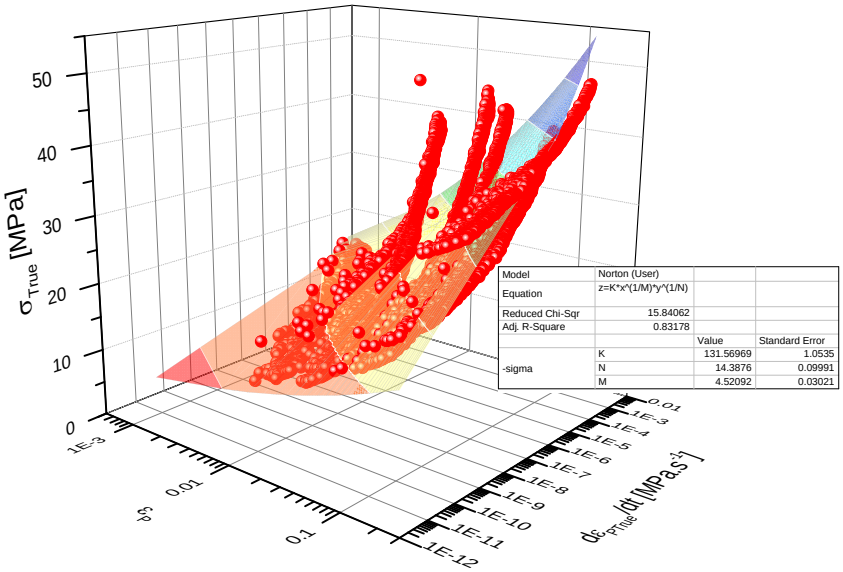

Figure II-14 Ajustement de la loi de Norton sur des expériences de relaxation

La loi de comportement viscoélastique consiste en un modèle de Maxwell généralisé (dans notre cas 8 couples ressort-amortisseur en parallèle). Les équations de Maxwell des modules de cisaillement et d'élasticité isostatique de Maxwell sont ajustées sur une expérience de relaxation. Ainsi pour chaque expérience de relaxation un ensemble de coefficients viscoélastique est déterminé [34]. Dans ce résumé les ensembles de paramètres correspondant aux essais de relaxation à 4.88 et 17.69 % ont été utilisés, ils ont été nommés respectivement VE (ε = 4.88 %) et VE (ε = 17.69 %).

Par ailleurs nous avons observé précédemment (Figure II-4b)) qu'il était possible de construire des courbes maîtresses avec des expériences de relaxation. On peut donc ajuster un modèle de Maxwell sur ces courbes maîtresses (CM VE) [35]. Dans ce cas la courbe maîtresse est centrée sur l'expérience de la déformation choisie. Dans la Figure II-15, qui présente la courbe maîtresse du CR39 à 30°C centré sur l'expérience à 4.88 % de déformation, les valeurs pour l'expérience à 4.88 % ne sont pas décalées. Les modules de cisaillement provenant de plus faibles déformations sont décalés horizontalement vers la gauche alors que ceux venant de plus hautes déformations

sont décalés vers la droite. L'ajustement présenté sur ce graphique est un modèle de Maxwell avec 18 constantes de temps pour couvrir tout le temps accessible convenablement. La qualité de l'ajustement est inférieure à celle obtenu dans les autres cas. Cela est probablement dû à un décalage imparfait des courbes expérimentales.

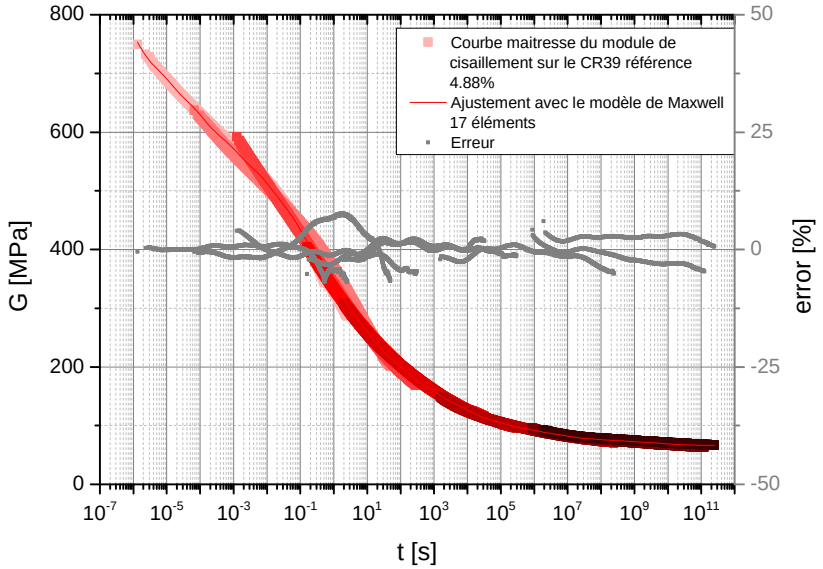

Figure II-15 Courbe maîtresse du CR39 décalée pour avoir l'expérience à 4.88 % de déformation, ajustée avec une équation de Maxwell généralisée

Comme expliqué précédemment, chaque expérience de relaxation permet de construire un ensemble de paramètres viscoélastiques. Il en va de même pour les courbes maîtresses. L'étude des paramètres viscoélastiques va être faite sur le CR39, le matériau le plus étudié dans ce travail. Par ailleurs le modèle de Maxwell généralisé est un opérateur mathématique dont l'ajustement est bon sur des phénomènes visqueux car il est hautement paramétré [36].

Pour comparaison, quatre lois de comportement viscoélastiques ont été analysées. Elles ont été identifiées comme montré précédemment à des déformations différentes. Les déformations choisies sont 4.88 et 17.69 %. Ces déformations correspondent aux déformations vraies d'expérience réalisée à 5 et 19.4 % de déformation. Pour chaque relaxation des courbes maîtresses sont construites. Ainsi on a deux lois de comportement pour des matériaux viscoélastiques « simples » et deux lois pour des matériaux viscoélastiques « complexes ».

Enfin un modèle élasto-plastique (EP) de type G'Sell Jonas est disponible dans la littérature [37-39]. Les coefficients sont calculés grâce à des essais d'indentation avec des indenteurs de formes différentes.

Pour améliorer la qualité de la simulation, les trajets de chargements expérimentaux sont utilisés dans la modélisation numérique. Les expériences de relaxation numériques sont pilotées par le déplacement de la traverse expérimentale et les expériences d'indentation numérique sont pilotées par la charge appliquée sur la sphère expérimentalement.

II.5.2. Relaxation uni-axiale

Les différentes lois de comportement sont testées sur des essais de relaxation. L'avantage de l'essai de relaxation est que la déformation est presque uniforme dans le matériau. Ainsi la qualité de la loi de comportement à une déformation donnée peut être évaluée.

II.5.2.1 Relaxation à 4.88 %

La Figure II-16 présente la contrainte en fonction du temps pour des essais de relaxation à 4.88 % de déformation. Le graphique a) montre en plus les résultats des essais numériques réalisés avec les lois viscoélastiques identifiées à 4.88 % de déformation. Le graphique b) affiche les résultats obtenus avec les lois viscoélastiques à 17.69 % de déformation. Le dernier graphique c) présente les résultats obtenus grâce aux lois élasto-plastique et viscoplastique. Les lois VE identifiées à 4.88 % de déformation sont très précises. Les valeurs initiales observées avec VE (ε=4.88 %) sont néanmoins peu représentatives. L'ajustement proposé par la loi CM VE (ε = 4.88 %) est de bien meilleure qualité pour les temps courts. En revanche, pour les temps longs les deux lois sont équivalentes. Cette conclusion est pertinente car les coefficients des deux lois VE sont très proches pour ces constantes de temps. Les lois VE (ε = 17.69 %) et CM VE (ε = 17.69 %) présentent des résultats éloignés de l'expérience. L'objectif de ce graphique est de démontrer la non précision d'une loi VE utilisée hors de son domaine de définition. Les paramètres rhéologiques des lois produisent un matériau plus raide qu'il n'est. En effet, la contrainte est beaucoup plus faible que dans la réalité. Ces lois de comportement n'ont pas été ajustées pour ces déformations. Enfin la loi VP donne une vague approximation des valeurs obtenues alors que la loi EP donne une bonne approximation de la réponse instantanée mais ensuite elle n'évolue pas dans le temps.

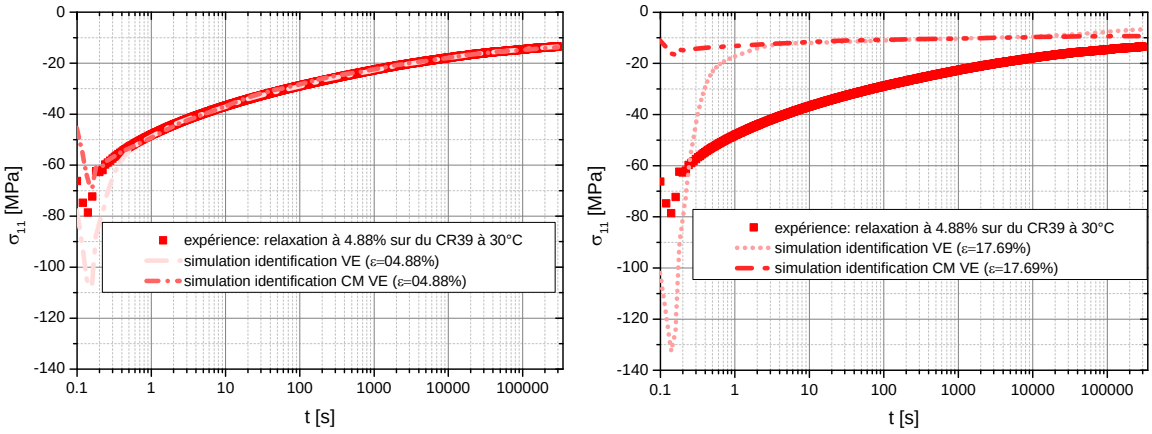

a) b)

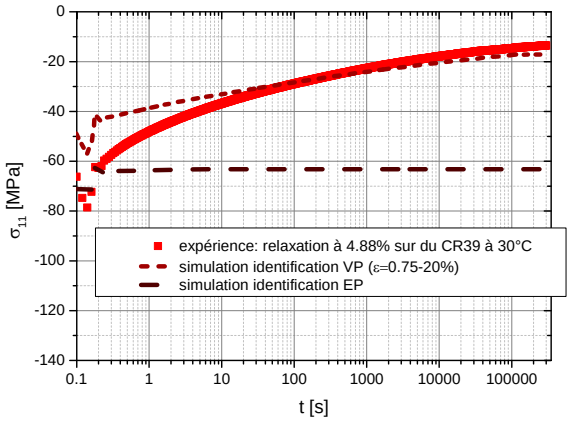

c)

Figure II-16 La contrainte en fonction du temps pour des expériences de relaxation faite sur du CR39 à 30°C a) lois VE 4.88 % b) lois VE 17.69 % c) lois EP et VP

II.5.2.2 Relaxation à 17.69 %

Sur la Figure II-17, la contrainte en fonction du temps pour un essai de relaxation à 17.69 % est présentée. Comme dans la Figure II-15, les résultats des lois VE (ε = 4.88 %) sont présentés en a), ceux des lois VE (ε = 17.69 %) en b), enfin ceux des lois EP et VP en c). Les contraintes des lois VE (ε = 4.88 %) sont beaucoup plus grandes que l'expérience donc la loi est trop souple. Les lois VE (ε = 17.69 %) démontrent une très bonne précision après le chargement, la loi VE (ε = 17.69 %) simple est beaucoup trop souple pendant le chargement tandis que CM VE (ε = 17.69 %) est trop dure. Finalement la loi EP reflète bien le chargement mais pas l'évolution ultérieure et la loi VP est un peu trop raide.

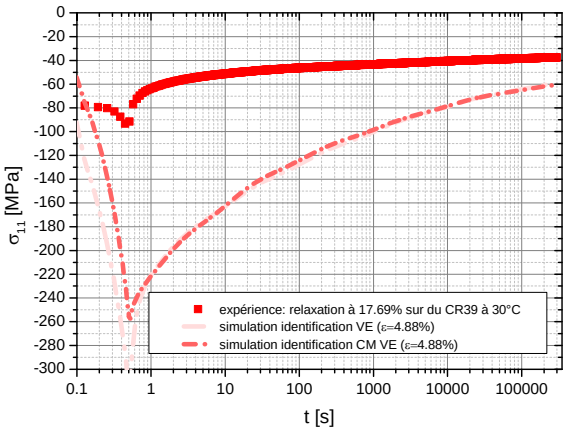

a)

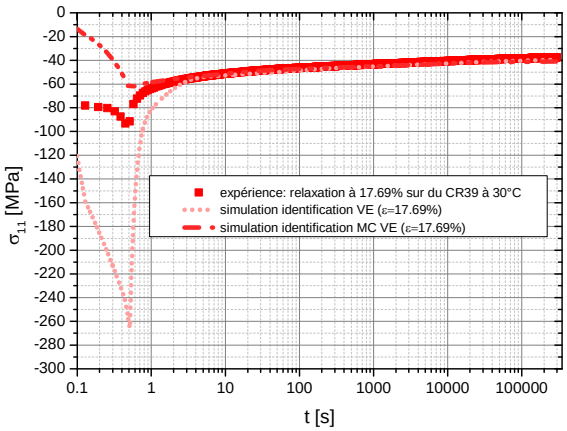

b)

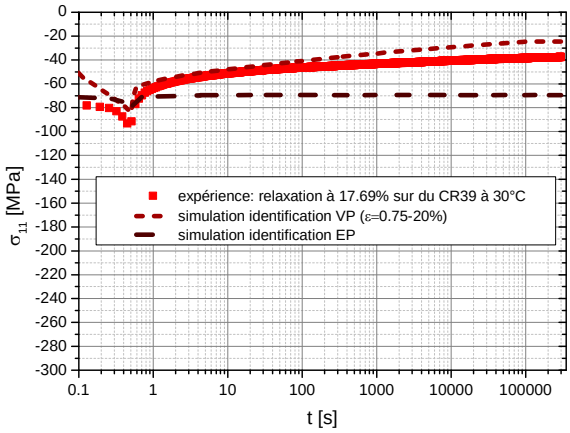

c)

Figure II-17 Contrainte en fonction du temps pour un essai de relaxation à 17.69 % de déformation et 30°C a) lois VE (ε = 4.88 %) et CM VE (ε = 4.88 %) b) lois VE (ε = 17.69 %) et CM VE (ε = 17.69 %) c) lois EP et VP

II.5.2.3 Conclusion partielle

Les lois VE sont très précises quand elles sont utilisées proche de la déformation pour laquelle elles ont été identifiées. Par ailleurs, l'utilisation de courbes maîtresses améliore la qualité de la simulation du chargement. En effet, les courbes maîtresses sont aussi ajustées sur des temps courts qui correspondent à la durée du chargement. Cette durée n'est pas prise en compte pour l'ajustement du matériau viscoélastique « simple ». Les courbes maîtresses sont ajustées pour des temps plus courts et plus longs. De plus, les simulations faites avec la loi EP donnent une contrainte instantanée juste mais ne présente aucun phénomène visqueux. Finalement la loi VP est universelle et donne une première approximation de l'évolution dans le temps du matériau dans tous les cas. Comme les indentations sont réalisées à une déformation selon Tabor entre 4 et 6 % (début et fin de courbe d'indentation sur le CR39 et le PMMA CN Figure II-6) [13, 40], les lois viscoélastiques à 4.88 % sont utilisées.

II.5.3. Indentation

La simulation du fluage d'indentation présente des intérêts pour de nombreuses applications [41-43]. Les résultats des simulations du fluage et de la recouvrance d'indentation sont présentés ci-dessous.

II.5.3.1 Fluage d'indentation

La pression moyenne de contact est représentée en fonction du temps sur la Figure II-18 a). Les données expérimentales décroissent avec le logarithme du temps. La simulation réalisée avec la loi de G'Sell Jonas ne décroit pas du tout. La valeur initiale de pression moyenne de contact est néanmoins juste. Au contraire la valeur initiale de la simulation avec la loi VE (ε = 4.88 %) est beaucoup trop forte et le reste sur la plage de temps simulée. Les simulations qui utilisent les lois CM VE (ε = 4.88 %) et VP, produisent des valeurs légèrement plus faibles que l'expérience mais décroissent de la même manière que celle-ci. La non-évolution de la simulation utilisant la loi plastique était attendue car le temps n'est pas pris en compte dans cette loi. Les hautes valeurs produites par la simulation avec la loi VE peuvent s'expliquer par le fait que les premières millisecondes de l'expérience de relaxation ne sont pas prises en compte et ainsi produisent une

erreur au début de l'expérience d'indentation qui se répercute sur l'ensemble de l'expérience. La courbe maîtresse corrige ce manque. En effet, la valeur initiale de pression moyenne de contact est beaucoup plus proche de l'expérience. La relative précision obtenue par la courbe du matériau VP vient du fait que cette loi est identifiée et donc valide pour un large domaine de déformation. Ainsi, chaque élément qui subit une contrainte a une déformation moyenne juste. La Figure II-18 b) présente la déformation normée en indentation selon Tabor pour les expériences et les simulations. La loi EP ne provoque aucun changement de déformation, prouvant ainsi son absence d'évolution en fluage. La simulation avec la courbe maîtresse donne une déformation supérieure à la déformation expérimentale. Au contraire les déformations provoquées par les lois VE et VP sont inférieures à l'expérimentale. La simulation la plus précise est celle effectuée avec la loi VP. En effet la réponse moyenne semble produire un bon compromis.

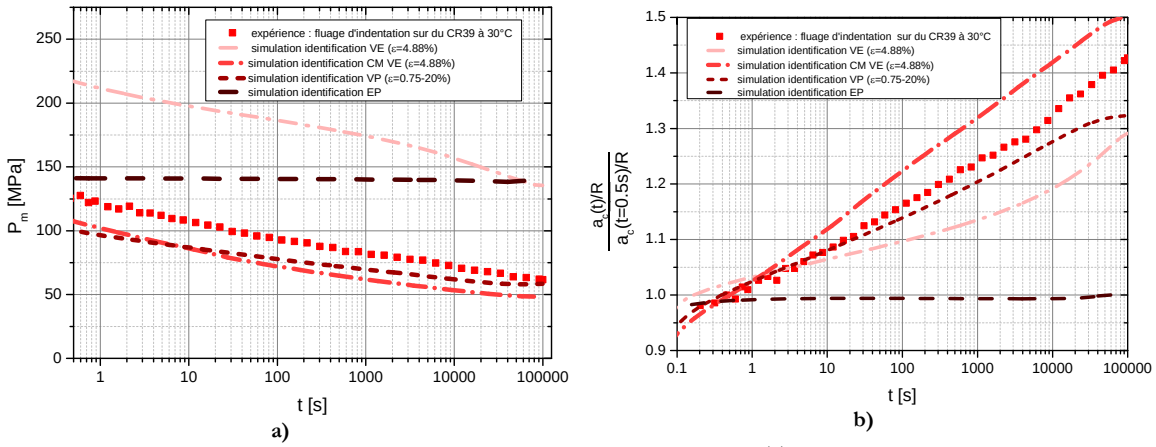

Figure II-18 a) la pression moyenne de contact et b) la déformation normée de Tabor en indentation pendant un essai de fluage d'indentation sur du CR39 en simulation et en expérimentale

En conclusion le comportement en fluage d'indentation du CR39, entre 4 et 6 % de déformation, peut être simulé avec le plus de précision par la courbe maîtresse à 4.88 % ou par la loi viscoplastique. Les deux lois montrent une pression moyenne de contact légèrement inférieure à la valeur expérimentale mais les déformations numériques normées encadrent les déformations expérimentales.

II.5.3.2 Recouvrance d'indentation

Les résultats des essais expérimentaux et numériques sont présentés sur la Figure II-19. Dans ces graphiques une déformation de 1 correspond à l'empreinte de fin d'indentation et de 0 à une recouvrance complète. Les courbes correspondant aux lois EP et VP sont horizontales. Elles représentent des recouvrances respectives de 45 et 20 % des empreintes d'indentation. Dans les deux cas, la partie élastique de l'empreinte recouvre et ensuite plus rien. La loi EP a conduit à une empreinte plus petite (voir Figure II-18 b)). C'est pourquoi la part de matériau déformée élastiquement est plus importante et donc aussi le pourcentage de recouvrance. Les deux autres simulations présentent des recouvrances complètes. La recouvrance immédiate de la loi VE (ε = 4.88 %) est d'environ 45 %, 20 % de plus que l'expérience. Cette recouvrance immédiate plus importante vient de la plus faible déformation finale. Au contraire la déformation finale observée pour la courbe de CM VE (ε = 4.88 %) est 5 % plus forte que l'expérience. La recouvrance immédiate de cette simulation est donc beaucoup plus proche de l'expérience. La loi

CM VE (ε = 4.88 %) permet une simulation proche de l'expérience nous confortant ainsi dans le fait que le CR39 est viscoélastique sur tout le domaine testé.

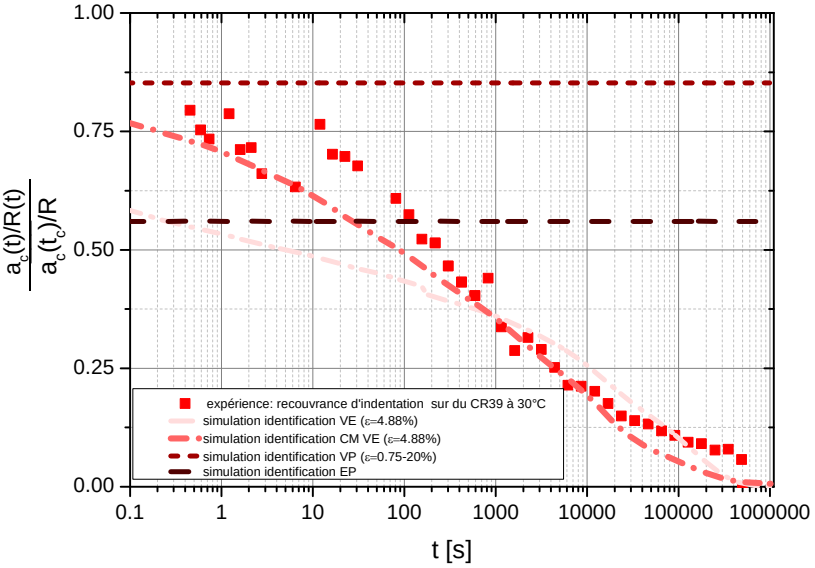

Figure II-19 déformation normée en recouvrance du CR39 pour des essais expérimentaux et en simulations

II.6. CONCLUSION GÉNÉRALE

Cette thèse présente la dépendance au temps des comportements mécaniques des matériaux polymères. En particulier, nous avons étudié la viscoélasticité dans le volume. Des courbes maîtresses (temps - déformation) ont été réalisées à partir d'expérience de relaxation. L'analyse du fluage et de la recouvrance nous ont permis d'observer l'apparition de la plasticité dans le cas du PMMA CN pour de longs temps d'indentation. Le CR39 présente, comme le PMMA CN, un comportement thermoplastique en dessous de sa température de transition vitreuse et élastomérique au dessus. Dans toute la gamme testée le CR39 ne présente qu'un comportement viscoélastique. L'analyse des essais montre que l'apparition de la plasticité dans le contact n'est possible à détecter que si on possède la courbe expérimentale correspondant à la phase de recouvrance. L'analyse de la phase de fluage n'est pas suffisante.

Par ailleurs la pression moyenne de contact nous a permis de créer des courbes maîtresses en déformation-temps-température, démontrant ainsi l'absence d'influence de la plasticité sur la viscoélasticité et une absence de viscoplasticité dans le comportement polymérique. Nous avons démontré l'équivalence des courbes maîtresses en contact et en volume, prouvant ainsi que l'on peut prédire une courbe maîtresse en connaissant l'autre. Une première analyse de la recouvrance après rayure est présentée pour la première fois dans cette thèse.

Puis le comportement mécanique des polymères est simulé par trois types de lois de comportement dans le logiciel MSC Marc. La loi élasto-plastique permet une prédiction juste de la relation contrainte-déformation au temps court. Elle ne présente pas d'effet de fluage. La loi viscoplastique donne une bonne représentation du fluage d'indentation par contre elle n'est pas utilisable pour simuler la recouvrance. La loi de comportement basée sur la courbe maîtresse démontre une très grande précision si elle est utilisée pour la déformation pour laquelle elle a été ajustée. Dans le cas du fluage d'indentation elle donne une idée précise de la déformation de

fluage normée. La recouvrance produite par la loi de comportement courbe maîtresse est juste à condition qu'il n'y ait pas de plasticité dans le contact.

Une voie d'amélioration, outre l'introduction d'un seuil de plasticité couplé à une loi de comportement de type VE, serait d'introduire des lois avec des comportements différents en fonction du mode de sollicitation (compression, traction et cisaillement) pour prendre en compte le caractère triaxial du test d'indentation.

II.7. BIBLIOGRAPHIE

[1] S.C. Tjong, Structural and mechanical properties of polymer nanocomposites, Materials Science and Engineering R: Reports, 53 (2006) 73-197.

[2] P. Bertrand-Lambotte, J.L. Loubet, C. Verpy, S. Pavan, Nano-indentation, scratching and atomic force microscopy for evaluating the mar resistance of automotive clearcoats: Study of the ductile scratches, Thin Solid Films, 398-399 (2001) 306-312.

[3] M. Mansha, C. Gauthier, P. Gerard, R. Schirrer, The effect of plasticization by fatty acid amides on the scratch resistance of PMMA, Wear, 271 (2011) 671-679.

[4] C. Gauthier, R. Schirrer, Time and temperature dependence of the scratch properties of poly(methylmethacrylate) surfaces, Journal of Materials Science, 35 (2000) 2121-2130.

[5] K. Yasui, Curable material containing photopolymerizable polymer and cured object, in: L. Nissan Chemical Industries (Ed.) USPTO, Nissan Chemical Industries , Ltd., united states of america, 2007.

[6] H. Hertz, Über die Berürhung fester elasticher Körper, Journal für die reine und angewandte Mathematik, 92 (1882) 156-171.

[7] W.C. Oliver, G.M. Pharr, Improved technique for determining hardness and elastic modulus using load and displacement sensing indentation experiments, J. Mater. Res., 7 (1992) 1564-1580.

[8] W.C. Oliver, G.M. Pharr, Measurement of hardness and elastic modulus by instrumented indentation: Advances in understanding and refinements to methodology, J. Mater. Res., 19 (2004) 3-20.

[9] A.C. Fischer-Cripps, A simple phenomenological approach to nanoindentation creep, Materials Science and Engineering A, 385 (2004) 74-82.

[10] S.E. Olesiak, M.L. Oyen, V.L. Ferguson, Viscous-elastic-plastic behavior of bone using Berkovich nanoindentation, Mech. Time-Depend. Mater., 14 (2010) 111-124.

[11] B.J. Briscoe, L. Fiori, E. Pelillo, Nano-indentation of polymeric surfaces, Journal of Physics D: Applied Physics, 31 (1998) 2395-2405.

[12] A. Rubin, C. Gauthier, R. Schirrer, The friction coefficient on polycarbonate as a function of the contact pressure and nanoscale roughness, Journal of Polymer Science, Part B: Polymer Physics, 50 (2012) 580-588.

[13] D. Tabor, The hardness of solids, Review of Physics in Technology, 1 (1970) 145.

[14] T. Chatel, C. Gauthier, H. Pelletier, V. Le Houerou, D. Favier, R. Schirrer, Creep of the contact with a spherical tip and recovery of the imprint on amorphous polymer surfaces, Journal of Physics D-Applied Physics, 44 (2011).

[15] I. Karapanagiotis, D.F. Evans, W.W. Gerberich, Dynamics of the leveling process of nanoindentation induced defects on thin polystyrene films, Polymer, 43 (2002) 1343-1348.

[16] Z.Y. Zhang, H.N. Dhakal, S.N. Surip, I. Popov, N. Bennett, Characterisation of roof tile coating degradation using nano-indentation test and surface profilometry, Polymer Degradation and Stability, 96 (2011) 833-838.

[17] T. Chatel, Fluage et recouvrance d'empreintes et de sillons sur suface de polymère, in, Université de Strasbourg, Strasbourg, 2010.

[18] J.S.S. Wong, H.J. Sue, K.Y. Zeng, R.K.Y. Li, Y.W. Mai, Scratch damage of polymers in nanoscale, Acta Materialia, 52 (2004) 431-443.

[19] W. Shen, S.M. Smith, H. Ye, F. Jones, P.B. Jacobs, Real time observation of viscoelastic creep of a polymer coating by scanning probe microscope, Tribology Letters, 5 (1998) 75-79.

[20] M. Wong, G.T. Lim, A. Moyse, J.N. Reddy, H.J. Sue, A new test methodology for evaluating scratch resistance of polymers, Wear, 256 (2004) 1214-1227.

[21] L.C.E. Struick, Physical Aging in Amorphous Polymers and Other Materials, Elsevier, Amsterdam, , 1978.

[22] J.J. Martinez-Vega, H. Trumel, J.L. Gacougnolle, Plastic deformation and physical ageing in PMMA, Polymer, 43 (2002) 4979-4987.

[23] J. Kolařík, Tensile creep of thermoplastics: Time-strain superposition of non-iso free-volume data, Journal of Polymer Science, Part B: Polymer Physics, 41 (2003) 736-748.

[24] M. Software, Volume A: Theory and User Information, in, 2012, pp. 813.

[25] F. Quadrini, E.A. Squeo, A. Guglielmotti, Indentation creep of polymers. I. Experimental, Polymer Engineering and Science, 50 (2010) 2431-2439.

[26] J. Kolařík, A. Pegoretti, Non-linear tensile creep of polypropylene: Time-strain superposition and creep prediction, Polymer, 47 (2006) 346-356.

[27] S. Jazouli, W. Luo, F. Bremand, T. Vu-Khanh, Application of time-stress equivalence to nonlinear creep of polycarbonate, Polym. Test, 24 (2005) 463-467.

[28] P.A. O'Connell, G.B. McKenna, Large deformation response of polycarbonate: Time-temperature, time-aging time, and time-strain superposition, Polymer Engineering and Science, 37 (1997) 1485-1495.

[29] J. Zhao, G.B. McKenna, Temperature divergence of the dynamics of a poly(vinyl acetate) glass: Dielectric vs. mechanical behaviors, Journal of Chemical Physics, 136 (2012).

[30] B.J. Briscoe, E. Pelillo, S.K. Sinha, Scratch hardness and deformation maps for polycarbonate and polyethylene, Polymer Engineering and Science, 36 (1996) 2996-3005.

[31] I.C. Choi, B.G. Yoo, Y.J. Kim, J.I. Jang, Indentation creep revisited, J. Mater. Res., 27 (2012) 3-11.

[32] K. Sakaue, S. Okazaki, T. Ogawa, Indentation technique for evaluation of master curve of creep compliance, Experimental Techniques, 35 (2011) 16-22.

[33] J. Lemaitre, J.-L. Chaboche, Mécanique des matériaux solides, Bordas, 1988.

[34] T. Chatel, V. Le Houérou, H. Pelletier, C. Gauthier, Numerical analysis of the creep of the contact and recovery of the imprint on amorphous polymer surfaces, Mech. Time-Depend. Mater., (2012) 1-15.

[35] L.C.A. Van Breemen, E.T.J. Klompen, L.E. Govaert, H.E.H. Meijer, Extending the EGP constitutive model for polymer glasses to multiple relaxation times, Journal of the Mechanics and Physics of Solids, 59 (2011) 2191-2207.

[36] P.E. Combette, Isabelle Physique des polymères propriété mécaniques, 6 rue de la sorbonne, paris, 2005.

[37] M.C. Baietto Dubourg, J. Rannou, A. Gravouil, H. Pelletier, C. Gauthier, R. Schirrer, 3D crack network during the scratching of a polymer: Comparison between experimental results and localized multigrid X-FEM, in, Ottawa, ON, 2009, pp. 3827-3836.

[38] C. G'Sell, J.J. Jonas, Determination of the plastic behaviour of solid polymers at constant true strain rate, Journal of Materials Science, 14 (1979) 583-591.

[39] J.L. Bucaille, E. Felder, G. Hochstetter, Mechanical analysis of the scratch test on elastic perfectly plastic materials with the three-dimensional finite element modeling, Wear, 249 (2001) 422-432.

[40] H. Pelletier, C. Gauthier, R. Schirrer, Experimental measurement and numerical simulation of the plastic strain during indentation and scratch tests on polymeric surfaces, J. Mater. Res., 24 (2009) 1184-1196.

[41] J. Krier, J. Breuils, L. Jacomine, H. Pelletier, Introduction of the real tip defect of Berkovich indenter to reproduce with FEM nanoindentation test at shallow penetration depth, J. Mater. Res., 27 (2012) 28-38.

[42] H. Jiang, R. Browning, H.J. Sue, Understanding of scratch-induced damage mechanisms in polymers, Polymer, 50 (2009) 4056-4065.

[43] F.L. Li, F.L. Peng, Y. Tan, W. Kongkitkul, M.S.A. Siddiquee, FE simulation of viscous behavior of geogrid-reinforced sand under laboratory-scale plane-strain-compression testing, Geotextiles and Geomembranes, 31 (2012) 72-80.

CHAPTER III. ZUSAMMENFASSUNG

CHAPTER III. ZUSAMMENFASSUNG 56
III.1. EINLEITUNG 57
III.2. EXPERIMENTALTEIL 57
III.3. VOLUMEN MECHANISCHEN EIGENSCHAFTEN VON CR39 60
III.3.1. Relaxation 60
III.3.2. Relaxationmoduln und Masterkurven 61
III.3.3. Fazit 63
III.4. KONTAKTANALYSE 63
III.4.1. Indentations-Kriechversuche 63
III.4.2. Indentations-Heilung 65
III.4.3. Masterkurve 66
III.4.4. Kratzer Heilung 68
III.4.5. Fazit 71
III.5. FINITE ELEMENT MODELLIERUNG 71
III.5.1. Materialmodelle 71
III.5.2. Bulk-Relaxationsexperiment 73
III.5.3. Indentation 75
III.5.4. Fazit 77
III.6. FAZIT 77
III.7. BIBLIOGRAPHIE 79

III.1. EINLEITUNG

Dank ihres geringen Gewichts finden Polymermaterialien zahlreiche Anwendungen [1]. Zudem sind Polymere grundsätzlich resistent gegen atmosphärische Einflüsse. Deswegen werden sie für Schutzbeschichtungen benutzt (Lacke, Smartphones,…) oder in Kompositen als Matrix eingesetzt (Reifen, Schiffsrumpf, …). Trotz dieser Stärken besitzen Polymere nur eine geringe Resistenz gegenüber mechanischer Beanspruchung. Sie sind relativ empfindlich, so dass ihre optischen oder ästhetischen Eigenschaften leicht durch Kratzer und Risse [2] beeinträchtigt werden können. Wegen ihrer schwachen mechanischen Eigenschaften werden Polymere bei hoher Reibung oft verkratzt [3, 4]. Um diese Schwächen zu vermeiden, müssen die Materialien entweder kratzresistent oder heilend sein. Heilende Materialien finden in vielen Bereichen Anwendung, zum Beispiel optische Linsen, Nagellack, berührungsempfindliche Bildschirme oder Lacke [5]. Es gibt im wesentlichen zwei Wege um die Heilung zu verbessern: Entweder wird das eigentliche Material mit einer dünnen Schicht geschützt oder seine Beständigkeit durch Zusatz von Partikeln (Nano-Füller) verbessert, um ein Kompositmaterial herzustellen. Das Ziel dieser Arbeit ist ein besseres Verständnis davon zu erhalten, wie die mechanischen Eigenschaften gefüllter Polymere und ihre Kratzbeständigkeit und im weiteren Sinn ihr Kontaktverhalten miteinander zusammenhängen. Dafür zwei spezifischen Aspekte wurden untersucht: das Polymer lange Zeit Verhalten und die Heilung. Diese Doktorarbeit wurde im Rahmen der International Research Training Group (IRTG soft matter) angefertigt.

Polymerproben wurden am Freiburger Materialforschungszentrum hergestellt. Im Besonderen wurden mit verschiedenen SiO_2-Partikeln verstärkte Polymethylmethacrylate (PMMA) hergestellt, die als Modell für Kompositmaterialien dienen sollen. Die mechanische Charakterisierung wurde in Straßburg durchgeführt.

III.2. EXPERIMENTALTEIL

Die klassische Charakterisierung von Polymeren erfolgt durch uniaxiale Prüftests. Das Prinzip dieser Tests besteht darin, eine konstante Dehnung oder Spannung anzulegen und die andere Größe zu messen. Ein ideales Material (rein elastisch oder elastoplastisch) reagiert sofort auf die angelegte mechanische Spannung, so wie im Falle von Glas und Metall an der Raumtemperatur. Im Gegensatz dazu werden bei Polymeren viskose Phänomene beobachtet. Um die viskoelastischen bzw. viskoplastischen Eigenschaften zu messen, werden Relaxations- und Kriechexperimente durchgeführt. So kann die Änderung der Spannung bzw. Dehnung bei konstanter Dehnung bzw. Spannung als Funktion der Zeit gemessen werden. Obwohl Polymere als Schutzschicht verwendet werden, sind Messungen am Bulk-Material nicht geeignet und nicht immer möglich. Die Standard-Härtemessung erfolgt durch Ausübung einer Gewichtskraft auf die Oberfläche und Beobachtung der verbliebenen Druckstelle. In diesem Fall kann nur die verbliebene Plastizität gemessen werden. Zum besseren Verständnis zeichnen neuere Instrumente während der Indentation die Kraft und die Eindringtiefe auf. Dann werden die elastischen Materialeigenschaften durch die Hertz-Gleichung bestimmt [6]. Bei elastoplastischen Materialien führt die Entlastungsanalyse der Kraft-Tiefe-Kurve während der Entlastungsphase (die als elastisch angesehen wird) mit dem Oliver-Pharr-Modell zu Elastizitätsmodul und Materialhärte [7, 8]. Aber für Polymere [9] und Knochen [10] ist das Modell zu ungenau. Tatsächlich zeigen diese

Materialien viskose Eigenschaften (die das Modell nicht berücksichtigt) und die Analyseergebnisse sind vom Test abhängig ("nose-problem") [11]. Zudem ist die Eindringtiefe eine Kombination von Auslenkung, die bei Polymeren größer ist als bei Metallen, und Kontakttiefe. Die Auslenkung ist hauptsächlich elastisch, wohingegen die Kontakttiefe eine Kombination elastischer, viskoelastischer, viskoplastischer und plastischer Eigenschaften ist.

Zurzeit gibt es kein analytisches Modell, um alle Beiträge aufzutrennen und dann mit ausreichender Genauigkeit die wahre Kontakttiefe während der Indentation auf Polymeroberflächen abzuschätzen. Ein Ausweg, um die Verwendung eines analytischen Modells zu vermeiden, liegt in der direkten Beobachtung des Kontakts durch das Probenmaterial (durchsichtige Probe) [4, 12] oder durch die Spitze (mit sphärischem Glasindenter). Wir haben einen spezifischen Apparat, das Microvisioscratch [4], entwickelt.

Wenn allerdings ein sphärischer Indenter für ein Kriechexperiment unter konstanter Belastung benutzt wird, steigt die Kontaktfläche, so dass die Tabor-Dehnung [13] wächst, obwohl der durchschnittliche Kontaktdruck während des Tests abfällt. Wegen dieses Effekts erscheint der Indentationskriechtest als ein komplexes Experiment, welches aber nahe an der wirklichen Polymerbeanspruchung liegt, die während des statischen Kontakts zweier funktionalisierter Oberflächen auftritt. Typische Kriechversuche, die mit unserem Microvisioscratch-Apparat durchgeführt wurden, sind in Abbildung III-1a) und b) dargestellt. Dieser spezifische Apparat ermöglicht es uns, in Abhängigkeit von der Zeit den Kontakt zwischen der Spitze und der deformierten Oberfläche während der Indentationsphase bei konstanter Belastung (Abbildung III-1b) und die Heilungsphase (Abbildung III-1c) direkt nach der Wegnahme der Spitze [14] zu beobachten. Leider können undurchsichtige Materialien mit unserem Microvisioscratch-Apparat nicht charakterisiert werden. Anstatt hindurchzuschauen (wenn die Probe transparent ist) erfolgte die Beobachtung durch die Indenterspitze. Um ein Bild zu erhalten, welches es erlaubt, mit genügend hoher Präzision den Kontaktradius abzuschätzen, wird eine Spitze mit großem Radius benötigt (mindestens 3,3 mm). Mit solchen Indentern werden sehr hohe Kräfte angelegt, um eine nicht rein elastische Verformung zu bekommen [14]. Abbildung III-1a) zeigt in-situ-Aufnahmen, die in einem selbstgebauten Makroindentationsapparat durchgeführt wurden, welcher in eine Instron-Zugmaschine eingebaut wurde. Diese Charakterisierung wurde zwischen -40°C und +95°C durchgeführt, was im Allgemeinen der Gebrauchstemperatur der Polymere entspricht.

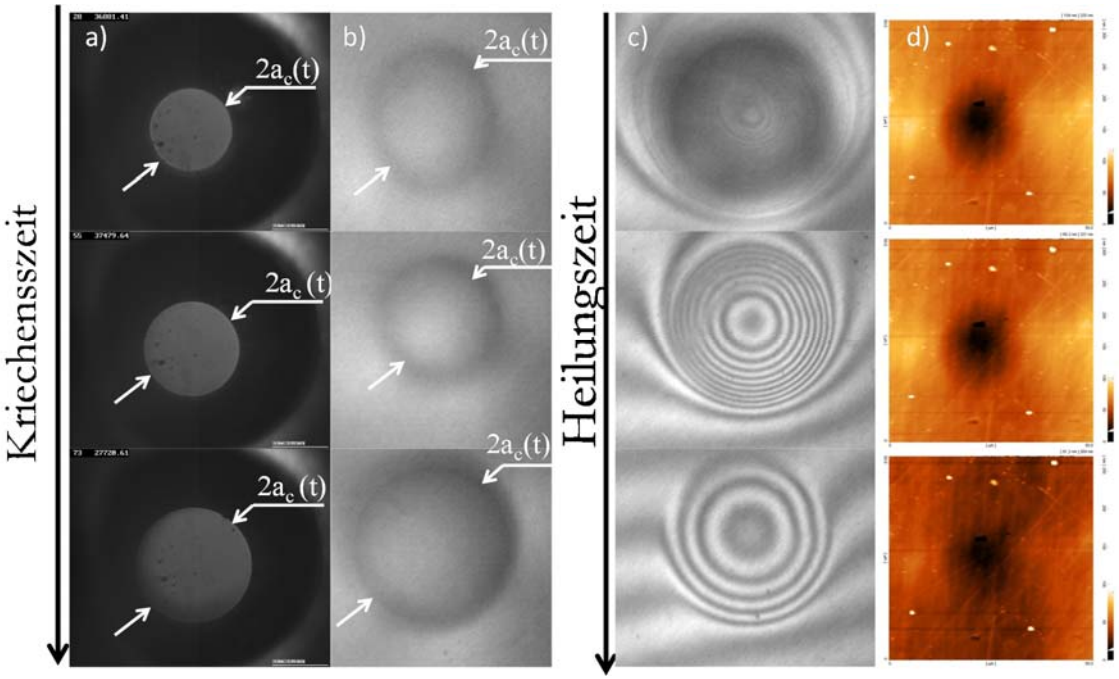

Abbildung III-1 Kriechbeobachtung a) durch die Spitze b) durch die Probe. Beobachtung der Heilung c) durch die Probe d) AFM-Aufnahme

Bei einem Beanspruchungsprozess gibt es zwei verschiedenen Phasen: die Kontaktphase und die Heilungsphase. Im Vergleich mit Metallen und Keramiken, die nicht heilen können, ist das Heilungsphänomen ein wichtiger Baustein, um die Resistenz des Polymers gegen Kontaktbelastung zu charakterisieren. Im Allgemeinen werden die permanente Vertiefung oder der Riss nach Indentation bzw. Kratztest mit AFM (siehe Abbildung III-1d)) oder mit Profilometrie [15, 16] bestimmt. Die Schwierigkeit besteht in der Zeitspanne zwischen Kontaktende und dem Ende der Bildaufnahme. Leider finden die meisten Veränderungen oder Entwicklungen der permanenten Vertiefung, resultierend aus viskoelastischem Verhalten, während dieser Zeitspanne statt [17]. Mit dem Microvisioscratch-Apparat [14] werden die ersten Bilder bereits nach 0,5 s aufgenommen, das heißt kurz nach dem vollständigen Entfernen der Spitze. Darüber hinaus werden in unseren Fall das Kriechen und die Heilung während einer sehr langen Zeitspanne beobachtet (normalerweise jeweils mehr als 24 Stunden). Wie aus Abbildung III-1 ersichtlich kann nun mit den verschiedenen Werkzeugen ein Ansatz über mehrere Größenordnungen vom Makro- bis zum Nano-Kontakt realisiert werden.

Mechanische Charakterisierung von Polymeroberflächen erfolgt auch mit Kratztests [18]. Erste Beschreibungen der Heilung von Rissen wurden von einigen Autoren [18-20] geliefert. Darin wurden jedoch keine Informationen über die Zeit vor 15 Minuten gegeben. In unserem Fall wurde die Heilungsphase durch den Microvisioscratch-Apparat (Abbildung III-2a)) beobachtet. Dann wurden die Bilder in eine 3D-Darstellung der Probe (Abbildung III-2b)) umgerechnet. Schließlich wurden daraus einige Profile entnommen. Abbildung III-2 c) stellt das Längenprofil gegen die Zeit dar. Zudem wurden einige Querprofile in definiertem Abstand zum Kratzerende entnommen. Der Abstand zum Kratzerende wurde relativ zum Kontaktradius während des Kratztests gewählt. So sind die gewählten Distanzen Vielfache des Kontaktradius (a_c) während des Kratztests, die untersuchten Distanzen waren 4 a_c und 9 a_c. In jedem Fall wurden die Rissbreite und -tiefe gemessen und analysiert.

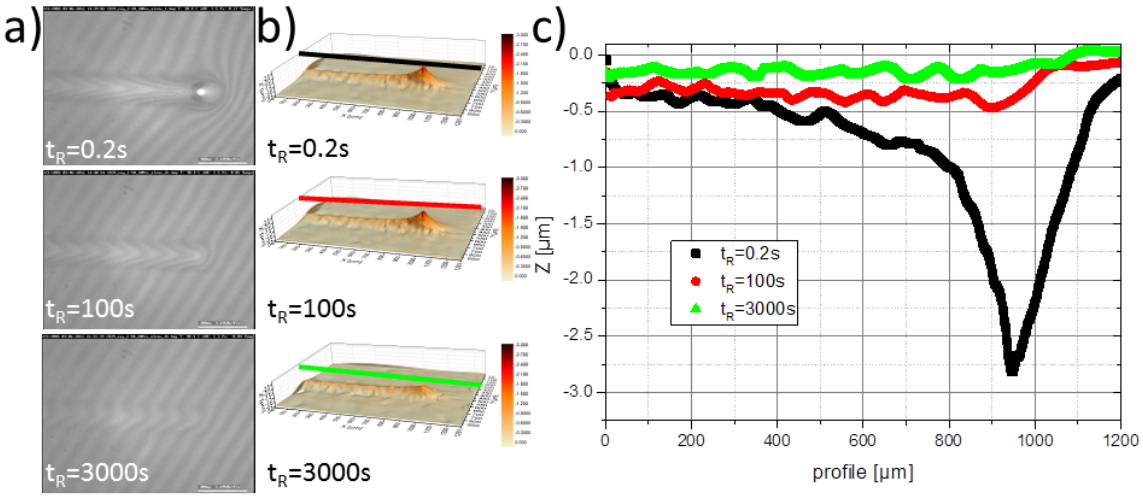

Abbildung III-2 a) Kratzerheilung im Laufe der Zeit b) 3D-Darstellung des Risses c) Längenprofile zu drei verschiedenen Zeiten

III.3. VOLUMEN MECHANISCHEN EIGENSCHAFTEN VON CR39

In diesem Kapitel wurden die mechanischen Eigenschaften von CR39, PMMA CN und PMMA 10 AlO(OH) untersucht. Zuerst werden die Relaxationsversuche vorgestellt. Dann werden die Relaxationsversuche benutzt, um eine Masterkurve zu erstellen.

III.3.1. Relaxation

Die sofortige Elastizität zeigt nicht alle mechanischen Eigenschaften von Polymermaterialien. In der Tat beobachteten Struick [21] und andere [22, 23] bei Polymeren eine Zeitabhängigkeit bei Kriech- oder Relaxationsversuchen. Wir entschieden, Kompressions-Relaxationsexperimente durchzuführen. Die Kompression wurde gewählt, da sie der Indentation am nächsten kommt. Relaxationsexperimente wurden gewählt, da die Software MSC Marc die Viskoelastizität aus Relaxationsversuchen berechnet [24].

Abbildung III-3 zeigt, wie sich für CR39 bei 30°C die wahre Spannung gegen die wahre Dehnung und Zeit ändert. Bei allen Kurven wurde die 10-fache Belastungszeit abgezogen, um das Auftreten von Belastungseffekten zu vermeiden. Der Verdunkelungsgradient wird für eine steigende Dehnung [0.75-22 %] verwendet. Bei jedem Versuch fällt die Spannung mit der Zeit ab. Zudem steigt bei CR39 (Abbildung III-3) die Anfangsspannung bis zu einer Dehnung von 4 % (schwarz punktierte Linie). Dann sinkt die Anfangsspannung um 10 % ab und steigt schließlich wieder an (schwarz gestrichelte Linie). Die Materialelastizität ist verantwortlich für die experimentelle Anfangsspannung bei geringer Dehnung. Dann, wenn die Zeit und/oder Dehnung steigt, spielt die zeitabhängige Elastizität von CR39 eine Rolle. Bei sehr hohen Dehnungen verhindert das Polymernetzwerk das Kriechen des Materials, und so steigt die Spannung wieder. CR39 reagiert erst elastisch, dann viskoelastisch. Einige weitere Versuche sind im Experimentalteil VI.2.2 dargestellt.

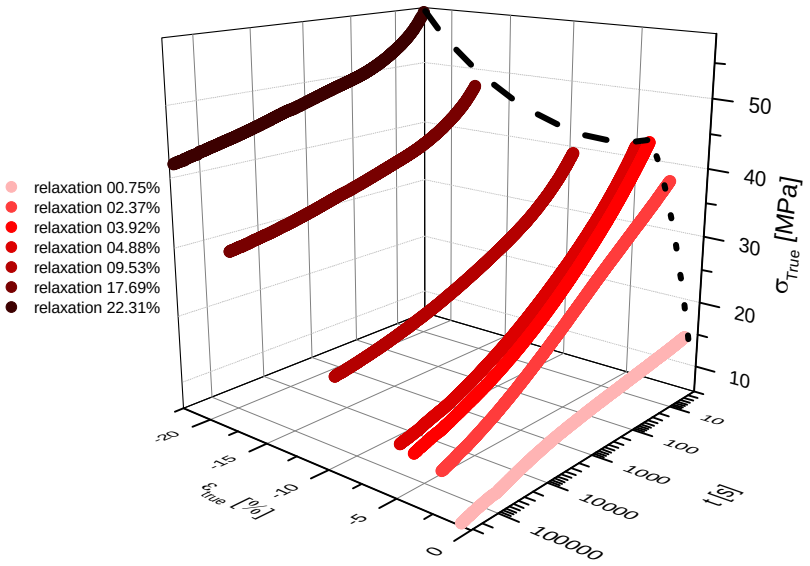

Abbildung III-3 CR39 Relaxation Experiment um 30°C

III.3.2. Relaxationmoduln und Masterkurven

Diese Versuchsreihe wurde verwendet, um die Relaxationsmoduln (siehe Gleichung in Equation V-11) in Abhängigkeit von der Zeit zu berechnen. Abbildung III-4 zeigt das Relaxationsmodul von CR39 gegen die Zeit. Bei jeder Kurve fällt das Relaxationsmodul ab. Höhere Dehnung führt zu kleineren Relaxationsmoduln. Schließlich ist die 0,75 %-Dehnungsrelaxation konvex, wohingegen alle höheren Dehnungsrelaxationen konkav sind. Masterkurven für die Abhängigkeit von der Dehnung und Temperatur wurden von verschiedenen Autoren bereits für HDPE [25], Polypropylen [23, 26], PC [27, 28] oder Polyvinylacetat [29] erstellt. Durch Verschiebung (nur horizontal) der Kurven in Abbildung III-4a) kann eine Masterkurve erstellt werden. Dazu wird eine Referenz gewählt, die Relaxation bei 0,75 % Dehnung. Dann wird die experimentelle Zeit mit einem Faktor a_T multipliziert. Die erhaltene Kurve ist in Abbildung III-4 b) dargestellt. Die starke Abnahme des Relaxationsmoduls bei Dehnung kann man jetzt über die Zeit beobachten. In der Tat sinkt das Relaxationsmodul nach 30 Millionen Jahrhunderten dramatisch auf 10 % des Anfangswertes. An diesem Punkt scheint das Relaxationsmodul ein Plateau zu erreichen. Dies wird wahrscheinlich durch das CR39-Netzwerk verursacht, welches das Kriechen verhindert. Schließlich kann die abgeschnitten und invertierte „S-Form“ der Kurve mit drei verschiedenen charakteristischen Relaxationen in Beziehung gesetzt werden: Elastizität, Kurzzeit-Viskoelastizität und Langzeit-Viskoelastizität.

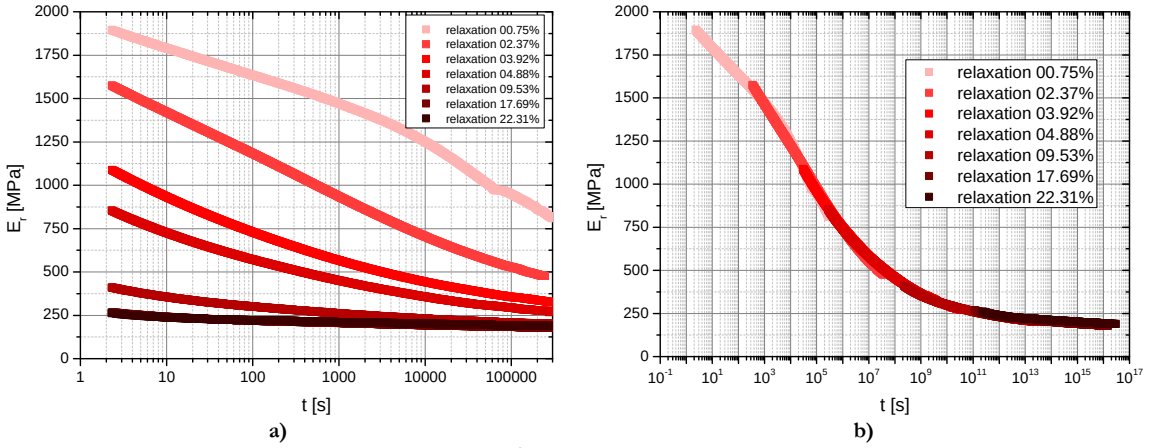

Abbildung III-4 a) Relaxationsmoduln von CR39 bei 30°C b) Relaxationsmodul-Masterkurve für CR39 mit 0.75 % Dehnung als Referenz

Die Verschiebungsfaktoren, die vorher für die Relaxationsmoduln benutzt wurden, sind in Abbildung III-5 für alle drei Materialien gegen die wahre Dehnung aufgetragen. Da alle Masterkurven die kleinere Dehnung als Referenz besitzen, ist der erste Punkt [0,75 %: 1]. Die Verschiebungsfaktoren von CR39 (rote Vierecke) steigen bis 5 % Dehnung stetig an. Zwischen 5 und 25 % wahrer Dehnung verläuft der Anstieg langsamer. PMMA CN (blaue Kreise) und PMMA 10 AlO(OH) (grüne Dreiecke) zeigen sehr ähnliches Verhalten. Die Verschiebungsfaktoren steigen linear bis 5 % Dehnung. Die Verschiebungsfaktoren liegen leicht über denjenigen von CR39. Über 5 % wahrer Dehnung, steigen die Verschiebungsfaktoren von PMMA CN und PMMA 10 AlO(OH) weiter fast linear an. Die Stagnation der Verschiebungsfaktoren von CR39 über 5 % Dehnung lässt vermuten, dass das Netzwerk den Materialfluss bremst. Im Gegensatz dazu ist der Fluss von PMMA CN und PMMA 10 AlO(OH) fast proportional zur angelegten Dehnung. Da beide PMMA-Arten dasselbe Fließverhalten zeigen, kann schlussgefolgert werden, dass die Partikel das Kriechen des Materials nicht so gut verhindern wie erwartet.

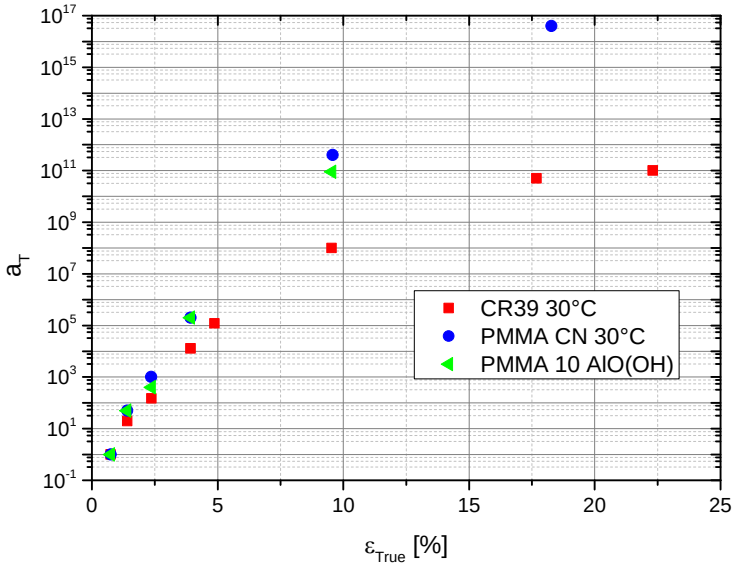

Abbildung III-5 Verschiebungsfaktoren für die drei verschiedenen Materialien gegen wahre Dehnung

III.3.3. Fazit

Das mechanischen Bulk-Eigenschaften von CR39, PMMA CN und PMMA 10 AlO(OH) wurden durch DMTA- und Relaxationsexperimente analysiert. Die Relaxation dieser Materialien wurde über lange Zeiträume beobachtet. Die Erstellung von Masterkurven bei 0,75 % Dehnung erlaubt die Vorhersage des viskoelastischen Verhaltens des Materials über Jahrhunderte.

III.4. KONTAKTANALYSE

III.4.1. Indentations-Kriechversuche

Indentations-Kriechversuche an den Polymeren CR39 und PMMA CN wurden zunächst bei Raumtemperatur durchgeführt. Sehr lange Indentationszeiten wurden benutzt. Dann wurde eine Anzahl bestimmter Temperaturen ausgewählt, um den Bereich der Polymer-Gebrauchstemperaturen abzudecken.

III.4.1.1 Raumtemperatur

Der Vergleich des Kriechens von CR39 und PMMA CN ist in Abbildung III-6 dargestellt. Die durchschnittliche Kontaktspannung (links) ist gegen die Indentationszeit aufgetragen. Alle Kriechbelastungen sind so gewählt, dass die anfängliche Tabor-Dehnung gleich 0,2 ist [13]. Trotzdem ist die anfängliche Kontaktspannung von CR39 und PMMA CN proportional zu den DMTA-Versuchen. Die durchschnittliche Kontaktspannung von CR39 fällt linear mit dem Logarithmus der Zeit ab. Im Gegensatz dazu scheint die durchschnittliche Kontaktspannung von PMMA CN zwei Abschnitte unterschiedlicher Steigung zu besitzen. Der erste liegt vor 100 s und der zweite nach 1000 s. Der Graph in Abbildung III-6b) stellt die normierte Tabor-Dehnung gegen die Zeit dar. Die Tabor-Dehnung ist der Kontaktradius geteilt durch den Kugelradius. In unseren Fall wurde dieser Wert durch sich selbst bei 0,5 s geteilt, um die Materialien miteinander zu vergleichen. Obwohl die Anfangsdehnung gleich ist, ist der Weg der normierten Dehnung für jedes Material verschieden. Die Dehnung von PMMA CN steigt stark an und erreicht ein Maximum, dann fällt die Kriechgeschwindigkeit ab. Im Gegensatz dazu beobachtet man bei CR39 eine niedrigere Kriechgeschwindigkeit, die zunimmt. Schließlich werden am Ende des Experiments ähnliche Dehnungen erhalten. So ist die Heilung vergleichbar. Die Verlangsamung des Kriechens von PMMA kann mit dem Auftreten von viskoplastischem Verhalten erklärt werden, wohingegen das beschleunigte Kriechen von CR39 mit viskoelastischen Veränderungen verbunden ist.

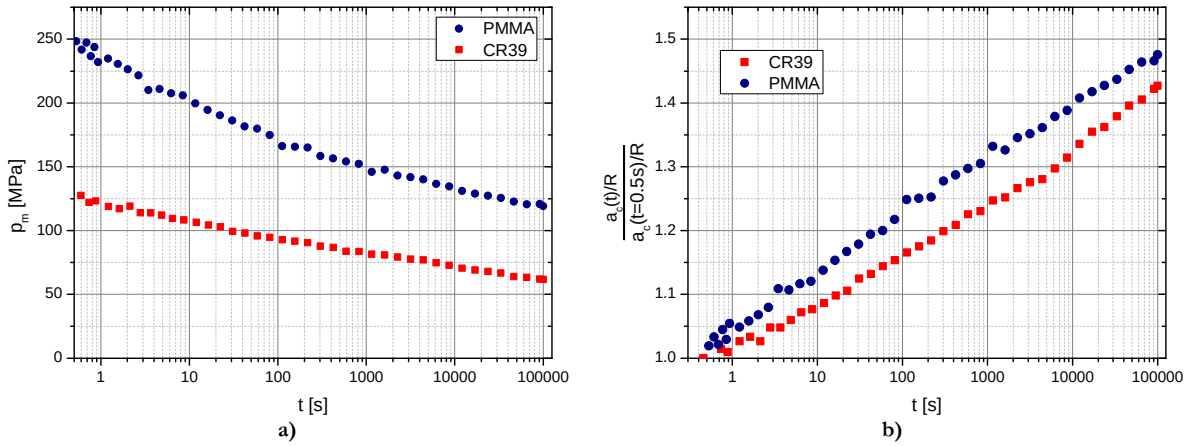

Abbildung III-6 Vergleich zwischen dem Indentations-Kriechen von CR39 und PMMA bei 30°C a) durchschnittliche Kontaktspannung gegen die Kriechzeit b) Normierte Tabor-Dehnung gegen Zeit

III.4.1.2 Einfluss der Temperatur

Polymere sind sehr stark temperaturabhängig, daher wird ihr Kontaktverhalten auch bei Veränderung der Temperatur beobachtet [2, 30, 31]. Die Ergebnisse von PMMA CN werden nicht alle hier aufgeführt, sie sind im teil VI.3.1.2 zu finden.

Indentations-Kriechversuche wurden an CR39 bei verschiedenen Temperaturen durchgeführt. Die durchschnittliche Kontaktspannung ist in Abbildung 7 Durchschnittliche Kontaktspannung gegen die Zeit bei verschiedenen Temperaturen (Anfangs-Tabor Dehnung von 4 %) für CR39 a) normal b) Masterkurve

dargestellt. In allen Fällen nimmt die durchschnittliche Kontaktspannung langsam mit dem Logarithmus der Zeit ab, aber die Geschwindigkeit des Abfalls ist temperaturabhängig. Die Steigung ist fast gleich bei den beiden niedrigsten Temperaturen und fällt dann stark mit der Temperatur ab (die durchschnittliche Kontaktspannung fällt bei höheren Temperaturen langsamer ab als bei niedrigeren Temperaturen). Hinzu kommt, dass für ein Material das Verhältnis der anfänglichen durchschnittlichen Kontaktspannungen bei zwei verschiedenen Temperaturen das gleiche ist wie das Verhältnis der Elastizitätsmoduln bei ebendiesen Temperaturen. Zum Beispiel ist das Elastizitätsmodul von CR39 bei -20°C ungefähr 80 % größer als bei 20°C. Die durchschnittliche Kontaktspannung von CR39 bei -20°C ist ebenfalls 80 % größer als die durchschnittliche Kontaktspannung bei 20°C. Diese Daten, der Abfall und der Anfangswert der durchschnittlichen Kontaktspannung, legen nahe, dass die unmittelbare durchschnittliche Kontaktspannung vom Elastizitätsmodul abhängt, das Kriechen jedoch, wie erwartet, nicht.

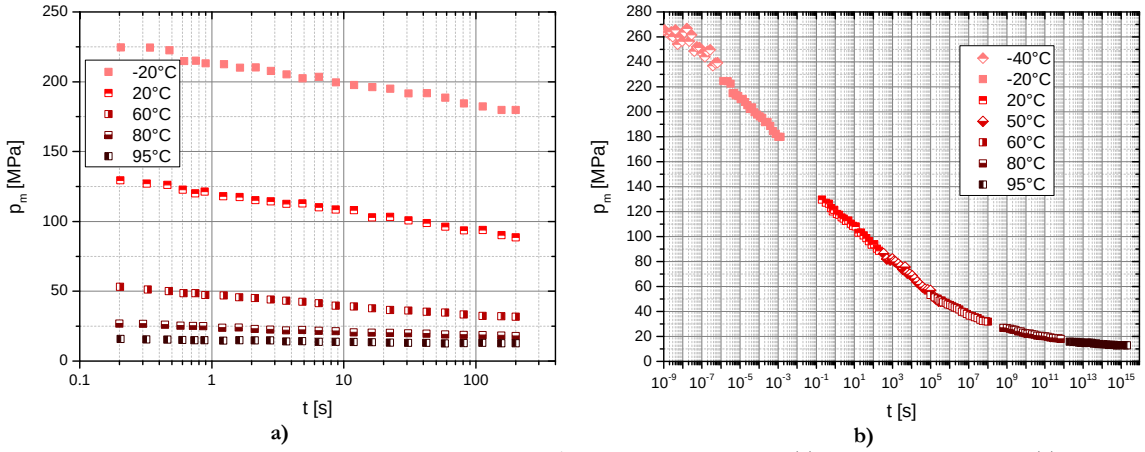

Abbildung 7 Durchschnittliche Kontaktspannung gegen die Zeit bei verschiedenen Temperaturen (Anfangs-Tabor Dehnung von 4 %) für CR39 a) normal b) Masterkurve

Anschließend können die Kurven in Abbildung 7 Durchschnittliche Kontaktspannung gegen die Zeit bei verschiedenen Temperaturen (Anfangs-Tabor Dehnung von 4 %) für CR39 a) normal b) Masterkurve

a) seitlich zu Masterkurven verschoben werden. Abbildung 7 Durchschnittliche Kontaktspannung gegen die Zeit bei verschiedenen Temperaturen (Anfangs-Tabor Dehnung von 4 %) für CR39 a) normal b) Masterkurve

b) zeigt die durchschnittliche Kontaktspannung gegen die Zeit bei allen gemessenen Temperaturen. Die Referenztemperatur wurde zu 30°C gewählt. Die CR39-Kurven fallen stark mit dem Logarithmus der Zeit bis 107 s ab. Dort besitzen die Kurven einen Wendepunkt. Der Wendepunkt entspricht einer Temperatur von 60°C. Dies lässt sich mit dem Glasübergang von CR39 erklären. Nach diesem Temperatur/Zeit-Übergang, wird das Fließen des Materials durch das Netzwerk verhindert und die gemessene durchschnittliche Kontaktspannung bleibt stabil. Einige andere Autoren haben schon Indentations-Masterkurven vorgestellt, aber diese stellen die Kriech- Nachgiebigkeit dar [25, 32]. Die Daten in Abbildung III-6 stimmen mit der so erhaltenen Masterkurve überein.

III.4.2. Indentations-Heilung

Die Indentations-Heilung wird durch die normierte Heilungsdehnung beobachtet. Da sie durch die Tabor-Dehnung am Ende des vorhergehenden Kriechversuchs normiert wurde, liegen die Werte zwischen 1 und 0. Trotzdem ist das Verständnis des Phänomens eine komplexe Angelegenheit: Ein Unterschied in der Heilung kann von einem Unterschied der Parameter (Material, Temperatur, Indentations-Kriechzeit,…) oder von einem Unterschied am Ende der Dehnung herrühren (wie bereits erläutert). Im Idealfall würde das Kriechen bei allen Experimenten bei der gleichen Tabor-Dehnung enden. Da dies aber eine hohe Anzahl von Experimenten bedingen würde (Versuch- und Irrtums-Methode), wird die anfängliche Tabor-Dehnung (a/R=0,2 bei 0,5 s) benutzt. Zudem treten während der Heilung zwei Dinge auf: die Deflexion um den Indenter (elastisch und viskoelastisch) und die Heilung des Abdrucks (Kombination von elastischen, viskoelastischen und plastischen Eigenschaften). Die größten Veränderungen finden während der ersten Sekunden der Heilung statt, daher ist die optische

Fokussierung schwierig und die Qualität der Aufnahmen gering. Je größer der Abdruck, desto schwieriger ist es, verlässliche Daten zu erhalten. Daher wurden ungenaue Daten mit einem grauen Dreieck gekennzeichnet.

In Abbildung III-8 wurde die normierte Heilungsdehnung in Abhängigkeit von der Heilungszeit beobachtet. Beide Kurven scheinen auf drei Viertel des anfänglichen Wertes für die Abdruckdehnung zu fallen. Dann nimmt die PMMA-Heilungsdehnung bis auf 25 % ihres Anfangswertes ab, während die Tabor-Heilungsdehnung von CR39 bis auf weniger als 5 % der anfänglichen Abdruckdehnung (Abdruck ist nicht mehr messbar) fällt. Darüber hinaus ist der Abfall für CR39 und PMMA verschieden. Die PMMA-Heilung scheint nach 100 s abzubremsen und nach 10 000 s aufzuhören. Im Gegensatz dazu hat die Heilung von CR39 zwei Gefälleabschnitte, einen zwischen 10 und 1000 s und den anderen zwischen 1000 s und 100 000 s. Die sofortige Heilung von 25 % kann in beiden Fällen der elastischen Heilung zugesprochen werden. Die verzögerte Heilung ist ein Zeichen von viskoelastischem Verhalten. Die zwei Gefälle von CR39 sind mit zwei verschiedenen viskoelastischen Vorgängen verbunden. Die PMMA-Heilung ist mit zwei Phänomenen verbunden. Zunächst erlaubt die PMMA-Viskoelastizität den Beginn der Heilung. Dann dringt die Heilung in das plastisch verformte Material ein, so dass die Heilungsgeschwindigkeit graduell abnimmt.

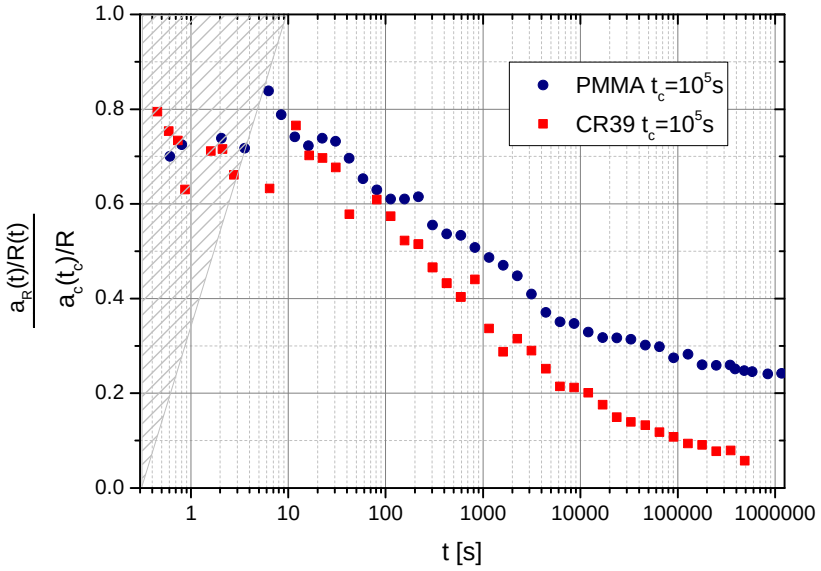

Abbildung III-8 Normierte Indentations-Heilungsdehnung gegen Heilungszeit von CR39 und PMMA bei 30°C

III.4.3. Masterkurve

In der Folge wurden zwei Arten von Masterkurven erhalten: Zeit-Dehnung und Zeit-Temperatur Die dehnungsabhängige Masterkurve wurde aus Bulk-Relaxationsversuchen erhalten. Sie ist in Abbildung III-4 b) für CR39 dargestellt. Da die Bulk-Masterkurven die Relaxationsmoduln (in 1000 MPa gemessen) und die Kontakt-Masterkurven die durchschnittliche Kontaktspannung (in 100 MPa gemessen) enthalten, können sie nicht direkt miteinander verglichen werden. Daher wurden die beiden Kurven durch einen gemeinsamen Punkt normiert. Alle CR39-Werte wurden durch den Wert am Punkt [1,2 s: 30°C: 4 % Dehnung] geteilt. Bei der Bulk-Masterkurve entspricht das dem Relaxationsmodul nach dem Ende der Belastung bei 3,92 % Dehnung

(E_r=1140 MPa). Bei der Kontakt-Masterkurve entspricht das der durchschnittlichen Kontaktspannung nach 1,2s der Indentation bei 30°C (p_m=125 MPa). Mit der Wahl dieser Referenzpunkte wurden die Masterkurven horizontal verschoben bis zum Erreichen dieses Referenzpunkts [1,2 s: 1]. Eine ähnliche Methode wurde für PMMA CN angewandt. Die erhaltenen Masterkurven sind in Abbildung III-9 a) und b) für CR39 und PMMA CN dargestellt. Bulk- und Kontakt-Masterkurve liegen bei CR39 und PMMA CN nahe beieinander. Daher betreffen Zeit, Temperatur und Dehnung dieselben Mechanismen. Ihr jeweiliger Einfluss ist aber anders. Eine weitere wichtige Beobachtung ist die Tatsache, dass Kontakt- und Bulk-Versuche zu denselben Masterkurven führen können. Wenn also die Kontakt-Temperaturabhängigkeit nicht bekannt ist (zum Beispiel bei PMMA 10 AlO(OH)), kann sie durch einen Bulk-Datensatz und einen Messpunkt eines Kontaktexperiments bestimmt werden. Das Umgekehrte trifft ebenfalls zu: Wenn die Kontakt-Masterkurve und ein Elastizitätsmodul bekannt sind, ist es die Bulk-Masterkurve ebenso (im Falle einer dünnen Schicht). Überdies kann der Einfluss der Plastizität auch aus diesen Kurven angeleitet werden. Bei CR39-Kontakt tritt keine Plastizität auf (siehe Indentations-Heilung). Hingegen stellt man bei PMMA-CN-Kontaktkurven Plastizität bei höherer Zeit/Temperatur/Dehnung fest. Wenn Plastizität in Relaxationsexperimenten auftritt, dann während der Belastung, nicht während der Spannungsrelaxation, welche rein viskoelastisch ist. Da die Belastung von den Daten abgezogen wurde, zeigen die Bulk-Experimente nur viskoelastisches Verhalten. Da die Kurvenformen bei CR39 und PMMA CN mit oder ohne Plastizität sich ähneln, beeinflusst die Plastizität die Viskoelastizität nicht. Ebenso gilt, wenn Viskoplastizität aufträte, sollte das die Zeitabhängigkeit der Kontaktkurve beeinflussen. Das ist nicht der Fall. Daher gibt es keine Viskoplastizität bei den untersuchten Polymeren.

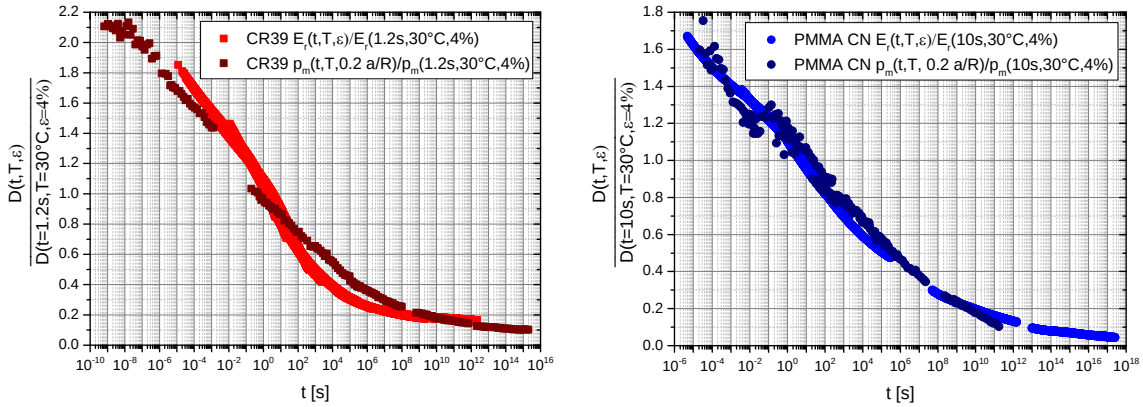

a) b)

Abbildung III-9 Normierte Masterkurve durch Relaxation und Indentation Experimente für CR39 a) zentriert nach 1.2 s um 30°C 4% Dehnung und b) PMMA CN zentriert nach 10 s um 30°C 4% Dehnung

Dazu die Abbildung III-9 kann beim DMTA Masterkurven hinzufügen fertiggestellt sein. Mehr Informationen über diesen Kurven können in VI.3.3 gefunden werden. Deswegen wurden drei anders Wege Masterkurve hergestellt. Das DMTA (Zeit-Temperatur Masterkurve), Relaxation (Zeit-Dehnung Masterkurve) und Indentation (Zeit-Dehnung-Temperatur Masterkurve) sind miteinander Kohärent. Diese Angemessenheit ist für beide Werkstoffe CR39 und PMMA CN in Abbildung III-10 beobachtet. Zum Schluss sind die Phänomen, die in die Werkstoffe stattfinden, ähnlich wie immer die Temperatur, Dehnung und Zeit.

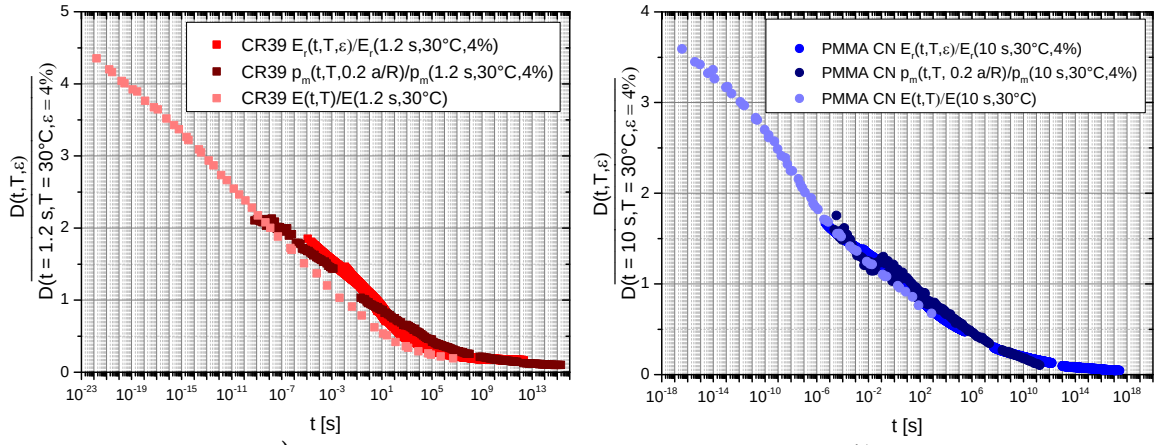

a) b)

Abbildung III-10 Normierte Masterkurve durch DMTA, Relaxation und Indentation Experimente für CR39 a) zentriert nach 1.2 s um 30°C 4% Dehnung und b) PMMA CN zentriert nach 10 s um 30°C 4% Dehnung

III.4.4. Kratzer Heilung

Aus den vorigen Abschnitten wurde ersichtlich, dass sphärisches Indentationskriechen und Heilung komplexe Experimente darstellen. Tatsächlich liegen Kratzer aber näher an der wirklichen Polymerbeanspruchung. Um diese Degradation zu verstehen, wurden mechanische Charakterisierungen von Polymeroberflächen auch anhand von Kratztests durchgeführt.

III.4.4.1 Generelle Information

Bei den beobachteten Kratzern traten weder Brüche noch Mikrorisse auf. Ausschließlich CR39 duktiles Verhalten wurde beobachtet. Die Entnahmestelle der verschiedenen Querprofile ist in Abbildung III-11 a) markiert. Ein Beispiel eines Querprofils in 4 a_c Abstand zum Kratzerende ist in Abbildung III-11 b) dargestellt. Die Achsen des Graphs sind nicht orthonormal, die y-Achse besitzt eine 350 mal größere Skala als die x-Achse. Daher erscheinen die Risse spitzer, als sie wirklich sind. Mit der Zeit heilt der Riss, die Tiefe nimmt ab. Auf beiden Seiten der Spur werden Wälle beobachtet; diese scheinen mit der Zeit niedriger zu werden .Auf der linken Seite wird eine Schulter beobachtet, die von der Interpolationsmethode stammt.

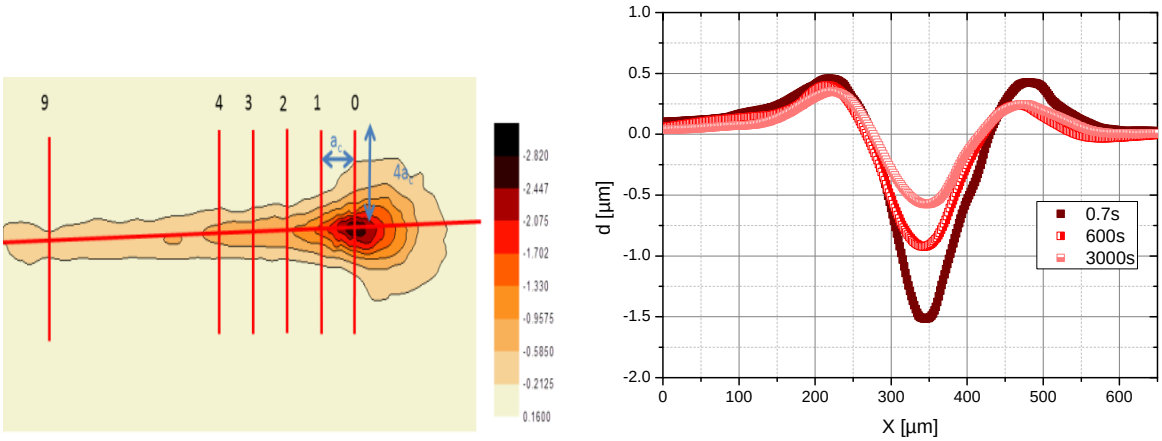

a) b)

Abbildung III-11 Schematische Darstellung der Entnahmestellen verschiedener Profile b) Drei Profile, entnommen zu verschiedenen Zeiten bei einem Abstand von 4a_c Kratzerende

III.4.4.2 Einfluss von der Kratzerendedistanz

Die Kratzer-Heilung gegen die Heilungszeit wurde zu verschiedenen Abständen vom Kratzerende beobachtet (Abbildung III-12). Gezeigt ist diejenige Zeit, die seit der Entfernung der Spitze von der Oberfläche verstrichen ist. Sie entspricht nicht der Zeit, die vergangen ist, seitdem die Spitze über das Material gefahren ist. Daher spiegeln nicht alle Querprofile dieselbe Heilungszeit wider. Zusätzlich verkomplizierend wirkt die Tatsache, dass die Materialien nicht immer dieselbe mechanische Vorgeschichte besitzen. Tatsächlich wird das Material vor und unter der Spitze, zusammengedrückt und Scherkräften unterworfen, hinter der Spitze wird es gespannt. Darüberhinaus wird auf dem Kratzer eine Kombination aus Scher-, Kompressions- und Zugvorformung beobachtet. Daher zeigt das Querprofil bei 0 a_c Material, das weniger Zugbeanspruchung unterlegen hat als bei 1 a_c, welches wiederum weniger als bei 2 a_c beansprucht wurde. Trotzdem zeigt die Abbildung III-12, dass die Tiefe für alle Distanzen mit der Zeit abnimmt. Alle Kurven treffen sich im Punkt [200 s: 0,4 µm]. Zudem scheint die Kratzerheilung für Abstände kleiner 3 a_c auf unterschiedlichen Wegen zu verlaufen, selbst wenn versucht wird, sie horizontal zu verschieben, um die unterschiedlichen Heilungszeiten zu kompensieren. Dieser Unterschied kommt wahrscheinlich von der unterschiedlichen mechanischen Vorgeschichte. Nach 4 a_c jedoch können die Kurven überlagert werden. Es kann daher angenommen werden, dass bei einem Abstand von 4 a_c zum Kratzerende das Material sämtlicher mechanischer Beanspruchung unterlegen hat. Daher werden weitere Untersuchungen überwiegend bei diesem Abstand durchgeführt werden.

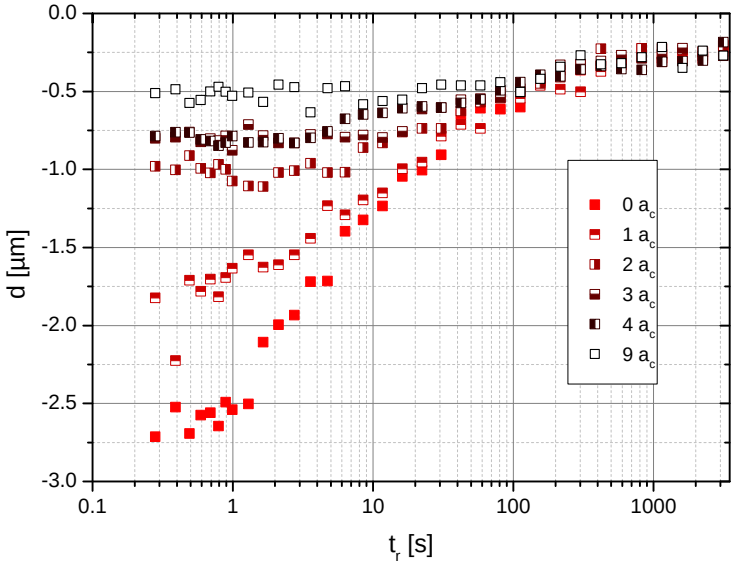

Abbildung III-12 Kratzerheilung für CR39 bei 30°C im Laufe der Zeit zu verschiedenen Abständen vom Kratzerende

III.4.4.3 Einfluss von Belastung

Die Abbildung III-13 a) stellt die Kratzerheilungstiefe in Abhängigkeit von der Zeit und der Tabor-Dehnung dar. Gezeigt ist diejenige Zeit, die seit der Entfernung der Spitze von der Oberfläche verstrichen ist. Die verschiedenen Dehnungen sind durch verschiedenen Kräfte erzeugt worden (in aufsteigender Reihenfolge: 1, 2.5 und 5 N). Die entsprechenden Kontakttiefen

sind 3.6, 9.5 und 14 µm. Am Anfang weist die Tiefe für einen Zeitraum von 2-3 s ein Plateau auf. Dann fällt die Tiefe mit der Zeit für alle Dehnungen ab. Die Endtiefen sind sehr klein im Vergleich mit den Kontakttiefen. Das Plateau liegt am Zeitursprung; die vergangene Zeit, seitdem die Spitze über das Material gefahren ist (oder seitdem die Hauptdehnung stattgefunden hat) ist ungefähr 30 s. Deswegen spielen 3 zusätzliche Sekunden Heilungszeit keine Rolle. Schließlich kann die Form der Kurve mit zwei verschiedenen Dehnungsverhalten in Beziehung gesetzt werden. Um diese Daten zu vergleichen, wird in Abbildung III-13 b) die normierte Tiefe als Funktion der Zeit dargestellt. Die Tiefe ist auf die anfängliche Heilungstiefe normiert. Das Plateau ist immer noch zu beobachten, und der Abfall ist für alle Kurve gleich. Allerdings sind die Kurven leicht zueinander verschoben. Eine mögliche Erklärung ist wieder der Zeitursprung. Da die Dehnungen unterschiedlich sind, ist die 4 a_c-Distanz unterschiedlich, weswegen auch die vergangene Zeit, seitdem die Spitze über das Material gefahren ist, unterschiedlich ist. Daher ist eine kleine Verschiebung zu erwarten.

Abschließend lässt sich sagen, dass für eine verdoppelte Dehnung die Heilungszeit zunimmt. Allerdings ist das Heilungsverhalten gleich, weil die normierten Heilungstiefen für alle Dehnungen gleich sind. Eine vollständige Heilung wurde in allen Fällen beobachtet.

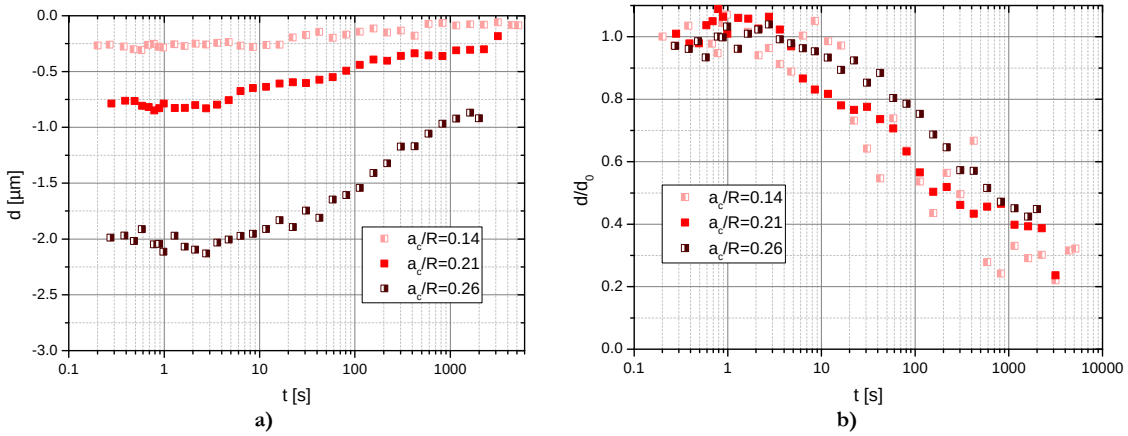

Abbildung III-13 a) Kratzerheilung für verschiedenen Dehnungen im laufe der Zeit für einen 4a_c-Abstand vom Kratzerende b) gleiches Experiment normiert auf die erste gemessene Tiefe

III.4.4.4 Fazit

In diesem Teil wurde die Kratzerheilung untersucht. Die 3D-Oberflächendarstellung erlaubte eine genaue Verfolgung der Kratzerheilung in Abhängigkeit von der Zeit. Dann wurden die Tiefen als Funktion der Zeit und des Abstands zum Ende des Kratzers dargestellt (die Abstände wurden in Vielfachen des Kontaktradius ausgedrückt). Der Abstand 4 a_c entspricht dem kürzesten Abstand, zu dem die ganze mechanische Vorgeschichte abgeschlossen ist. Anschließend wurde die Heilung nur an diesem Abstand gemessen. Fünf verschiedene Kratzer wurden unter drei verschiedenen Kräften und drei verschiedenen Geschwindigkeiten der Spitze ausgeführt. Je höher die Kraft oder je geringer die Geschwindigkeit der Spitze, desto größer die anfängliche verbleibende Tiefe. Trotzdem waren die Heilungen in allen Fällen zueinander proportional, daher wurde keine Plastizität beobachtet. Nur Langzeit-Viskoelastizität (siehe Masterkurve im teil VI.3.4.3) wurde beobachtet.

III.4.5. Fazit

Dieser Teil war dem Verständnis des mechanischen Verhaltens von Polymeren gewidmet. Im Besonderen wurde die Viskoelastizität untersucht. Dehnungs-Zeit-Masterkurven wurden aus Kompressions-Relaxationsversuchen konstruiert. Die Analyse von Indentations-Kriechen und -Heilung erlaubte bei PMMA CN die Beobachtung des Beginns der Plastizität bei langen Indentationszeiten oder hohen Temperaturen. CR39 zeigte wie PMMA CN thermoplastisches Verhalten unter der Glasübergangstemperatur und darüber elastomeres Verhalten. Im experimentell abgedeckten Bereich zeigte CR39 nur Langzeit-Viskoelastizität. Darüberhinaus ermöglichte die durchschnittliche Kontaktspannung die Erstellung von Dehnungs-Zeit-Temperatur-Masterkurven mit einer sehr genauen Übereinstimmung mit den Bulk-Masterkurven. Dadurch wurde bewiesen, dass die Plastizität keinen Einfluss auf die Viskoelastizität hat und dass die untersuchten Polymere keine Viskoplastizität besitzen. Eine Analyse der unmittelbaren Kratzerheilung von CR39 wurde in dieser Arbeit zum ersten Mal gezeigt

III.5. FINITE ELEMENT MODELLIERUNG

III.5.1. Materialmodelle

Schließlich wurden Simulationen mit Finite-Elemente-Modellen durchgeführt, um die Heilungsphase besser zu verstehen. Um die viskosen Materialeigenschaften zu charakterisieren, wurden mehrere uniaxiale Tests durchgeführt. Die aufgebrachten Dehnungen lagen zwischen 0,5 % und 20 %. Eine 3D-Darstellung des Datensatzes wird in Abbildung III-3 gezeigt. Aus diesen Experimenten wurden zwei verschiedene Materialmodelle abgeleitet. Das erste Modell ist viskoplastisch und basiert auf einer Norton-Gleichung (Mehr Infos in Teil VII.2.4). Dieses Modell gibt die Spannung in Abhängigkeit der tatsächlichen plastischen Dehnung und tatsächlichen plastischen Dehnungsrate wieder. Abbildung III-14 stellt die Oberfläche dar, die an die experimentellen Daten angepasst wurde. Die Norton-Gleichung [33] und deren angepasster Koeffizient sind auch in der Abbildung enthalten.

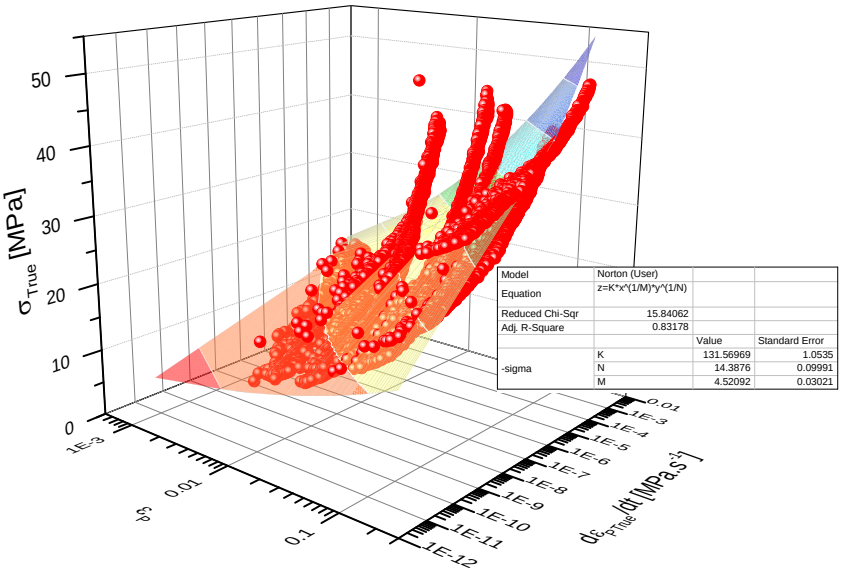

Abbildung III-14 Norton Gleichung und angepasste Koeffizienten

Das viskoelastische Modell besteht aus einem verallgemeinerten Maxwell-Modell (in unseren Fall 8 parallele Federn-Dämpfer). Die Gleichungen für das Maxwell-Schubmodul und das Kompressionsmodul werden dann an ein Relaxationsexperiment angepasst. So wird für jedes Experiment ein Satz VE-Koeffizienten [34] berechnet. In dieser Zusammenfassung werden die Parametersätze für 4,88 % und 17,69 % Dehnung benutzt und jeweils VE (ε = 4,88 %) und VE (ε = 17,69 %) benannt.

Zudem wurde schon gezeigt (Abbildung III-4b)), dass es möglich ist, Masterkurven aus Relaxationsexperimenten zu erstellen. Deswegen kann ein verallgemeinertes Maxwell-Modell an die Masterkurve angepasst werden (MC VE) [35]. In diesem Fall ist die Referenz der Masterkurve der Relaxationsversuch bei 4,88 % Dehnung. Das bedeutet, dass in Abbildung III-15 die Werte des Relaxationsexperimentes bei 4,88 % Dehnung nicht verschoben werden. Die Schubmoduln, die kleineren Dehnungswerten entsprechen, sind nach links verschoben, wohingegen diejenigen, die größeren Dehnungswerten entsprechen, nach rechts verschoben sind. Das angepasste Maxwell-Modell besitzt in diesem Fall 18 parallele Federn-Dämpfer, und somit 18 Zeitkonstanten. Die Übereinstimmung Modell-Experiment ist wohl deswegen gering, weil sehr viele Daten angepasst werden müssen und wegen der nicht-idealen Verschiebung.

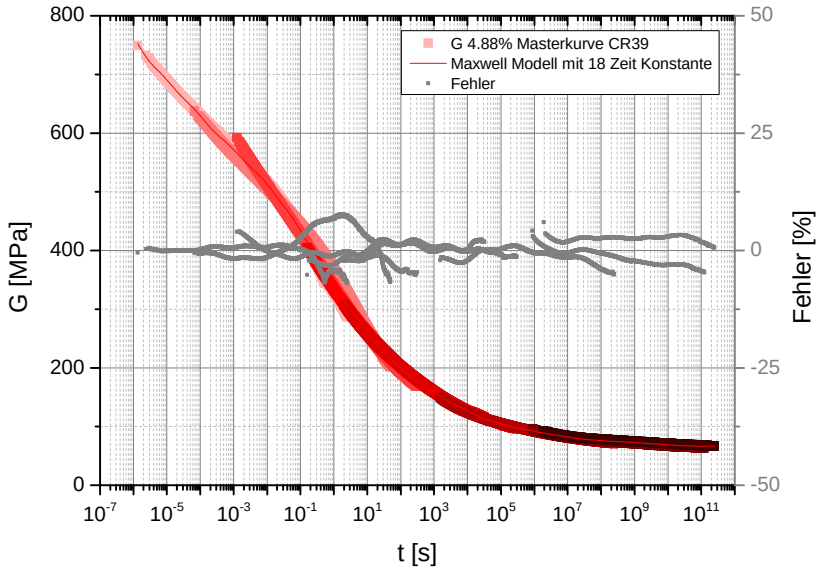

Abbildung III-15 CR39 Masterkurve mit Referenz bei 4,88 % Dehnung, angepasst an die Maxwell Gleichung

Wie bereits erläutert, wird für jedes Experiment ein Satz VE-Koeffizienten berechnet, ebenso bei der Masterkurve. Die Untersuchung der viskoelastischen Parameter wird nur an CR39, dem am besten charakterisierten Material, durchgeführt. Das Maxwell-Modell ist eine mathematische Beschreibung, die sich dank ihrer hohen Parameterisierung gut an viskose Phänomene anpassen lässt [36].

Zum Vergleich wurden vier viskoelastische Modelle untersucht. Diese wurden an verschiedene Dehnungsrelaxationsexperimente angepasst. Die ausgewählten Dehnungen betrugen 4,88 % und 17,69 %. Diese Dehnungen entsprechen den wahren Dehnungen der Relaxationsexperimente bei 5 und 19,4 %. Für beide Relaxationsexperimente wurden Masterkurven erstellt. So wurden zwei „einfache“ Maxwell-Modelle und zwei Masterkurven-Maxwell-Modelle erhalten.

Schließlich wurde für das elastoplastische Modell die aus der Literatur bekannte G'Sell-Jonas-Gleichung [37-39] benutzt. Die Koeffizienten wurden aus Indentationsexperimenten mit verschieden geformten Indentern bestimmt.

Um die Simulationsqualität zu verbessern, wurde die experimentale Auslenkung des Auslegers in den Finite-Elemente-Modellcode eingebettet. Dies bedeutet, dass die numerischen Modelle von den experimentellen Daten geführt werden.

III.5.2. Bulk-Relaxationsexperiment

Die verschiedenen Materialmodelle wurden an einem einfachen Relaxationsexperiment getestet. Der Vorteil des Relaxationsexperimentes ist, dass die Dehnung des Materials nahezu uniform erfolgt. Daher kann die Qualität des Modells für eine gegebene Dehnung überprüft werden. Alle Vergleiche wurden anhand von CR39 durchgeführt, für das die meisten Daten zur Verfügung stehen.

III.5.2.1 Relaxationsexperiment 4.88 %

Abbildung III-16 zeigt die Spannung als Funktion der Zeit für ein Relaxationsexperiment bei 4,88 %. Links sind die viskoelastischen Modelle bei 4,88 % Dehnung dargestellt (VE und MC VE), rechts die viskoelastischen Modelle bei 17,69 % (VE und MC VE) und darunter die viskoplastischen und elastoplastischen Modelle. Die besten Modelle sind die VE-Modelle (ε = 4,88 %), die schlechtesten sind EP- und VE(ε = 17,69 %)-Modell. Bemerkenswert ist, dass die VE-Modelle bei 4,88 % sehr genau mit dem Experiment übereinstimmen. Die Anfangsspannung des „einfachen" viskoelastischen Modells bei 4,88 % zeigt nur eine geringe Übereinstimmung. Die 4,88 %-Masterkurve zeigt im Kurzzeitbereich bessere Ergebnisse. Bei langen Zeiten ist die Qualität beider Modelle gleich, was zu erwarten war, da die Maxwell-Koeffizienten bei diesen Zeitkonstanten nahe beieinander liegen. Das viskoelastische Modell bei 17,69 % reagiert zu hart im Vergleich mit dem Experiment (die Spannung ist viel kleiner als in Wirklichkeit). Diese Modelle wurden nicht für diese Dehnung angepasst. Schließlich liefert das viskoplastische Modell eine grobe Schätzung der durchschnittlichen Spannungswerte, während das elastoplastische Modell die unmittelbare Antwort gut wiedergibt, aber nicht über die Zeit gesehen.

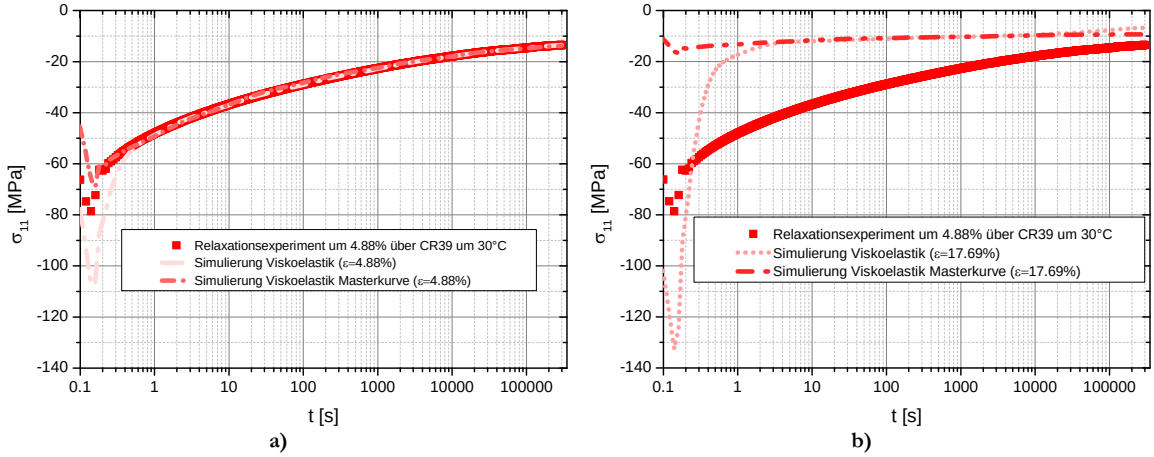

a) b)

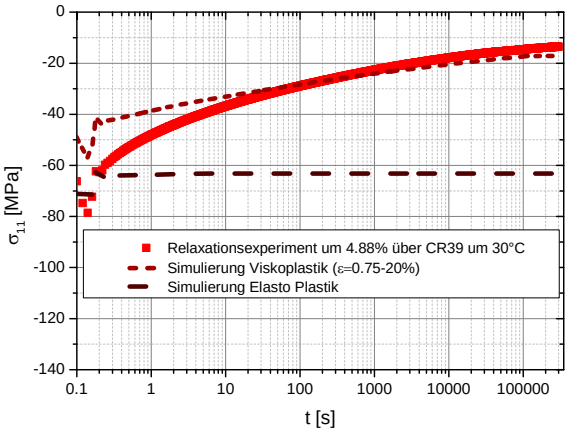

c)

Abbildung III-16 Experimentelle und simulierte Spannung gegen die Zeit für das Dehnungsrelaxationsexperiment an CR39 bei 4,88 % und 30°C a) viskoelastisches Modell bei 4,88 % b) viskoelastisches Modell bei 17,69 % c) Elastoplastisches und viskoplastisches Modell

III.5.2.2 Relaxationsexperiment 17.69 %

Die Ergebnisse von Experiment und Simulation des Relaxationsexperimentes bei 17,69 % sind in Abbildung III-17 dargestellt. Abbildung III-17 a) zeigt das viskoelastische Modell bei 4,88 %, Abbildung III-17 b) das viskoelastische Modell bei 17,69 % und Abbildung III-17 c) das elastoplastische und viskoplastische Modell. Die Spannungen der viskoelastischen Modelle bei 4,88 % sind viel höher als im Experiment, die Modelle also zu weich. Hingegen zeigt das viskoelastische Modell bei 17,69 % eine sehr gute Annäherung nach der Belastung, aber das einfache viskoelastische Modell ist zu weich während der Belastung, während das MC-VE-Modell zu hart ist. Das elastoplastische Modell liefert eine gute Annäherung der Belastung, aber nicht der Relaxation. Das viskoplastische Modell ist etwas zu hart.

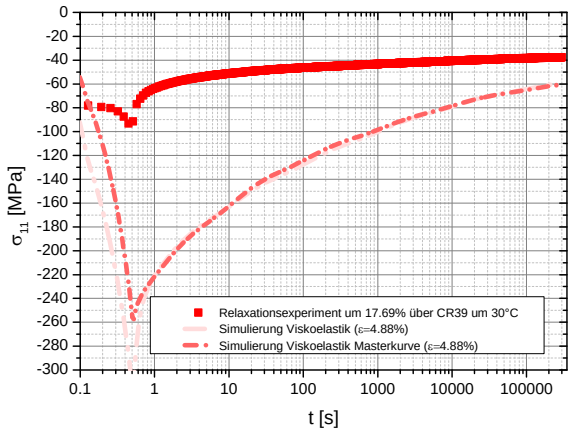

a)

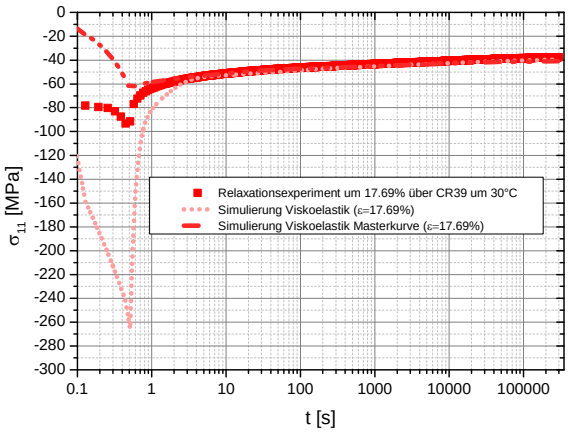

b)

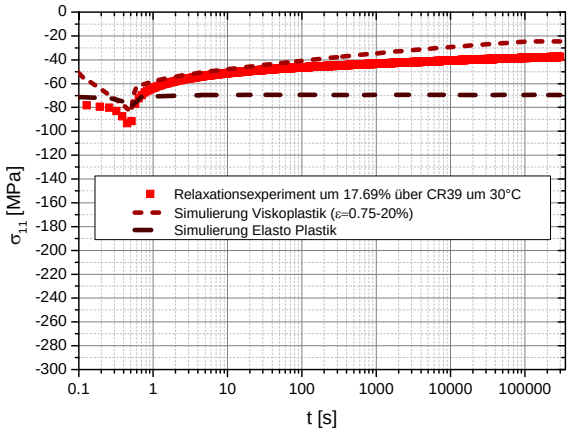

c)

Abbildung III-17 Experimentelle und simulierte Spannung gegen die Zeit des 17,69 %-Dehnungsrelaxationsexperimentes mit CR39 bei 30°C a) Viskoelastisches Modell bei 4,88 % b) Viskoelastisches Modell bei 17,69 % c) Elastoplastisches und viskoplastisches Modell

III.5.2.3 Fazit

Die VE-Modelle sind sehr genau, wenn die Spannung in etwa derjenigen entspricht, für die sie erstellt wurden. Die Verwendung von Masterkurven verbessert die Qualität der Simulation der Belastung. In der Tat liefern die MC-VE-Modelle für kurze Zeiten eine gute Übereinstimmung. Das elastoplastische Modell gibt eine gute Näherung der Anfangsspannung, aber keine viskosen Phänomene wieder. Das einzige Materialmodell, das eine ungefähre Annäherung jedes Experimentes erlaubt, ist das viskoplastische Modell. Da die mittleren Tabor-Dehnungen zwischen 4 und 6 % liegen (Anfang und Ende der Indentation von CR39 und PMMA CN) [13, 40], werden das viskoelastische Modell (ε = 4,88 %) und das viskoelastische Masterkurven-Modell (ε = 4,88 %) benutzt.

III.5.3. Indentation

Die Simulation des Indentationskriechens ist in den letzten Jahren für viele Anwendungen in den Blickpunkt des Interesses gerückt [41-43]. Daher ist eine Validierung der Materialmodelle notwendig. Das Indentationskriechen und die Heilung von CR39 werden im Folgenden vorgestellt.

III.5.3.1 Indentations-Kriechen

Die durchschnittliche Kontaktspannung in Abhängigkeit von der Zeit ist in Abbildung III-18a) dargestellt. Die experimentellen Daten fallen mit dem Logarithmus der Zeit ab. Das G'Sell-Jonas-Modell gibt den Abfall nicht wieder. Der Anfangswert stimmt aber trotzdem. Im Gegensatz dazu ist der Anfangswert des einfachen VE-Modells viel zu hoch und bleibt so während des gesamten Experimentes. Die viskoelastische Masterkurve bei 4,88 % und die viskoplastische Modellkurve liegen leicht unter der experimentallen Kurve, fallen aber korrekt mit der Zeit ab. Die Unveränderlichkeit des viskoelastischen Modells kam erwartet, da die Zeit in der G'Sell-Jonas-Gleichung nicht vorkommt. Der hohe Wert des viskoelastischen Modells kann damit erklärt werden, dass die ersten Millisekunden des Relaxationsexperiments nicht berücksichtigt werden, ein Fehler, der durch das gesamte Experiment mitgeschleppt wird. Die Masterkurve korrigiert

diesen Fehler und liefert in der Tat einen viel genaueren Wert für die durchschnittliche Kontaktspannung. Die relative Genauigkeit des viskoplastischen Modells liegt an dem weiten Deformationsbereich. Deswegen zeigen alle getesteten Materialien einen recht guten Zusammenhang zwischen Spannung und Dehnung. Der Graph in Abbildung III-18 b) zeigt die experimentelle normalisierte Tabor-Dehnung und die Simulationsergebnisse. Wie schon bemerkt, zeigt das EP-Modell keinerlei Entwicklung und beweist somit das Fehlen von Veränderung nach Belastung. Die Deformation der Masterkurve liegt leicht über dem Experiment. Im Gegensatz dazu liegen die VE- und VP-Modelle unter dem Experiment. Am nächsten dran liegt das VP-Modell. In der Tat scheint die durchschnittliche Antwort auf jede Deformation einen guten Kompromiss zu liefern.

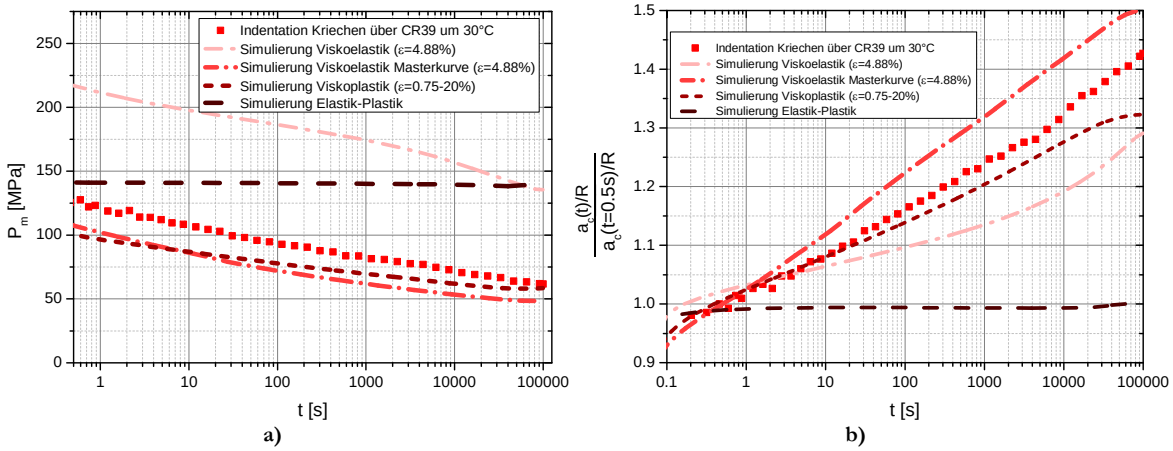

Abbildung III-18 a) Durchschnittliche Kontaktspannung und b) normierte Tabor-Dehnung bei 30°C von Experiment und Simulation für CR39

Zusammenfassend kann das Indentations-Kriechverhalten von CR39 bei 4-6 % durchschnittlicher Tabor-Dehnung am besten mit einer viskoelastischen Masterkurve bei 4,88 % oder einem viskoplastischen Modell erklärt werden. Beide Modelle zeigen eine etwas geringere durchschnittliche Kontaktspannung als das Experiment, die simulierten Dehnungen liegen im Rahmen der experimentellen Dehnung.

III.5.3.2 Indentations-Heilung

Die Ergebnisse der experimentellen und simulierten Indentationsheilung sind in Abbildung III-19 dargestellt. Die elastoplastischen und viskoplastischen Modellkurven verlaufen waagerecht. Sie zeigen jeweils 45 % und 20 % der Heilung. In beiden Fällen heilen sie unmittelbar den elastischen Teil des Abdrucks und dann nicht mehr. Die elastische Modell führte zu einem kleineren Abdruck (siehe Abbildung III-18 b)), daher ist der elastisch verformte Materialanteil größer und ebenso der geheilte Anteil. Die beiden anderen Modelle zeigen eine vollständige Heilung. Die unmittelbare Heilung des VE-Modells bei 4,88 % beträgt etwa 45 %, das sind 20 % mehr als im Experiment. Diese große unmittelbare Heilung rührt von der kleineren Deformation am Ende des Abdrucks her. Im Gegensatz dazu ist die die Enddehnung des viskoelastischen Masterkurven-Modells bei 4,88 % um 5 % größer als im Experiment. Die unmittelbare Heilung der Simulation liegt dann sehr viel näher am Experiment. Das viskoelastische Masterkurven-Modell bei 4,88 % gibt das Experiment sehr akkurat wieder, daher kann davon ausgegangen werden, dass CR39 im abgedeckten Bereich viskoelastisch ist.

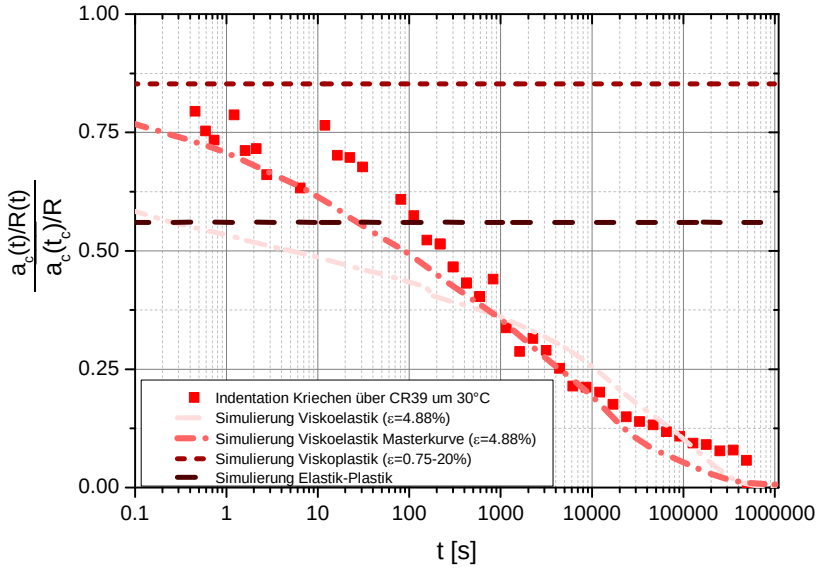

Abbildung III-19 Experimentelle und simulierte Heilung im Indentations-Kriechversuch für CR39

III.5.4. Fazit

Drei verschiedene Materialmodelle wurden in die Software MSC Marc integriert. Das elastoplastische Modell ermöglicht eine sehr gute Vorhersage der Spannung-Dehnungs-Beziehung für die untersuchten Polymere, zeigt aber keinerlei durch den Kriech-Effekt bedingte Veränderungen. Das viskoplastische Modell gibt eine gute Darstellung der durchschnittlichen Kontaktspannung.

Das Masterkurven-Modell schließlich besitzt eine sehr hohe Präzision, wenn es bei der passenden Dehnung benutzt wird. Im Fall von Indentations-Kriechen gibt es die normierte Tabor-Dehnung akkurat wieder. Die Heilung der Masterkurven erfolgt mit großer Genauigkeit, solange keine Plastizität an der Deformation beteiligt ist (Details siehe Simulationsteil VII.5.3).

Um die Simulationsqualität zu verbessern, sollte ein mit einer Plastizitätsgrenze versehenes viskoelastisches Masterkurvenmodell verwendet werden. Der nächste Schritt zur Verbesserung der Materialmodelle wäre die Differenzierung der Kompressions-, Zieh- und Scherantwortverhaltens.

III.6. FAZIT

Diese Arbeit erklärt die zeitliche Abhängigkeit des mechanischen Verhaltens von Makromolekülen. Im Besonderen wurde die Viskoelastizität im Bulk untersucht. Dehnungs-Zeit-Masterkurven wurden aus den Kompressions-Relaxationsexperimenten erstellt. Die Indentations-Kriechmessung und -Heilung ermöglichte die Beobachtung des Beginns der Plastizität in PMMA CN bei langen Indentationszeiten. CR39 zeigte wie PMMA CN thermoplastisches Verhalten unter der Glasübergangstemperatur, darüber elastomeres Verhalten. Im experimentell abgedeckten Bereich zeigte CR39 nur Langzeit-Viskoelastizität. Durch die Beobachtung der Heilungsphase wurde bestimmt, ob ein Material viskoelastisch oder elastoplastisch ist. Darüber hinaus ermöglichte die durchschnittliche Kontaktspannung die Erstellung von Dehnung-Zeit-

Temperatur-Masterkurven mit einem sehr genauen Übergang zur Bulk-Masterkurve. Damit wurde bewiesen, dass Plastizität keinen Einfluss auf Viskoelastizität hat und dass die untersuchten Polymeren keine Viskoplastizität besitzen. Die Äquivalenz zwischen Kontakt- und Bulk-Masterkurven wurde aufgezeigt und bewiesen, dass bei Kenntnis der einen Kurve die andere vorhergesagt werden kann. Eine Analyse der unmittelbaren Kratzerheilung von CR39 wurde zum ersten Mal in dieser Arbeit beschrieben.

Anschließend wurde die Simulation des mechanischen Verhaltens von Polymeren durch drei verschiedene Materialmodelle in die Software MSC Marc integriert. Das elastoplastische Modell ermöglicht eine sehr gute Voraussage der unmittelbaren Spannungs-Dehnungs-Beziehungen an den untersuchten Polymeren, nicht aber der Kriech-Effekte. Das viskoplastische Modell gibt eine relativ gute Darstellung der Entwicklung der durchschnittlichen Kontaktspannung.

Zuletzt zeigt das VE-Masterkurven-Modell eine sehr hohe Präzision, wenn es für die passende Dehnung verwendet wird. Im Falle von Indentations-Kriechen liefert es eine akkurate Abbildung der normierten Tabor-Dehnung. Die Heilung wird genau wiedergegeben, solange keine Plastizität an der Deformation beteiligt ist.

Um die Simulationsqualität zu verbessern, könnte die viskoelastische Masterkurve mit einer Plastizitätsgrenze versehen werden. Eine weitere Verbesserung, insbesondere für Kratzersimulationen, würde durch die Differenzierung von Kompression, Traktion und Scherung erreicht werden. Raum für Verbesserungen bietet auch die Simulation der Indentations-Heilungsphase.

Um ein besseres Verständnis der Polymermaterialien zu erzielen, sollten der Beziehung Zeit-Temperatur-Deformation Elemente der Molekulardynamik und Bruchmechanik hinzugefügt werden.

III.7. BIBLIOGRAPHIE

[1] S.C. Tjong, Structural and mechanical properties of polymer nanocomposites, Materials Science and Engineering R: Reports, 53 (2006) 73-197.

[2] P. Bertrand-Lambotte, J.L. Loubet, C. Verpy, S. Pavan, Nano-indentation, scratching and atomic force microscopy for evaluating the mar resistance of automotive clearcoats: Study of the ductile scratches, Thin Solid Films, 398-399 (2001) 306-312.

[3] M. Mansha, C. Gauthier, P. Gerard, R. Schirrer, The effect of plasticization by fatty acid amides on the scratch resistance of PMMA, Wear, 271 (2011) 671-679.

[4] C. Gauthier, R. Schirrer, Time and temperature dependence of the scratch properties of poly(methylmethacrylate) surfaces, Journal of Materials Science, 35 (2000) 2121-2130.

[5] K. Yasui, Curable material containing photopolymerizable polymer and cured object, in: L. Nissan Chemical Industries (Ed.) USPTO, Nissan Chemical Industries , Ltd., united states of america, 2007.

[6] H. Hertz, Über die Berürhung fester elasticher Körper, Journal für die reine und angewandte Mathematik, 92 (1882) 156-171.

[7] W.C. Oliver, G.M. Pharr, Improved technique for determining hardness and elastic modulus using load and displacement sensing indentation experiments, J. Mater. Res., 7 (1992) 1564-1580.

[8] W.C. Oliver, G.M. Pharr, Measurement of hardness and elastic modulus by instrumented indentation: Advances in understanding and refinements to methodology, J. Mater. Res., 19 (2004) 3-20.

[9] A.C. Fischer-Cripps, A simple phenomenological approach to nanoindentation creep, Materials Science and Engineering A, 385 (2004) 74-82.

[10] S.E. Olesiak, M.L. Oyen, V.L. Ferguson, Viscous-elastic-plastic behavior of bone using Berkovich nanoindentation, Mech. Time-Depend. Mater., 14 (2010) 111-124.

[11] B.J. Briscoe, L. Fiori, E. Pelillo, Nano-indentation of polymeric surfaces, Journal of Physics D: Applied Physics, 31 (1998) 2395-2405.

[12] A. Rubin, C. Gauthier, R. Schirrer, The friction coefficient on polycarbonate as a function of the contact pressure and nanoscale roughness, Journal of Polymer Science, Part B: Polymer Physics, 50 (2012) 580-588.

[13] D. Tabor, The hardness of solids, Review of Physics in Technology, 1 (1970) 145.

[14] T. Chatel, C. Gauthier, H. Pelletier, V. Le Houerou, D. Favier, R. Schirrer, Creep of the contact with a spherical tip and recovery of the imprint on amorphous polymer surfaces, Journal of Physics D-Applied Physics, 44 (2011).

[15] I. Karapanagiotis, D.F. Evans, W.W. Gerberich, Dynamics of the leveling process of nanoindentation induced defects on thin polystyrene films, Polymer, 43 (2002) 1343-1348.

[16] Z.Y. Zhang, H.N. Dhakal, S.N. Surip, I. Popov, N. Bennett, Characterisation of roof tile coating degradation using nano-indentation test and surface profilometry, Polymer Degradation and Stability, 96 (2011) 833-838.

[17] T. Chatel, Fluage et recouvrance d'empreintes et de sillons sur suface de polymère, in, Université de Strasbourg, Strasbourg, 2010.

[18] J.S.S. Wong, H.J. Sue, K.Y. Zeng, R.K.Y. Li, Y.W. Mai, Scratch damage of polymers in nanoscale, Acta Materialia, 52 (2004) 431-443.

[19] W. Shen, S.M. Smith, H. Ye, F. Jones, P.B. Jacobs, Real time observation of viscoelastic creep of a polymer coating by scanning probe microscope, Tribology Letters, 5 (1998) 75-79.

[20] M. Wong, G.T. Lim, A. Moyse, J.N. Reddy, H.J. Sue, A new test methodology for evaluating scratch resistance of polymers, Wear, 256 (2004) 1214-1227.

[21] L.C.E. Struick, Physical Aging in Amorphous Polymers and Other Materials, Elsevier, Amsterdam, , 1978.

[22] J.J. Martinez-Vega, H. Trumel, J.L. Gacougnolle, Plastic deformation and physical ageing in PMMA, Polymer, 43 (2002) 4979-4987.

[23] J. Kolařík, Tensile creep of thermoplastics: Time-strain superposition of non-iso free-volume data, Journal of Polymer Science, Part B: Polymer Physics, 41 (2003) 736-748.

[24] M. Software, Volume A: Theory and User Information, in, 2012, pp. 813.

[25] F. Quadrini, E.A. Squeo, A. Guglielmotti, Indentation creep of polymers. I. Experimental, Polymer Engineering and Science, 50 (2010) 2431-2439.

[26] J. Kolařík, A. Pegoretti, Non-linear tensile creep of polypropylene: Time-strain superposition and creep prediction, Polymer, 47 (2006) 346-356.

[27] S. Jazouli, W. Luo, F. Bremand, T. Vu-Khanh, Application of time-stress equivalence to nonlinear creep of polycarbonate, Polym. Test, 24 (2005) 463-467.

[28] P.A. O'Connell, G.B. McKenna, Large deformation response of polycarbonate: Time-temperature, time-aging time, and time-strain superposition, Polymer Engineering and Science, 37 (1997) 1485-1495.

[29] J. Zhao, G.B. McKenna, Temperature divergence of the dynamics of a poly(vinyl acetate) glass: Dielectric vs. mechanical behaviors, Journal of Chemical Physics, 136 (2012).

[30] B.J. Briscoe, E. Pelillo, S.K. Sinha, Scratch hardness and deformation maps for polycarbonate and polyethylene, Polymer Engineering and Science, 36 (1996) 2996-3005.

[31] I.C. Choi, B.G. Yoo, Y.J. Kim, J.I. Jang, Indentation creep revisited, J. Mater. Res., 27 (2012) 3-11.

[32] K. Sakaue, S. Okazaki, T. Ogawa, Indentation technique for evaluation of master curve of creep compliance, Experimental Techniques, 35 (2011) 16-22.

[33] J. Lemaitre, J.-L. Chaboche, Mécanique des matériaux solides, Bordas, 1988.

[34] T. Chatel, V. Le Houérou, H. Pelletier, C. Gauthier, Numerical analysis of the creep of the contact and recovery of the imprint on amorphous polymer surfaces, Mech. Time-Depend. Mater., (2012) 1-15.

[35] L.C.A. Van Breemen, E.T.J. Klompen, L.E. Govaert, H.E.H. Meijer, Extending the EGP constitutive model for polymer glasses to multiple relaxation times, Journal of the Mechanics and Physics of Solids, 59 (2011) 2191-2207.

[36] P.E. Combette, Isabelle Physique des polymères propriété mécaniques, 6 rue de la sorbonne, paris, 2005.

[37] M.C. Baietto Dubourg, J. Rannou, A. Gravouil, H. Pelletier, C. Gauthier, R. Schirrer, 3D crack network during the scratching of a polymer: Comparison between experimental results and localized multigrid X-FEM, in, Ottawa, ON, 2009, pp. 3827-3836.

[38] C. G'Sell, J.J. Jonas, Determination of the plastic behaviour of solid polymers at constant true strain rate, Journal of Materials Science, 14 (1979) 583-591.

[39] J.L. Bucaille, E. Felder, G. Hochstetter, Mechanical analysis of the scratch test on elastic perfectly plastic materials with the three-dimensional finite element modeling, Wear, 249 (2001) 422-432.

[40] H. Pelletier, C. Gauthier, R. Schirrer, Experimental measurement and numerical simulation of the plastic strain during indentation and scratch tests on polymeric surfaces, J. Mater. Res., 24 (2009) 1184-1196.

[41] J. Krier, J. Breuils, L. Jacomine, H. Pelletier, Introduction of the real tip defect of Berkovich indenter to reproduce with FEM nanoindentation test at shallow penetration depth, J. Mater. Res., 27 (2012) 28-38.

[42] H. Jiang, R. Browning, H.J. Sue, Understanding of scratch-induced damage mechanisms in polymers, Polymer, 50 (2009) 4056-4065.

[43] F.L. Li, F.L. Peng, Y. Tan, W. Kongkitkul, M.S.A. Siddiquee, FE simulation of viscous behavior of geogrid-reinforced sand under laboratory-scale plane-strain-compression testing, Geotextiles and Geomembranes, 31 (2012) 72-80.

CHAPTER IV. BIBLIOGRAPHY

CHAPTER IV. BIBLIOGRAPHY 82
IV.1. INTRODUCTION 83
IV.2. POLYMERIC MATERIALS 83
IV.2.1. Polymer fabrication 83
IV.2.2. Polymer applications 83
IV.3. GENERAL MECHANICS 83
IV.3.1. Boltzmann superposition principle 84
IV.4. CONTACT MECHANIC 88
IV.4.1. Indentation 88
IV.4.2. Scratch 92
IV.4.3. Conclusion 95
IV.5. ANALYTICAL MODELING 95
IV.5.1. Simple rheological model 95
IV.5.2. Generalized model 97
IV.5.3. Indentation 98
IV.6. FINITE ELEMENT MODELING 99
IV.6.1. Model 99
IV.6.2. Constitutive law 100
IV.7. CONCLUSION 102
IV.8. BIBLIOGRAPHY 104

IV.1. INTRODUCTION

Polymers are materials formed by the repetition of small molecules thus forming long molecules (or macromolecules). They are commonly called plastics or rubber. This chapter will introduce some basics on the polymeric material then a description of their bulk mechanical behavior followed by their contact behavior finally some models predicting their behavior are presented.

IV.2. POLYMERIC MATERIALS

IV.2.1. Polymer fabrication

Nature produced its own polymers: wood, protein, AND or rubber. The human fabrication of polymers is nonetheless relatively recent (in comparison with the first human fabrication of ceramics or metals) [1, 2]. A first explanation on the possible reaction mechanism was given by Staudinger a century later for poly methyl methacrylate (PMMA) [2, 3], thus founding the radical polymerization concept. CR39, also done by radical polymerization, appeared a few years later [4].

IV.2.2. Polymer applications

Since their first use in South America (as rubber ball), the polymers have been used for numerous applications. Indeed, polymers and related composites (polymeric matrix with fillers or additives[5]) have been widely used in aerospace [6], automotive [7, 8], microelectronic [9] food packaging [10], and biomedical applications [11, 12], due to their adequate strength, lightness, ease of processing and low cost [12]. PMMA reflects these multiple applications. PMMA is commonly used as denture base [13], bone replacement [14] but also as paint [15] or in microelectronic or as lenses for its optical properties [16, 17]. CR39 is also used for this particular application [4]. The improvement of the polymer scratch and indentation resistance for this kind of application is one of the objectives of this thesis. It can be done by filler addition [18].Naturally the improvement should not be at the detriment of the optical transparence.

IV.3. GENERAL MECHANICS

As seen previously, polymers can have a very wide range of application. This is generally due to their very low weight. On the counter part their mechanical behavior is more complex than for metals or ceramics. Indeed metals have an elastic plastic comportment. On the contrary ceramics are elastic fragile. Polymers [19] have:

- an elastic behavior, at low temperature or high speed, where the Hooke's law is dominant. This means that the stress is time independent.

Hooke's law	$\sigma = E\varepsilon$	Equation IV-1

- a viscous comportment, at high temperature or low speed, the stress is related to the deformation speed by the Newton equation (see Equation IV-2). In this case the stress is time dependent.

Newton's fluid equation	$\sigma = \eta\dot{\varepsilon}$	Equation IV-2

The real behavior is a mix of the two previously quoted behaviors. This occurs at average speed and temperature. This material presents a viscoelastic behavior. The polymer has a slow time dependent behavior.

Each new behavior is associated with a different transition temperature and thus an increase in molecular mobility. The elastic behavior is observed for temperatures below the T_β. The Newtonian fluid behavior takes place above the T_α, if the plastic is not vulcanized.

Depending on the T_α position relative to the room temperature, the aspect of the material will be different:

- $T>T_\alpha$ a fluid or if reticulated a very soft solid
- $T_\alpha > T > T_\beta$ a deformable solid
- $T_\beta > T$ a brittle solid

Clearly depending on the goal application, different polymers are used. In this manuscript I will predominantly discuss the mechanical properties in the temperature range [T_β: T_α].

IV.3.1. Boltzmann superposition principle

As the mechanical properties are time dependent, two major ways to determine the mechanical properties of polymers exist either applying a constant stress or strain and measuring the other one over time, or applying an oscillatory force at different frequencies. In both cases the Boltzmann [20, 21] principle applies. It says that a viscoelastic deformation caused by several stresses is equal to the sum of all the deformation issued from those stresses.

Master curves

Leaderman proposed in 1941 that "[…] the effect of temperature is thus seen to cause a shift of the sigmoidal creep curve along the axis of logarithmic time" [22]. Indeed he observed that viscoelastic mechanical properties such as deflection creep or creep recovery could be shifted laterally by the influence of temperature. Thereafter several other authors proposed to observe the mechanical behavior of polymer versus temperature and time. In particular Ferry [23] proposed the graphics shown in Figure IV-1 a). The right plot presents the storage compliance at different temperatures versus the logarithm of frequency. It was not possible to acquire data, at a fix temperature, with higher frequency because of the apparatus inertia. On the contrary obtaining very low frequency is possible, but require a very long machine immobilization. Ferry shifted the material curves to obtain the master curves pictured in Figure IV-1 b). Therefore utilizing the temperature as a way to understand the material comportment at very short and very long time or frequency has become relatively common in books addressing polymeric properties [19, 21, 24, 25].

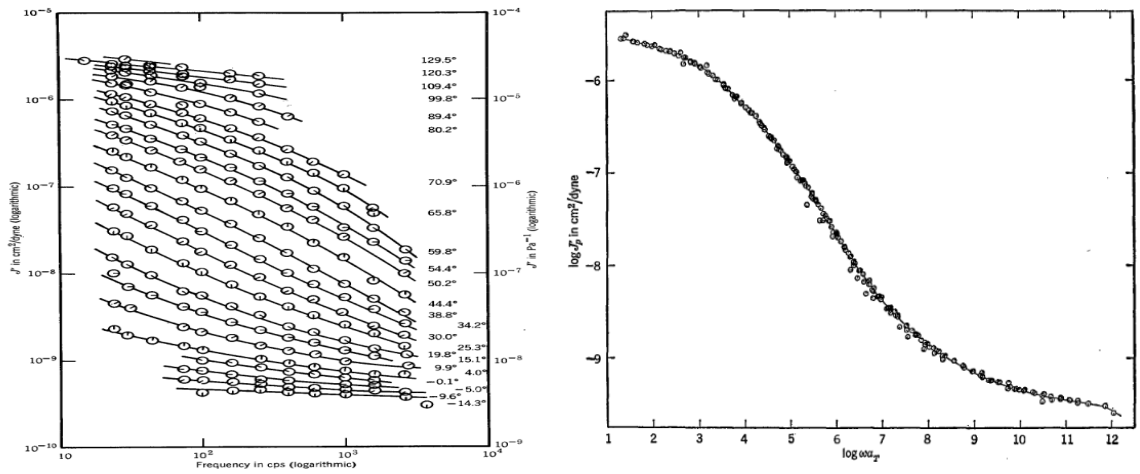

a) b)

Figure IV-1 Storage compliance of poly(n-octyl methacrylate) in the transition zone between glasslike and rubberlike consistency, plotted logarithmically against frequency at 24 temperatures as indicated [22] b)composite curve obtained by plotting the data of a) with reduced variables, representing the behavior over an extended frequency scale at temperature T0=100°C [23]

The shift factor $\log(a_T)$ is introduced and is defined in Equation IV-3, where T is a temperature expressed in Kelvin, T_R the reference temperature, τ a characteristic molecular relaxation time, and D a mechanical descriptor (e.g. viscosity).

Shift factor definition [19]	$a_T = \frac{\tau_T}{\tau_{T_R}} = \frac{\eta(T)}{\eta(T_R)}$	Equation IV-3

Thus the time-temperature equivalence principle is expressed in Equation IV-4.

Time-temperature principle	$D(T_R, t) = D(T, a_T t)$	Equation IV-4

Figure IV-2 presents the used shift factor in Figure IV-1 as a function of the temperature. The chosen temperature of reference is 100°C. There is roughly one point per temperature. The line is the result of the Equation IV-5.

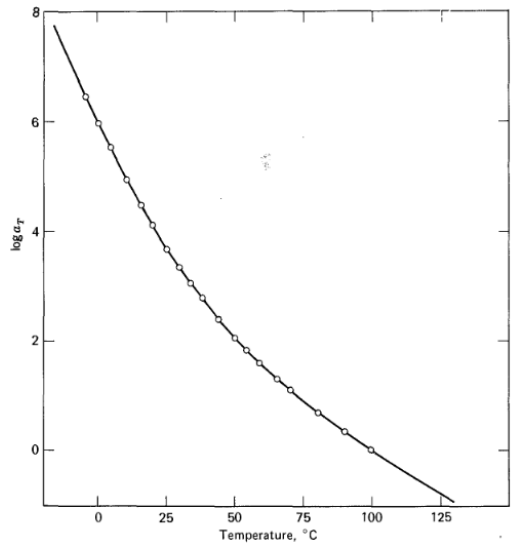

Figure IV-2 Temperature dependence of the shift factor a_T used in plotting Figure I 1 b). Points, chosen empirically; curve from Equation I 5 [22]

Williams, Landel and Ferry (W.L.F.) proposed in 1955 an empirical equation to determine the shift factor [26]. The Equation IV-5 shows the W.L.F. equation where C_1 and C_2 are constants depending on the polymer and reference temperature.

W.L.F. equation [26]	$\log(a_T) = \frac{-C_1(T - T_R)}{C_2 + (T - T_R)}$	Equation IV-5

Although WLF equation and master curves are originally only experimental there was a wish to also find a theoretical ground for these observations. The more common theory is called the free volume theory. It supposes that the volume occupied by the material (V_T) can be divided as the volume occupied by atoms (V_o) and the free volume (V_f) as described in Equation IV-6.

Free volume theory	$V_T = V_o + V_f$	Equation IV-6

Then the glass transition shows a strong volume change. This concept is represented on Figure IV-3. The specific volume increases strongly through the glass temperature. The shown coefficients α_1 and α_2 are the slopes of the specific volume versus temperature below and above the glass transition.

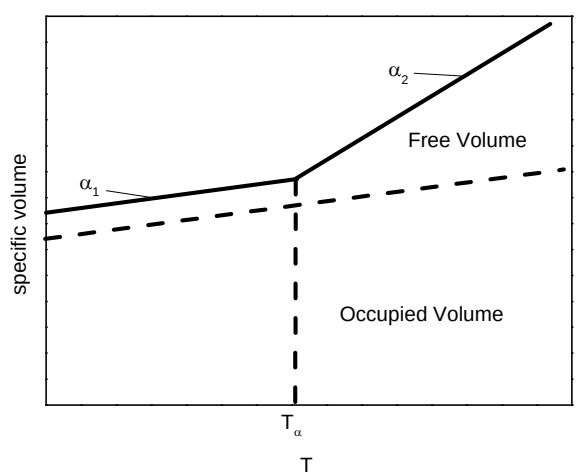

Figure IV-3 Apparition of free volume in a polymer around the glass transition

Thus one can express the free volume as Equation IV-7 below T_α and Equation IV-8 above T_α.

$T<T_\alpha$	$V_f = V_{T_\alpha}$	Equation IV-7
$T>T_\alpha$	$V_f = V_{T_\alpha} + (\alpha_2 - \alpha_1) \times T - T_\alpha$	Equation IV-8

Doolittle presented an equation linking the viscosity and the free volume [27]. The Equation IV-9 is reproduced from his publication.

Doolittle's equation[27]	$\eta = A \times exp(B \times \frac{V_o}{V_f})$	Equation IV-9

Moreover for simplification, one can define f as the ratio of free volume over total volume. (See Equation IV-10)

Fraction of free volume definition	$f = \frac{V_f}{V_T} \approx \frac{V_f}{V_o}$	Equation IV-10

By combining Equation IV-3, Equation IV-9 and Equation IV-10, one obtains trivially the Equation IV-11.

	$\log(a_T) = \log\left(\frac{\eta(T)}{\eta(T_\alpha)}\right) = -\frac{(B/(2.3 \times f_\alpha)) \times (T - T_\alpha)}{f_\alpha/(\alpha_2 - \alpha_1) + (T - T_\alpha)} = \frac{-C_1 \times (T - T_\alpha)}{C_2 + (T - T_\alpha)}$	Equation IV-11

Therefore we have a theoretical value for the coefficient for the temperature between T_α and T_α+100°C. Even if the W.L.F. theory is only valid above the glass transition, one has to note that master curves are sometimes obtained with properties crossing the glass transition [28-30]. Moreover Ferry [31] and other present a vertical shift factor which is sometimes necessary but whose value is generally small and therefore sometimes neglected [23, 32, 33]. The vertical shift is not always used [29, 34] but seems to lead to polemic discussions [35, 36]. Moreover several authors [37, 38], using the vertical shift factor, acknowledge not knowing its origin below the glass transition.

Knauss was one of the first to present the free volume theory applied in the case of different concentration in solvent and different strain degrees [39]. Kolařík rewrote this theory and added a comparison of the respective influence of the different factors [38].

Outside of the free volume theories other theory were presented to predict the short term isothermal behavior of polymers such as the Kolhrausch-Williams-Watts theory [40, 41].

Later on other authors proposed to make time-strain or time-stress master curves [42]. Then O'Connell and McKenna demonstrated on polycarbonate a non-equivalence between time-strain and time-temperature master curves [36]. Their conclusion is that only the time temperature is valid as it is the most commonly used.

IV.4. CONTACT MECHANIC

The classical characterization of polymers is performed by uni-axial tests. Nevertheless, as polymers are used as protective layers [43], bulk measurements are not appropriated and not always possible [44]. Therefore contact measurements are used in particular indentation and scratch.

IV.4.1. Indentation

IV.4.1.1 Principle

The first hardness scale was enunciated by Mohs [45]. It was constructed for mineral friction. Later on hardness measurements were done by applying a dead weight on a surface and then observe the residual imprint (Vickers [46] Brinell). In this case only the residual plasticity can be measured. In order to have a better understanding, more recent instruments record the load and depth during indentation. Then, the elastic material properties are determined through the Hertz equation [47]. The Equation IV-12 displays the Hertz equation in the case of a perfectly smooth sphere-plan elastic contact with $h_c(t)$ the contact depth F the applied load, R the tip radius and E^* the reduced modulus as defined in Equation IV-13. In this second equation E_1 and E_2 are the Young's moduli, ν_1 and ν_2 the Poisson's ratio, of both materials in contact. In the case of a material 1 being glass and material 2 a polymer ($E_1 >> E_2$), the second part of equation is valid.

Hertz Equation for a rigid sphere-plan contact	$h_c^{\frac{3}{2}} = \frac{3}{4} \times \frac{F}{\sqrt{R}} \times \frac{1}{E^*}$	Equation IV-12
reduced modulus	$\frac{1}{E^*} = \frac{1-\nu_1^2}{E_1} + \frac{1-\nu_2^2}{E_2}$ $if\ E_1 \gg E_2\ \ then\ \ \frac{1}{E^*} \approx \frac{1-\nu_2^2}{E_2}$	Equation IV-13

Lee and Radok introduced a viscoelastic material [48] in Hertz equation, thus giving linear viscoelasticity indentation equation. There is no plasticity in this model; it supposes a purely viscoelastic material.

Tabor defined in 1970 the average strain in the case of a spherical indentation on polymer [49].

Tabor strain	$\langle \varepsilon \rangle = k \times \frac{a_c}{R}$	Equation IV-14

In Equation IV-14 the ε is the deformation, a_c the contact radius, k a coefficient close to 0.2. More recently it was confirmed by finite element modeling [50].

IV.4.1.2 Deformation shape below the indenter

Figure IV-4 a) presents the stress distribution of uniform and a Hertz pressure acting on a spherical area of radius a (in this thesis this value is generally called a_c). On the lower part, the stress distributions below the contacts are observed. Figure IV-4 b) shows a specific case: the Von Mises stress in the bulk below a rigid sphere–soft plane contact. The image was produced by MSC Marc. In both case, we can observe that the stress varies with the depth and the distance toward the contact center. Thus the relation stress-strain is not the same in the whole material and then the strain levels are different depending on the position.

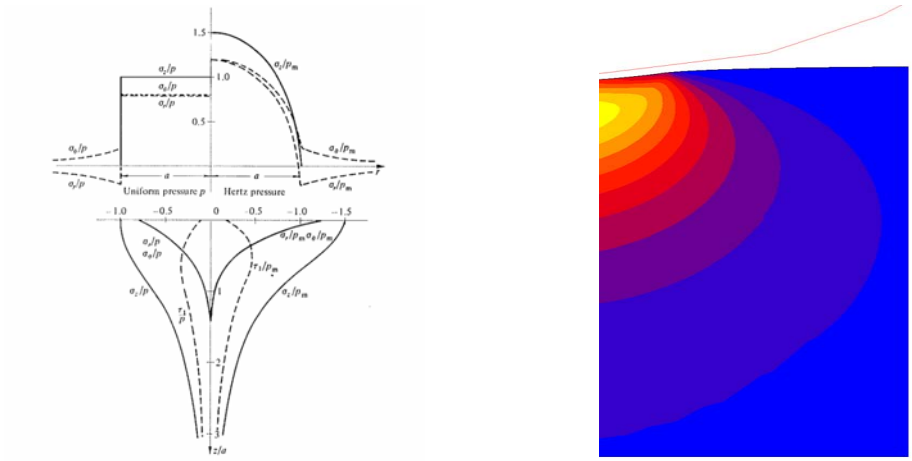

a) b)

Figure IV-4 a) Stress distributions at the surface and along the axis of symmetry caused by (left) uniform pressure and (right) Hertz pressure acting on a circular area radius a [51] b) Von Mises Stress in spherical indentation simulated with MSC Marc

IV.4.1.3 Load-depth curves

Oliver & Pharr developed an analysis of the load-depth curves unloading. The unloading is supposed to be elastic, then the Young's modulus and the material hardness can be determined by indentation [52, 53]. But for polymers [54] and bones [55] the Oliver & Pharr model is not accurate. Indeed, these materials present viscous properties (not taken into account in the model) and the analysis results are test dependent ("nose-problem") [56, 57]. Figure IV-5 a) shows a zoom of load-depth curves [57]. The differences between the curves are the unloading speed. The slower curves led to the more important nose. This apparition of polymer viscoelasticity induces change in the calculated rheological properties. Thus, Beyaoui et al. measured the elastic modulus of a PMMA as a function of the nano-indentation holding time (Figure IV-5 b)) (No nose is observed in their indentation). They claim to obtain a stable value after 100 s of holding time. Nonetheless the Young's modulus and other mechanical rheological parameters are still experiment dependent.

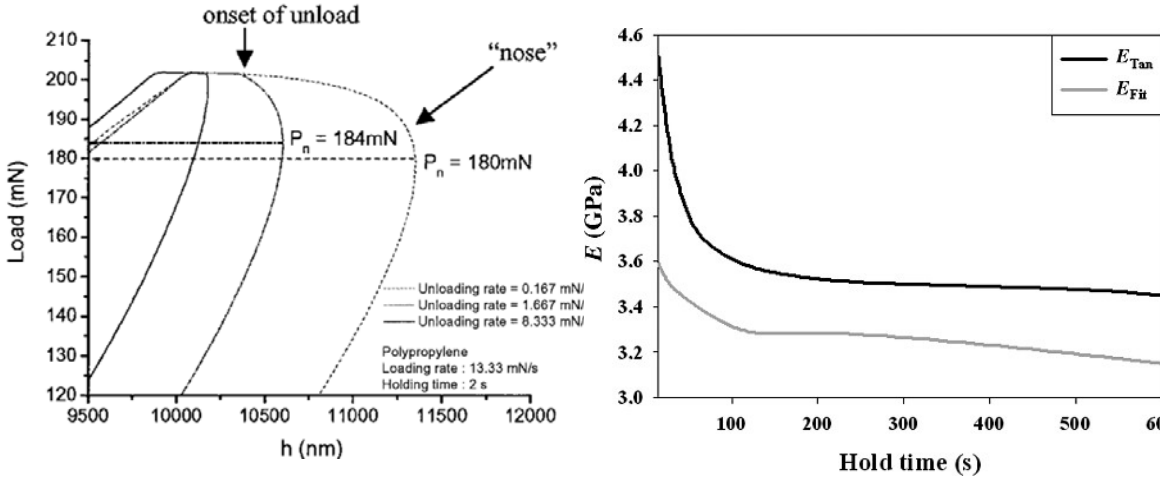

a) b)

Figure IV-5 a) Load versus displacement curves of PP at different unloading rates. All three experiments had the same loading rate to the same peak load and the same holding time before unload [57] b) Elastic modulus as a function of hold time (PMMA $\dot{L}/L$ = 0.05 s-1). [58]

Furthermore, the penetration depth is the combination of the deflection, more important in case of polymers than for metals, and contact depth. Deflection is mainly elastic, whereas contact penetration is a combination of elastic viscoelastic and plastic properties. Therefore several models appeared to estimate the contact depth, knowing the total penetration depth [59, 60].

IV.4.1.4 Indentation master curves

Sakaue et al. used a Berkovich and a conical indenter [61]. They measured the indentation depth and the residual imprint depth (by AFM) at different temperature. Thus they could calculate the viscoelastic indentation depth and then the indentation creep compliance which they compared to tensile creep compliance observing a good agreement (Figure IV-6 a)).

Quadrini et al. made indentation creep compliance master curves with a macro flat punch indenter [62]. They compared their data with DMA and tensile creep measurements again obtaining a good agreement. Figure IV-6 b) presents indentation creep compliance master curves extracted from their publication. In the presented graphic, they superpose their results to obtain a standard master curve at different indentation loads.

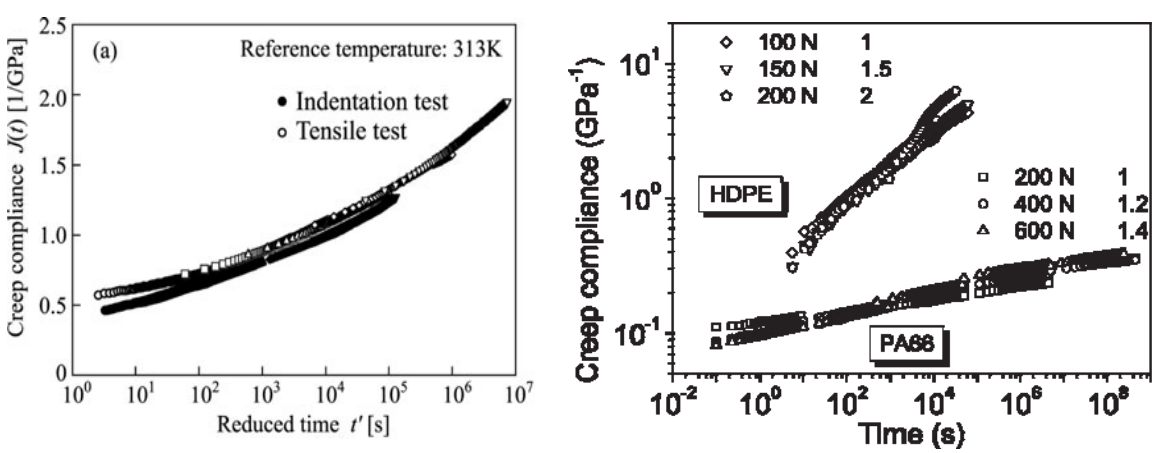

a) b)

Figure IV-6 a) Viscoelastic characteristics evaluated by indentation test. Master curve of creep compliance at a reference temperature of 313 K [61] b) Superposition of the master curves of indentation creep compliances [62]

IV.4.1.5 Indentation recovery

As we observed previously, the indentation recovery quantification is a key toward the determination of elastic, viscoelastic and plastic proportion in contact. In literature the recovery is generally observed by inline AFM or profilometry [61, 63, 64]. In Figure IV-7 a) the recovery is followed over several hours, there is no evolution of the imprint after 24 hours. Thus they consider the material as plastically deformed [61]. Figure IV-7 b) presents a cross section extracted of an AFM image [63]. To observe a significant recovery, the authors choose to increase the temperature of the material. The difficulty is the delay between end of contact and the end of imaging process. Unfortunately the major changes or evolutions of the residual imprint, related to viscoelastic behavior, are observed during this corresponding time [65]. Therefore to observe an evolution of the recovery, very long time or a temperature increase are needed.

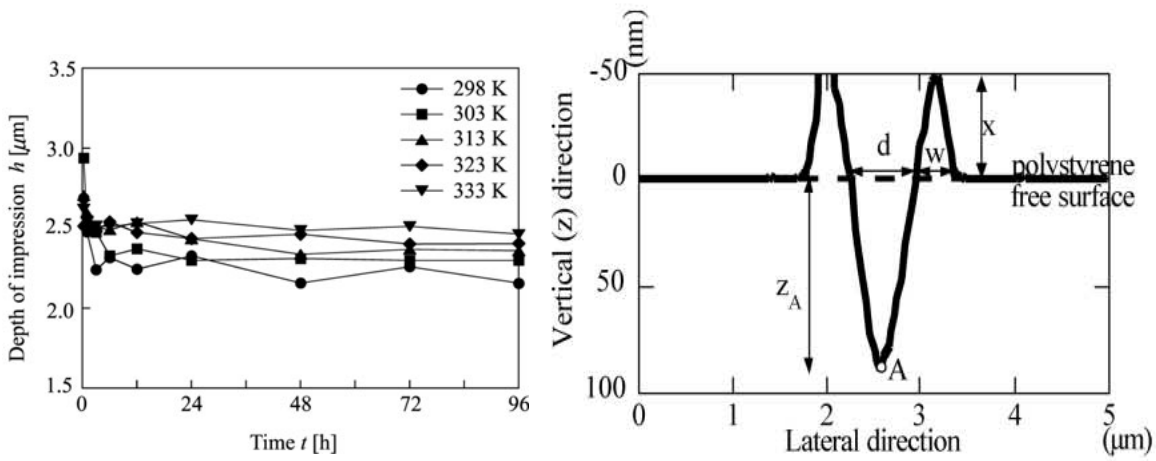

a) b)

Figure IV-7 a) Time variations of maximum depth of impression [61] b) AFM cross section of a shallow indent right after the indentation and before any thermal treatment above T_g (t = 0) [63]

IV.4.1.6 Recent improvement in indentation

On the contrary, Chatel et al. observed the imprint recovery by an interferometry method [66, 67]. This method enabled them to observe the short time viscoelasticity (0.5s). More details on this technique can be found in chapter materials and methods V.4.2.3.1. Figure IV-8 a) presents the Tabor normalized deformation versus time for three different experiments. They also presented the results from the Lee and Radok model [48]. Thus, the observed phenomena are not linearly viscoelastic. Then they observe the recovery (Figure IV-8 b)) versus recovery time. The full recovery is not observed for the two higher initial strains. Thus they can conclude on the presence of plasticity or not inside the material.

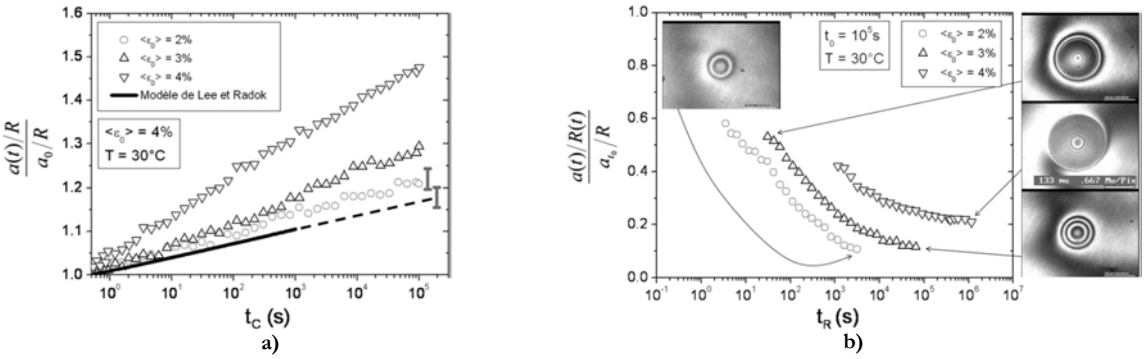

Figure IV-8) Creep phase-evolution of the representative strain as a function of the creep time for different initial ratios $<\varepsilon_0>$- comparison of experimental results with the viscoelastic contact model of Lee and Radok (R = 400 µm, T=30°C, $<\varepsilon_0>$ fixed at t_C = 0.5 s [66] b) Recovery phase- evolution of the representative strain as a function of the recovery time for different initial mean contact strains (T=30°C, $t_0=10^5$ s, $<\varepsilon_0>$ fixed at t_C during the creep phase [66]

IV.4.2. Scratch

IV.4.2.1 Scratching method

As the second contact technique, scratch is far more complex than indentation. For a spherical indenter, the difficulties are: deflection, average strain, strain gradient, stress and strain gradient which are time and temperature dependent in all experiments. Indeed the moving tip induces an important additional strain rate and an asymmetry in the imprint. But, this corresponds to an important way of polymer damaging [7, 68, 69].

In particular two types of scratch are differentiated: mar and scratches. The almost invisible scratch corresponds to mar, when they are present in great quantities they become visible, for example the keys or nail traces on cars doors are generally caused by marring. The others are scratches that form large grooves or debris [70].

In practice there are three technics used to scratch polymer: either a constantly improving scratch load and a constant scratch speed [71-74] or a constantly improving scratch speed and a constant load or a constant scratch speed and load [75-78].

IV.4.2.2 Microvisioscratch master curves

Gauthier et al. presented in 2000 a new apparatus that enabled them to observe directly the contact and the groove during and just after the scratch [75]. Thus they could determine the shear stress at yield and the mean strain rate near the moving tip. Figure IV-9 shows the Scissions shear stress at the interface versus the strain rate and the master curves constructed with these data. Two different slopes are observed in this graphic. Therefore, the scission shear stress is a temperature activated process like other mechanical properties.

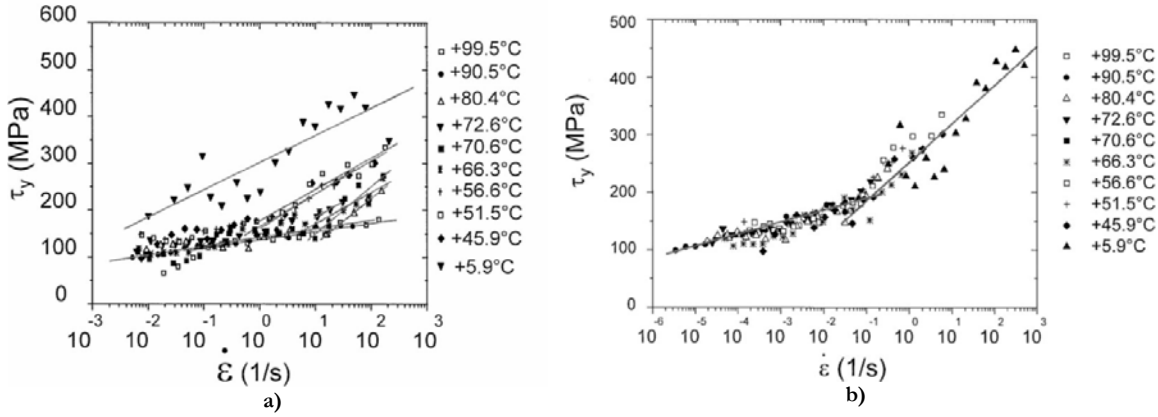

Figure IV-9 a) Scission shear stress at the interface versus strain rate b) Mastercurves for the scission shear stress versus strain rate at 20°C. There are two regimses of scission stres, below and above 10^{-1} s^{-1} [75]

IV.4.2.3 Recovery observation generality

The recovery observation is not always performed but several technics are used. The recovery is very often observed by the application of a post scan at a low load. Difficulty is that the second passage of the tip does not take into account the shape of the groove [78]. In this case only the recovery depth is observed.

Another possibility is to move the imprint quickly under an Atomic Force Microscope (AFM) [7, 68] or a profilometer [72]. Figure IV-10 a) presents a classical profilometry observation. The depth and the shape of the groove are clearly visible and analyzable. Moreover the volume of the pile up can also be estimated. Figure IV-10 b) shows the observed recovery depth versus time by an AFM. Then, the sample is heated to observe a progressive recovery over 2 years (estimated time thank to time-temperature equivalence). In the case where an inline apparatus is used, the time between the end of scratch and the end of imaging process is at least 5 minutes. When the machines are not bounded, the time is even more important. Moreover a change of experimental condition (temperature, humidity) by moving the sample is observed. These images enable nonetheless the determination of the profile depth and shape.

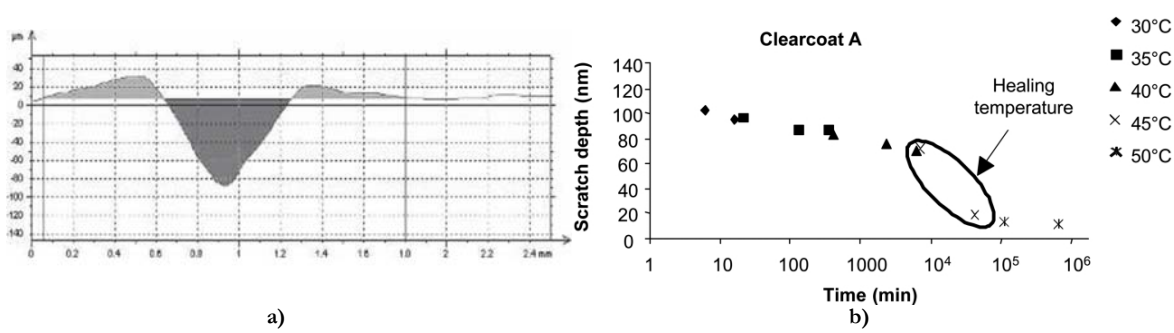

Figure IV-10 a) A profile of a scratch trace on a PTFE surface for the applied load of 15.0 N. The profile is perpendicular to the side and goes through the center of the groove [72]. b) Time-temperature superposition curve of scratch depth vs. time for clearcoat A. The reference temperature is 30°C. A first plateau is followed by a decrease of the scratch depth and then by a second plateau. The decrease of the scratch depth occurs at "healing temperature" [68].

The fracture damage is often observed by Scanning Electron Microscopy (SEM) [73, 74, 78, 79]. Typical observations are presented in Figure IV-11 a) and b). Indeed these images show the fracture mechanisms in the near surfaces region.

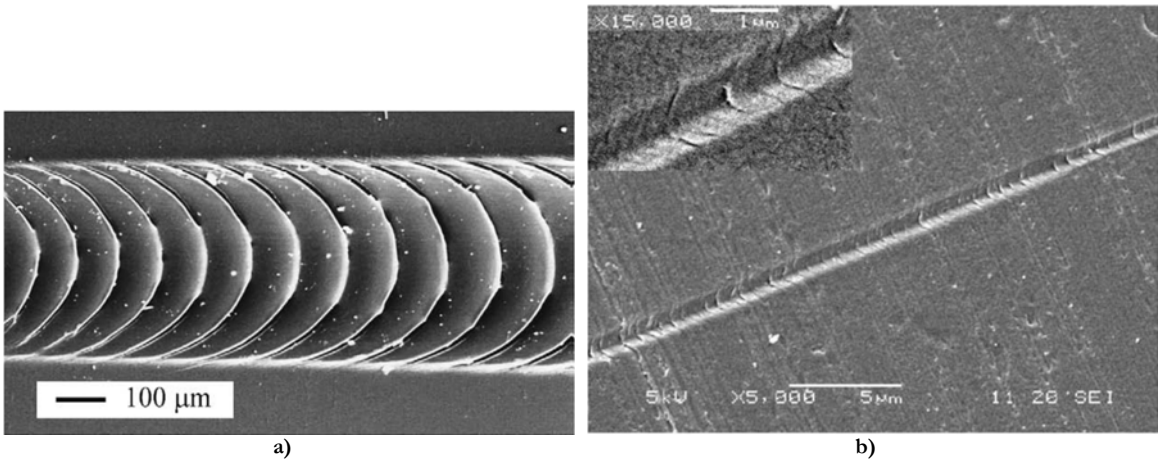

a) b)

Figure IV-11 a) SEM of fish-scale damage for thermoplastic olefins [74] b) SEM micrograph of scratch properties of epoxies with different crosslink densities, polished with 3 µm particle size diamond paste, being scratched by indenter with radius = 80 nm showing the scratch morphologies. The inset shows the scratch in larger magnification [79].

IV.4.2.4 Recent scratch recovery observation

More recently, Thibaud Chatel presented in his PhD thesis, pictures of the scratch recovery [65]. Actually, Figure IV-12, extracted from his thesis, shows a summary of the influences of different parameters on the scratch recovery experiment with a spherical tip. In this figure, t_R is the recovery time, µ the friction coefficient, a/R the Tabor deformation and V the tip speed. The higher the scratching deformation or the friction coefficients are, the larger the recovery grooves. The quicker the tip speed is the smaller the recovery groove.

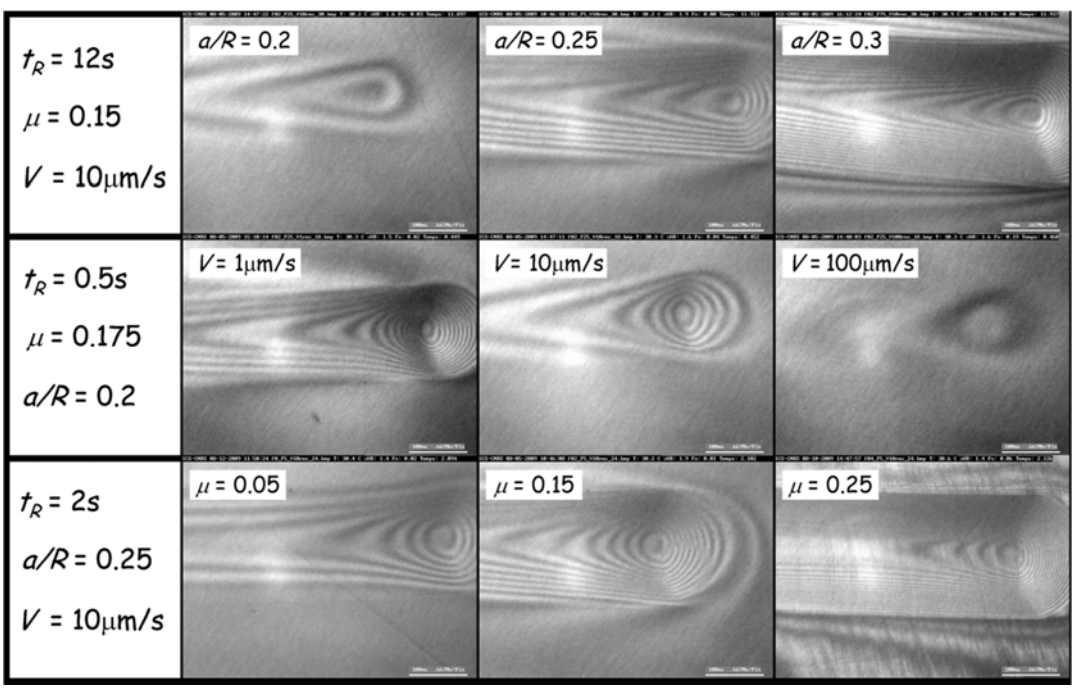

Figure IV-12 Experimental picture - Visualization of residual groove for different experimental condition [65]

IV.4.3. Conclusion

The indentation principle, despite its commonness, is still not fully understood. Indeed, for a spherical indenter the stress gradient below the indenter is complex. Then, polymers are neither elastic nor elasto-plastic but viscoelastic and viscoplastic. Therefore, the load-depth curve, which analysis has become quite common, is still a subject of discussion. Moreover the long time dependency of polymer implies an increase in difficulty. Nonetheless, the time-temperature master curves allow the community to predict the long time material behavior. Another way of understanding the material behaviors is to observe the recovery after indentation. Generally it is done by either AFM or profilometry but the observation is often done long after the end of test. More recently, Chatel et al. presented new methods to follow the indentation deformation and recovery.

On the other hand, the scratch experiment enables to have a damaging close to the reality but nonetheless controlled. Some master curves of scratch properties were done by Gauthier et al. Besides, the recovery can be observed by AFM or profilometry with the same drawbacks as for indentation. Furthermore, the SEM permits to observe scratch induced fracture.

IV.5. ANALYTICAL MODELING

The objective of this chapter part is to present different model that are used to simulate and evaluate the properties of polymeric material in bulk and indentation.

IV.5.1. Simple rheological model

IV.5.1.1 Maxwell model

The Maxwell model is defined by a spring and a dashpot as displayed on Figure IV-13.

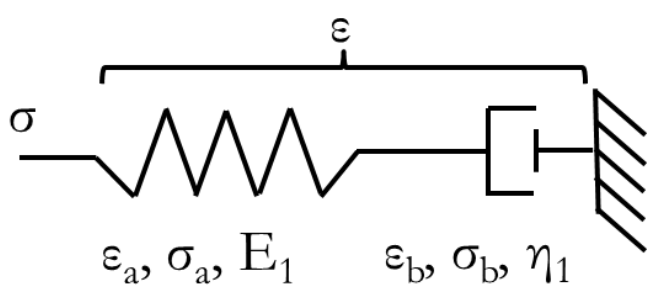

Figure IV-13 Rheological Maxwell model

Where ε_a, ε_b and σ_a, σ_b are respectively the strain and stress in the spring and in the dashpot. The overall strain and stress are ε and σ. The stress-strain relation for a spring and a dashpot are respectively displayed in

Stress-strain spring relation	$\sigma_a = E_1 \times \varepsilon_a$	Equation IV-15

Stress-strain dashpot relation	$\sigma_b = \eta_1 \times \frac{d\varepsilon_b}{dt}$	Equation IV-16

As the spring and dashpot are in series, one can add the strains to obtain the total strain and the stress is equal.

	$\sigma_a = \sigma_b = \sigma$	Equation IV-17
	$\varepsilon = \varepsilon_a + \varepsilon_b$	Equation IV-18

Using the derivative of Equation IV-15 and Equation IV-16 in Equation IV-18 one obtain

	$\frac{d\varepsilon}{dt} = \frac{1}{E_1} \times \frac{d\sigma}{dt} + \frac{\sigma}{\eta_1}$	Equation IV-19

This equation can be simplified in a stress relaxation case. Where the strain is constant thus the derivative of the strain is null. Thus

stress equation for a Maxwell model in relaxation	$\sigma = \sigma_0 \times \exp(-\frac{E_1}{\eta_1} t)$	Equation IV-20

Thus one can define a characteristic time τ_1 equal to η_1/E_1. The default of this model is that the relaxation decrease can generally not be represented by only one term. Furthermore a full recovery can never be observed.

IV.5.1.2 Kelvin-Voigt model

The Kelvin-Voigt model is constituted by a spring and a dashpot as shown in Figure IV-14.

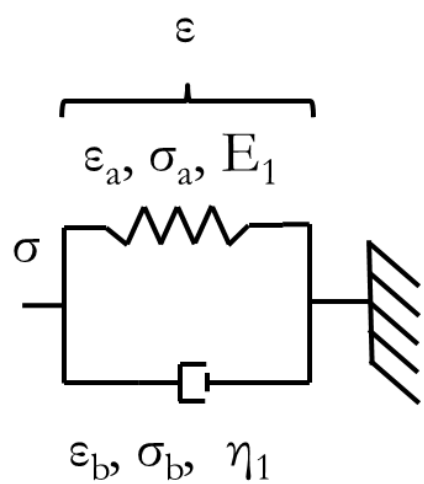

Figure IV-14 Rheological Kelvin Voigt Model

Where, as previously, ε_a, ε_b and σ_a, σ_b are respectively the strain and stress in the spring and in the dashpot. The overall values are given by ε and σ. The Equation IV-15 and Equation IV-16 are still valid but one has to modify the Equation IV-17 and Equation IV-18 into Equation IV-21 Equation IV-22

	$\sigma = \sigma_a + \sigma_b$	Equation IV-21

	$\varepsilon = \varepsilon_a = \varepsilon_b$	Equation IV-22

And thus

	$\sigma = E_1 \times \varepsilon + \eta_1 \times \frac{d\varepsilon}{dt}$	Equation IV-23

In the case of creep under constant stress σ_0, the strain can be easily expressed as:

	$\varepsilon = \frac{\sigma_0}{E_1} \times (1 - \exp\left(-\frac{E_1}{\eta_1} \times t\right))$	Equation IV-24

As before, the strain cannot be precisely defined by only one time term. On the contrary to the Maxwell model a full recovery can always be observed, which again is not realistic.

IV.5.2. Generalized model

As the description with both simple model demonstrated one time constant is not enough to describe the viscoelastic solid. Therefore two different ways of adding time constant are known in literature: either the Generalized Maxwell model as presented in Figure IV-15 a) or the generalized Voigt model as in Figure IV-15 b).

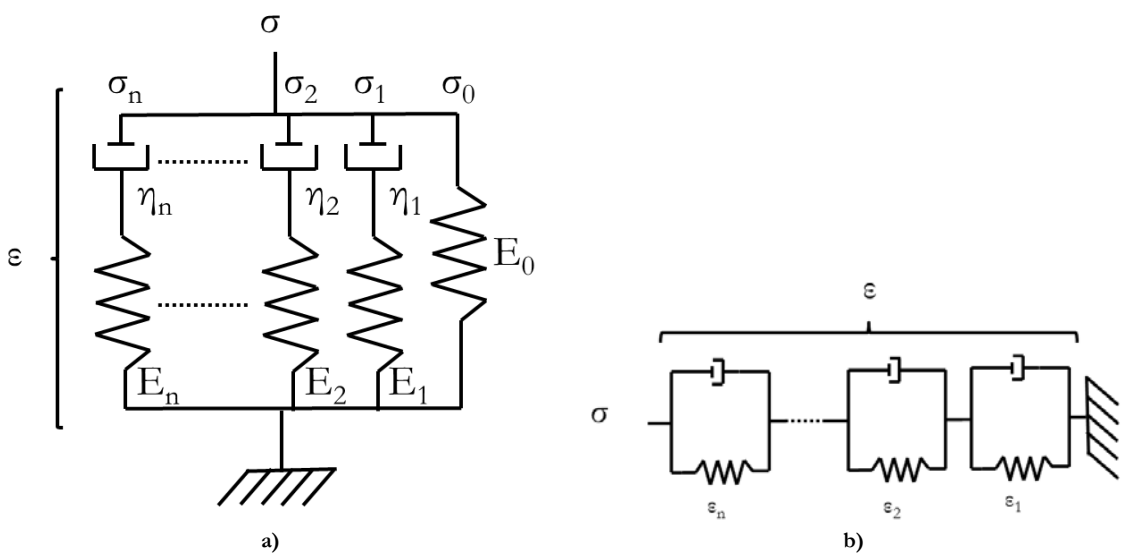

Figure IV-15 a) Generalized Maxwell model b) generalized Kelvin-Voigt model

The generalized Maxwell model answers to the following equation:

	$\varepsilon = \varepsilon_a = \varepsilon_b = \varepsilon_n$	Equation IV-25
	$\sigma = \sigma_1 + \sigma_2 + \cdots + \sigma_n$	Equation IV-26

Thus, in the particular case of a stress relaxation, by injecting Equation IV-20 in Equation IV-26, one obtains

	$\sigma(t) = \sigma_0 + \sigma_1 \exp\left(-\frac{E_1}{\eta_1} \times t\right) + \sigma_2 \exp\left(-\frac{E_2}{\eta_2} \times t\right) + \cdots + \sigma_n \exp\left(-\frac{E_n}{\eta_n} \times t\right)$	Equation IV-27

By finally dividing by ε:

Maxwell relaxation modulus spectra	$E(t) = E_0 + \sum_{i=1}^{n} E_i \times \exp\left(-\frac{t}{\tau_i}\right) with\ \tau_i = \frac{\eta_i}{E_i}$	Equation IV-28

The relaxation spectra can then be written under the form of a sum or an integral. In Equation IV-29 H(τ) is the relaxation time spectrum.

Relaxation modulus	$E(t) = E_0 + \int_{-\infty}^{\infty} H(\tau) \times \exp\left(-\frac{t}{\tau}\right) d(\ln(\tau))$	Equation IV-29

The analogous method leads with the Kelvin-Voigt element to the creep compliance, see Equation IV-30 where L(τ) is the retardation time spectrum.

Creep compliance	$J(t) = J_0 + \int_{-\infty}^{\infty} L(\tau) \left[1 - \exp\left(-\frac{t}{\tau}\right)\right] d(\ln(\tau))$	Equation IV-30

IV.5.3. Indentation

Some authors presented analytical equations for the indentation creep of polymers. In particular Fischer-Cripps summarized in a simple phenomenological approach the analytical equation for the spherical indentation depth with a Maxwell representation of creep, a three element Voigt model and a four element Kelvin Voigt model [54]:

Maxwell model	$h^{\frac{3}{2}}(t) = \frac{3}{4}\frac{F}{\sqrt{R}}\left[\frac{1}{E_1^*} + \frac{1}{\eta_1}\right]$	Equation IV-31
Three element Voigt model	$h^{\frac{3}{2}}(t) = \frac{3}{4}\frac{F}{\sqrt{R}}\left[\frac{1}{E_1^*} + \frac{1}{E_2^*}(1 - \exp\left(-\frac{E_2}{\eta_2}t\right))\right]$	Equation IV-32
four element Maxwell-Voigt model	$h^{\frac{3}{2}}(t) = \frac{3}{4}\frac{F}{\sqrt{R}}\left[\frac{1}{E_1^*} + \frac{1}{\eta_1}t + \frac{1}{E_2^*}(1 - \exp\left(-\frac{E_2}{\eta_2}t\right))\right]$	Equation IV-33

In particular Oyen [80] or Cheng et al. [60] compare with success their experimental results to predictions from three or four elements viscoelastic model. Figure IV-16 presents the comparison between experimental indentation depth and analytical models depth versus time as proposed by Fischer-Cripps [54] and Oyen [80]. In practice the creep holding times are generally shorter than 100 s. On the other hand Chatel et al. [81] in accordance with Ward [21] demonstrated that a good representation of the viscoelastic behavior requires a Maxwell or a Voigt element per time decade. That is probably why Cheng, Fischer-Cripps and Oyen obtain good predictions for short time with three or four elements model. Longer indentation creep experiments are not often available, and the analytical equation for a more complex model is not known.

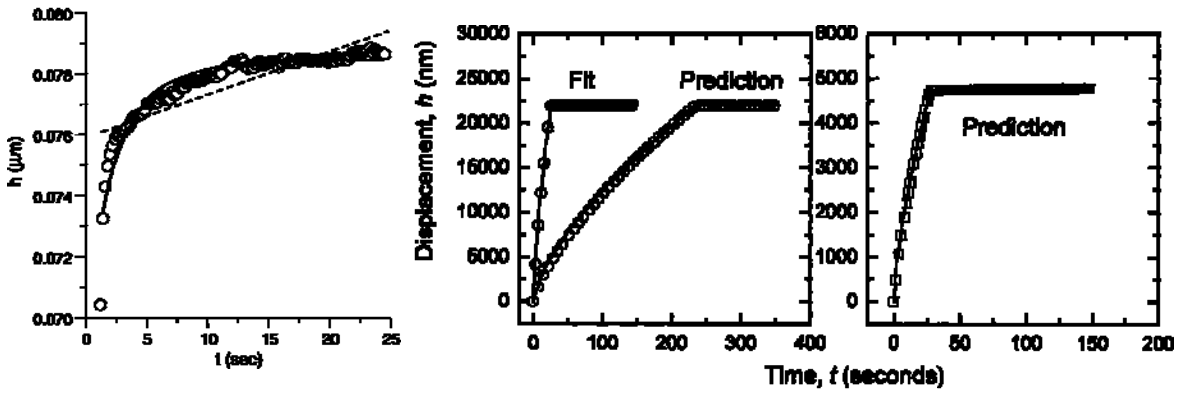

a) b)

Figure IV-16 a) Creep response for hold period of 20 s at 10mN on a 1 µm Al film on silicon with a spherical indenter 20 µm nominal radius (36 µm actual radius). Data points show experimental results. The solid line shows the fitted response according to Equation IV-32 (three-element Voigt model). The dotted line shows the response according to Equation IV-31 (two-element Maxwell model). [54] b) Urethane indentation ramp-and-hold creep experimental data (open symbols) for three different loading protocols: P_{max} = 10 mN, t_R = 20 and 200 s; P_{max} = 1 mN, t_R = 20 s. The creep portion of the 10 mN, 20 s data were fit to obtain creep function parameters. Predictions (solid lines) were made for the full ramp-hold responses for each load–rise time combination using the parameters obtained in the single creep fit and the two-time constant relaxation function [80].

IV.6. FINITE ELEMENT MODELING

As the analytical solution is not available, a numerical solution is searched. The principle is that the mechanical response of the material is known in a simple case (for example uni axial). Then a more complex problem is divided in a large number of smaller problems which will be solved numerically. This part will present some generalities about the model then about certain material law that are used.

IV.6.1. Model

The higher the discretization of the model the more precise the response is. But all the sites have not the same importance. In particular the contact area is more discretized than the rest. Furthermore, when it exists, the symmetry enables to reduce the size of the model and thus the calculation time. In spherical indentation, 2D models are generally used to simulate indentation [67, 82, 83] (Figure IV-17 a)). A 3D model is used for example when one wants to determine the influence of the tip defects [84].

Sometimes the apparition region of contact creep is further refined [34] (Figure IV-17b)). It enables a better stability of the calculi and smaller differences between two integration steps.

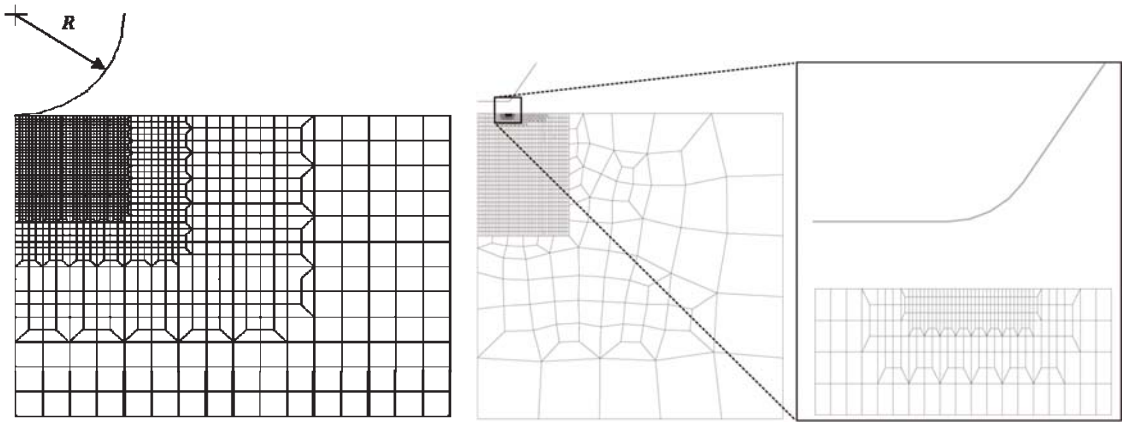

a) b)

Figure IV-17 a) Example axisymmetric (rigid) hemisphere and finite element mesh [82]. b) Finite element mesh, with mesh refinement [34]

IV.6.2. Constitutive law

Different laws are used to represent the mechanical properties of a polymer. They are presented by increasing complexity.

IV.6.2.1 G'Sell Jonas law

The G'Sell Jonas material law is a very commonly used material law. G'Sell and Jonas proposed in 1979 to evaluate a polymeric material by an elastic part and a plastic part. Equation IV-34 presents the plasticity threshold [85].

G'sell Jonas plasticity law [85]	$\sigma_{\text{true}}(\varepsilon_{\text{true}}, \dot{\varepsilon}_{\text{true}}, T) = K.e^{\frac{a}{T}}.(1 - e^{-\omega\varepsilon_{\text{true}}}).e^{h_g\,\varepsilon_{\text{true}}^2}.\dot{\varepsilon}_{\text{true}}^{m}$	Equation IV-34

Where σ_{true} is the true stress, $\varepsilon_{\text{true}}$ the true deformation, $\dot{\varepsilon}_{\text{true}}$ the true strain rate and T the temperature. K, a, ω and m are material dependent constants respectively called the consistency, thermal coefficient, viscoelasticity parameter and the strain sensitivity. Bucaille et al. presented a remarkable development of this law. In particular, he proposed to determine the different coefficient by nano-indentation [83, 86]. Figure IV-18 a) and b) present load-depth curve during the loading phase for experiments and simulations tests [83]. Bucaille and Felder compare the importance of the tip defect on the simulation precision (ϱ is the Berkovich defect tip radius). The comparison of the experimental result and the simulation with a perfect Berkovich indenter (ϱ = 0 nm) led to an inaccurate prediction of the simulation (Figure IV-18 a)). But, if the tip defect is taken into account (ϱ = 455 nm), the simulation produce a very good prediction of the indentation (Figure IV-18 b)). Thus Bucaille et al. propose a well identified law, which has become a reference in indentation simulation [50, 61, 70, 87, 88].

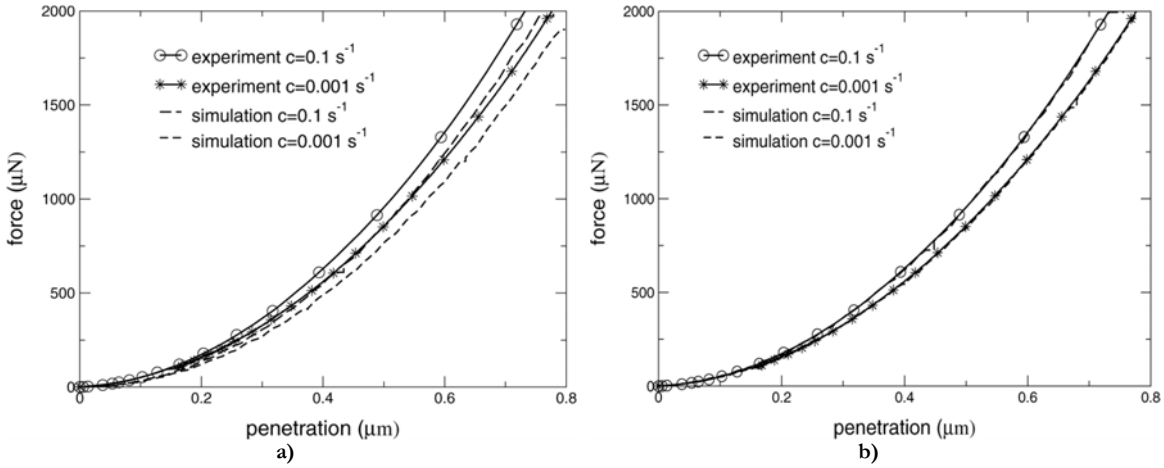

Figure IV-18 Force-penetration curves during loading for a polycarbonate. Comparison between the experimental curves (Berkovich indenter) and the numerical curves (μ = 0, ϱ = 0 nm and ϱ = 455 nm). For more legibility the curves for the intermediate loading rate (c = 0.01 s-1) are not plotted. (a) ϱ = 0 nm. (b) ϱ = 455 nm. [83]

IV.6.2.2 Norton's law

A standardly used constitutive law for the metal plasticity is the Norton's law as defined by Lemaitre and Chaboche [89].

Norton's law	$\dot{\varepsilon}_{vp} = \left(\frac{K \times \varepsilon_{vp}^{\frac{1}{M}}}{\sigma}\right)^{N}$ $\sigma = K \times \varepsilon_{p}^{1/M} \times \dot{\varepsilon}_{p}^{1/N}$	Equation IV-35

This law supposes like the precedent that there is no viscoelasticity in the material.

IV.6.2.3 Generalized Maxwell

The generalized Maxwell model material is very widely used to represent a viscoelastic material [34, 67, 81, 90]. It is generally introduced in the numerical code in the form of Equation IV-28. Nonetheless other forms exist; in particular equations calculated from DMTA experiments can be used (much more complex). The important advantage of this material law is the possibility to add one or more spring-dashpot pair to increase the amount of parameters and to refine the model quality.

IV.6.2.4 Master curves

More recently Van Breemen et al. identified a generalized Maxwell material on a master curve of polycarbonate [34]. They used this new law on flat punch indentation and notch impact test Figure IV-19 a) and b) respectively. A very good correlation between the experimental and numerical results is observed as long as no fracture was experimentally observed (Figure IV-19 b)).

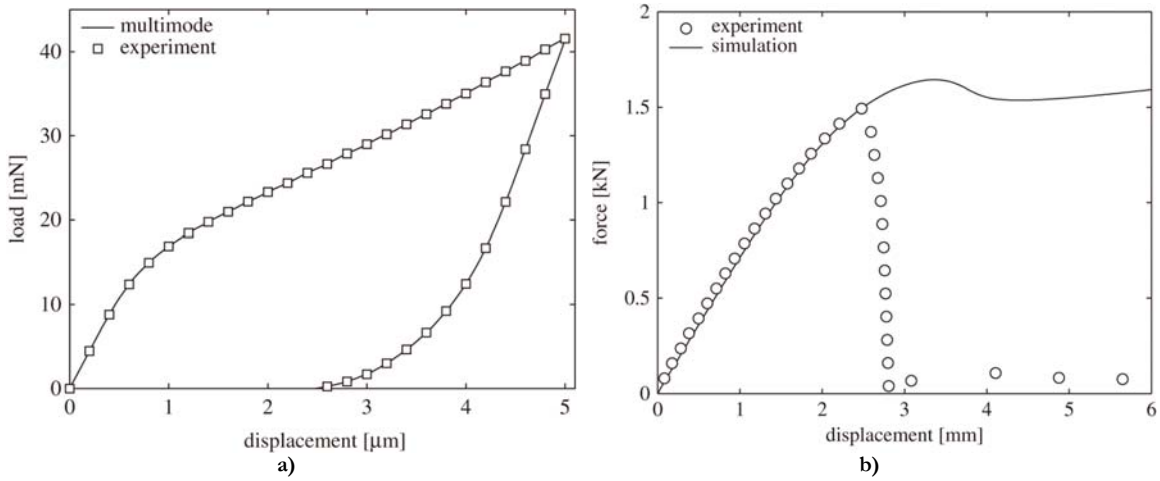

Figure IV-19 a) Flat-tip indentation symbols are experiments ; lines are result of modeling using the multi-mode EGP-model b) Load versus displacement curve for a notched tensile bar; symbols are experiments; line is computational result without failure criterion.

IV.6.2.5 Strain rate dependent plasticity

Since several years, the same team have introduced in their finite element modeling code strain rate dependent viscoplastic material [91, 92]. Moreover the stress-strain material response is not monotonous for the studied domain. Indeed after the beginning of the plasticity the stress versus strain decreases and increases again. Figure IV-20 a) and b) present true stress versus true strain in uniaxial compression for simulation and experimental tests. The simulation are conducted with the above mentioned material model law. A good prediction of the plastic behavior is done.

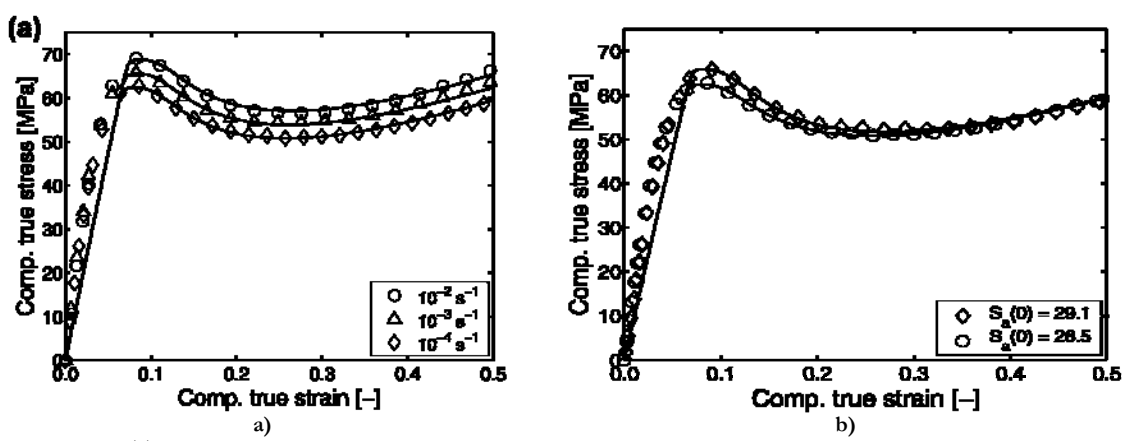

Figure IV-20 True stress vs true strain in uniaxial compression, model prediction (solid lines) compared to experimental results (symbols) a) for different strain rates b) for different initial states at a strain rate of 10-4 s^{-1}. [91]

IV.7. CONCLUSION

Polymers are actually present in our everyday life. There mechanical properties were and still are subject of numerous researches and part of innovative materials. But, their long time mechanical behavior is still poorly understood.

In particular the indentation behavior and more generally contact behavior are not well understood. Indeed, the indentation depth is a combination of elastic, viscoelastic and plastic properties. The deconvolution of the signal is not done; either the material is supposed elasto-

plastic or viscoelastic. To really differentiate between viscoelastically and plastically deformed material, the recovery must be monitored. But, literature showed generally a single observation 15 minutes after the end of solicitation. Moreover the imaging process was so slow that the material was still evolving when the first images were taken. Thus the creep could not be well understood. Thereafter the contact simulations were done with incomplete informations. Then the property gradient below the indenter is not well simulated and the indentation recovery is not understood.

Furthermore, the scratch recovery is again very poorly understood. Generally, the recovery is observed long after the scratch and only the irreversible or very slowly reversible behavior is examined.

Moreover very few correlations are done between the observed indentation properties and the bulk mechanical properties. Then we are not able to compare the surface and bulk mechanical properties, thus making complex the differentiation between surface and material effect.

As we remarked a lack in the state of the art, we will try to: (i) deconvoluate the different material contribution, (ii) analyze and understand the indentation and scratch recovery, (iii) introduce self-consistent material law in the simulations methods and (iv) correlate surface and bulk mechanical properties.

IV.8. BIBLIOGRAPHY

[1] E. Simon, Ueber den flüssigen Storax (Styrax liquidus), Annalen der Pharmacie, 31 (1839) 265-277.

[2] D. Braun, Origins and Development of Initiation of Free Radical Polymerization Processes, International Journal of Polymer Science, 2009 (2009).

[3] H. Staudinger, H.W. Kohlschütter, Über hochpolymere Verbindungen, 55. Mitteil.: Über Poly-acrylsäure, Berichte der deutschen chemischen Gesellschaft (A and B Series), 64 (1931) 2091-2098.

[4] J.L. Bruneni, More Than Meets The Eye, in, PPG industries, Inc., Pittsburgh, 1997.

[5] A. Mkaddem, A. Ben Soussia, M. El Mansori, Wear resistance of CVD and PVD multilayer coatings when dry cutting fiber reinforced polymers (FRP), Wear, 302 (2013) 946-954.

[6] A.B. Soussia, A. Mkaddem, M. El Mansori, Effect of coating type on dry cutting of glass/epoxy composite, Surface and Coatings Technology, 215 (2013) 413-420.

[7] P. Bertrand-Lambotte, J.L. Loubet, C. Verpy, S. Pavan, Understanding of automotive clearcoats scratch resistance, Thin Solid Films, 420-421 (2002) 281-286.

[8] A.C. Schüssele, F. Nübling, Y. Thomann, O. Carstensen, G. Bauer, T. Speck, R. Mülhaupt, Self-healing rubbers based on NBR blends with hyperbranched polyethylenimines, Macromolecular Materials and Engineering, 297 (2012) 411-419.

[9] L. Biniek, N. Leclerc, T. Heiser, R. Bechara, M. Brinkmann, Large scale alignment and charge transport anisotropy of pBTTT films oriented by high temperature rubbing, Macromolecules, 46 (2013) 4014-4023.

[10] C. Silvestre, D. Duraccio, S. Cimmino, Food packaging based on polymer nanomaterials, Progress in Polymer Science (Oxford), 36 (2011) 1766-1782.

[11] G.M.E. Pozza, H. Harris, M.J. Barthel, J. Vitz, U.S. Schubert, P.J. Lutz, Macromonomers as well-defined building blocks in the synthesis of hybrid octafunctional star-shaped poly(ethylene oxide)s, Macromolecular Chemistry and Physics, 213 (2012) 2181-2191.

[12] M. Vielhauer, P.J. Lutz, G. Reiter, R. Mülhaupt, Linear and star-shaped POSS hybrid materials containing crystalline isotactic polystyrene chains, Journal of Polymer Science, Part A: Polymer Chemistry, 51 (2013) 947-953.

[13] P.A. Raj, A.R. Dentino, Denture polymers with antimicrobial properties: A review of the development and current status of anionic poly(methyl methacrylate) polymers, Future Medicinal Chemistry, 5 (2013) 1635-1645.

[14] P.L. Lai, L.H. Chen, W.J. Chen, I.M. Chu, Chemical and physical properties of bone cement for vertebroplasty, Biomedical Journal, 36 (2013) 162-167.

[15] K.M. JAE, DECO PRINT FILM AND TOUCH PANEL, in, 2013.

[16] R.Q. Frazer, R.T. Byron, P.B. Osborne, K.P. West, PMMA: An essential material in medicine and dentistry, Journal of Long-Term Effects of Medical Implants, 15 (2005) 629-639.

[17] D.L. Chen, P.F. Yang, Y.S. Lai, A review of three-dimensional viscoelastic models with an application to viscoelasticity characterization using nanoindentation, Microelectronics Reliability, 52 (2012) 541-558.

[18] B. Golaz, S. Tetouani, N. Diomidis, V. Michaud, S. Mischler, Processing and tribology of thermoplastic polyurethane particulate composite materials, Journal of Applied Polymer Science, 125 (2012) 3745-3754.

[19] P.E. Combette, Isabelle Physique des polymères propriété mécaniques, 6 rue de la sorbonne, paris, 2005.

[20] L. Boltzmann, Zur Theorie der elastischen Nachwirkung, Annalen der Physik, 241 (1878) 430-432.

[21] I.M. Ward, Mechanical properties of solid polymers, Bristol, 1979.

[22] H. Leaderman, Textile Materials and the Time Factor: I. Mechanical Behavior of Textile Fibers and Plastics, Textile Research Journal, 11 (1941) 171-193.

[23] J.D. Ferry, Viscoelastic properties of polymers, United States of America, 1980.

[24] J.L. Halary, F. Lauprêtre, L. Monnerie, Mécanique des matériaux polymères, Paris, 2008.

[25] H.-G. Elias, Makromoleküle, wiley-vch, Neustadt, 2001.

[26] M.L. Williams, R.F. Landel, J.D. Ferry, The temperature dependence of relaxation mechanisms in amorphous polymers and other glass-forming liquids, Journal of the American Chemical Society, 77 (1955) 3701-3707.

[27] A.K. Doolittle, Studies in newtonian flow. II. the dependence of the viscosity of liquids on free-space, Journal of Applied Physics, 22 (1951) 1471-1475.

[28] V. Le Houérou, PROPRIETES MECANIQUES DES SURFACES DE POLYMERES, in, Master 2 Matériaux parcours Polymères à l'UdS, 2012.

[29] H. Lu, X. Zhang, W.G. Knauss, Uniaxial, shear, and poisson relaxation and their conversion to bulk relaxation: Studies on poly(methyl methacrylate), Polymer Composites, 18 (1997) 211-222.

[30] T.W. Sirk, K.S. Khare, M. Karim, J.L. Lenhart, J.W. Andzelm, G.B. McKenna, R. Khare, High strain rate mechanical properties of a cross-linked epoxy across the glass transition, Polymer, 54 (2013) 7048-7057.

[31] R.S. Marvin, E.R. Fitzgerald, J.D. Ferry, Measurements of Mechanical Properties of Polyisobutylene at Audiofrequencies by a Twin Transducer, Journal of Applied Physics, 21 (1950) 197-203.

[32] W. Philippoff, Further Dynamic Investigations on Polymers, Journal of Applied Physics, 25 (1954) 1102-1107.

[33] I.L. Hopkins, The Ferry Reduction and the Activation Energy for Viscous Flow, Journal of Applied Physics, 24 (1953) 1300-1304.

[34] L.C.A. Van Breemen, E.T.J. Klompen, L.E. Govaert, H.E.H. Meijer, Extending the EGP constitutive model for polymer glasses to multiple relaxation times, Journal of the Mechanics and Physics of Solids, 59 (2011) 2191-2207.

[35] A. Vananroye, P. Leen, P. van Puyvelde, C. Clasen, TTS in LAOS: Validation of time-temperature superposition under large amplitude oscillatory shear, Rheologica Acta, 50 (2011) 795-807.

[36] P.A. O'Connell, G.B. McKenna, Large deformation response of polycarbonate: Time-temperature, time-aging time, and time-strain superposition, Polymer Engineering and Science, 37 (1997) 1485-1495.

[37] P.A. O'Connell, G.B. McKenna, Arrhenius-type temperature dependence of the segmental relaxation below Tg, Journal of Chemical Physics, 110 (1999) 11054-11060.

[38] J. Kolařík, Tensile creep of thermoplastics: Time-strain superposition of non-iso free-volume data, Journal of Polymer Science, Part B: Polymer Physics, 41 (2003) 736-748.

[39] W.G. Knauss, I.J. Emri, Non-linear viscoelasticity based on free volume consideration, Computers and Structures, 13 (1981) 123-128.

[40] R. Kohlrausch, Ueber das Dellmann'sche Elektrometer, Annalen der Physik, 148 (1847) 353-405.

[41] G. Williams, D.C. Watts, Non-symmetrical dielectric relaxation behaviour arising from a simple empirical decay function, Transactions of the Faraday Society, 66 (1970) 80-85.

[42] S. Matsuoka, C.J. Aloisio, H.E. Bair, Interpretation of shift of relaxation time with deformation in glassy polymers in terms of excess enthalpy, Journal of Applied Physics, 44 (1973) 4265-4268.

[43] M. Chowdhury, P. Freyberg, F. Ziebert, A.C.M. Yang, U. Steiner, G. Reiter, Segmental relaxations have macroscopic consequences in glassy polymer films, Physical Review Letters, 109 (2012).

[44] M. Barletta, A. Gisario, The role of the substrate in micro-scale scratching of epoxy-polyester films, Applied Surface Science, 257 (2011) 4449-4463.

[45] F. Mohs, über die Classification der Mineral Cörper, 1805.

[46] e. standard, EN ISO 6507-1 in, 2005, pp. 20.

[47] H. Hertz, Über die Berürhung fester elasticher Körper, Journal für die reine und angewandte Mathematik, 92 (1882) 156-171.

[48] E.H. Lee, J.R.M.A. Radok, The Contact Problem for Viscoelastic Bodies, Journal of Applied Mechanics, 27 (1960) 444.

[49] D. Tabor, The hardness of solids, Review of Physics in Technology, 1 (1970) 145.

[50] H. Pelletier, C. Gauthier, R. Schirrer, Experimental measurement and numerical simulation of the plastic strain during indentation and scratch tests on polymeric surfaces, J. Mater. Res., 24 (2009) 1184-1196.

[51] K.L. Johnson, Contact mechanics, (1985).

[52] W.C. Oliver, G.M. Pharr, Improved technique for determining hardness and elastic modulus using load and displacement sensing indentation experiments, J. Mater. Res., 7 (1992) 1564-1580.

[53] W.C. Oliver, G.M. Pharr, Measurement of hardness and elastic modulus by instrumented indentation: Advances in understanding and refinements to methodology, J. Mater. Res., 19 (2004) 3-20.

[54] A.C. Fischer-Cripps, A simple phenomenological approach to nanoindentation creep, Materials Science and Engineering A, 385 (2004) 74-82.

[55] S.E. Olesiak, M.L. Oyen, V.L. Ferguson, Viscous-elastic-plastic behavior of bone using Berkovich nanoindentation, Mech. Time-Depend. Mater., 14 (2010) 111-124.

[56] B.J. Briscoe, L. Fiori, E. Pelillo, Nano-indentation of polymeric surfaces, Journal of Physics D: Applied Physics, 31 (1998) 2395-2405.

[57] A.H.W. Ngan, B. Tang, Viscoelastic effects during unloading in depth-sensing indentation, J. Mater. Res., 17 (2002) 2604-2610.

[58] M. Beyaoui, P.E. Mazeran, M.F. Arvieu, M. Bigerelle, M. Guigon, Analysis of nanoindentation curves in the case of bulk amorphous polymers, International Journal of Materials Research, 100 (2009) 943-949.

[59] A.C. Fischer-Cripps, Elastic-plastic behaviour in materials loaded with a spherical indenter, Journal of Materials Science, 32 (1997) 727-736.

[60] L. Cheng, X. Xia, L.E. Scriven, W.W. Gerberich, Spherical-tip indentation of viscoelastic material, Mechanics of Materials, 37 (2005) 213-226.

[61] K. Sakaue, S. Okazaki, T. Ogawa, Indentation technique for evaluation of master curve of creep compliance, Experimental Techniques, 35 (2011) 16-22.

[62] F. Quadrini, E.A. Squeo, A. Guglielmotti, Indentation creep of polymers. I. Experimental, Polymer Engineering and Science, 50 (2010) 2431-2439.

[63] I. Karapanagiotis, D.F. Evans, W.W. Gerberich, Dynamics of the leveling process of nanoindentation induced defects on thin polystyrene films, Polymer, 43 (2002) 1343-1348.

[64] Z.Y. Zhang, H.N. Dhakal, S.N. Surip, I. Popov, N. Bennett, Characterisation of roof tile coating degradation using nano-indentation test and surface profilometry, Polymer Degradation and Stability, 96 (2011) 833-838.

[65] T. Chatel, Fluage et recouvrance d'empreintes et de sillons sur suface de polymère, in, Université de Strasbourg, Strasbourg, 2010.

[66] T. Chatel, C. Gauthier, H. Pelletier, V. Le Houerou, D. Favier, R. Schirrer, Creep of the contact with a spherical tip and recovery of the imprint on amorphous polymer surfaces, Journal of Physics D-Applied Physics, 44 (2011).

[67] T. Chatel, H. Pelletier, V. Le Houérou, C. Gauthier, D. Favier, R. Schirrer, Original in situ observations of creep during indentation and recovery of the residual imprint on amorphous polymer, J. Mater. Res., 27 (2012) 12-19.

[68] P. Bertrand-Lambotte, J.L. Loubet, C. Verpy, S. Pavan, Nano-indentation, scratching and atomic force microscopy for evaluating the mar resistance of automotive clearcoats: Study of the ductile scratches, Thin Solid Films, 398-399 (2001) 306-312.

[69] S. Mischler, A.I. Muñoz, Wear of CoCrMo alloys used in metal-on-metal hip joints: A tribocorrosion appraisal, Wear, 297 (2013) 1081-1094.

[70] M. Wong, G.T. Lim, A. Moyse, J.N. Reddy, H.J. Sue, A new test methodology for evaluating scratch resistance of polymers, Wear, 256 (2004) 1214-1227.

[71] W. Brostow, B. Bujard, P.E. Cassidy, H.E. Hagg, P.E. Montemartini, Effects of fluoropolymer addition to an epoxy on scratch depth and recovery, Materials Research Innovations, 6 (2002) 7-12.

[72] W. Brostow, W. Chonkaew, L. Rapoport, Y. Soifer, A. Verdyan, Grooves in scratch testing, J. Mater. Res., 22 (2007) 2483-2487.

[73] H. Chakraborty, A. Sinha, N. Mukherjee, D. Ray, P. Protim Chattopadhyay, Indentation and scratch behavior of functionalized MWCNT-PMMA composites at the micro/nanoscale, Polymer Composites, (2013).

[74] H. Jiang, R. Browning, H.J. Sue, Understanding of scratch-induced damage mechanisms in polymers, Polymer, 50 (2009) 4056-4065.

[75] C. Gauthier, R. Schirrer, Time and temperature dependence of the scratch properties of poly(methylmethacrylate) surfaces, Journal of Materials Science, 35 (2000) 2121-2130.

[76] C. Gauthier, S. Lafaye, R. Schirrer, Elastic recovery of a scratch in a polymeric surface: Experiments and analysis, Tribology International, 34 (2001) 469-479.

[77] M. Mansha, C. Gauthier, P. Gerard, R. Schirrer, The effect of plasticization by fatty acid amides on the scratch resistance of PMMA, Wear, 271 (2011) 671-679.

[78] M. Barletta, S. Pezzola, S. Vesco, V. Tagliaferri, F. Trovalusci, Experimental evaluation of plowing and scratch hardness of aqueous two-component polyurethane (2K-PUR) coatings on glass and polycarbonate, Progress in Organic Coatings, (2013).

[79] J.S.S. Wong, H.J. Sue, K.Y. Zeng, R.K.Y. Li, Y.W. Mai, Scratch damage of polymers in nanoscale, Acta Materialia, 52 (2004) 431-443.

[80] M.L. Oyen, Spherical indentation creep following ramp loading, J. Mater. Res., 20 (2005) 2094-2100.

[81] T. Chatel, V. Le Houérou, H. Pelletier, C. Gauthier, Numerical analysis of the creep of the contact and recovery of the imprint on amorphous polymer surfaces, Mech. Time-Depend. Mater., 17 (2013) 581-595.

[82] J. Wang, T.C. Ovaert, Computational mechanical property determination of viscoelastic/plastic materials from nanoindentation creep test data, J. Mater. Res., 24 (2009) 1245-1257.

[83] J.L. Bucaille, E. Felder, G. Hochstetter, Identification of the viscoplastic behavior of a polycarbonate based on experiments and numerical modeling of the nano-indentation test, Journal of Materials Science, 37 (2002) 3999-4011.

[84] J. Krier, J. Breuils, L. Jacomine, H. Pelletier, Introduction of the real tip defect of Berkovich indenter to reproduce with FEM nanoindentation test at shallow penetration depth, J. Mater. Res., 27 (2012) 28-38.

[85] C. G'Sell, J.J. Jonas, Determination of the plastic behaviour of solid polymers at constant true strain rate, Journal of Materials Science, 14 (1979) 583-591.

[86] J.L. Bucaille, Simulation numérique de l'indentation et de la rayure des verres Organiques, in, École Nationale Supérieure des Mines de Paris, Paris, 2001, pp. 239.

[87] M.M. Hossain, H. Jiang, H.J. Sue, Effect of constitutive behavior on scratch visibility resistance of polymers-A finite element method parametric study, Wear, 270 (2011) 751-759.

[88] L.C.A. Van Breemen, L.E. Govaert, H.E.H. Meijer, Scratching polycarbonate: A quantitative model, Wear, 274-275 (2012) 238-247.

[89] J. Lemaitre, J.-L. Chaboche, Mécanique des matériaux solides, Bordas, 1988.

[90] P.J. Dooling, C.P. Buckley, S. Hinduja, The onset of nonlinear viscoelasticity in multiaxial creep of glassy polymers: A constitutive model and its application to PMMA, Polymer Engineering and Science, 38 (1998) 892-904.

[91] E.T.J. Klompen, T.A.P. Engels, L.E. Govaert, H.E.H. Meijer, Modeling of the postyield response of glassy polymers: Influence of thermomechanical history, Macromolecules, 38 (2005) 6997-7008.

[92] L.C.A. Van Breemen, Contact mechanic in glassy polymer, in, Teschnische Universiteit Eindhoven, Eindhoven, 2009.

CHAPTER V. MATERIALS & METHODS

CHAPTER V. MATERIALS & METHODS 110
V.1. INTRODUCTION 111
V.2. POLYMERS ORIGIN 111
V.2.1. Industry product 111
V.2.2. Lab made product 113
V.2.3. Summary of available samples 115
V.3. SURFACE TEXTURE 116
V.3.1. Clean surfaces and no texture 116
V.3.2. Glass 116
V.3.3. Teflon spray 116
V.3.4. Kapton film 116
V.4. MECHANICAL CHARACTERIZATION 117
V.4.1. Bulk characterization 117
V.4.2. Indentation 122
V.4.3. Scratch 132
V.5. OTHER CHARACTERIZATIONS 134
V.5.1. Optical microscope 134
V.5.2. Differential scanning calorimeter 134
V.5.3. Transmission Electron Microscopy (TEM) 135
V.6. CONCLUSION 136
V.7. BIBLIOGRAPHY 137

V.1. INTRODUCTION

The objectives of this chapter are the material presentation and the presentation of the different characterization techniques (machine specificity, experimental setup) used during this thesis. In particular Poly(methyl methacrylate) (PMMA) and polyallyl diglicol (CR39) history and fabrication technics are shown. The way to obtain a clean surface is presented. Then the characterization technics and methods are explained. Conventional methods are used to determine rheological properties such as Poisson ratio, Young's, shear and bulk modulus. Polymers are nowadays very often used as protecting layer. Then their degradation is done by indentation or scratching thus both of these methods are used to characterize and compare the different materials. Actually the indentation creep recovery, the scratch and its recovery analysis are presented. Finally some other characterizations are used in this thesis such as thermo gravimetric analysis and transmission electron microscopy.

V.2. POLYMERS ORIGIN

The materials used during this thesis are polymers. A distinction is done between the polymers that are purchased in a solid form (can be tested without further treatment) and the products that are manufactured.

V.2.1. Industry product

V.2.1.1 PMMA

Plexiglas (one of PMMA commercial name) was invented by Otto Rohms and was at the beginning the specialty of the firm Rohm & Haas. In particular its very high transparency was the major sale argument. Indeed this transparency, along with polymer good resistance to atmospheric and chemical attack, make it a very good choice for numerous applications such as protection glass, bottle glass, law enforcement shield. Moreover PMMA relative low weight in comparison with glass renders it very attractive for building (in replacement of glass see example in Figure V-2 or automotive industry in particular aeronautics (windshield). The methyl methacrylate (monomer in Figure V-1a) polymerizes by free radical polymerization. The Poly (Methyl MethAcrylate) (PMMA) general formula is presented in Figure V-1b). In our case three different kinds of PMMA were studied.

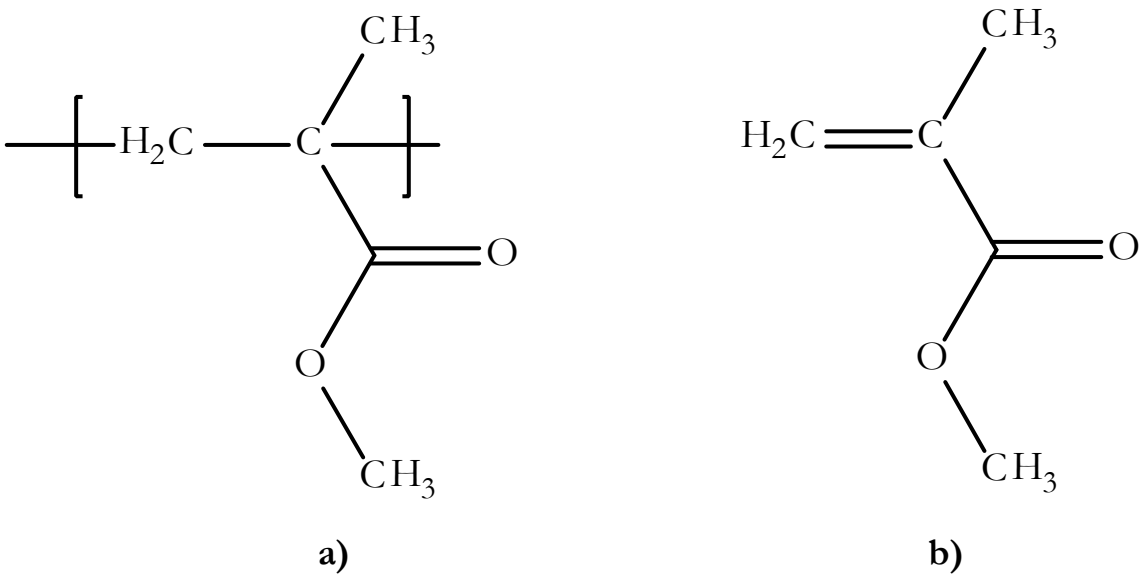

Figure V-1 scheme of a) Methyl Methacrylate monomer and b) poly (Methyl MethAcrylate)

Figure V-2 example of PMMA utilization a plastic window for houses

Three different industrial grades of PMMA are used during this thesis. They were all purchased at ARKEMA. The first is the PMMA CN (Coulée Normal) which has a molecular mass of 2500 000g/mol. Then PMMA Extruded is measured. Its molecular mass is much smaller and is around 5000g/mol. Finally a reticulated PMMA, PMMA CNR (Coulée Normal Réticulé) is observed, its molecular mass is considered infinite.

V.2.1.2 CR39 essilor

On the contrary to previously presented polymers CR39 is more recent and more expensive. The name comes from Columbia Resine 39 because it was the 39th attempt to create a transparent reticulated polymer. The firsts applications were for aeronautics, fuel monitors for bomber during the WW II were made in CR39 and a reinforced CR39 was used for the fuel tank. After the war a rest of CR39 was used to make glasses. The greater advantage of this material is his remarkable resistance to scratch, around 40 times higher than PMMA. Figure V-3 shows an example of

actual advertisement for CR39 by Essilor. In this case the polymer is further protected by several clear coats.

Figure V-3 CR39 utilization example [1]

The allyl diglycol, which formula is in Figure V-4 a), is the monomer. The polymerization is done by free radical polymerization. An example of the formed network can be seen in Figure V-4 b).

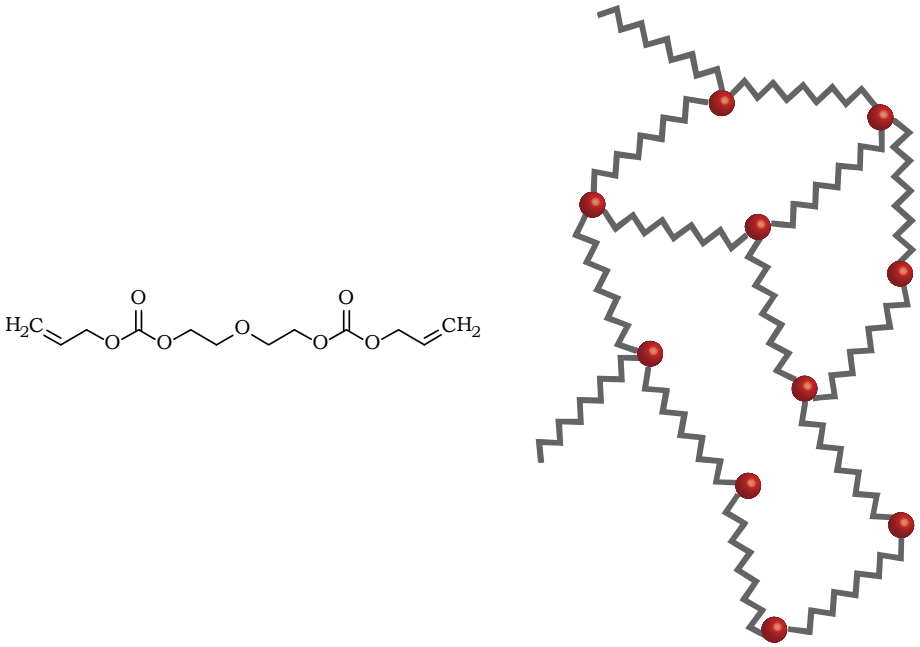

a) **b)**

Figure V-4 a) scheme of allyl diglycol b) scheme of CR39 network

V.2.2. Lab made product

V.2.2.1 Process

The PMMA sample preparation procedure is given below:

Solution preparation is done by weighting the MMA, the Plexit® 55 (Evonik : PMMA (55%), MMA (45%)), the fillers and the dispersant agent (N-[3-(Trimethoxysilyl)propyla]aniline and

aerosil see V.2.2.2.4). The solution is strongly mixed. Then the solution is mixed and degased under 100mbar.

The Azobisisobutyronitrile (AIBN, C8H12N4) is added to the solution. The mass added corresponds to 8% of MMA mass. Reactants are mixed again under vacuum.

Mould preparation: a watertight steel mould is bolt with a 8mm spacing. The inside walls are sometimes protected with Teflon or a Kapton film.

The solution is poured out on the open side of the mould. The pouring is conducted slowly so that no bubbles are captured in the solution. The mould is not sealed to allow bubbles to be eliminated.

The filled mould is heated in a drying oven at 63°C for 24 hours. Then the temperature is raised to 120°C. After these preparation times the polymerization is finished.

V.2.2.2 Fillers

There are two major ways to improve the curing: either protect the bulk material with a thin layer or improve the bulk resistance by modifying the material by reticulation or with nano-charges in order to create a composite. Fillers are neither soluble nor miscible products, which are mixed in a polymer. The goal is to increase one or more properties of the final product, called composite. Fillers are classed in four main shapes: spherical, lamellae, needles and fibers[2]. In this thesis, we use fillers of spherical form. Their size is in the range [2nm:100nm], smaller than light wavelength in order to insure transparency. Moreover classification is also done by chemical composition. Different types of charges were tested: AlO(OH), SiO2.

V.2.2.2.1 AlO(OH)

The boehmite (AlO(OH)) particle was discovered at the beginning of the 20th century in Germany. It is used as filler for protective layer or in catalysis. In our case the fillers Disperal® from Sasol Company are simply add to the bulk. This filler is claimed to show very good dispersion behavior in polymers and coatings[3]. The Disperal® OS1 from Sasol Company was used for the sample. Its size is around 10nm and it is covered with p-toluene Sulfonic acid, to increase its dispersibility. One sample containing 10% in mass was fabricated.

V.2.2.2.2 SiO_2

SiO2 particles are more commonly used as fillers than aluminum oxide. In particular they are also known for being good mechanical reinforcements[2]. Indeed they are used in numerous applications: boat shell, windsurfing, car body, electro-magnetic carters, …

V.2.2.2.3 Nanopox® A 410

This is a nanosilica particle sold by Evonik industries. It is enrobed in epoxy resins. It is claimed to improve modulus, hardness, toughness, compressive properties and fatigue resistance without changing the transition temperature[4].

V.2.2.2.4 Aerosil

Aerosil particles have approximately a size of 12nm. It is sold by Evonik industries. They are used as dispersant agent [5].

V.2.2.2.5 Functionalized Stöber particles

Stöber particles were also prepared in order to serve as additive in PMMA. The prepared particles size was 100nm. The water: ethanol ratio at the beginning of the reaction determines the particles size. The preparation is done as follows:

- Ammoniac (39.2 mL), Ethanol (1368.5 mL) and water (0.22mL) are mixed together.
- Then Tetra Ethyl Orthosilicate (92.1mL) is added. Then it mixed during 12 hours.
- The obtained products are rinsed four times in ethanol. Each time the solvent is evaporated.
- Finally the particles are let to dry in an oven for 2 days.

In order to facilitate the insertion of the particles in the matrix, two different end groups were added: either an acrylate groups or a thiol group. The objectives are respectively a copolymerization of the end group in the PMMA chains and that the thiol group plays the role of an initiator

V.2.3. Summary of available samples

A table summary presenting the origin and filler content of each sample is presented below:

Name	Fillers	Quantity [weight %]	Origin
CR39	-	-	Essilor
PMMA CN			Arkema
PMMA ba (basis)	aerosil TMSPA	0.5 0.5	lab made
PMMA 10 AlO(OH)	Boehmite	10	lab made
PMMA 10 nanopox	nanopox	10	lab made
PMMA20 nanopox	nanopox	20	lab made
PMMA 2.5 stt	stöber thiol aerosil TMSPA	2.5 0.5 0.5	lab made
PMMA 2.5 sta	stöber acrylat aerosil TMSPA	2.5 0.5 0.5	lab made

V.3. SURFACE TEXTURE

V.3.1. Clean surfaces and no texture

The interest in a clean surface is driven by surface characterization. Indeed dirt acts as a lubricant on surfaces; dirty scratched surfaces are less damaged than clean ones.

V.3.2. Glass

In order to have a perfectly smooth surface and to be able to open the mould, the mould wall can be in glass. The obtained surface is then smooth in comparison to the tip size (R=2µm for the smallest tip used). The two major drawbacks are the fragility of the glass mould (temperature shock) and the difficulty to unmold the sample when an important amount of fillers is added. SiO2 fillers tend to stick on the mould walls.

V.3.3. Teflon spray

To protect the mould, a Teflon spray is used. Nevertheless the spray makes a surface texture and a grease layer on the sample. Both of them rending indentation difficult and scratching impossible. A surface example can be seen in Figure V-5.

Figure V-5 Example of surface dirtiness and rugosity after use of a teflon spray

V.3.4. Kapton film

Finally the use of Kapton films is the more feasible. Kapton (Figure V-6) is a polymer that is sticked on the inner wall of the mould. After 4-5 heating cycles the kapton film tends to decompose. Nonetheless the surface is usable.

Figure V-6 Kapton film as it looks before use

V.4. MECHANICAL CHARACTERIZATION

V.4.1. Bulk characterization

V.4.1.1 Instron® machine

The uniaxial Instron® 4500 (Figure V-7) tensile machine permits traction, compression and shear measurement. The temperature range is [-70°C: +180°C]. Force sensor maximum capacity is 10kN with a 1N precision during loading phase and a resolution of 0.2N. Displacement range speed is [1µm/s: 10mm/s]. The used extensometer (Figure V-7b)) has a +/-5mm variation possibility with a 0.5µm precision. The axial extensometer was placed at the middle of the sample where the higher deformation should occur.

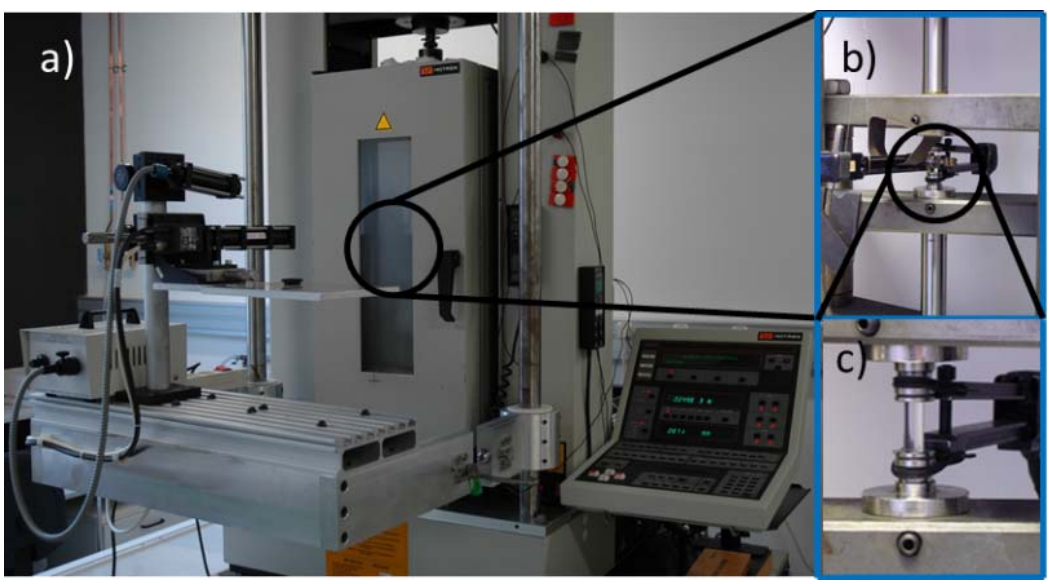

Figure V-7 a) Uniaxial tensile machine b)Uniaxial sample positioned in the machine with longitudinal and axial extensometers c)uniaxial sample (transparent polymer) with longitudinal extensometer

V.4.1.2 Uniaxial measurement generality

The majority of the bulk measurements were done in compression for two reasons: the major part of indentation solicitation consist in compression and compression samples require less material. The bulk characterizations are conducted on cylindrical samples (Figure V-7 b)). Their height, l_0, is roughly 12.5mm, their diameter, d_0=5mm so the area S0 is around 20mm^2.

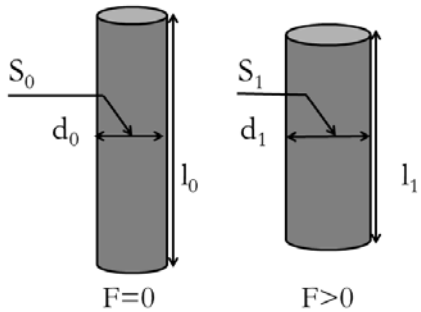

Figure V-8 Uniaxial samples schemes with geometrical information

From these measurements engineering and true, stress and strain are calculated according to the following equation:

engineering longitudinal strain	$\varepsilon^l = 100 \times \frac{(l_0 - l_1)}{l_0}$	Equation V-1
true longitudinal strain	$\varepsilon^l_{true} = 100 \times \ln(1 + \varepsilon^l)$	Equation V-2
engineering axial strain	$\varepsilon^a = 100 \times \frac{d_1}{d_0}$	Equation V-3
true axial strain	$\varepsilon^a_{true} = 100 \times \ln(1 + \varepsilon^a)$	Equation V-4
engineering stress	$\sigma = \frac{F}{S_0}$	Equation V-5
true stess	$\sigma_{true} = \frac{F}{S_1} = \frac{\sigma}{(1 + \varepsilon^a)^2}$	Equation V-6

One can observe that the strains are dimensionless, they are presented in percent. Whereas stresses have the dimension of a pressure and are expressed in mega Pascal.

Figure V-9 presents engineering stress and strain over time for a relaxation experiment. Later on, except when specified, true value will be presented (the same graphs with true values is in Figure V-11). Several experiments types can be conducted with this machine such as Dynamic Mechanical Temperature Analysis, relaxation, creep and cycling.

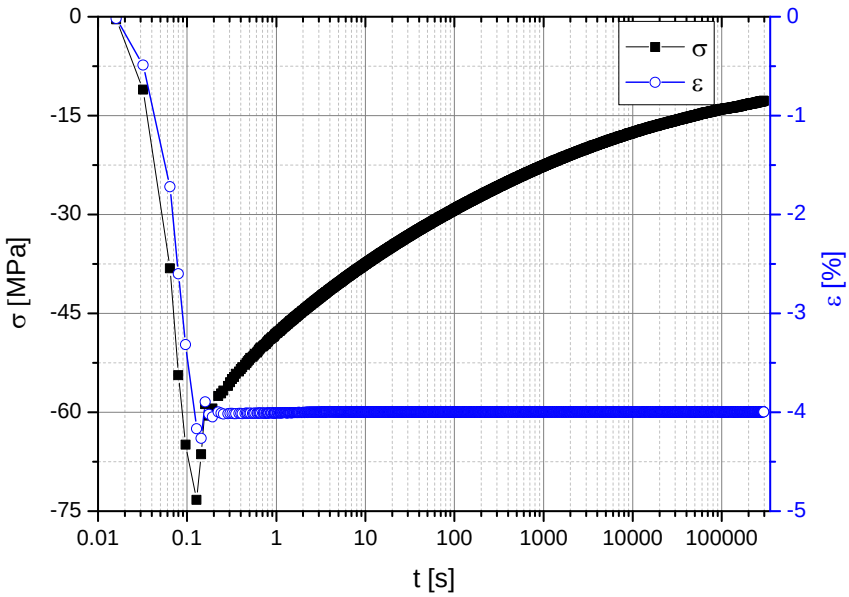

Figure V-9 Relaxation experiment presented with engineering stress and strain

V.4.1.3 Dynamic Mechanical Temperature Analysis (DMTA)

We consider a sample of length l0 and of section S0. Under a sinusoidal force over time, sample is compressed from a length (l0-l1). The strain remains small (under 2%). The Equation V-7, defining Young's modulus for pure elasticity, does not hold for polymers. Indeed a typical curve is presented in Figure V-10 a). The observed response is not linear. The ellipse is defined by two complex coefficients E' and E". They represent respectively the real and unreal part of the Young's modulus. E' corresponds to the Figure V-10 a) curve slope[6]. Whereas E" is proportional to the curve opening. The Young's modulus is then defined by Equation V-8. Then the Poisson coefficient and the loss factor are respectively defined by Equation V-9 and Equation V-10.

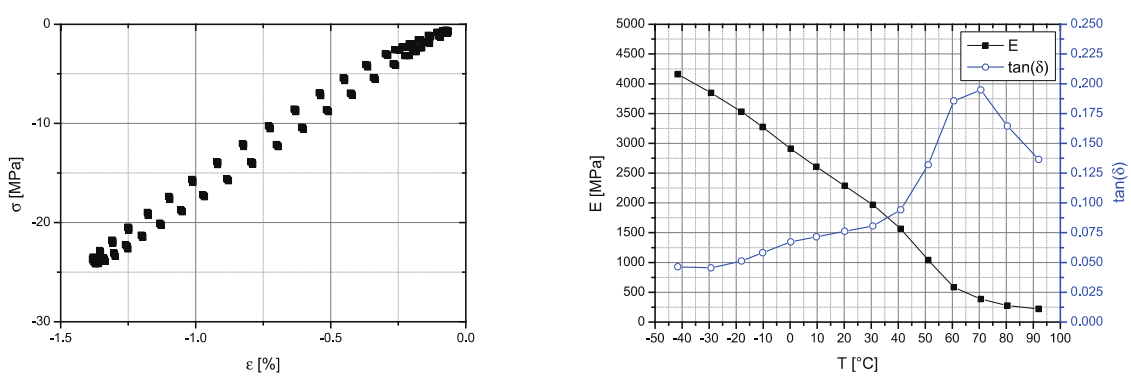

a) b)

Figure V-10 a) Stress versus strain for DMTA experiment at 30°C and 0.5Hz b) CR39 Young's modulus and mechanical loss in function of temperature at 0.05Hz

pure elasticity	$\sigma_{true} = E \times \varepsilon_{true}^{l}$	Equation V-7

Young's modulus	$E = \sqrt{E'^2 + E''^2}$	Equation V-8
Poisson Coefficient	$\nu = \frac{1 - \varepsilon^a}{1 - \varepsilon^l}$	Equation V-9
Loss factor	$\tan(\delta) = \frac{E''}{E'}$	Equation V-10

The DMTA measurement aims to characterize mechanically the polymer in temperature. So every 10°C a measurement is done. The Figure V-10 b) example shows a strong decrease of mechanical properties with temperature. DMTA are conducted on samples which were held at a given constant temperature for 15 minutes. Then sinusoidal compression strain amplitude, at a given frequency, is applied. In our example, Figure V-10 b), a 1% strain and 0.05Hz frequency are used. Measurements give the Young's modulus, Poisson coefficient and loss factor (tan(δ)) versus temperature. Mechanical characteristics of polymers are strongly time and temperature dependent. A strong decrease of mechanical properties is generally observed around the vitreous temperature T_α. The graph presents a typical curve obtained for DMTA measurements.

V.4.1.4 Relaxation

A relaxation experiment consists in following the stress with time for a fixed strain and temperature. At the experiment start, a given strain is applied quasi instantly to the sample. The stress is recorded during the experiment [6, 7]. In our case, the experiment last for 300 000s or 3.3 days. A relaxation sample curve is presented in Figure V-11. Though Equation V-11, Equation V-12 and Equation V-13, the relaxation, shear and bulk moduli are respectively determined with time.

Relaxation Modulus	$E(t) = \frac{\sigma(t)}{\varepsilon^l(t)}$	Equation V-11
Shear modulus	$G(t) = \frac{\sigma(t)/\varepsilon^l(t)}{2 \times (1 + \upsilon)}$	Equation V-12
Bulk modulus	$K(t) = \frac{\sigma(t)/\varepsilon^l(t)}{3 \times (1 - 2\upsilon)}$	Equation V-13

These experiments are used to determine the viscous parameter used in the numerical part.

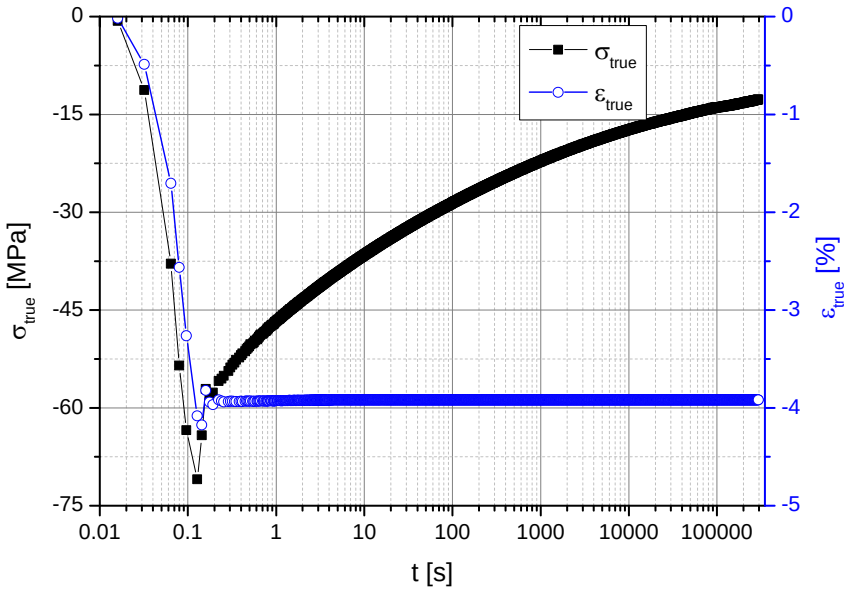

Figure V-11 True stress and strain versus time for a relaxation test on CR39 at 30°C

V.4.1.5 Creep

A creep experiment consists in following the strain with time for a fixed stress and temperature. In practice a dead weight is applied on the sample in an adiabatic chamber. The strain is recorded during experiment. A sample curve is shown in Figure V-12 a). This experiment last for 100 000s or 1 day. These experiments are used to validate, in the Finite Element Modeling code, the coefficient calculated from the relaxation experiment.

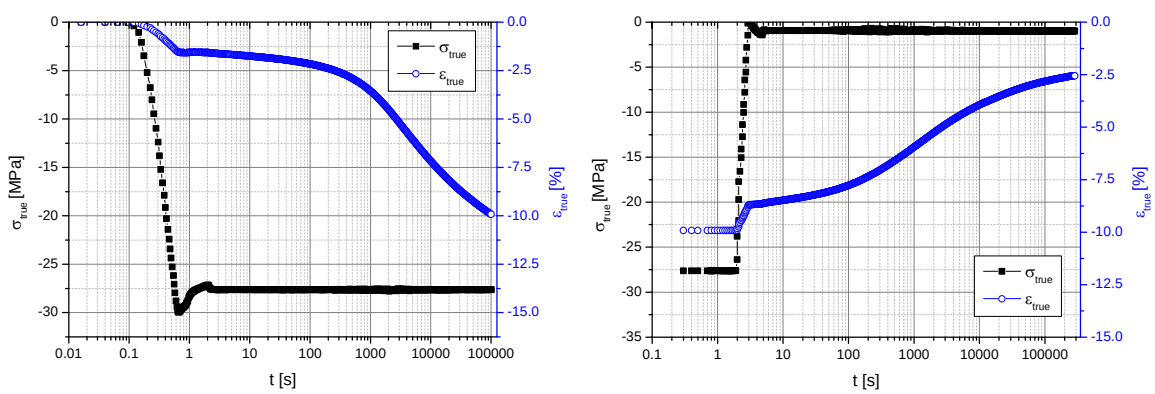

a) b)

Figure V-12 a) Stress and deformation versus time for a creep test on CR39 at 30°C b) Stress and strain versus time for creep recovery on CR39 at 30°C

The creep recovery consists in following the strain with time for a fixed stress and temperature after a creep experiment. After the creep experiment the load is quickly reduced to a minimum that serves to hold the sample in place [6, 7]. The whole experiment takes place in the adiabatic chamber. The recovery time is set to 300 000s. A creep recovery sample curve is presented in Figure V-12b). The recovery is used to further validate the coefficient inserted in the Finite Element Modeling code.

V.4.2. Indentation

V.4.2.1 Indentation generality

A comprehension of indentation goes through the two contact body study. The first study was done by Hertz in 1882 [8] (a scheme of the notation used is presented in Figure V-13). He demonstrated that the contact radius can be expressed (Equation V-14) in function of load and material constants. The combined modulus Equation V-15 and the combined radius Equation V-16 can be simplified in the case of a rigid indenter on a flat soft surface (for example glass or diamond indenter on polymer surface). This specific case is discussed below with the additional notations presented in Figure V-14 a). Actually Figure V-14 b) explains the contact radius ac(t), the contact depth hc(t), the total radius at(t) and the total depth ht(t).

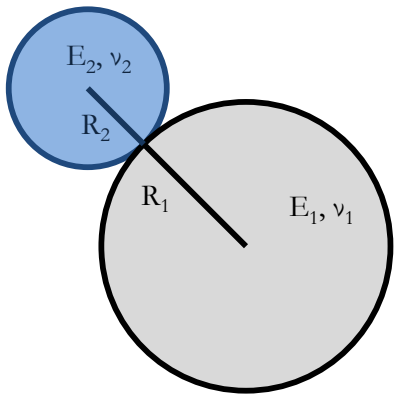

Figure V-13 schematic representation of contact between two solid materials

contact radius Hertz Theory	$a_c^3 = \frac{3}{4} \times \frac{F \times R^*}{E^*}$	Equation V-14
combined elastic modulus	$\frac{1}{E^*} = \frac{1-v_1^2}{E_1} + \frac{1-v_2^2}{E_2}$ if $E_1 \gg E_2$ then $E^* = \frac{E_2}{1-v_2^2}$	Equation V-15
combined radius	$\frac{1}{R^*} = \frac{1}{R_1} + \frac{1}{R_2}$ if 1 is flat $R_1 \to \infty$ then $R^* = R_2$	Equation V-16

One can easily demonstrate the geometrical relations presented in Equation V-17. Furthermore Fischer-Cripps presented the Equation V-17 and Equation V-18 [9].

geometrical relations	$a_c = \sqrt{2 \times h_c \times R - h_c^2}$ $h_c = R - \sqrt{R^2 - a_c^2}$	Equation V-17
total penetration depth	$h_t^3 = \left(\frac{3}{4E^*}\right)^2 \times \frac{F^2}{R}$	Equation V-18

Mean contact pressure	$p_m = \left(\frac{4E^*}{3\pi}\right)\frac{a_c}{R} = \frac{F}{\pi a_c^2}$	Equation V-19

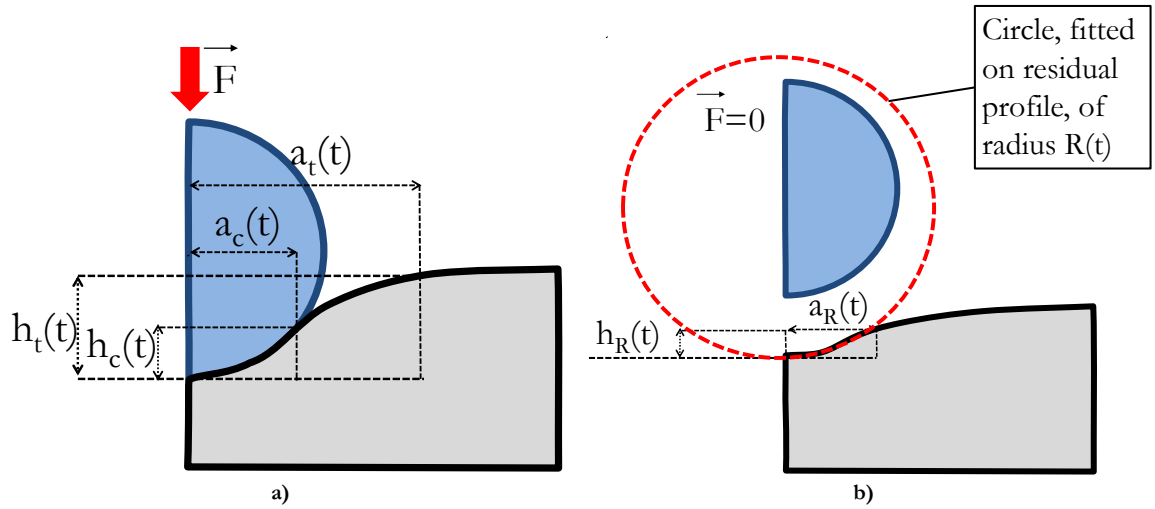

Figure V-14 a) schematic representation of the hard sphere-soft plane contact and size definition b) Definition of the recovery radius and imprint curvature

From these measurements several quantities are calculated such as Tabor deformation [10] (Equation V-20). To compare the creep of different materials we have introduce a normalized creep Tabor deformation Equation V-21 [11], where $a_c(t)$ is the contact at a time t and R is the indenter tip radius as defined previously (Figure V-14 a)). The creep deformation is normalized by the deformation at 0.5 s or end of loading time, after all loading effects took place. The recovery characterization needs also quantifying size. Knowing the recovery imprint profile shape, one can define the "contact" radius ($a_R(t)$) and a circle that fit on this profile (R(t))(see Figure V-14 b)). By identification to indentation creep deformation, the recovery deformation coefficient is defined in Equation V-22. In a similar way as for indentation creep the normalized recovery deformation is defined in Equation V-23 [11]. The recovery deformation is normalized by the deformation at the end of creep (t_c).

Tabor strain	$\langle\varepsilon\rangle = \frac{a_c(t)}{R}$	Equation V-20
Normalized Tabor creep deformation	$\frac{a_c(t)/R}{a_c(0.5s)/R}$	Equation V-21
Recovery deformation	$\frac{a_R(t)}{R(t)}$	Equation V-22
Normalized recovery deformation	$\frac{a_R(t)/R(t)}{a_c(t_c)/R}$	Equation V-23

Indentation is performed on three different scales with four different machines. Two nano-indenters, the Microvisioscratch [12, 13] and a macro indenter. All indentations were done with spherical tip for practical reasons: parallelism defaults are lower in case of a spherical tip, no contact observations through other tips are possible and more spherical tips (meaning more deformations can be reached) are available in the lab. Spherical tips have some drawbacks.

During creep, the imposed force is constant and the contact area increases. Thus the strain increases and the mean contact pressure decreases. Due to this effect, the indentation creep test appears as a complex experiment, but close to real polymer degradation during static contact between two functionalized surfaces.

V.4.2.2 Nano indentation

V.4.2.2.1 Nano indentation principle

Nano indentation is a technique used to characterize mechanical properties of materials and in particular layers characteristics. Figure V-15 a) presents a typical indentation curve. The loading increases linearly during 4s. Then the load is held constant, the creep can be observed during this period. Finally unloading is done with the same ramp as loading. The same experiment is plotted in a load-depth curve in Figure V-15 b).

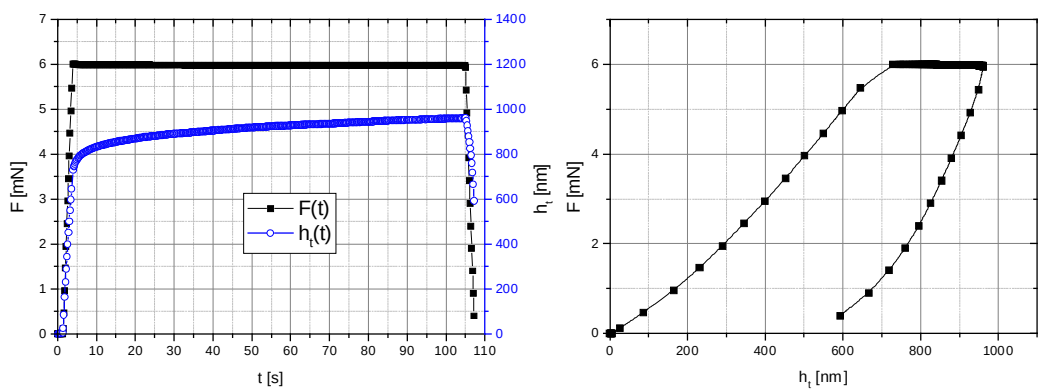

a) b)

Figure V-15 a) Force and depth versus time for an indentation creep on CR39 at room temperature b) Load-depth indentation curve on CR39 at 30°C

In this thesis, nano indentation loadings are done by the method of constant load rate. The used indenters are sphero-conical made of diamond mounted on stainless steel. Their tips radii are 2µm, 5µm, 22µm, 50µm and 100µm. The cone angle is 90°. Indentations are done so that we do not go into the conical parts of the tips.

V.4.2.2.2 Nano Indenter XP®MTS

Parts of the mechanical measurements were done with the nano-indenter XP® (Nano instrument inc., Oak Ridge, Tennessee, USA) [9, 14]. The available tips radii are 5 and 50µm. The XP®MTS machine maximum force is 0.5N. After indentation the tip is removed from the sample and the imprint is analyzed under an inline AFM in order to measure depth and contact radius. The first measure is done five minutes after the indentation end. Thus the first three decades, corresponding to [0.3s-300s], are not observed. Unfortunately the major changes or evolutions of the residual imprint or groove, related to viscoelastic behavior, are observed during this corresponding time[15].

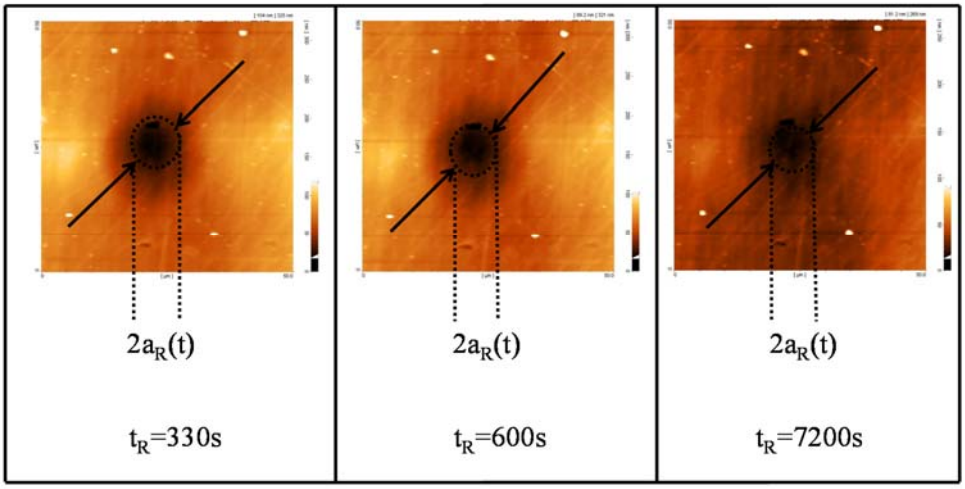

Figure V-16 AFM recovery observation after nano-indentation on CR39 at 30°C

V.4.2.2.3 Nano Indenter CSM

The CSM nano-indenter, in Figure V-17, was also used, available tips radii being 2, 22 and 100 µm. The nano indenter maximum force is 0.1N. Furthermore it has, as the previous machine, an inline AFM and additionally an optical microscope and a scratch tester to observe the recovery a few minutes after the end of solicitation. The specificity of this indenter is the presence of an optical system below the sample. The contact can then be observed during the experiment, example Figure V-18, thus leading to ac and hc using Equation V-17. Furthermore the machine gives the total depth (ht), from which one can determine the total contact radius (at). Finally the normalized deformation can be calculated (Equation V-21).

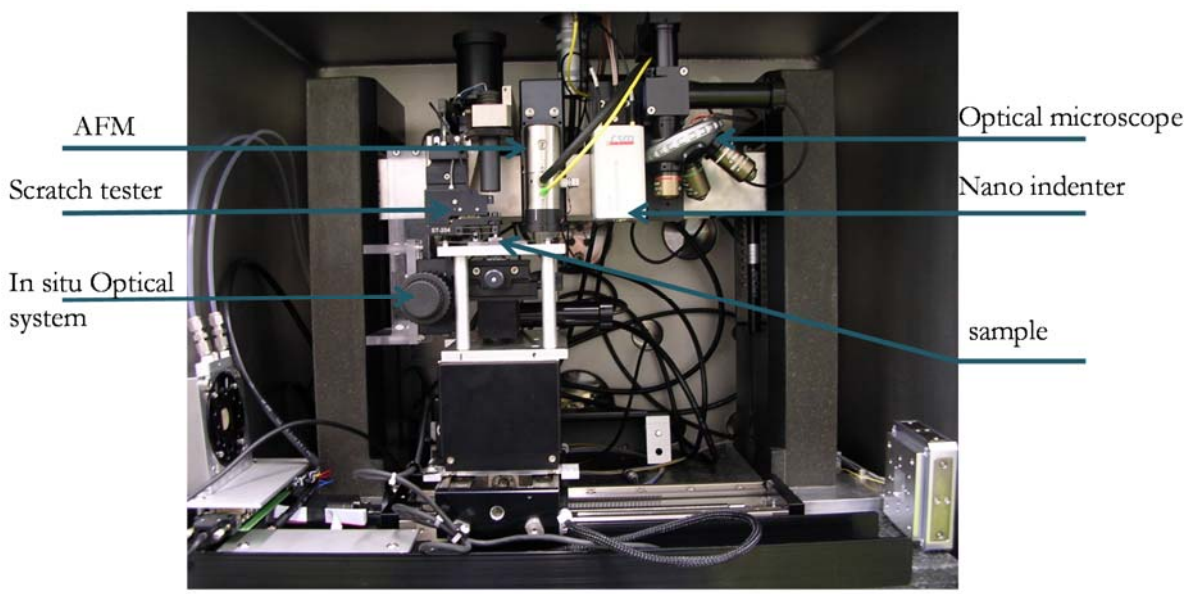

Figure V-17 Nano-indenter photography and legend

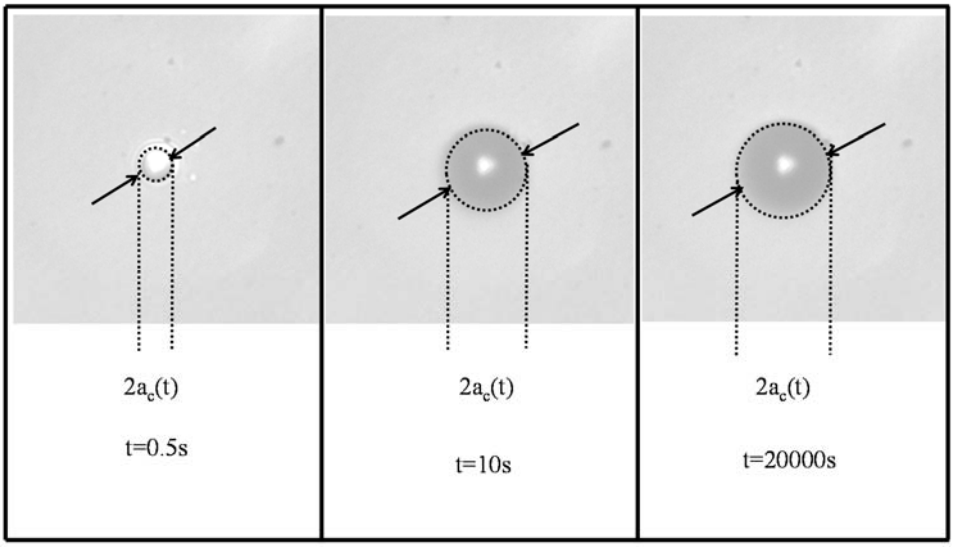

Figure V-18 Nano-indentation creep observation of CR39 at 30°C with CSM nano-indenter in situ optical system

V.4.2.3 Micro and macro Indentation

V.4.2.3.1 Lab made apparatus the Microvisioscratch

The Microvisioscratch, team lab made apparatus (Figure V-19) enables also the caption of pictures (Figure V-21) through the camera. The Microvisioscratch was initially built for scratch observation [14]. The available force range is 0.1N-25N with a precision of 1%. In this thesis the sphere radii used are 116, 400 and 3300 µm. The principle of micro and macro indentation is slightly different from the nano-indentation one. Indeed generally in nano indentation we record the applied load and the displacement of the tip. Here the load is also applied to the tip but the displacement is not recorded because the machines conception does not allow it. That is why the image technique presented above is used. The micro-indentation creep experiment consists in following the deformation of the material under a constantly load sphere at a constant temperature. In practice the load is chosen so that the Tabor deformation (Equation V-20) at 0.5s (long after the overloading phase) is equal to 0.2. Then the load is maintained constant for the creep time (typically 100 000s). For example Figure V-20 presents the measured contact radius and force for a micro indentation experiment.

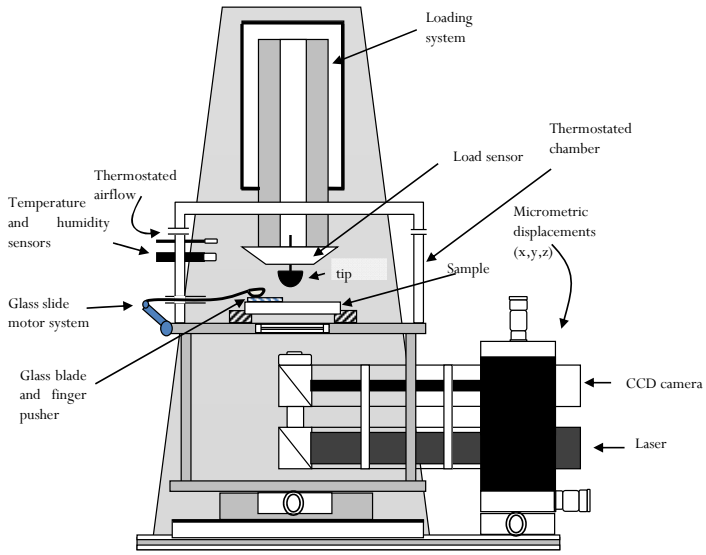

Figure V-19 Micro visio scratch schematic representation

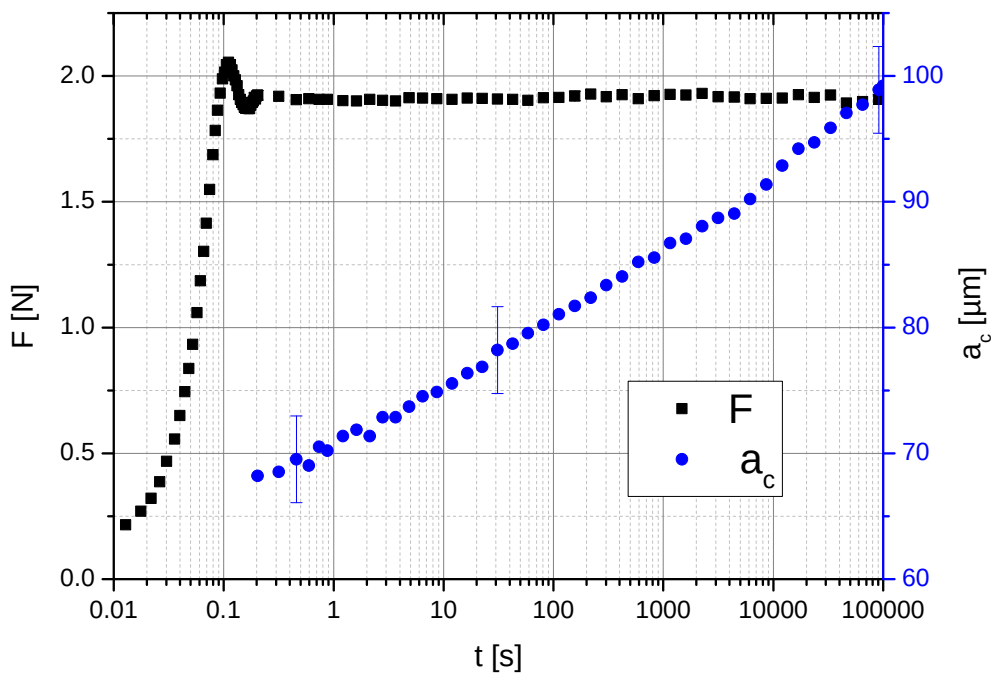

Figure V-20 Force and contact radius with time for a micro indentation

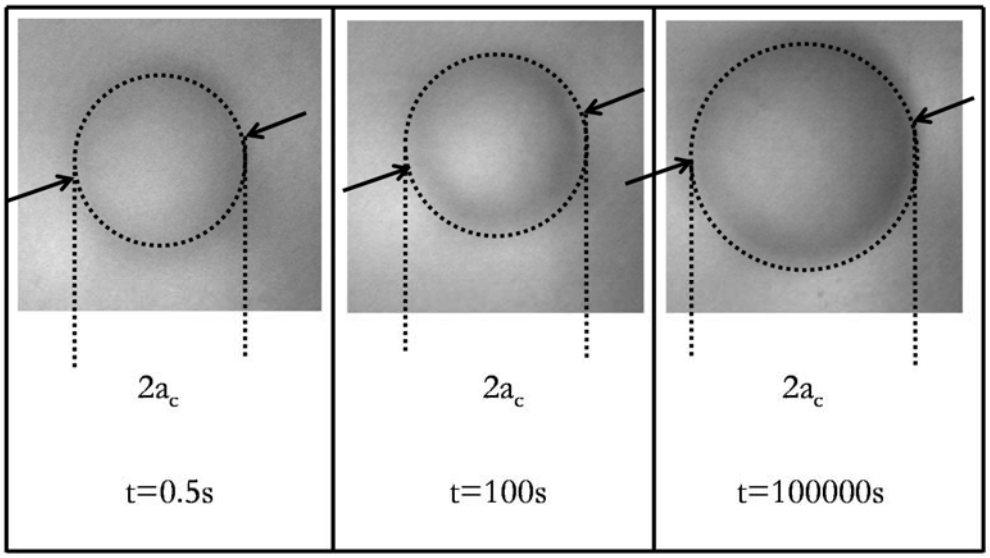

Figure V-21 Micro-indentation in situ observation on CR39 at 30°C

The machine (Figure V-19) can also be used for indentation recovery measurement. After the end of the creep time the tip is removed as quickly as possible and a glass slide (in blue in Figure V-19 scheme) is thrown on the imprint. Interference fringes are built between the sample-air limit and the air-glass limit (Figure V-22). In Figure V-22 several additional fringes can be observed outside of the contact, this corresponds to a misalignment between the sample and the glass. Indeed dirt between the glass and the sample can slightly tilt the glass, leading to these additional fringes.

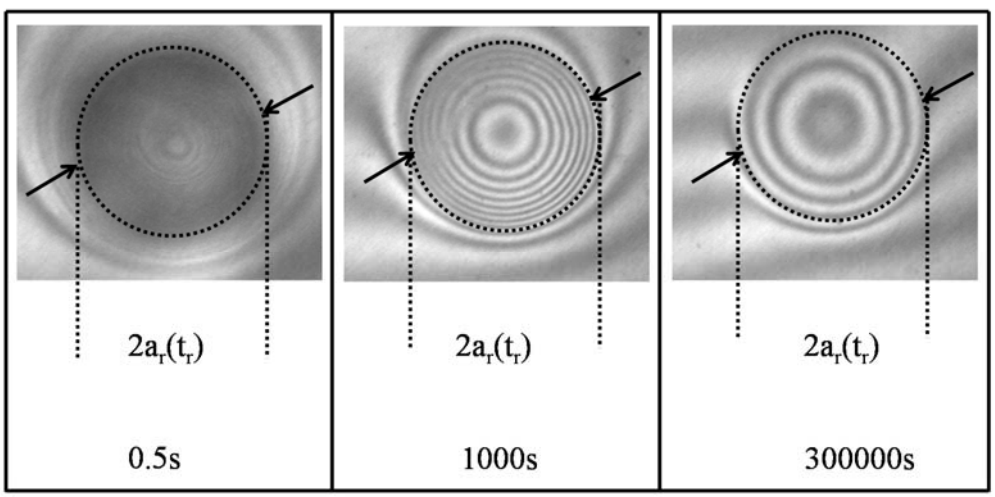

Figure V-22 In situ recovery observation after micro-indentation on CR39 at 30°C "contact" radius measurement

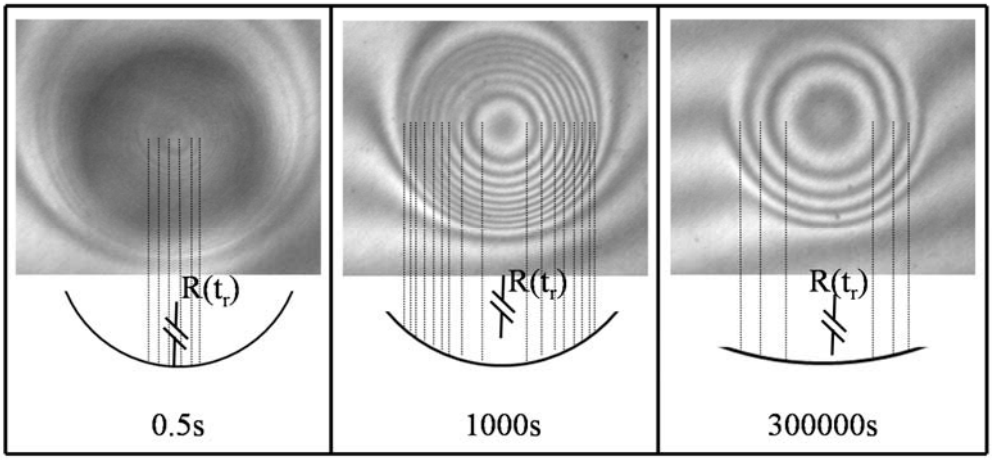

Figure V-23 In situ recovery observation after micro-indentation on CR39 measurement of R(t)

Figure V-22 presents the "contact" recovery radius measurement for three images. These measurements are not sufficient to completely characterize the recovery. The imprint shape plays an important role in the recovery characterization. Figure V-23 explain how this shape is taken into account. The depth difference between two white fringes is λ/2 (λ being the laser light wavelength). Thus, by pointing every fringe an imprint profile can be extracted. A circle is fitted on this profile. Its radius increases during the recovery. Figure V-24 presents typical raw data extracted from the recovery images, evolution of "contact" recovery radius and radius of recovery imprint with time are presented.

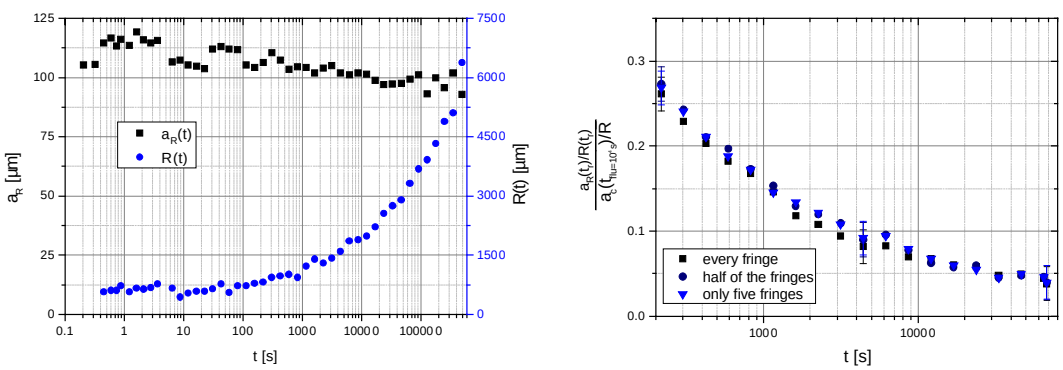

a) b)

Figure V-24 a) measured "contact" recovery radius and fitted radius of recovery imprint b) Comparison between different method for measuring deformation recovery

With these two measurements, the recovery Tabor deformation is calculated. A first example of these results can be seen in Figure V-24. On the first image of Figure V-23 all the fringes in the contact cannot be seen. Can we use so little information to characterize the imprint shape? To answer this question, a set of images, where all the fringes are visible, was analyzed three times with three different methods. First method builds a profile with all the black and the white fringes (called "every fringe"). The second one constructs a profile with two fringes to the left and all the fringes to the right of the imprint center (called "half of the fringes"). The third analyses only two fringes to the left and three fringes to the right (called "only five fringes"). The plotted curve, Figure V-24, demonstrates a difference which is within the experimental error. Thus, when the fringes are discernable all the fringes are counted, when not, only all the discernable fringes are

measured. Even with this technique, the very first images are not observed because they are too blurred.

V.4.2.3.2 Macro Indenter

In the case of non-transparent material, the contact cannot be observed through the sample. Therefore the indenter tip, made of glass Figure V-25, can serve to see the contact. In order to see something the curvature radius must be much higher than for other experiment. Indeed a tip radius of 3300µm is a minimum. Nevertheless to have a Tabor deformation equal to 0.2, Hertz theory [8] for a purely elastic material predicts a 300N force. This cannot be done with the Microvisioscratch.

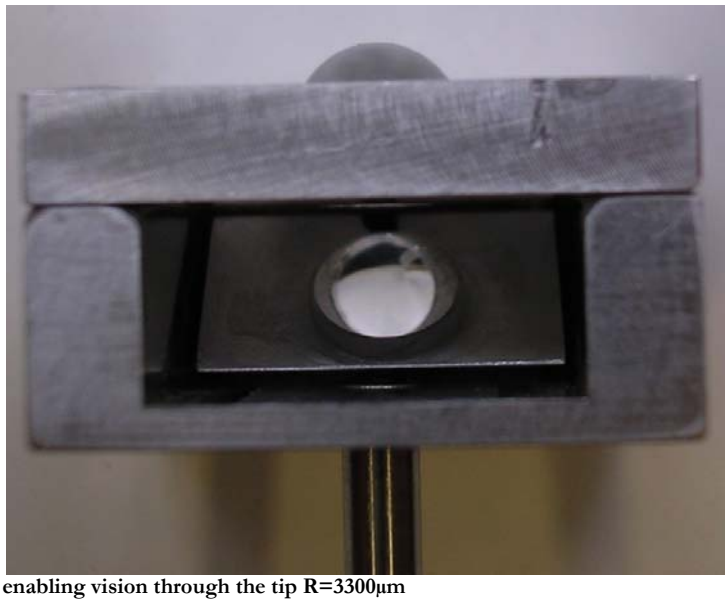

Figure V-25 Indenter enabling vision through the tip R=3300µm

Therefore the same principle as previously described has been adapted in the Instron tensile machine. The machine limitation is the indenter break. Around 1000N the glass indenter will break. Figure V-26 shows a scheme of the machine with the indenter and the vision. Some pictures taken with this apparatus are presented in Figure V-27. Typical information obtained from these experiments are similar to the one presented for Microvisioscratch in Figure V-20.

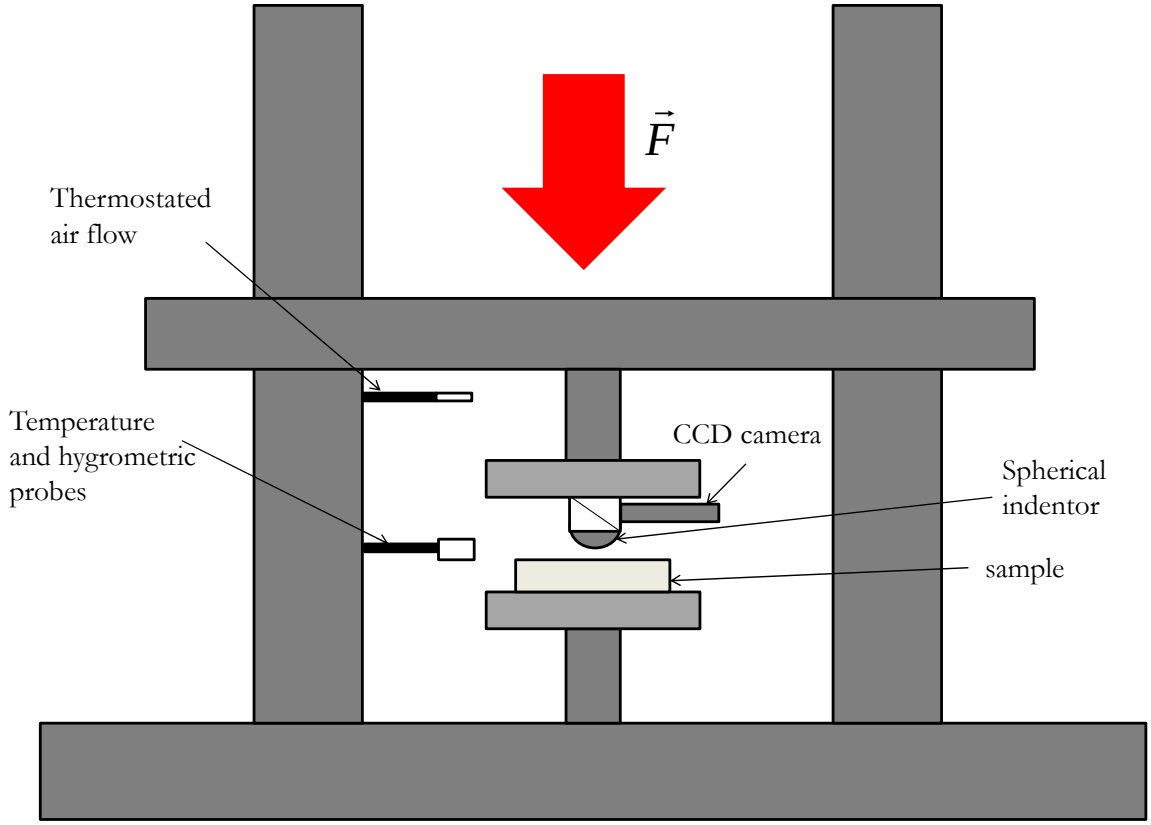

Figure V-26 Macro-indenter with vision through the tip principle

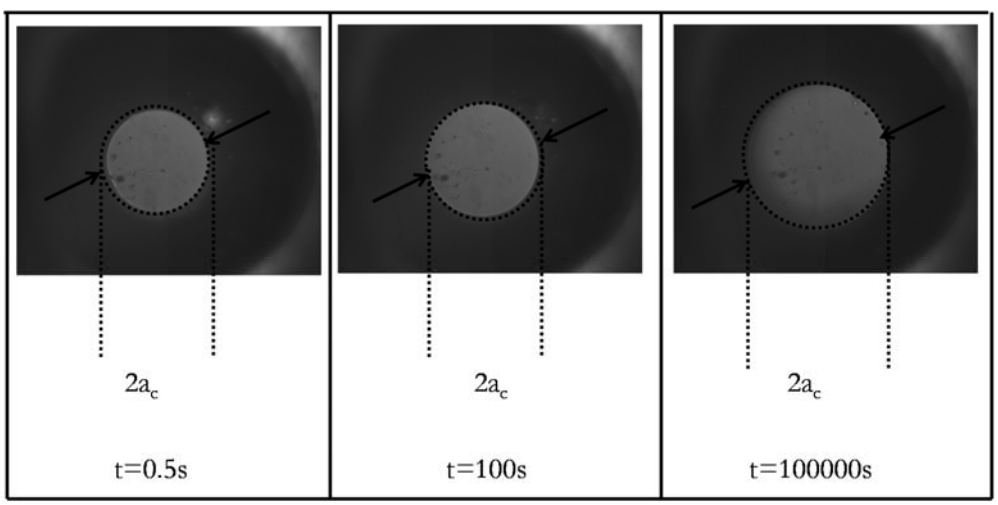

Figure V-27 Creep imprint observation in macro indentation

V.4.2.4 Principle validation

A comparison between macro indentation, micro indentation and nano indentation was done to check the experiment similarity. We use the Microvisioscratch experiment as a pivot for the average size of its contact and because of its higher flexibility. In Figure V-28 a), presenting the results coming from macro and micro indenter, both mean contact pressure and normalized strain are equal within the experimental error. Therefore indentation creep experiments, coming from these different sources, are comparable.

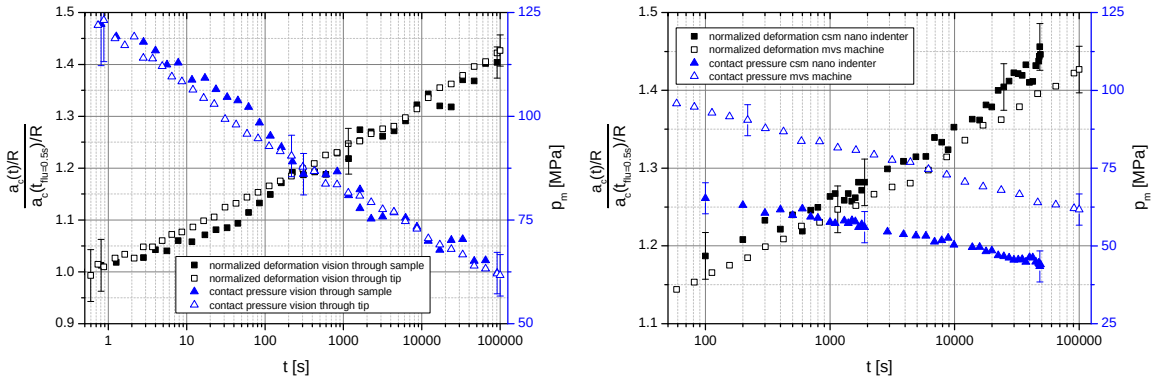

a) b)

Figure V-28 a) 29 Comparison between two indentation system microvisioscratch and instron, with two different vision methods b) Comparison between two indentation systems: nano indenter and Microvisioscratch

The same experiment was conducted to compare nano and micro indentation. Figure V-28 b) presents the mean contact pressure and the normalized creep deformation with time. Although the normalized deformation seems similar, the mean contact pressure is clearly smaller. So the material seems softer on the surface than in the bulk. Macro and nano indentation experiments are not comparable.

V.4.3. Scratch

V.4.3.1 Micro scratch

V.4.3.1.1 Groove fabrication in situ observation

The study of scratch is old; it started with Friedrich Mohs in 1805 [16]. Less than scratch, Friedrich Mohs was studying the material resistance to scratch, leading him to his famous scale of mineral hardness. The first descriptions of the groove recovery were given by several authors [17-19]. Nevertheless, no information was given during the first 15 minutes for these experiments. Thanks to the Microvisioscratch apparatus, the groove formation (Figure V-30) and recovery phase (Figure V-31a)) was observed directly after the scratch. The Microvisioscratch apparatus has the same specificity as mentioned in V.4.2.3.1. Its speed range is [1µm -10 00 µm/s.] with 5% precision.

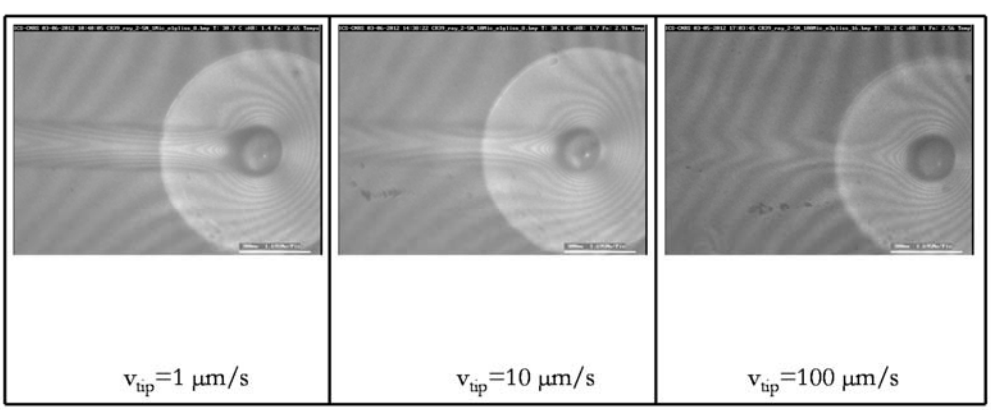

Figure V-30 In situ groove formation for three scratching velocity decades

V.4.3.1.2 Groove recovery in situ observation

The groove recovery is observed with time (Figure V-31 a)). Each fringe is pointed and assigned to a specific length. Then this XYZ point cloud is computed to give the XYZ 3D surfaces observable in Figure V-31 b).

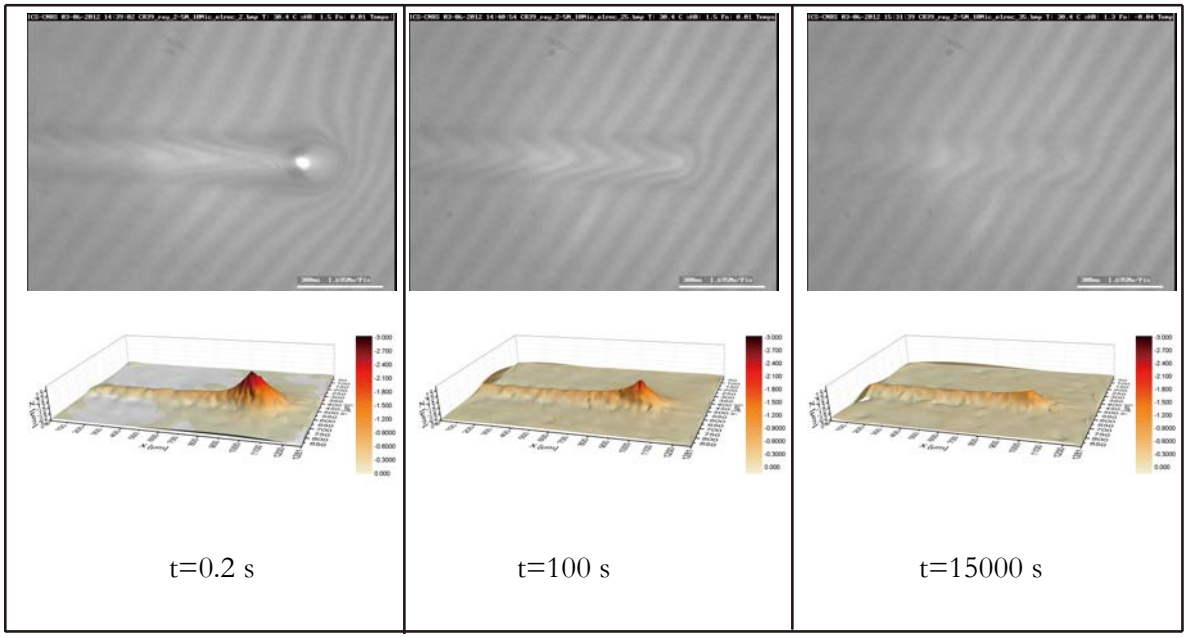

Figure V-31 a) Groove recovery picture b) 3D representation of the surface

Figure V-31 b) data is then used to extract profiles and observe them with time. The position of the extracted profile is presented in Figure V-32. The first profile named "0" is taken at the end of scratch point. The next profile is taken at one contact radius of the precedent and so on until the end of image. They are named after their distance towards the end of scratch point. The total length of the profiles is four times the contact radius.

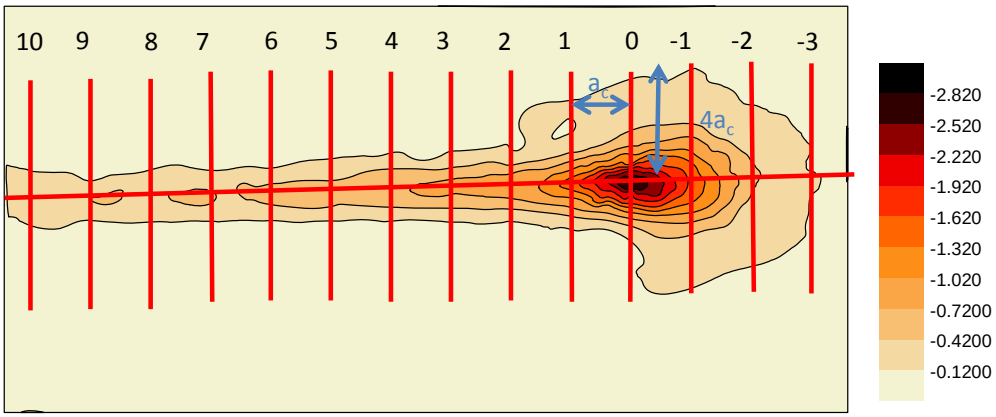

Figure V-32 From the 3D surface the presented red profile are extracted

A profile explaining the analysis is plotted in Figure V-33. On each profile an analysis is done to recover the depth (d) and the groove width (w). The depth is equal to the maximum minus the minimum altitude. The groove width is determined, using the distance between the points where the derivative is equal to zero.

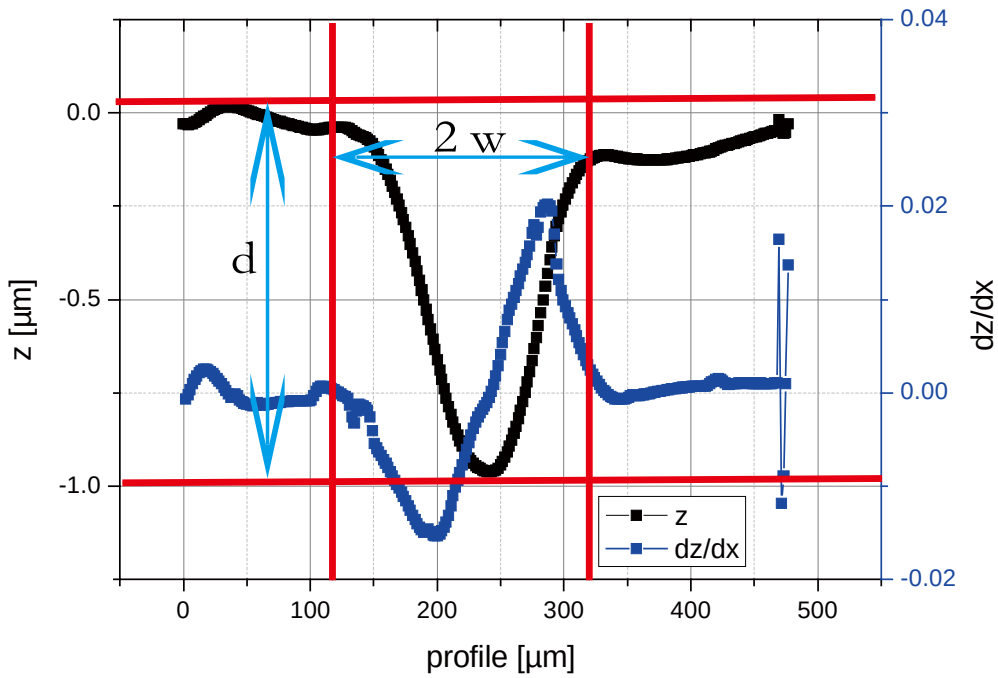

Figure V-33 Profile analysis to recover depth and groove width

V.5. OTHER CHARACTERIZATIONS

V.5.1. Optical microscope

Samples are observed under optical microscope. This instrument is more common than a Microvisioscratch and it gives a quick idea of the sample transparency, surface roughness and eventual presence of dirt on the sample. Figure V-34 shows on the left a clean transparent smooth sample, ideal for mechanical testing. Whereas on the right a dirty rough non transparent is presented. A scratch analysis is of course harder to conduct on this second surface.

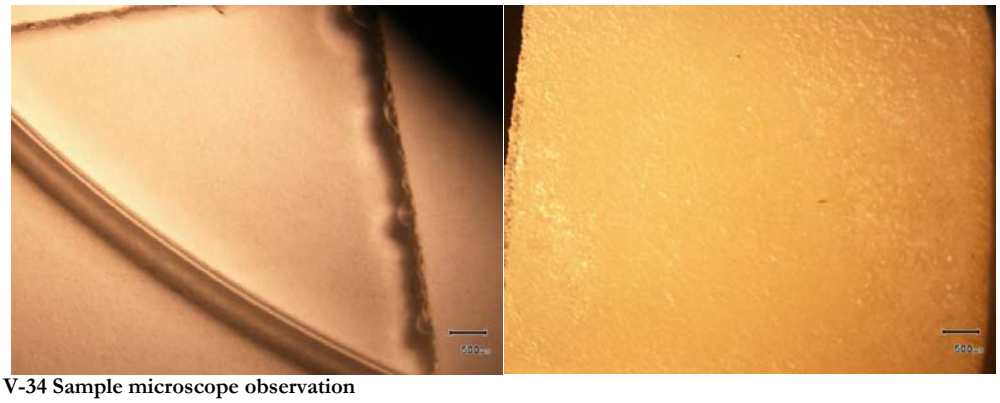

Figure V-34 Sample microscope observation

V.5.2. Differential scanning calorimeter

To precisely determine the materials transition temperature, a differential scanning calorimeter is used. Figure V-35 presents the PMMA vitreous transition temperature. The slope break in the curves, observed at the same temperature, occurs at 110°C.

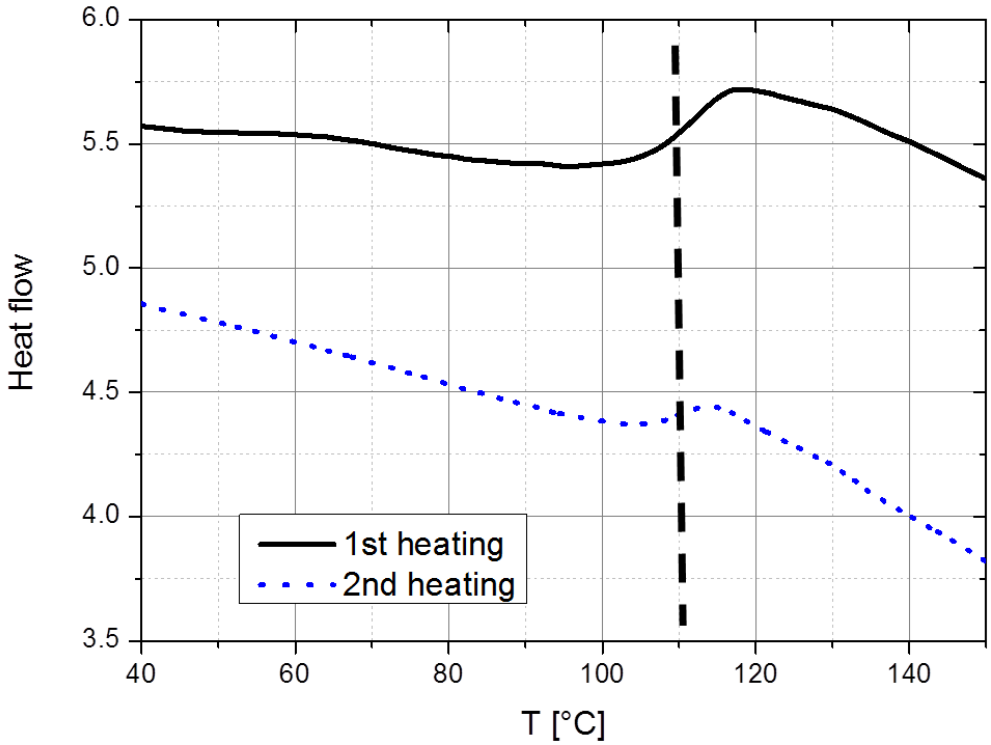

Figure V-35 Typical results presenting PMMA CN vitreous transition

V.5.3. Transmission Electron Microscopy (TEM)

The transmission electron microscopy is used to determine the fillers dispersity. For example, the sample observed in Figure V-36 presents some aggregates. Nevertheless a complete segregation is not observed.

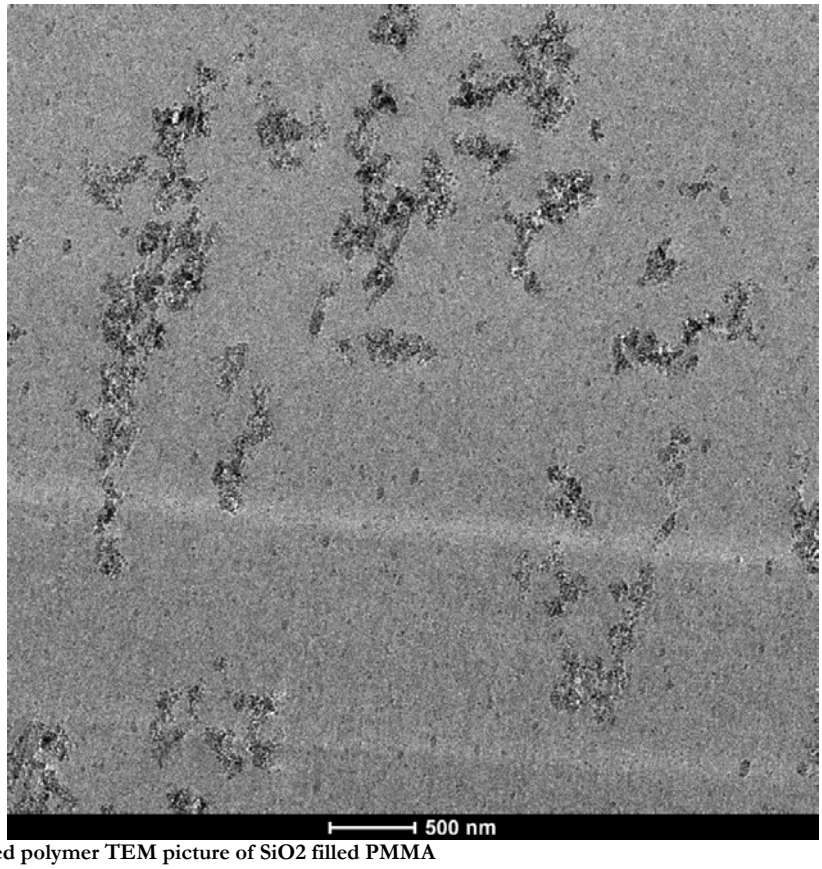

Figure V-36 Filled polymer TEM picture of SiO2 filled PMMA

V.6. CONCLUSION

Bulk mechanical properties are characterized by the Instron® uniaxial tensile and compression machine. Purely elastic and viscous properties are acquired through DMTA, relaxation, "creep-recovery" and cycling. Moreover contact properties are determined at three different scales. Classical Nano indentation method limitations are presented: the contact depth is not known, the recovery is difficult to observe. The Microvisioscratch® allows us to directly observe transparent material creep and recovery for a larger contact. Non-transparent polymers creep is observable through the tip in the modified uniaxial machine. The comparison between both creep measurements demonstrates the similarity of solicitation on the different scales. Furthermore the contact recovery properties were observed during and after a scratch test.

Finally basic polymer characterization was conducted to determine the surface "quality", the materials transition temperatures and the fillers dispersion and quantities.

V.7. BIBLIOGRAPHY

[1] Essilor, Essilor Crizal® Alizé® +, in.

[2] J.-P.D. Trotignon, A. ;Piperaud, M. ; Verdu, J. , Précis de matières plasiques, NATHAN ed., Edition Nathan, 9 rue Méchain,75014 Paris, 2006.

[3] S. Germany, Dispersible boehmites - DISPERAL / DISPAL, in.

[4] EVONIK, NANOPOX A products, in, EVONIK Industries.

[5] Evonik, Free flow with AEROSIL® fumed silica, in, 2013.

[6] J.L. Halary, F. Lauprêtre, L. Monnerie, Mécanique des matériaux polymères, Paris, 2008.

[7] I.M. Ward, Mechanical properties of solid polymers, Bristol, 1979.

[8] H. Hertz, Über die Berürhung fester elasticher Körper, Journal für die reine und angewandte Mathematik, 92 (1882) 156-171.

[9] A.C. Fischer-Cripps, The IBIS handbook of nanoIndentation, Fischer-Cripps Laboratories Pty Ltd, P.O. Box 9, Forestville NSW 2087 Australia, 2009.

[10] D. Tabor, The hardness of solids, Review of Physics in Technology, 1 (1970) 145.

[11] T. Chatel, C. Gauthier, H. Pelletier, V. Le Houerou, D. Favier, R. Schirrer, Creep of the contact with a spherical tip and recovery of the imprint on amorphous polymer surfaces, Journal of Physics D-Applied Physics, 44 (2011).

[12] C. Gauthier, R. Schirrer, Time and temperature dependence of the scratch properties of poly(methylmethacrylate) surfaces, Journal of Materials Science, 35 (2000) 2121-2130.

[13] C. Gauthier, S. Lafaye, R. Schirrer, Elastic recovery of a scratch in a polymeric surface: Experiments and analysis, Tribology International, 34 (2001) 469-479.

[14] W.C. Oliver, G.M. Pharr, Improved technique for determining hardness and elastic modulus using load and displacement sensing indentation experiments, J. Mater. Res., 7 (1992) 1564-1580.

[15] T. Chatel, Fluage et recouvrance d'empreintes et de sillons sur suface de polymère, in, Université de Strasbourg, Strasbourg, 2010.

[16] F. Mohs, über die Classification der Mineral Cörper, 1805.

[17] W. Shen, S.M. Smith, H. Ye, F. Jones, P.B. Jacobs, Real time observation of viscoelastic creep of a polymer coating by scanning probe microscope, Tribology Letters, 5 (1998) 75-79.

[18] J.S.S. Wong, H.J. Sue, K.Y. Zeng, R.K.Y. Li, Y.W. Mai, Scratch damage of polymers in nanoscale, Acta Materialia, 52 (2004) 431-443.

[19] M. Wong, G.T. Lim, A. Moyse, J.N. Reddy, H.J. Sue, A new test methodology for evaluating scratch resistance of polymers, Wear, 256 (2004) 1214-1227.

CHAPTER VI. EXPERIMENTAL RESULTS

CHAPTER VI. EXPERIMENTAL RESULTS 138
VI.1. INTRODUCTION 139
VI.2. COMPARISON BETWEEN BULK MECHANICAL PROPERTIES OF CR39, PMMA CN AND PMMA 10 ALO(OH) 139
VI.2.1. DMTA 139
VI.2.2. Relaxation 141
VI.2.3. Relaxation modulus and master curves 143
VI.2.4. Influence of environmental atmosphere 147
VI.2.5. Conclusion 148
VI.3. CONTACT ANALYSIS 148
VI.3.1. Indentation Creep 148
VI.3.2. Indentation Recovery 152
VI.3.3. Master curves comparison 156
VI.3.4. Scratch recovery analysis 157
VI.3.5. Conclusion 162
VI.4. INFLUENCE OF FILLERS ADDITION 162
VI.4.1. SiO_2 and AlO(OH) addition 162
VI.4.2. Comparison between other SiO_2 fillers with different end groups 165
VI.4.3. Conclusion 168
VI.5. CHAPTER CONCLUSION 168
VI.6. BIBLIOGRAPHY 170

VI.1. INTRODUCTION

This chapter illustrates all the experimental results obtained during this thesis. This thesis is the continuation of Thibaud Chatel PhD. Therefore lots of comparisons are conducted with the model material (PMMA CN) used in his thesis [1]. I used his raw data for PMMA CN and completed it when necessary. The objectives of this chapter are multiple: understanding the long time behavior of model polymers materials, analyzing the contact creep and recovery and presenting possible ways to improve contact properties.

First the bulk long time mechanical behavior of CR39, PMMA CN and PMMA 10 AlO(OH) is investigated. Especially the master curve construction is explained.

Then the comparison of the indentation creep and recovery of the two team model materials (CR39 and PMMA CN) are examined. Special focus is drawn on the contact creep and short time recovery after indentation or scratch.

Finally the filler addition influence is explored. Particular attention will be given to link material characterization and contact properties.

VI.2. COMPARISON BETWEEN BULK MECHANICAL PROPERTIES OF CR39, PMMA CN AND PMMA 10 ALO(OH)

In this chapter part, the bulk mechanical properties of the CR39, PMMA CN and PMMA 10 AlO(OH) are observed. First, DMTA experiment results are compared. Secondly relaxation experiments are presented. Thirdly the relaxation experiments are used to construct master curves. Finally a side study on the experimental proceeding (humidity) is performed.

VI.2.1. DMTA

Dynamic Mechanical Thermal Analysis (DMTA) experiments were conducted in the temperature range [-60°C: +100°C] at 0.05 Hz. Figure VI-1 presents the measured Young's moduli (filled symbols) and loss coefficient (open symbols) versus temperature for CR39 (red square), PMMA (blue circles) and PMMA 10 AlO(OH) (green triangle). The Young's moduli steadily decline over temperature. The PMMA CN Young's modulus is roughly 50% and 16 % higher than CR39 and PMMA 10 AlO(OH) Young's moduli respectively. Furthermore CR39 and PMMA 10 AlO(OH) Young's moduli dramatically drop toward high temperature. Over the temperature range, the loss coefficients trends slowly rise. PMMA CN loss coefficients present one peak at 0°C and a marked increase close to 90°C. PMMA 10 AlO(OH) loss coefficient shows the same trend but a few degrees lower. Finally CR39 loss coefficient has two peaks: one around 30°C and the second more intance around 65°C. The PMMA Young's moduli behaviors are classically observed in thermoplastic polymers[2]. On the contrary CR39 Young's modulus behavior is the signature of a thermoset polymer. The loss coefficient peaks mark the transition temperatures of the materials. Thus the CR39 vitreous temperature is around 65°C but as it is reticulated some mechanical

properties are still observed above the transition temperature (above 100°C). The observed smaller peaks, at lower temperature, correspond to the β transition temperature. The transition temperature are in accordance with other literature works [3-6] and DSC measurements. The slightly PMMA 10 AlO(OH) lower transition temperature than PMMA CN can be explained by a higher molecular weight of PMMA CN, a plasticizer effect or a combination of both [5].

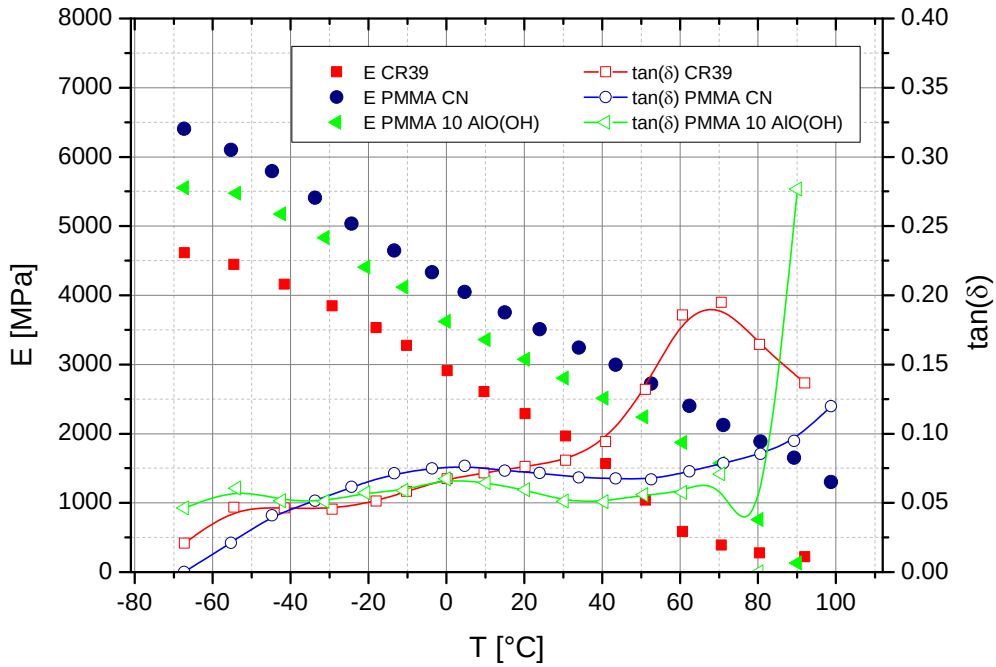

Figure VI-1 Comparison of Dynamic Mechanical Thermal Analysis experiment for CR39, PMMA CN and PMMA 10 AlO(OH) at 0.05 Hz

Figure VI-2 a) shows the DMTA results obtained for CR39 at different temperature and 3 frequencies. From these data one can build a temperature-frequency master curves as explained by Williams Landel and Ferry [7].

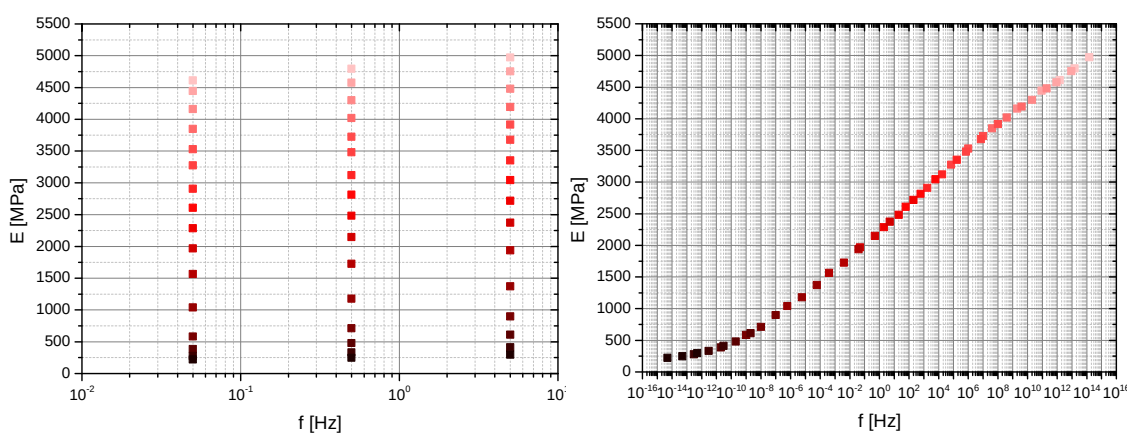

Figure VI-2 a) DMTA experiment on CR39 at different temperature and frequency b) frequency temperature master curves from the previous data

By converting the frequencies in time, one obtain the Figure VI-3 time-temperature master curves for CR39, PMMA CN and PMMA 10 AlO(OH). The master curves are done for a temperature of 30°C.

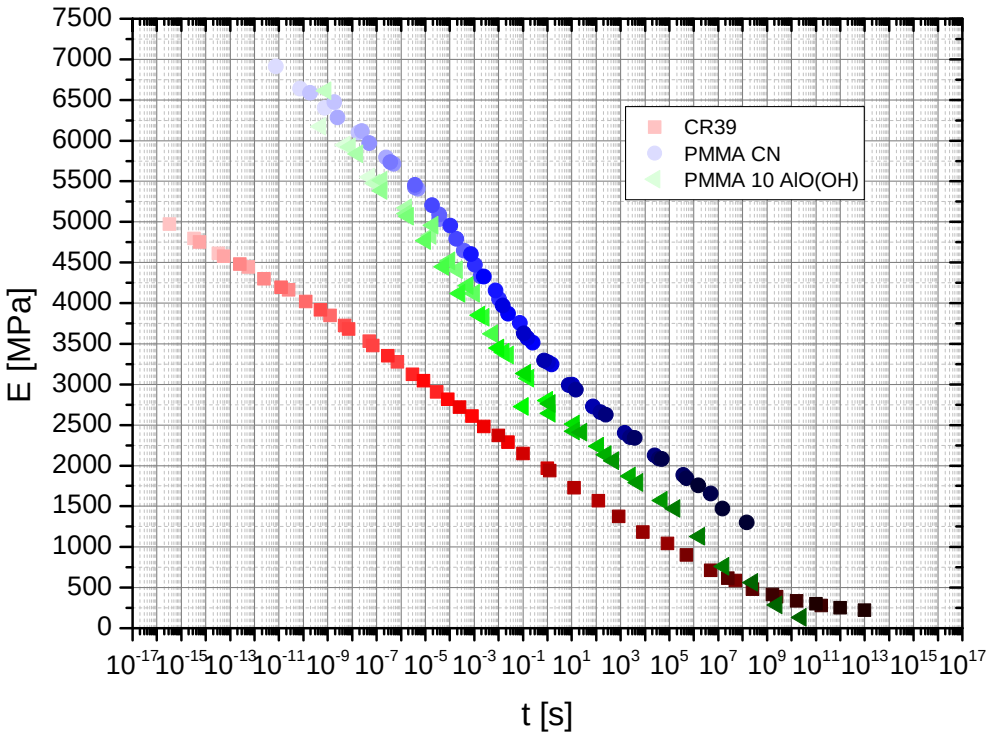

Figure VI-3 time-temperature master curves for CR39, PMMA CN and PMMA 10 AlO(OH)

VI.2.2. Relaxation

The instantaneous elasticity does not reflect all the possibility of the polymeric material. Indeed Struick [6] and other authors [4, 8] observed polymeric time dependency by creep or relaxation experiments. We chose to do compression relaxation. The compression was chosen because it is closer to indentation. The relaxation experiments were chosen because MSC Marc viscoelasticity is related to relaxation formalism [9].

The graphics, Figure I-3, Figure VI-5 and Figure VI-6 present the true stress versus true deformation and time for respectively CR39 PMMA CN and PMMA 10 AlO(OH) at 30°C. For all the curves 10 times the loading time are removed to prevent the observation from loading effects. The darkening gradient is used for an increasing deformation level [0.75-22%]. For each experiment the stress gradually declines over time. Furthermore, for CR39 (Figure I-3), the starting stresses grow up over deformation until 4% deformation (black dotted line). Then the starting stress drops by 10% and finally increases again (black dashed line). The material elasticity is responsible for the experimental starting stress at low deformation. Then when time and/or deformation increase CR39 time dependent elasticity evolves. At very high deformation the cross-linking blocks the material flow and thus increases the stress again. CR39 is elastic then viscoelastic.

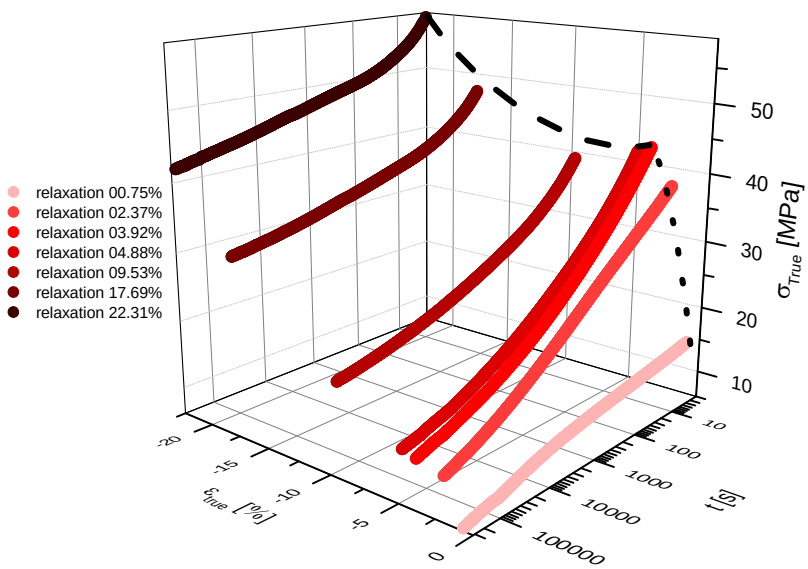

Figure VI-4 3D representation of a relaxation series on CR39 at 30°C (reproduction of Figure I-3)

In Figure VI-5, up to 4% true deformation, the true initial stress increases almost linearly with the strain. Above 4% deformation the true stress drops strongly. A 4% deformation is the elasticity limit of PMMA according to Jardret et al. [10]. Above this value the stresses drop is associated with PMMA plasticity. This is confirmed by the sample shapes: cylinders have a barrel like form after experiment at high deformation and not recover their initial shape. So PMMA is elastic at the beginning of the experiment then viscoelastic over time and plastic for deformations higher than 4%.

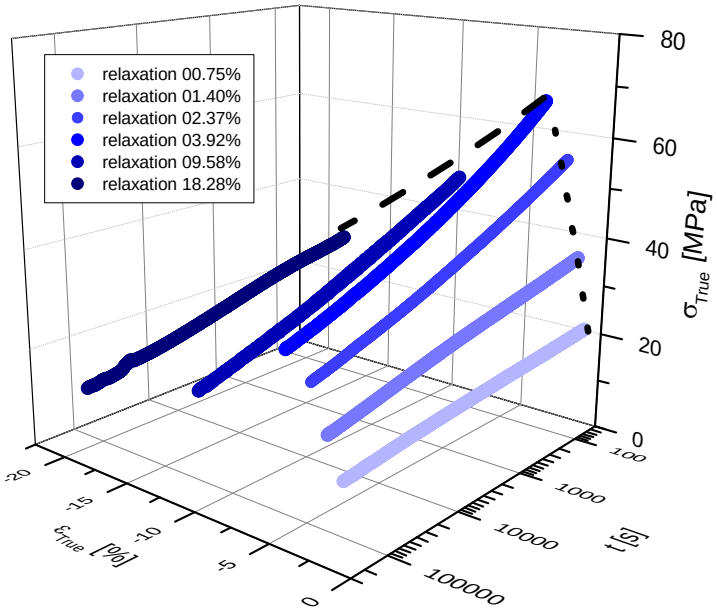

Figure VI-5 3D representation of relaxation series on PMMA CN at 30°C

Finally, Figure VI-6 presents PMMA 10 AlO(OH) relaxation experimental set. The observations are similar to PMMA CN. Thus the PMMA 10 AlO(OH) has an elastic behavior for short time and deformation. Followed by a viscoelastic behavior versus time. At high deformation plasticity effect is observed (slower starting stress). By comparing the three graphs together, the mechanical properties ratio, observed in DMTA, is verified under 4% deformation: PMMA CN true stress is respectively 50% and 16% higher than CR39 and PMMA 10 AlO(OH) true stress.

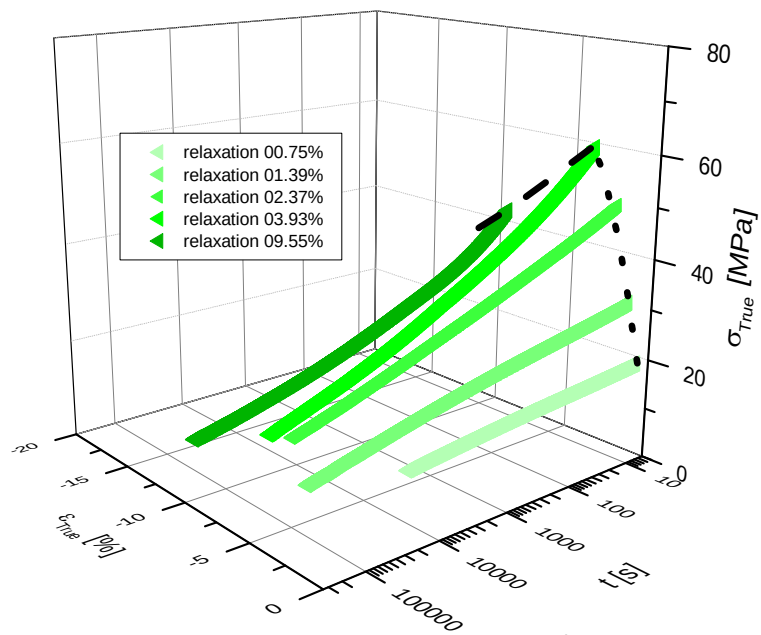

Figure VI-6 3D representation of relaxation series on PMMA 10 AlO(OH) at 30°C

VI.2.3. Relaxation modulus and master curves

These experimental sets are used to calculate the relaxation modulus over time (see Equation V-11). Figure VI-7 represents the CR39 elastic moduli versus time. For each curve the relaxation modulus is decreasing. The higher deformation leads to smaller relaxation modulus. Finally the 0.75% deformation relaxation is convex whereas all higher deformation relaxations are concave. Master curves versus strain, not temperature, were already proposed by several authors on high density Poly-ethylene (HDPE) [11], Polypropylene [8, 12], Polycarbonate (PC) [13, 14] or Poly(vinyl acetate)[15]. By translating (horizontally uniquely) Figure I-4 a) curves, one can construct a master curve of the relaxation modulus. To do so a reference is chosen: the relaxation at 0.75% deformation. Then the experimental time is multiplied by a shift factor called a_T. The obtained curve is shown in Figure VI-7 b). The strong decrease of relaxation modulus over deformation is now present over time. Indeed the relaxation modulus dramatically dropes to 10% of its initial value after 30 million centuries. At this point the relaxation modulus seems to reach a plateau. This is probably due to the CR39 cross-linking that blocks the flow. Finally the truncated and inverted "S-like" observed shape can be related to three different regime of relaxation: elastic (not present in the Figure VI-7 and related to the instantaneous response), short time viscoelasticity, long time viscoelasticity.

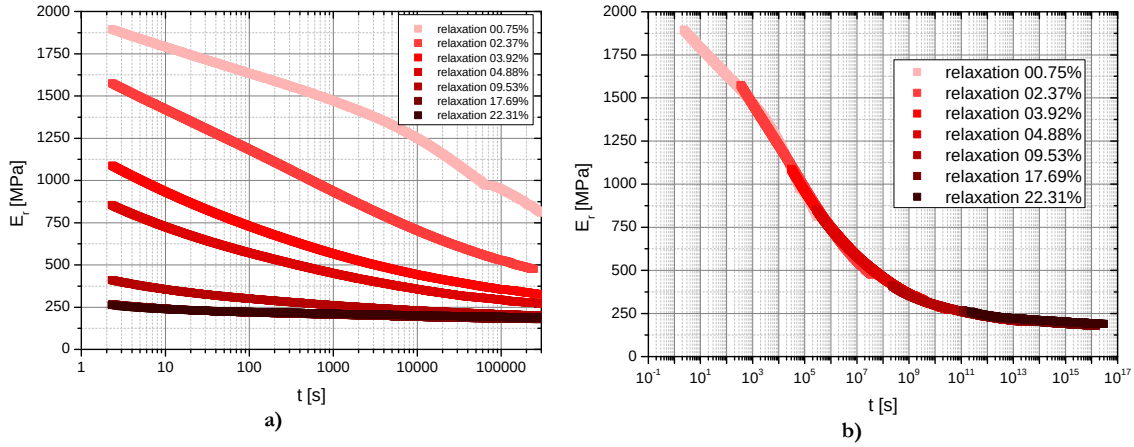

Figure VI-7 a) Relaxation modulus for CR39 at 30°C, b) Relaxation modulus master curve for CR39 at 30°C with 0.75% deformation as reference (reproduction of Figure I-4)

The same calculations were done on PMMA CN to construct Figure VI-8a) curves. As before the convex and concave shapes are observed. The obtained values are, for those available, in accordance by Lu et al. and Sane et al. [16, 17]. However the curvature is less pronounced than for CR39. Then the curves were more shifted to form a master curve (Figure VI-8b)) than for CR39. The "S-like" shape is still here but the time spread is much higher (100 000 times longer). The curves shape is associated as before to elasticity, short time viscoelasticity and long time viscoelasticity.

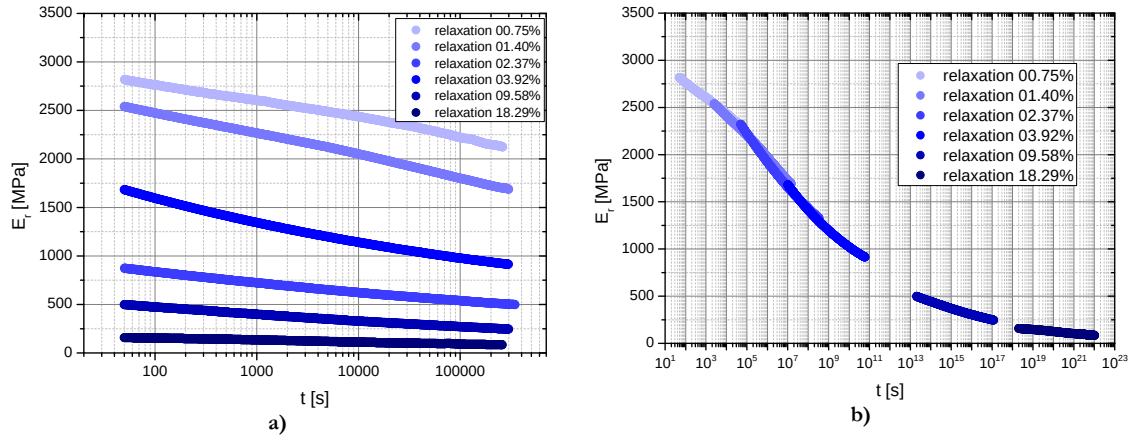

Figure VI-8 a) relaxation modulus for PMMA at 30°C b) relaxation modulus master curve for PMMA at 30°C with 0.75% deformation as reference

Finally the calculations were conducted on PMMA 10 AlO(OH) relaxation experiments. The curves presenting the relaxation modulus versus time are shown in Figure VI-9a). Whereas the shifted ones are presented in Figure VI-9b). The decrease of the relaxation moduli is also observed. Like for the previous materials the "S-like" shape is observed. Nonetheless the curvature is even lower than for PMMA CN. Possible explanations for this behavior are a smaller molecular weight or a break in the polymer entanglements due to the presence of (creating smaller domain and then a liquid behavior).

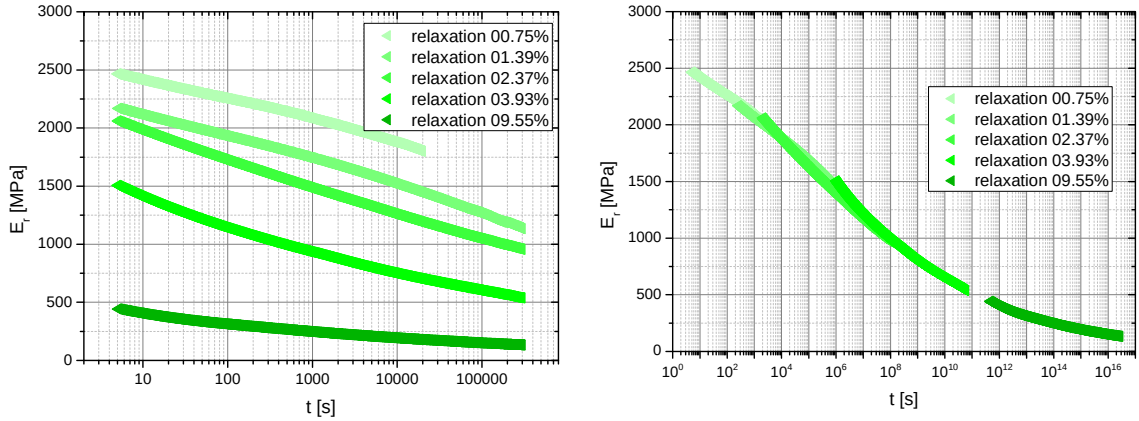

Figure VI-9 a) Relaxation modulus for PMMA 10AlO(OH) at 30°C b) Relaxation modulus master curve for PMMA 10 AlO(OH) at 30°C with 0.75% deformation as reference

A general remark has to be done on this data set. McKenna[14] presents comparison between time-temperature and time-strain master curves. The final conclusion of his work is non-equivalence between the both master curves. As the time-temperature master curves are widely accepted and used, he stipulates that in the case of Polycarbonate at least the time-strain master curves are inaccurate.

The shift factors, used for the relaxation moduli, are plotted versus the true deformation in Figure VI-10. As all the master curves were taken relative to the smaller deformations, in all cases the first point is (0.75%, 1). CR39 (red square) shift factors steady increase up to 5% true deformation. Then, between 5 and 25 % true deformation there is a gradual increase. PMMA CN (blue circles) and PMMA 10 AlO(OH) (green triangles) have very similar behaviors. The shift factors increase linearly versus deformation up to 5%. The CR39 shift factors slows donwn whereas above 5% true deformation, the shift factors for PMMA CN and PMMA 10 AlO(OH) continue to increase almost linearly. CR39 shift factors stagnation suggests that above 5% the cross-liniking slow down the material flow. On the contrary for PMMA CN and PMMA 10AlO(OH), flow is almost proportional to the imposed deformation. As both PMMA samples have the same flow behavior, let us conclude that the fillers not block the creep process into the material.

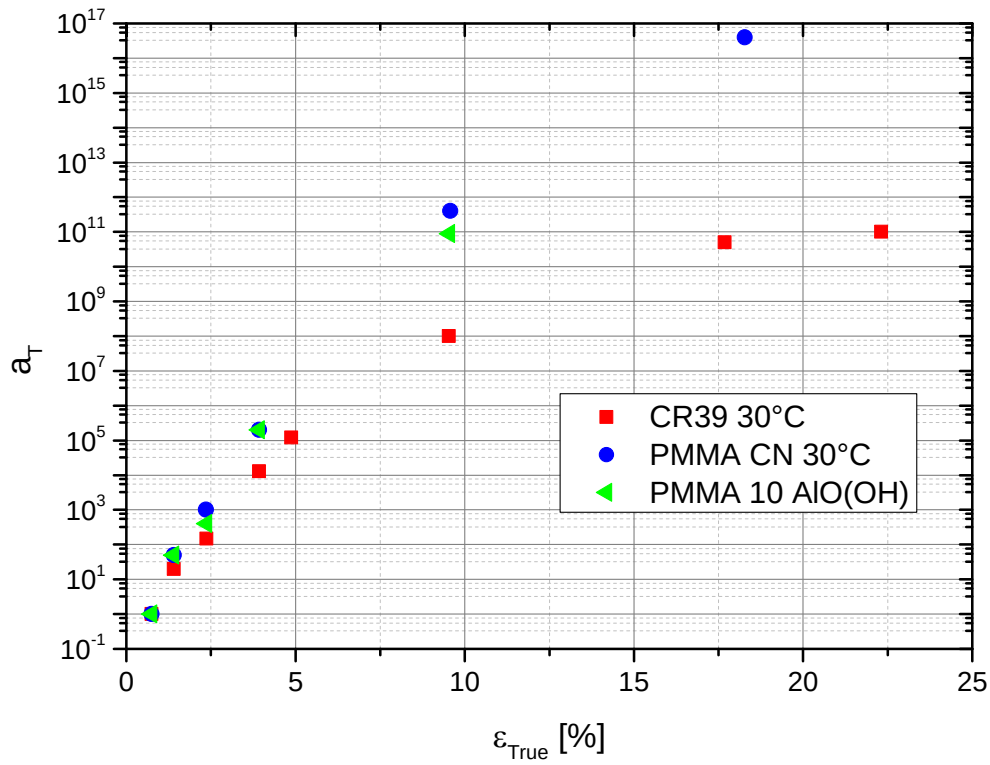

Figure VI-10 Shift factors for the different materials versus true strain (reproduction of Figure I-5)

Figure VI-11 presents the combination of the two different master curves. The first master curves are obtained by DMTA experiments and centered at 30°C. The second master curves are the time-deformation master curves previously discussed. No further shift was used, neither horizontal nor vertical. A very good agreement is observed but the DMTA values are slightly lower than the relaxation modulus. This is probably explained by a non equivalent strain in the relaxation and the DMTA experiments.

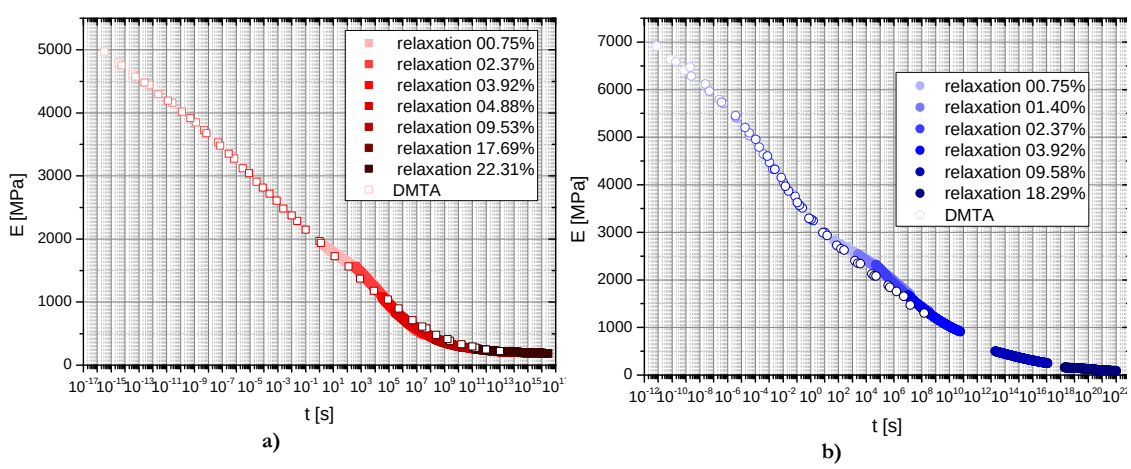

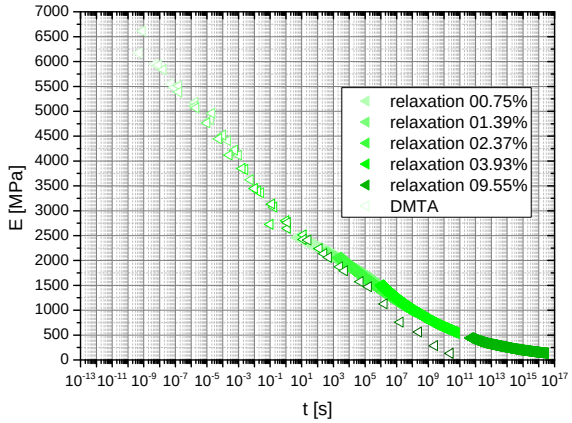

c)

Figure VI-11 Combination of the time temperature and the time-deformation for a) CR39, b) PMMA CN and c) PMMA 10 AlO(OH)

VI.2.4. Influence of environmental atmosphere

For each material the relaxation experiments were conducted in a relatively short time range (roughly 2 winter months). The year period is important because buildings are heated in winter. Then the relative humidity is relatively low (around 30%). Whereas in summer the relative humidity is directly the outdoor humidity. The CR39 is particularly influenced by the relative humidity. Three experiments were conducted under different atmosphere, the first was done in spring during a rainy day then the second in winter and finally a sample was held in an oven for 24 hours at 60°C. The relaxation moduli for these three experiments are presented in the Figure VI-12. The starting relaxation modulus is ambient relative humidity dependent. The higher the relative humidity, the lower the relaxation modulus. Furthermore, the decreasing rate is also relative humidity dependent. The higher the humidity is, the lower the decreasing rate is. This moisture influence is also confirmed and observed by Knauss and Kenner on Poly(vinyl acetate) [18] or on Polyvinyl alcohol by Cheng et al.[19].

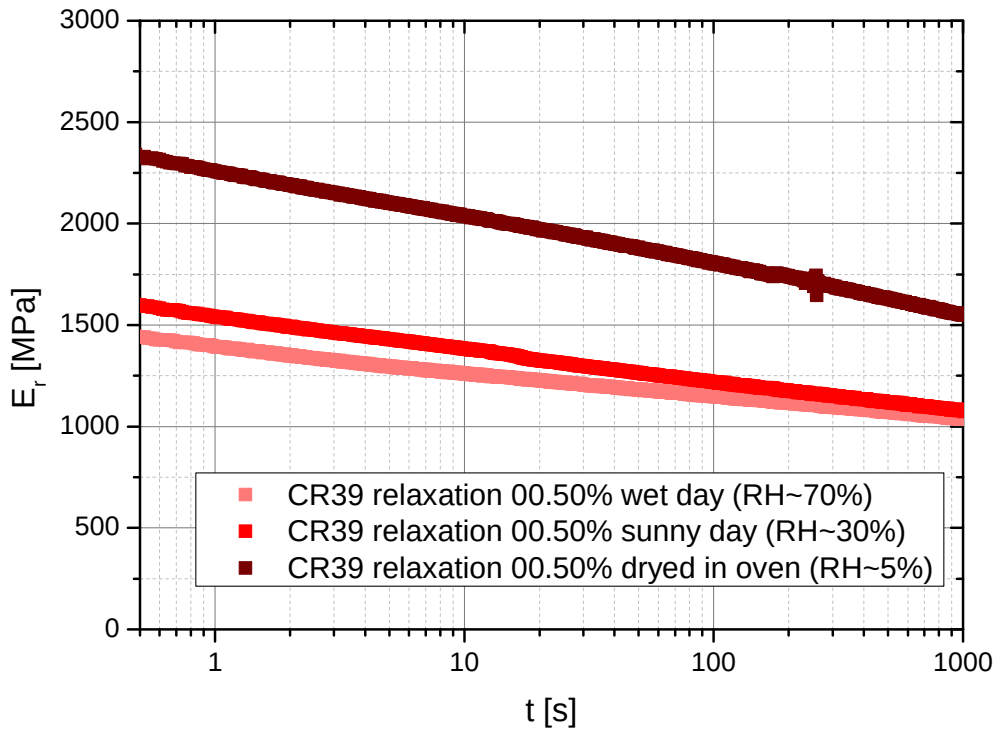

Figure VI-12 Influence on the experimental relaxation modulus of CR39 depending on ambient atmosphere

VI.2.5. Conclusion

The bulk mechanical properties of CR39, PMMA CN and PMMA 10 AlO(OH) were analyzed by DMTA and relaxation experiment. We observed higher Young's modulus for PMMA CN than for PMMA 10 AlO(OH) which is higher than CR39. The relaxation of these materials were observed over long times. The construction of master curves at the glance of 0.75% enables the prediction of the material viscoelastic comportment over centuries. Finally it should be pointed out that CR39 has a humidity dependent behavior. Thus we can highlight that all our experiments are done under controlled temperature and atmosphere.

VI.3. CONTACT ANALYSIS

The chapter part presents comparison between different materials mechanical contact behavior. The optical and esthetical properties of polymers can be strongly affected by indentation or scratch [20]. Thus this chapter part is divided in three parts. The first concerns the indentation creep. Then the indentation recovery is evaluated. Finally the scratch recovery is analyzed.

VI.3.1. Indentation Creep

Indentation creep of both polymers is first conducted at room temperature. Very long indentation creep times are used. Then a set of temperatures is chosen to cover the utilization temperature of polymers in general.

VI.3.1.1 Room temperature

The creep comparison of CR39 and PMMA CN is presented in Figure VI-13. The mean contact pressure (left) and normalized Tabor deformation (right) are displayed versus indentation time. An explanation on these notations is held in part V.4.2.1. All the creep loads are chosen so that the initial Tabor deformations are equal to 0.2. Nonetheless the starting mean contact pressure of CR39 and PMMA CN follow the observed ratio in Figure VI-1. CR39 mean contact pressure decreases linearly versus logarithm of time. On the contrary PMMA CN mean contact pressure decrease seems to have two distinct slopes. The first is below 100s, the second is above 1000s. Although the initial deformation is the same, the path of the normalized deformation is different for each material (Figure VI-13 b)). PMMA CN deformation increases quickly and then seems to reach a maximum then the creep speed decelerates. On the contrary the CR39 has an initial slower creep speed and accelerates afterwards. Finally similar deformations are obtained at the end of experiment. Thus the recoveries are comparable. The slowdown in PMMA CN creep can be attributed to the apparition of plasticity or a change in the viscoelasticity phenomenon, whereas the creep acceleration in CR39 is associated with an evolution of the viscoelasticity.

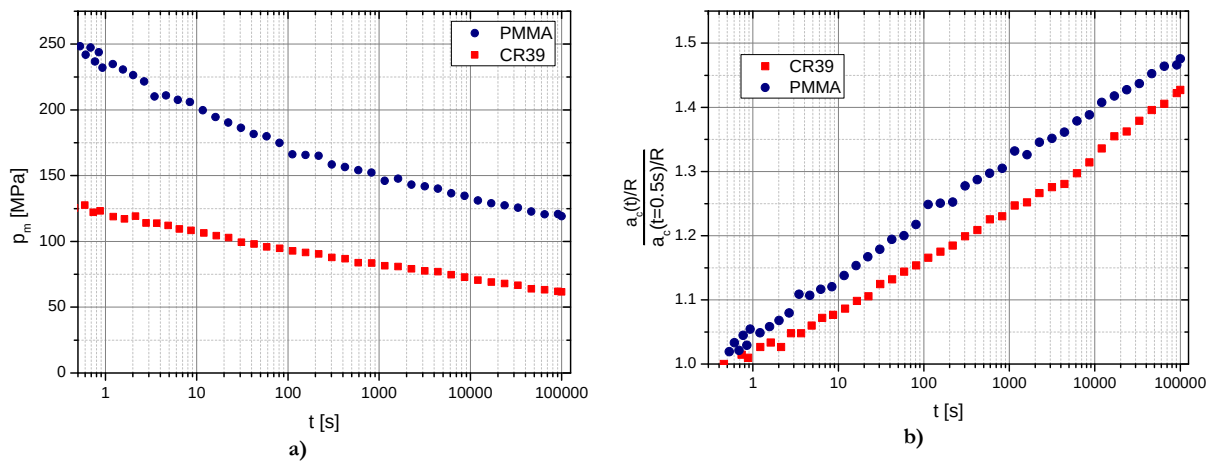

Figure VI-13 Mean contact pressure (a) and Normalized indentation creep deformation (b) versus creep time for CR39 and PMMA at 30°C (reproduction of Figure I-6)

VI.3.1.2 Influence of temperature

Polymers are very strongly temperature dependent, thus their contact behavior can also be explored over temperature [21-23]. In this part the mean contact pressure and the normalized Tabor deformation are studied separately for clarity reasons.

VI.3.1.2.1 Mean contact pressure

Indentation creep experiments were conducted at different temperatures on CR39 and PMMA CN. The mean contact pressure versus time and temperature for CR39 and PMMA CN, available in both case, are presented in Figure VI-14. In all cases the mean contact pressure decreases slowly as a function of the logarithm of time but the decreasing slopes are temperature and material dependent. The slope is almost the same for the two lower CR39 temperatures, and then it is strongly increasing over temperature (the mean contact pressure decrease slower for high temperature than for low temperature). Furthermore the ratio of the mean contact pressure at the

beginning of the experiment for one material at two different temperatures is equal to the ratio of the Young's modulus for the same material at the same temperatures. For example CR39 Young's modulus at -20°C is roughly 80% higher than CR39 Young's modulus at 20°C. The CR39 mean contact pressure at -20°C is also 80% higher than the CR39 mean contact pressure at 20°C. These data, slopes and initial mean contact pressure, suggest as expected that the instantaneous mean contact pressure is mostly dependent on the Young's modulus whereas the creep is not.

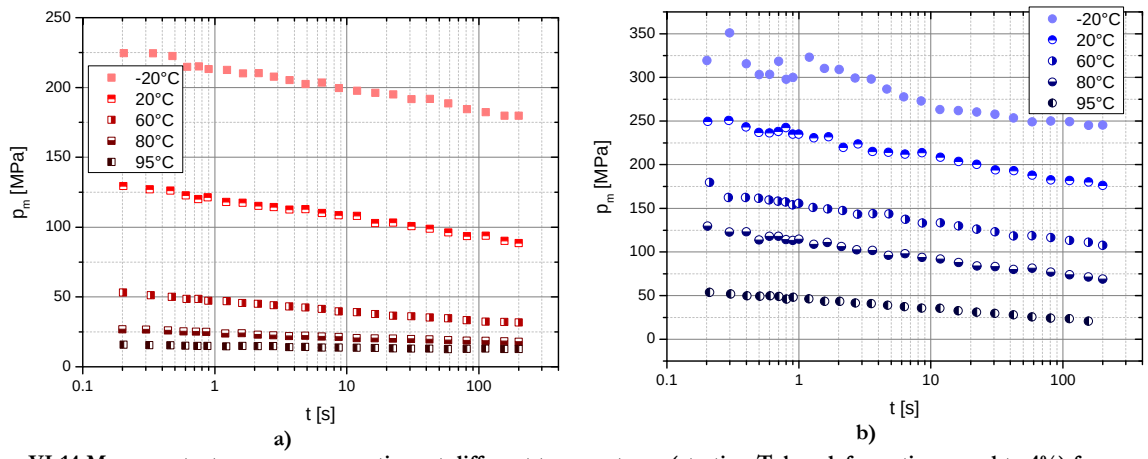

Figure VI-14 Mean contact pressure versus time at different temperatures (starting Tabor deformation equal to 4%) for CR39 (a) and PMMA CN (b)

Subsequently, the curves in Figure I-7 can be shifted laterally to form master curves. Figure VI-15 presents the mean contact pressure versus time at all available temperatures. The chosen reference temperature is 30°C. The CR39 curves strongly decrease as a function of time until it reaches 10^7 s. The bending occurs for a temperature of 60°C. This is explained by the glass transition of CR39. After this transition temperature/time, the material is retained by the cross-linking and the measured mean contact pressure is stable. PMMA CN mean contact pressure also decreases over time, but a shoulder is observed around 0°C. Moreover Figure VI-1 demonstrates the presence of a beta transition around 0°C for PMMA CN, then one can conclude that the transition temperature slow down the indentation creep. Some other authors already presented indentation master curves but they used the creep compliance [11, 24]. The available data, Figure I-6, are in accordance with the so constructed master curve.

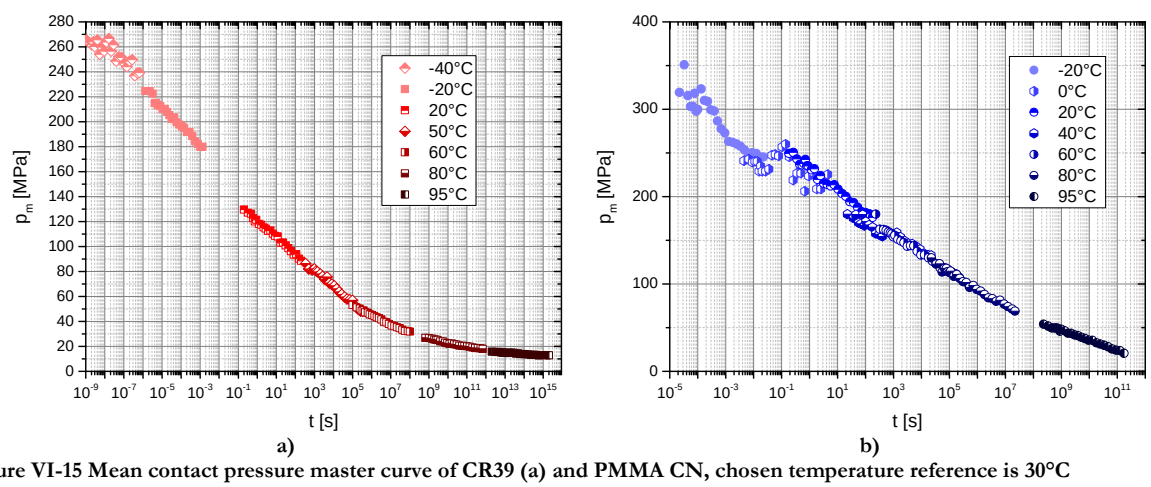

Figure VI-15 Mean contact pressure master curve of CR39 (a) and PMMA CN, chosen temperature reference is 30°C

VI.3.1.2.2 Normalized Tabor deformation

In addition to the previous data, the normalized deformation at different temperature over time is shown in Figure VI-16 for CR39. The graph on the left shows the temperature below the glass transition whereas the graph on the right shows the temperature above. The normalized Tabor creep deformation rise over time. Below the T_α, the higher the temperature, the more important the creep is. On the contrary above the T_α, the higher the temperature, the smaller the normalized Tabor creep deformation is. This behavior is typical for thermoplastic polymers viscosity below T_α and elastomeric or rubber-like behavior above T_α. Actually this behavior is more often observed in uni-axial creep test. A rubber sample is placed in an adiabatic chamber above its glass temperature, and then the temperature is elevated. A sample contraction is then observed [25]. Our experiments, conducted at constant temperature but comparing different temperatures, reflect the same effect.

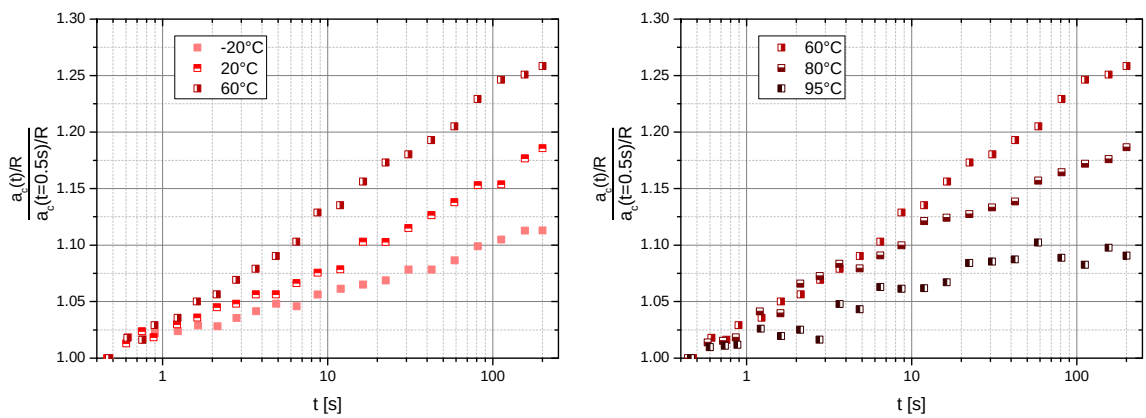

Figure VI-16 Normalized creep Tabor deformation versus time below (a) and above (b) the glass temperature of CR39

The normalized creep Tabor deformation of PMMA as a function of time and temperature is represented in Figure VI-17. The higher the temperature, the more important the creep is. This behavior is typical for a polymer below its T_α. All the temperatures below 95°C possess a logarithm of time linear behavior. On the other side after the 10 first seconds of creep at 95°C, the curve maintains the linearity (linearity is highlighted by the black line). Then the normalized creep Tabor deformation is 160% of the initial deformation. As it is clearly another creep regime. The recovery of this indentation will not be studied in the Indentation Recovery part (I.4.2).

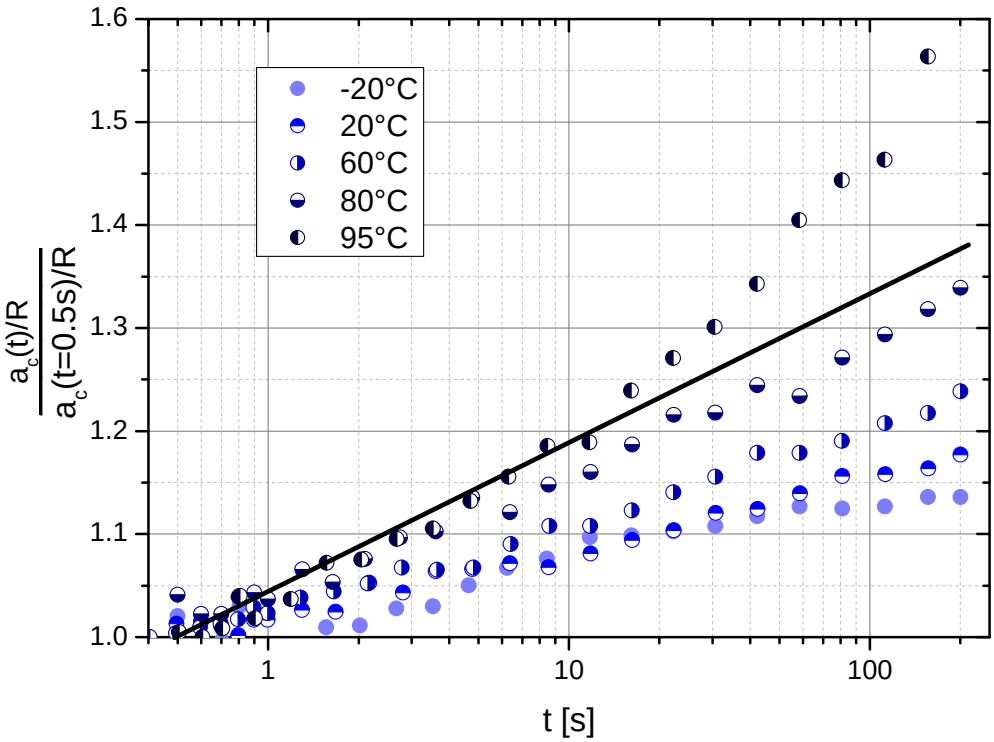

Figure VI-17 Normalized indentation creep deformation versus creep time for PMMA CN at different temperature

VI.3.2. Indentation Recovery

The indentation recovery observation is done through the normalized indentation recovery deformation. As it is normalized by the Tabor deformation at the end of the previous creep experiment the values are between 1 and 0. Nonetheless the phenomenon comprehension is complex: a difference in recovery can be due to the parameter difference (material, temperature, indentation creep time …) or to the end of indentation state (already discussed in previous part). It would be ideal to end the creep at the same Tabor deformation for all experiment. As it would require a very large number of experiments (trial and error process), the start Tabor deformation (a/R=0.2 at 0.5 s) is used. Moreover during the recovery two phenomena occur: the deflection around the indenter (elastic and viscoelastic) and the imprint (combination of elastic viscoelastic and plastic properties) recover. The major changes occur during the first seconds of recovery, thus the optical focus is hard to obtain and the image quality is poor. The larger the imprint, the more difficult it is to obtain reliable data. Hence a gray shaded triangle is drawn on the unreliable data. These chapter parts will present the comparison of the recovery of CR39 and PMMA CN at room temperature, at different temperature and finally after different indentation creep time.

VI.3.2.1 Room temperature

In Figure VI-18, the normalized recovery deformation is observed versus the recovery time. Both curves seem to drop to ¾ of the initial imprint deformation then PMMA CN recovery deformation decreases to 25% of its initial value whereas CR39 recovery Tabor deformation decreases until less than 5% of the initial imprint deformation (the imprint is no longer measurable). Furthermore the decreasing slopes are different for PMMA CN and CR39. PMMA CN recovery seems to slow down at 100s and almost stop after 10 000s. On the contrary CR39

recovery has 2 slopes: one between 10 and 1000s and the second one between 1000s and 1 000 000s. The immediate recovery of 25% can be associated in both cases to the material elastic recovery. The delayed recovery is the sign of a viscoelastic behavior. The CR39 two slopes can be associated with two different Viscoelastic behaviors. The PMMA CN recovery is associated with two phenomena. First the PMMA CN Viscoelasticity enables the beginning of the recovery. Then the recovery progressively enters in the plastically deformed material, thus the recovery speed gradually slows down until it stops. The recovery analysis illustrates then in which case the material is plastically deformed and in which case it is not, information that we could not determine simply by the indentation creep analysis.

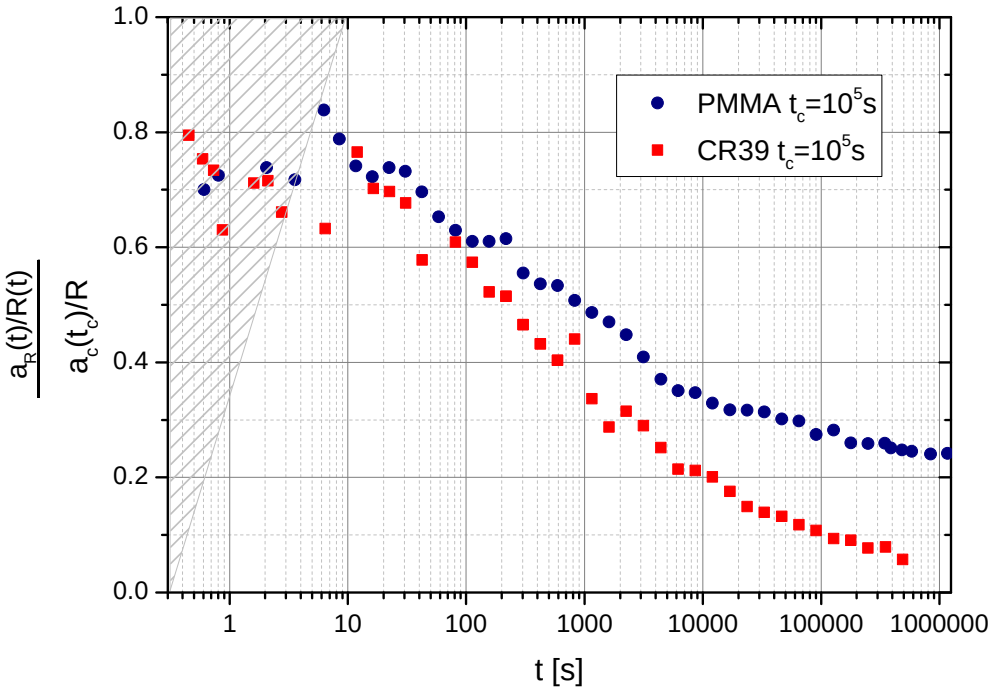

Figure VI-18 Normalized indentation recovery deformation versus recovery time for PMMA and CR39 at 30°C (reproduction of Figure I-8)

VI.3.2.2 Influence of temperature

The normalized indentation recovery deformation versus time for temperatures below (left) and above (right) glass transition temperature are shown in Figure VI-19. All the curves strongly decrease over time until an almost full recovery (Indeed the scattering system does not enable the measure of very small imprints.). The major observation for both these graphs is that, at least, 60% of the imprints recover within 1 second. 10 minutes is generally the elapsed time between end of contact and end of AFM or profilometry imaging process [26-28]; at that moment one can observe 95% of recovery. Furthermore the recovering slopes are linear versus the logarithm of time. For these short indentation creep times, only viscoelasticity, non-necessarily linear, is observed below and above the glass transition temperature.

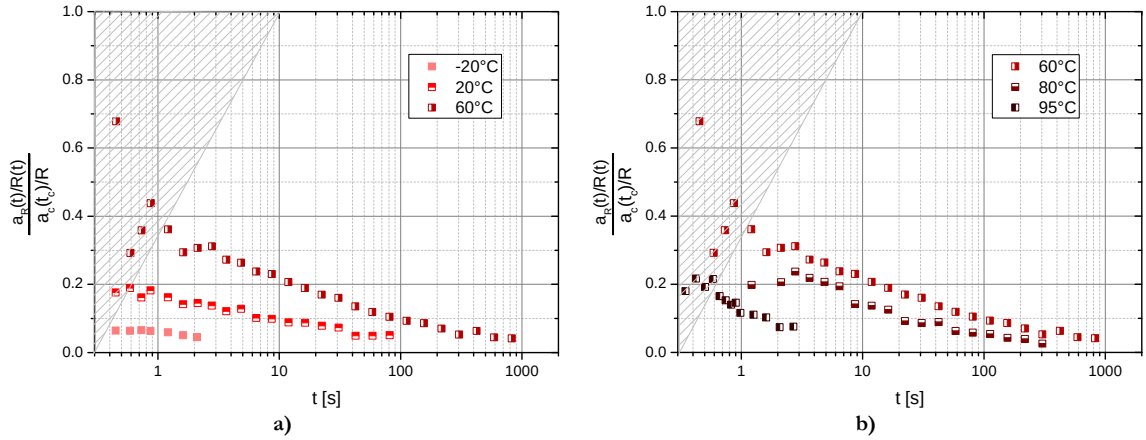

Figure VI-19 Normalized indentation recovery deformation versus recovery time for CR39 at temperature below (a) and above glass temperature

For PMMA CN, as the temperature increases the final creep deformation increases as well (see Figure VI-17) but not outside the observed value for CR39 (see Figure VI-16) (if we exclude the experiment conducted at 95°C). PMMA CN indentation recovery deformation is observed in Figure VI-20 versus time and temperature. The elastic recovery is present and proportionally more pronounced at the lower temperature. The lowest temperature being the only one were a linear slope over the logarithm of time can be observed. Then by increasing the temperature, the progressive apparition of plateau values is observed on the figure. The -20°C experiment illustrates a typical viscoelastic behavior. At higher temperature the progressive appearance of a permanent deformation demonstrates a plastic behavior.

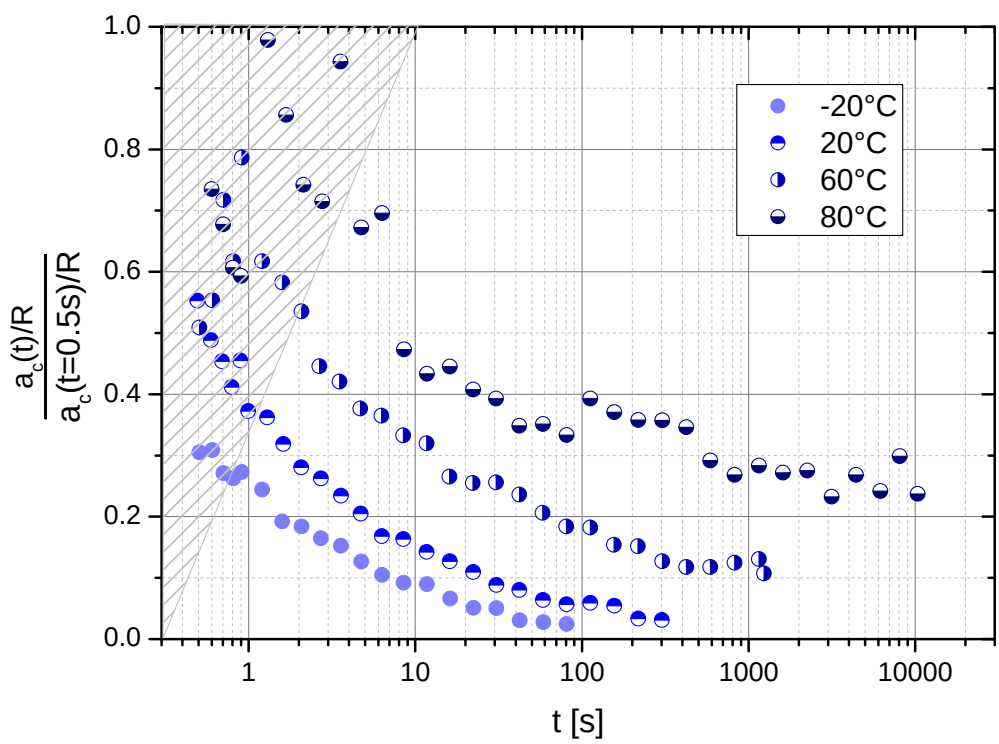

Figure VI-20 Normalized indentation recovery deformation versus recovery time for PMMA CN at different temperatures

VI.3.2.3 Influence of creep time

Several experiments were conducted with different creep times. Five different holding times were chosen, one per time decade. The creep is the same as the one observed in Figure VI-21 b), but cut at the corresponding time. Thus the final Tabor deformations are different. CR39 and PMMA CN indentation recovery deformation versus time and creep time are shown in Figure VI-21. For CR39 (left) all indentations fully recover. The recovery after 100 s, or less, of indentation is linear over the logarithm of time. Whereas two different slopes are observed for the two longest indentation creep time. The 1000 s indentation creep is an intermediate between the two behaviors. Furthermore for these three longer indentations the full recovery is observed in roughly ten times the indentation creep. PMMA CN displays a similar behavior. Short time indentation (10 s) is linear over logarithm of time then all other indentation recovery illustrate the two slopes behaviors. When the creep time is below or equal to 1000 s, a full recovery is observed in PMMA CN; over 1000s of indentation creep only partial recovery is observed. Around 20% of the imprint is plasticized below the contact. CR39 once again illustrates a long time viscoelasticity with two major domains: below and above 1000 s. These two domains were also observed in the CR39 indentation creep. Thereafter PMMA CN displays two slopes of viscoelasticity and plasticity.

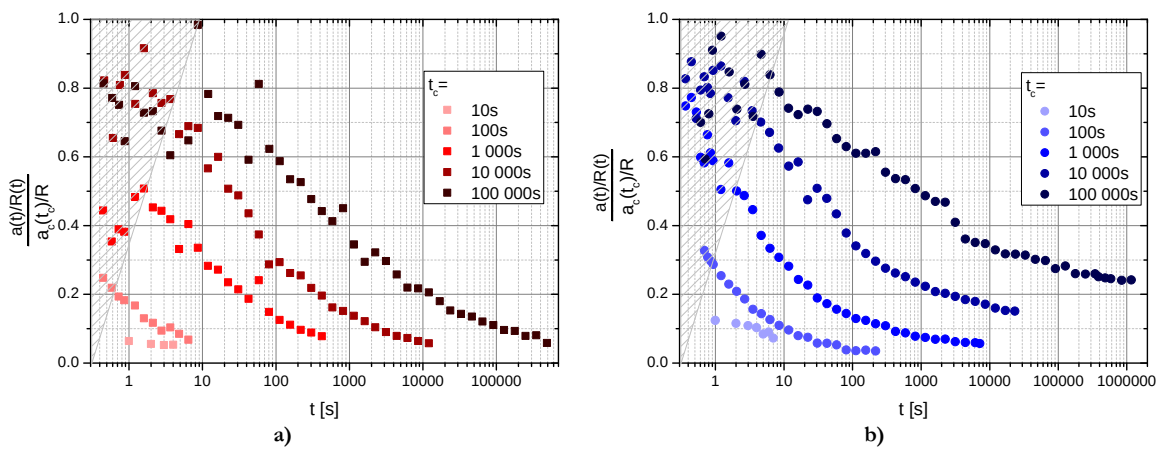

Figure VI-21 CR39 (a) and PMMA CN (b) normalized indentation recovery deformation versus time at 30°C after different creep holding time

VI.3.2.4 Partial conclusion

We observed the recovery of CR39 and PMMA CN versus time, temperature and creep time. The more important observation is the importance of instantaneous and short time (less than 10 minutes) recovery. This highlights the necessity to observe the contact during and very shortly after indentation. In all done experiments the CR39 fully recovers. In case of high indentation creep deformation, the recovery can be divided in two parts each having a linear slope versus the logarithm of time. PMMA CN also presents viscoelasticity versus the logarithm of time but also in certain more "extreme" cases it presents some plasticity.

VI.3.3. Master curves comparison

Thereafter, we acquired two different types of master curves. The deformation dependent master curves were done uni-axially with relaxation experiments. They are presented in Figure I-4 b), Figure VI-8 b), Figure VI-9 b) and Figure VI-11 for CR39, PMMA CN and PMMA 10 AlO(OH) respectively. As the bulk master curves present the relaxation modulus (measured in 1000 of MPa) and the contact master curves show the mean contact pressure (measured in 100 of MPa), they can not be compared directly. Thus we choose to normalize using a data point that both master curves have in common. All the CR39 values will be divided by the value of the data point [1.2s: 30°C: 4% deformation]. For the bulk master curves this corresponds to the relaxation modulus at the end of loading for the 3.92% deformation relaxation (1140 MPa). For the contact master curves this corresponds to the mean contact pressure after 1.2s of indentation at 30°C (125 MPa). The PMMA CN master curves will be divided by the data point [10s: 30°C: 4%] (different time because of different uni-axial loading time and thus different time cut). Thus the bulk and contact master curves are respectively divided by 1925 MPa and 200 MPa. With these reference points chosen, one has to shift horizontally the master curves to adjust these reference points respectively to [1.2 s, 1] and [10 s, 1]. The obtained master curves are shown for CR39 and PMMA CN in Figure I-9 a) and b) respectively. Bulk and contact master curves are very close for CR39 and PMMA CN. Thus, time, temperature and deformation affect the same mechanisms. Their respective influences over it are different. One other major observation is the fact that contact and bulk experiments can lead to the same master curves. Thus if the contact temperature dependence is not known (PMMA 10 AlO(OH) for example), it can be estimated with the whole bulk experimental set and one contact experiment. The reverse is also true: knowing the contact master curve and one Young's modulus the bulk master curve could be determined (this would be the case for thin layer). Moreover the influence of the plasticity can also be deduced from these curves. There is no plasticity in CR39 contact (see part I.4.2). On the contrary, there is plasticity in PMMA CN contact curves for the higher deformation and temperature and for the longer time. If there is plasticity in relaxation experiment, this occurs during loading and not during the stress relaxation which is purely viscoelastic. As the loading part was removed from the data, the bulk experiment display only viscoelastic behavior. As the curves shapes for CR39 and PMMA CN are similar with or without plasticity, the plasticity does not affect the viscoelasticity of polymers. Similarly if there was viscoplasticity, it should affect the time dependence. So there is no viscoplasticity in the tested polymers.

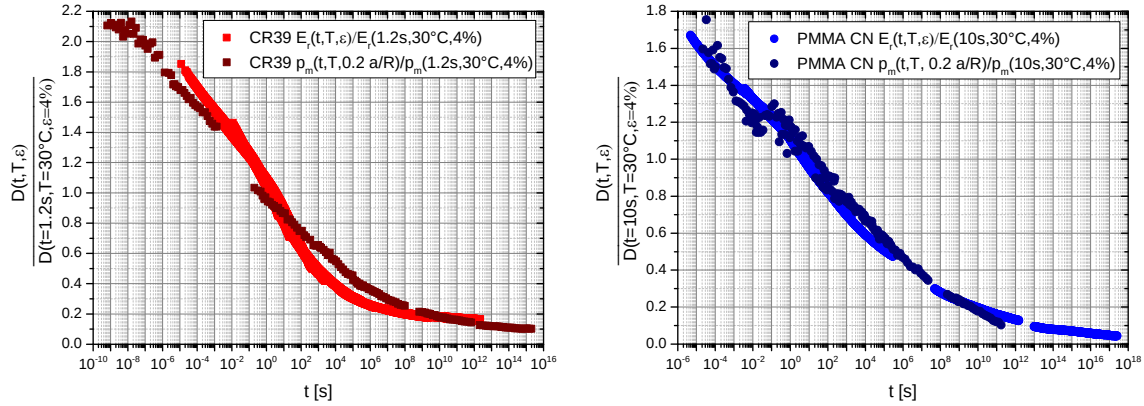

a) b)

Figure VI-22 Comparison of normalized Master curves out of relaxation and contact experiments for a) CR39 centered after 1.2 s of solicitation, at 30°C for a deformation of 4% and b) PMMA CN centered after 10 s of solicitation, at 30°C for a deformation of 4%

Moreover Figure VI-22 can be completed by master curves obtained from DMTA experiments (see Figure VI-11). Thus one obtains three differently produced master curves. The DMTA (time-temperature master curve), relaxation (time-deformation master curve) and the indentation (time-temperature-deformation master curve) master curves are coherent with each other. This adequacy is observed for both materials CR39 and PMMA CN in Figure VI-23. As a conclusion the phenomena occurring in the materials for the three experiments are similar whatever the temperature, deformation or time of solicitation.

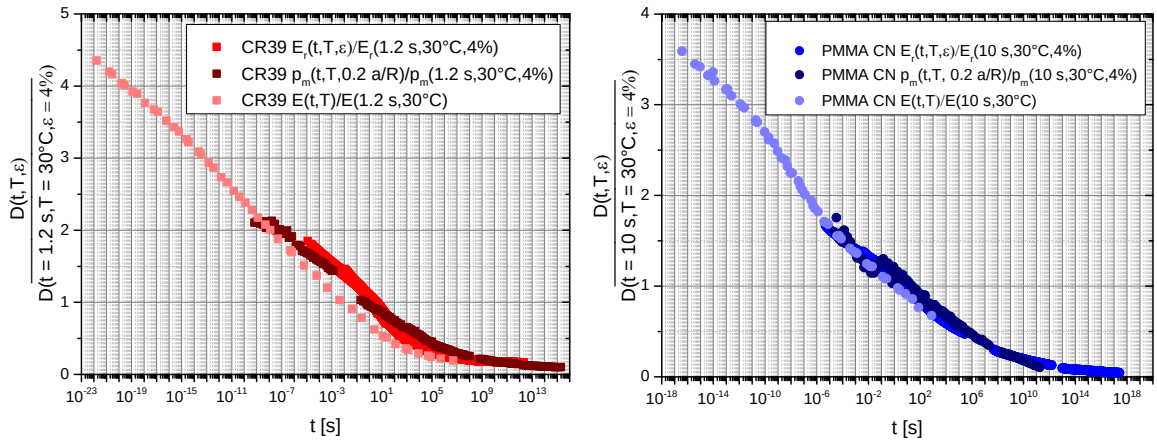

a) b)

Figure VI-23 Comparison of normalized master curves out of DMTA, relaxation and contact experiments for a) CR39 centered after 1.2s of solicitation, at 30°C for a deformation of 4% and b) PMMA CN centered after 10s of solicitation, at 30°C for a deformation of 4%

VI.3.4. Scratch recovery analysis

As we have observed and concluded from the previous part, the spherical indentation creep and recovery is a complex experiment, but close to real polymer degradation during static contact between two functionalized surfaces. Possible polymer degradations are scratching and marring. Thus in order to understand these degradations, mechanical characterizations of polymeric surfaces are also done by scratch experiments [29]. Nonetheless the comprehension is even more complex, indeed all difficulty observed in indentation are still present and one adds the complexity of a moving tip. First description of the groove recovery was given by several authors

[29-31]. Nevertheless no information was given before 10-15 minutes. In our case the recovery phase was observed on CR39 only with the Microvisioscratch system. Then the images were computed into a 3D representation of the sample. Finally some cross-profiles were extracted. The position of the cross profile is determined by their distance to the end of scratch. Distances are measured in multiples of the contact radius. This chapter part is divided into three subparts. First, general observations of the scratch recovery are conducted. Secondly, the influence of the charge is investigated. Finally the influence of the tip speed is examined.

VI.3.4.1 Scratch Generality

In the performed scratch neither cracking nor crazing were observed but only ductile behavior was observed. One example of a cross profile at a 4 a_c distance from end of scratch is presented in Figure VI-24. The graphs scales are not orthonormal; the y axis is 350 more zoomed than the x axis. So the groove appears sharper than it really is. The groove depth decreases over time. Furthermore on both sides of the groove, pile ups can be observed, they seem to decrease over time too. Then a shouldering is observed on the left side of the groove. This is due to the interpolation method.

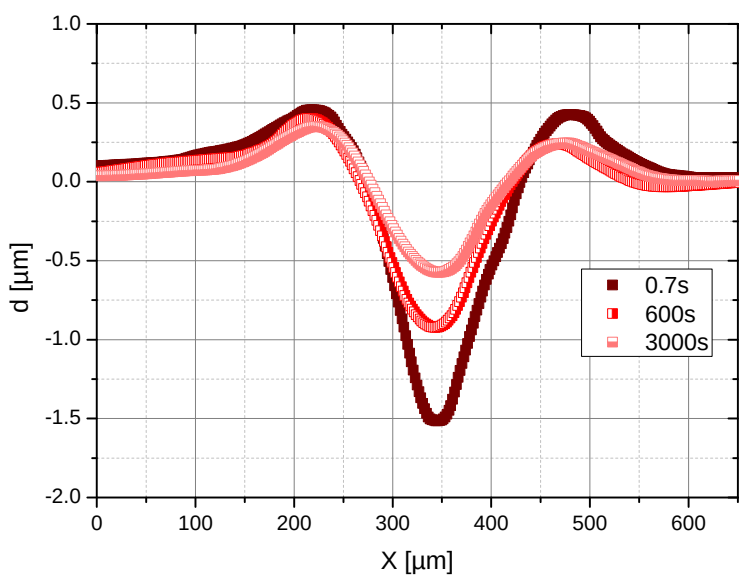

Figure VI-24 Three profiles taken at different times at a 4ac distance from end of scratch

The scratch depth recovery is observed versus recovery time at different distances from the end of scratch in Figure VI-25. The time displayed is the time elapsed since the tip removal from surface. This is not the same as the time since the tip passed over the material. Thus all the cross-profiles do not reflect the same recovery time. Additional complexity comes from the fact that all the material did not have the same mechanical history. Indeed in front and below the tip, the material is compressed and sheared, and then behind the tip the material is tensed. Furthermore on the scratch sides combinations of shear, compression and tensile deformation are observed. Thus the cross-profile at 0 a_c, image material which was submitted to less tensile stress than the material at 1ac which underwent even less than the one at 2 a_c. Nonetheless Figure VI-25 demonstrates that, the depth decreases as a function of time for all distances. All the curves join at the point [200 s: -0.4 µm]. Furthermore the scratch as up to a distance of 3ac seems to follow a different path even if we try to shift them laterally to take into account the different recovery

time. The difference probably comes from different mechanical history. We can then assume that at a 4ac distance from end of scratch the material lived almost all the mechanical solicitation. Therefore following studies will mostly be conducted at this distance.

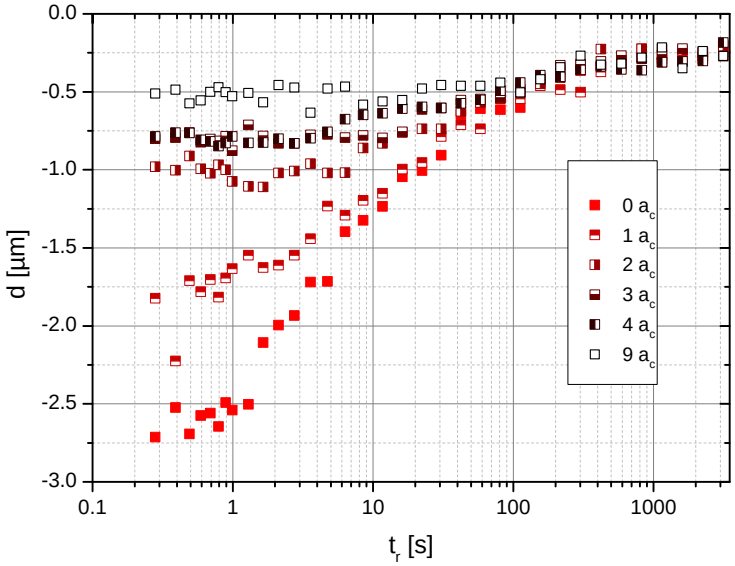

Figure VI-25 Scratch recovery depth of CR39 at 30°C versus time at different distances of the end of scratch (reproduction of Figure I-12)

In addition to the depth, the groove width can also be extracted from the computed surface. Figure VI-26 presents the groove width at a 4ac distance from the end of scratch versus time. The groove width slightly decreases over recovery time. The percentage of total width recovery is roughly 15%. This value must be compared with a 95% depth recovery in the same condition. Furthermore the data are generally more imprecise (the data are extracted from the derivative of the computed cross profile). These two informations, partially confirmed by Brostow et al. [32], lead us to mostly analyze the recovery depth.

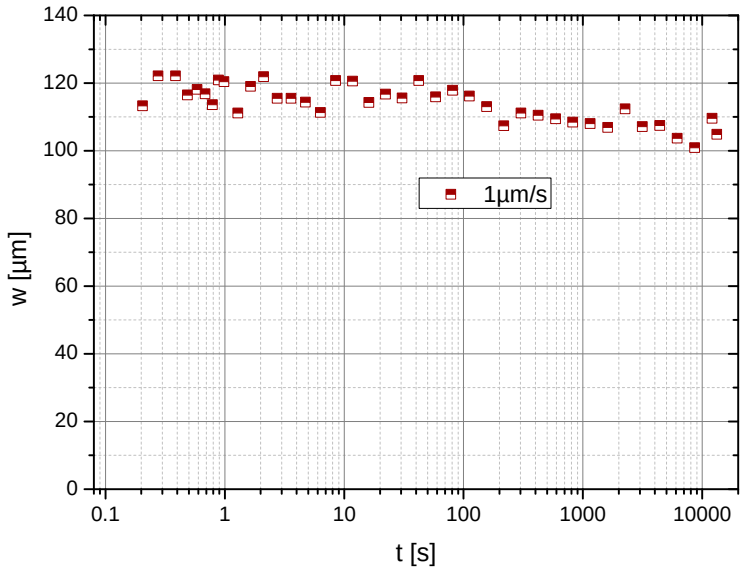

Figure VI-26 Recovery width at a 4aC distance from end of scratch versus time since tip removal on CR39 on an experiment with slow tip speed (1 µm/s, 2.5 N)

Figure VI-27 presents the recovery depth after scratch (left) and after indentation (right) for CR39 at 30°C. The depths in front of the tip are also observed. The depth at a_c is relatively important but this might be explained by the fact that the tip removal is done while the tip is still going forward. At 2 a_c and 3 a_c no pile up in front of the scratch is observed. On the contrary the surface is lower than the average. The recovery at 2 a_c and 3 a_c are proportionally (less than 20%) law in comparison with the groove recovery but it illustrates the importance of the deflection and its time dependent recovery. By comparison with indentation recovery depth, one can observe that deeper and more permanent deformations occur after a scratch than after indentations.

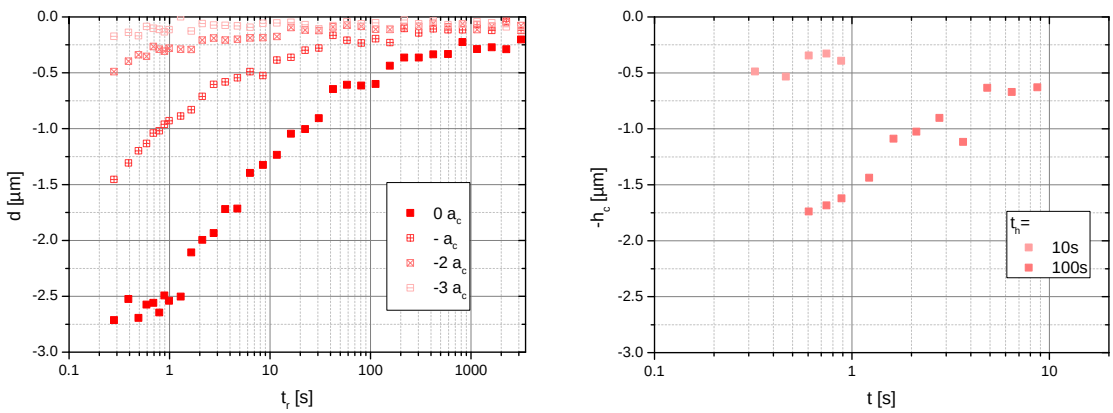

Figure VI-27 a) Depth recovery, at end and in front of scratch, versus recovery time after a scratch at p_m = 100 MPa and 10 µm/s b) Recovery contact depth after indentation at p_m = 125 MPa on CR39 in both cases

VI.3.4.2 Influence of the scratch deformation

As we have seen before, the material at -4ac was submitted to the whole mechanical history. Therefore all the following graphs concern the recovery observed for the cross profile at 4 a_c. Figure VI-28 a) shows the recovery depth over time and deformation. The chosen time origin is the time elapsed since the tip removal from surface. The different deformations are obtained through different load on the tip (from the smaller to the higher deformation 1, 2.5, 5 N). The contact depths measure respectively 3.6, 9.5 and 14 µm. In all cases there is a plateau value for the first 2-3 seconds of the measure. Then the depth decreases over time for all deformations. The final depths are very small compared to the contact depth. The plateau comes from the chosen time origin, the elapsed time since the tip center passed (or since the major strain took place) is about 30 s. Thus three more seconds of recovery do not influence strongly the recovery. The curves shape can give the impression of two different behaviors for different deformations. In order to compare the proportional recovery speed, the Figure VI-28 b) presents the same data but normalized by the first measured depth. The plateau value is still observed and the decrease speeds are identical. The curves are shifted. One possible explanation is again the time origin, as the deformations are different; the 4 a_c distance is different thus the time since the tip center passed is different. Therefore a small shift in time can occur.

In conclusion doubling the deformation increases the time to obtain a full recovery. Nonetheless the recovering mechanisms are similar because the normalized recovery is the same for all deformations. In all cases no measurable permanent deformation was observed.

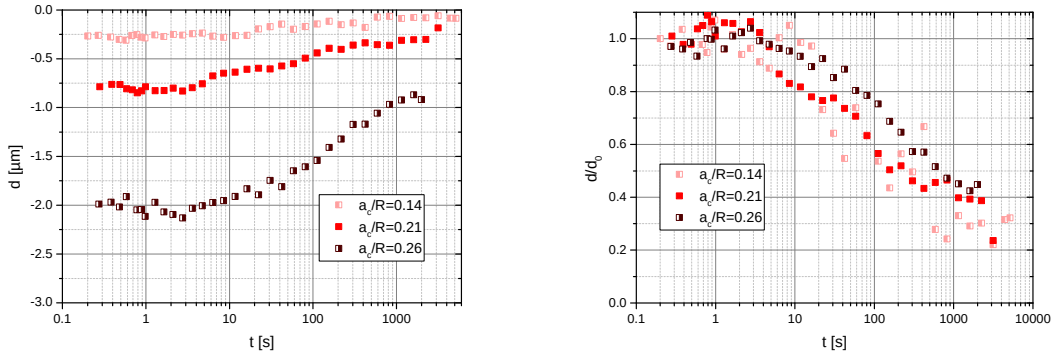

a) b)

Figure VI-28 a) Influence of the scratching Tabor deformation on the recovery depth at a 4 a_c distance from end of scratch versus time elapsed since tip removal on CR39 at 30°C b) same experience normed by the first measured recovery depth (reproduction of Figure I-13)

VI.3.4.3 Influence of the scratch speed

Figure VI-29 a) shows the recovery depth over time and scratch speed. At the beginning of the observation plateau value are observed. The plateau duration is 0.8, 3 and 10 seconds for the 1 µm/s, 10 µm/s and 100 µm/s respectively. The decreasing slopes are proportional for all the solicitations. The difference in tip speed implies a different time for the tip to travel along the 4ac distance. Thus the relative importance of the first recovery seconds increases with increasing tip speed, which is the reason why the plateau time changes. The curves shape similarity comes from the viscoelasticity response of the material for the whole tested range. Then the results observation conducted us to shift the high speed curves. The Figure VI-29 b) presents the recovery depth over shifted time. The shifts coefficient are 200 and 100 000 for 10 µm/s and 100 µm/s respectively. The master curve shows on a probable full recovery and groove disappearance of the experiment with the slower tip speed after 8 years.

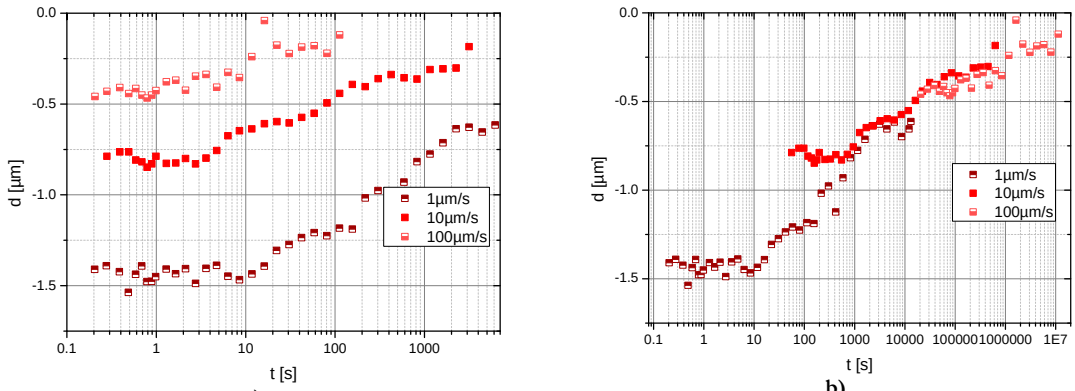

a) b)

Figure VI-29 a) Influence of the scratching speed on the recovery depth at a 4 a_c distance from the end of scratch versus time since tip removal on CR39 at 30°C b) Master curve obtained by laterally shifting the previous data

VI.3.4.4 Partial conclusion

The scratch recovery of CR39 was examined in this section. We observed that the computed surfaces enable us to follow the recovery as a function of time. Then the depths were plotted as a function of time and distance to the end of scratch (the distances were chosen as multiple of the contact radius). The 4 a_c distance corresponds to the shorter distance, thus the shorter elapsed

time, where the whole mechanical history occurred. The recovery is then only studied at this distance. Afterwards the load and scratch speed influences are studied. The higher the load, or the slower the scratch speed, the higher the beginning residual depth. Nonetheless the recovery was demonstrated to be proportional to each other in all cases, thus no plasticity was observed. Only long time (see master curve) viscoelastic behavior was observed.

VI.3.5. Conclusion

The indentation creep and recovery of PMMA CN and CR39 was studied. We observed that PMMA CN present viscoelastic behavior for low deformation and plastic behavior for high deformation. The high deformation can be triggered by a long indentation time or a high temperature. The recovery observation demonstrated that plastically deformed materials do not recover. On the contrary full recovery was observed for CR39 in all indentation experiments. Thus leading to the conclusion that the CR39 displayed a viscoelastic behavior on the whole tested range. Thereafter the construction of master curves demonstrated that the deformation, the temperature and the time influences the material differently, but always following the same rules. Finally a first analysis of the instantaneous scratch recovery was presented. The results analysis highlighted the importance of the tensile stress behind the indenter, leading us to further analyze the depth and groove at a 4 contact radius distance (where all mechanical history occurred). We noticed that the width recovers much slower than the depth. Moreover the scratch load and speed do not influence the proportional recovery. The curves were only shifted by a certain factor.

VI.4. INFLUENCE OF FILLERS ADDITION

Several filler additions were conducted in order to obtain reinforced transparent samples. Indeed a light, transparent, indentation and scratch resistant, material has a very high number of possible applications [20, 33, 34]. Nonetheless the creeping mechanism can lead to strong damages of the properties [35].

VI.4.1. SiO_2 and AlO(OH) addition

VI.4.1.1 General observation

Transmission Electronic Microscopy pictures of the filled samples are presented in Figure VI-30. The PMMA filled with 10% of nanopox (SiO_2 particles), Figure VI-30 a), presents small aggregates (500 nm). The aggregates are close from one another and let white spaces between aggregates packs. The PMMA 20 nanopox is filled with the same fillers but at a higher percentage (20%), Figure VI-30 b). The particles still make aggregates (500 nm) but there are more particles outside the agglomerates. Some spaces are nonetheless observed outside of the agglomerates. In both cases the particles are spherical with a diameter of 25 nm ± 5 nm. Figure VI-30 c) is a TEM image of PMMA 10 AlO(OH). In this case very big aggregates (6 µm) are observed. Furthermore a very small quantity of fillers is dispersed in the bulk. The measurable particles size is roughly of 30 nm ± 6 nm. Both nanopox filled PMMA are translucent whereas PMMA 10 AlO(OH) is matte.

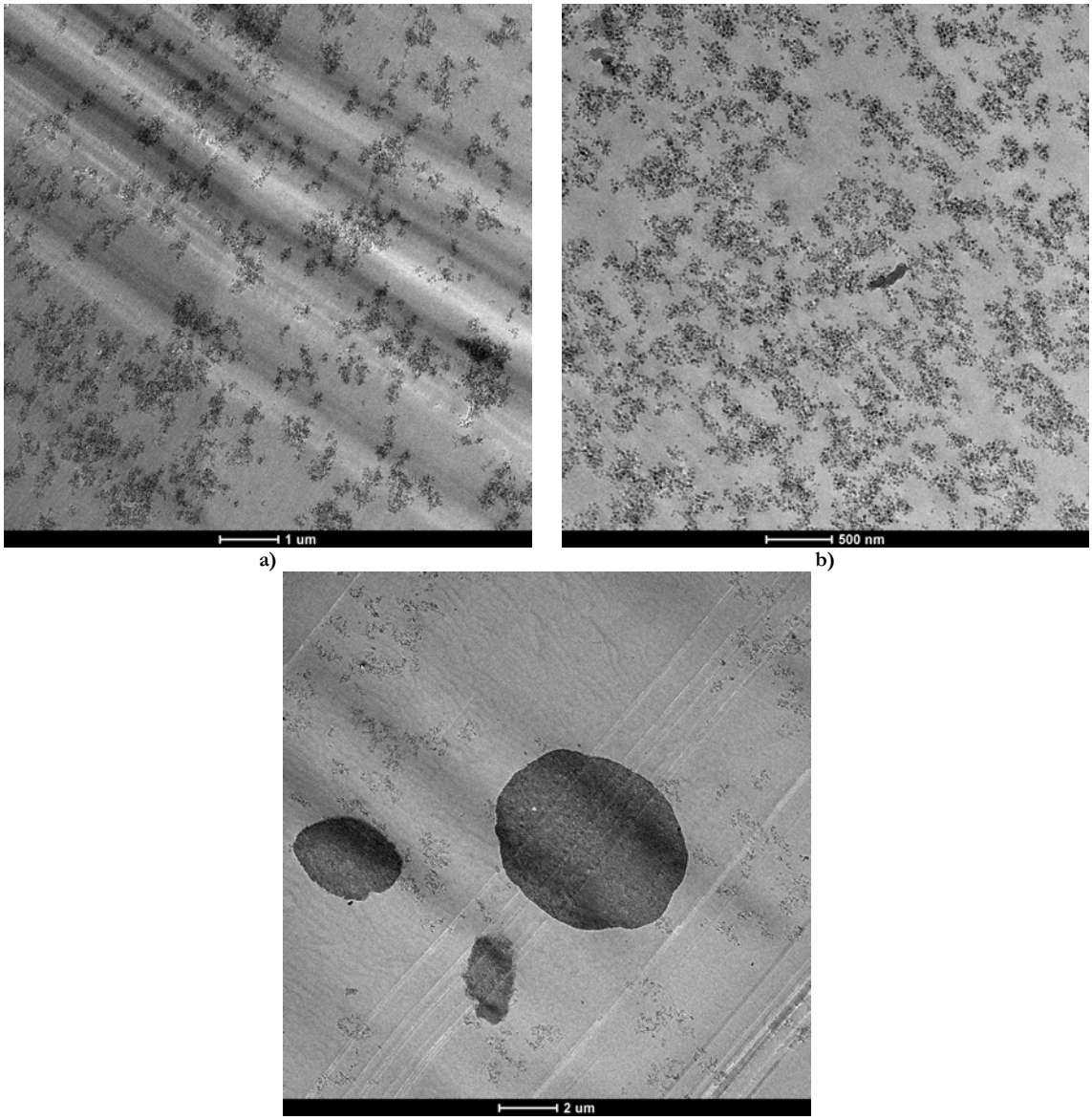

a) b) c)

Figure VI-30 TEM picture PMMA filled with a) 10% of nanopox b) 20% nanopox c) 10%AlO(OH)

The transition temperature of the materials are measured in DSC and presented in Table VI-1. The presence of particle strongly decreases the value of the glass transition temperature. In particular 10% of AlO(OH) lower the glass transition of 20°C. Moreover the addition of 10% of nanopox decreases less the glass transition. The further increase of particle seems to enhance the glass transition temperature. These effects are commented in the next part.

Material	DSC measured glass temperature
PMMA ba (basis)	114°C
PMMA 10 AlO(OH)	95°C
PMMA 10 nanopox	105°C
PMMA 20 nanopox	111°C

Table VI-1 results of the DSC experiments

VI.4.1.2 Bulk analysis

The Figure VI-31 shows the results of DMTA experiment on PMMA ba, PMMA 10 nanopox, PMMA 10 AlO(OH) and PMMA 20 nanopox. The Young's moduli and loss coefficient versus temperature at 0.05 Hz are presented on the two graphs. In all cases Young's moduli decrease strongly over temperature. The behaviors are thus similar to PMMA CN. For PMMA 10 AlO(OH) and PMMA 10 nanopox at low temperature there is a plateau (less marked for PMMA 10 nanopox). Then at high temperature the loss of mechanical properties occurs earlier. Moreover in the temperature range [-40°C: 60°C] the Young's moduli are ordered from smaller to higher value PMMA 10 AlO(OH), PMMA ba, PMMA 10 nanopox and PMMA 20 nanopox. Thus one can conclude that nanopox increase the mechanical properties of PMMA: the higher the percentage (in the tested range) the higher the Young's moduli. On the contrary PMMA 10 AlO(OH) decreases the Young's moduli of the samples. Furthermore the addition of particles tends to shift the glass temperature towards low temperatures. This was indeed observed in the previous part VI.4.1.1. This assumption is supported by the fact that the addition of external plasticizer is known to decrease the T_α [2].

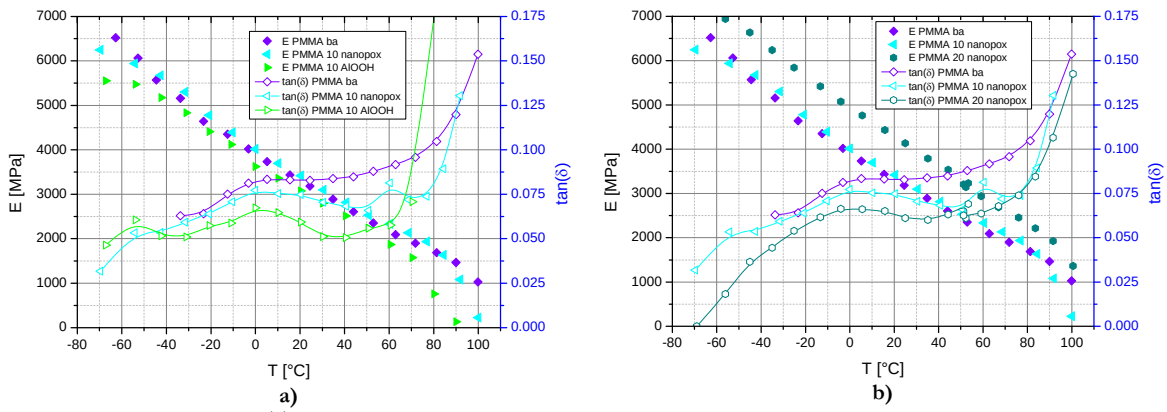

Figure VI-31 Comparison of DMTA experiment for different fillers (a) or different fillers quantity (b) at 0.05Hz

VI.4.1.3 Indentation analysis

Thereafter the filled samples are indented with the macro-indentation machine. This new macro-indentation machine was developed during this PhD. The Figure VI-32 presents the results of macro indentation creep on PMMA ba, PMMA 10 AlO(OH), PMMA 10 nanopox and PMMA 20 nanopox. On the left the mean contact pressure over time is shown. The PMMA ba mean contact pressure decreases from 250 MPa to 110 MPa over 100 000 s. This curve has to be compared with the almost identical data observed for PMMA CN (see Figure I-6 a). Then 10% filler addition slightly increases the mean contact pressure for the whole experiment. Finally the 20% nanopox addition increases the mean contact pressure by 25%. Figure VI-32 b) shows the normalized creep deformation over time. The information presented in this graph is a bit noisy. Nonetheless it seems that curves with fillers are below the curve without fillers. Thus one can conclude that fillers improve the material by requiring a higher mean contact pressure and eventually slightly slowing down the PMMA creeping.

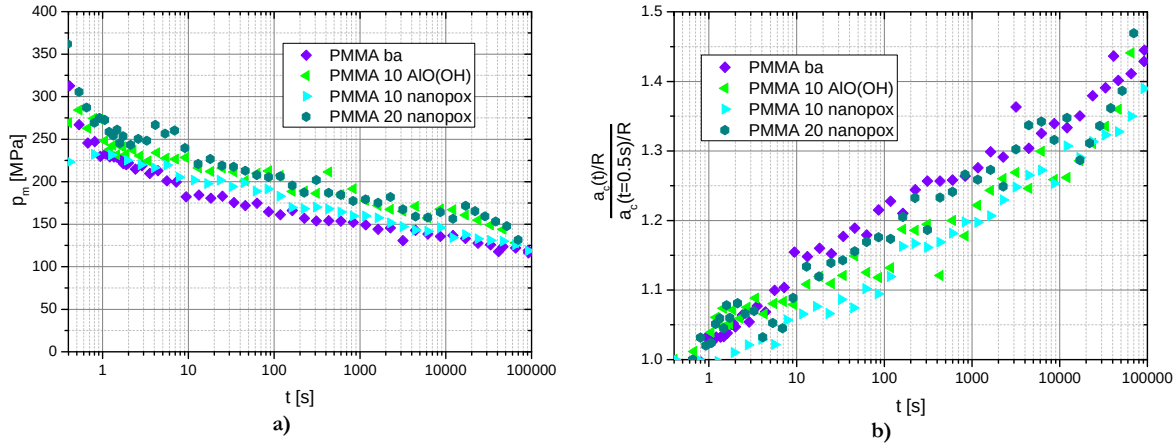

Figure VI-32 a) Mean contact pressure over time and b) Normalized indentation creep at 30°C for PMMA filled with AlO(OH) and nanopox

Figure VI-33 presents a prediction of the mean contact pressure versus time for PMMA 10 AlO(OH). The master curve in Figure VI-11c) is used. In order to make this value proportional to a mean contact pressure, the values are multiplied by the instantaneous mean contact pressure of PMMA CN (see Figure I-6 a)) over PMMA CN Young's modulus at 30°C (see Figure VI-1). The macro indentation mean contact pressure data for PMMA 10 AlO(OH) are added on the curve. The mean contact pressure master curve demonstrates by this method a first row approximation. Indeed, if the mean contact pressure is not known, not measureable, this method would give an approximation of the mean contact pressure.

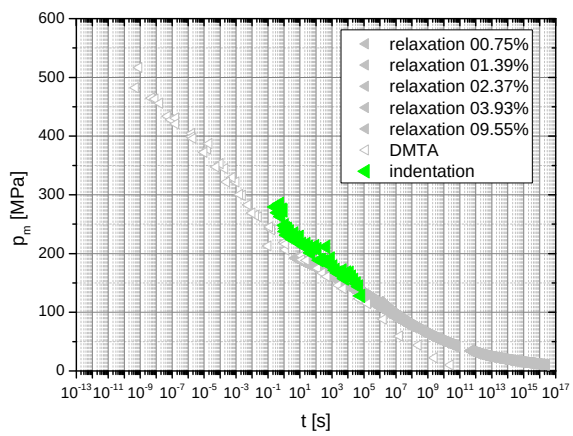

Figure VI-33 Prediction of the mean contact pressure versus time through relaxation and DMTA experiment

VI.4.2. Comparison between other SiO_2 fillers with different end groups

VI.4.2.1 General Observation

In order to have transparent samples lower quantities were used. The hope is that if the samples are transparent, the fillers are homogeneously dispersed in the sample. Thus forming "internal" plasticizer, the fillers should then not influence the transition temperatures and still increase the mechanical properties. This problem is considered in this chapter part. Figure VI-34 presents

TEM picture of PMMA with 2.5% stöber acrylate (sta) (a), with 2.5% stöber thiol (stt) (b) and with 2.5% nanopol (c) particles. In all three cases the particles form aggregates. Furthermore in all three cases the aggregates are close to one another. Moreover particle in the middle of empty spaces are observed between aggregates group. The aerosil particles size is found to be close to 13 nm. The Stöber particles have a size around 25 nm whereas the nanopol particles are around 20 nm. Because of the aggregates, the samples are not transparent but only translucent.

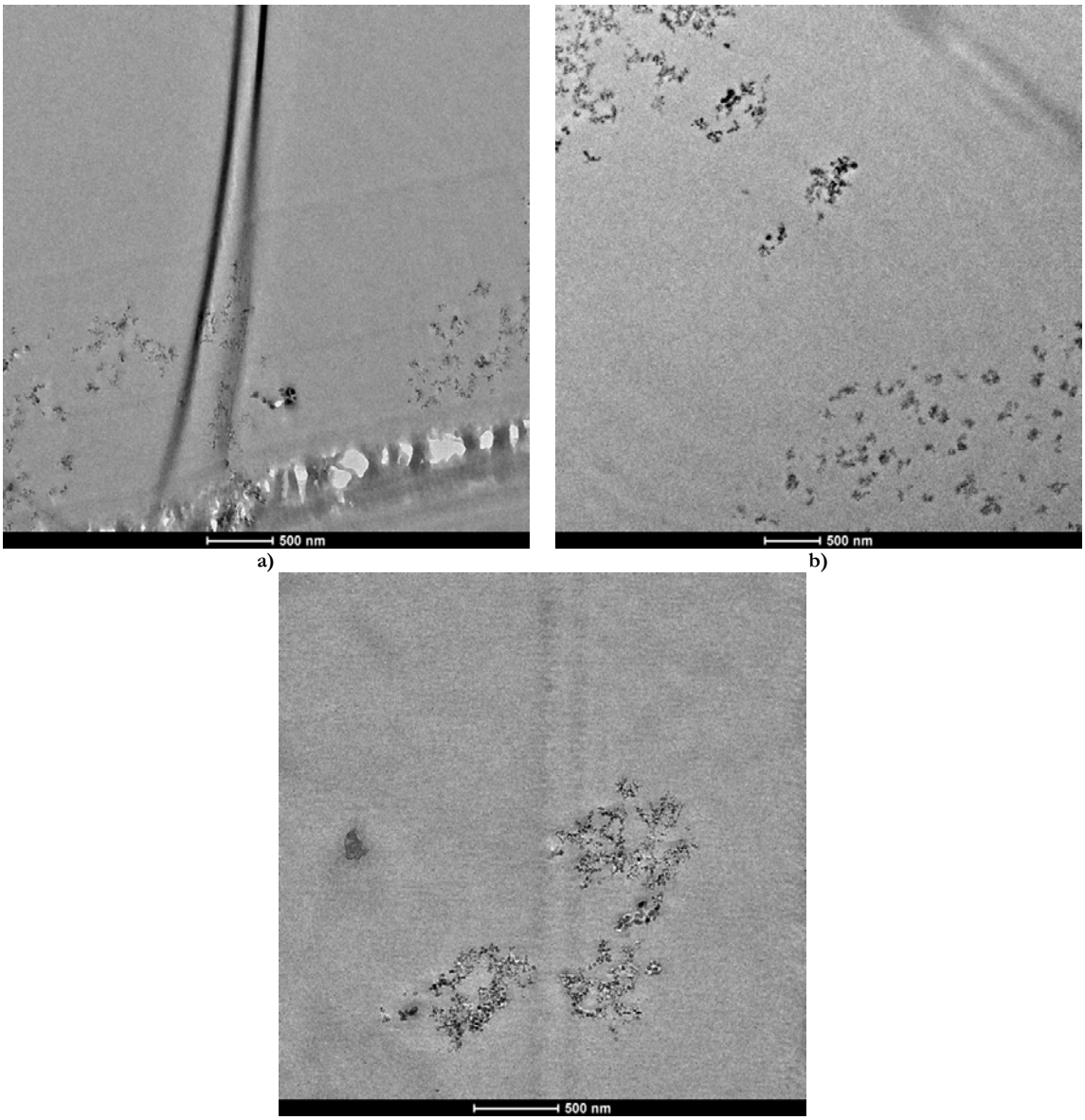

Figure VI-34 TEM pictures of PMMA 2.5 sta(a) PMMA 2.5stt (b) and PMMA 2.5 nanopol (c)

VI.4.2.2 Bulk analysis

After the general characterization some DMTA experiments were done. The Figure VI-35 introduces the Young's moduli and loss coefficient factors of PMMA Ba, PMMA 2.5sta, PMMA 2.5 stt and PMMA 2.5 nanopol over temperature. At low temperature the higher Young's modulus is obtained by the pure material then in decreasing order PMMA 2.5 sta, PMMA 2.5

nanopol and finally PMMA 2.5 stt. In the temperature range [-20°C: 80°C], all Young's moduli are equal within experimental error. At high temperature, PMMA 2.5 stt and PMMA 2.5 nanopol have a strong decrease of Young's moduli. The high temperature Young's modulus of PMMA 2.5 sta was not recorded. The loss coefficient observation shows the glass transition temperature around 95°C with a slight shift toward low temperature for filled material. On the contrary the T_β around 0°C does not move. Finally the T_γ around -50°C increases. Thus one can conclude on a plasticizer effect of the filler on the T_α, no effect on the T_β and an anti-plasticizer effect on the T_γ. The apparitions of the transition temperatures influence more the filled materials in the temperature tested domain.

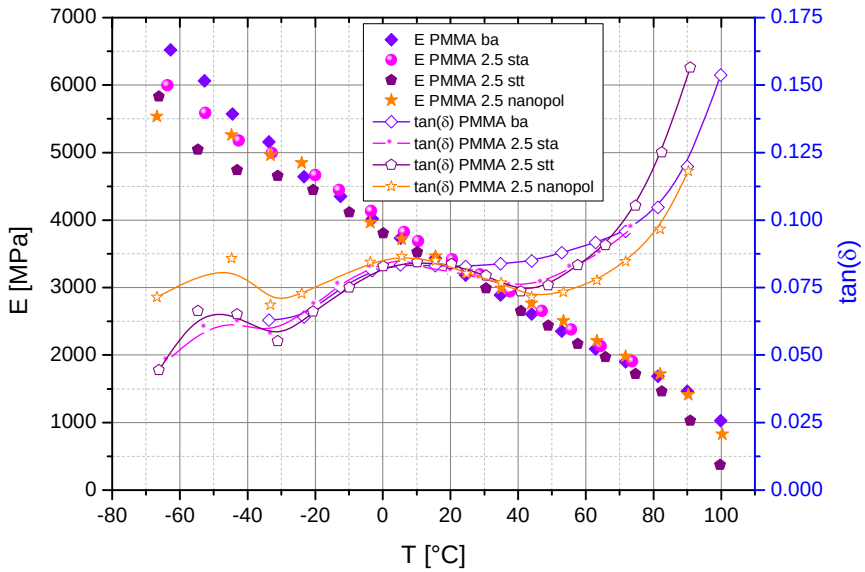

Figure VI-35 Comparison of DMTA experiment for PMMA charged with different Stöber particles at 0.05Hz

VI.4.2.3 Indentation analysis

Figure VI-36 shows the mean contact pressure (a) and the normalized indentation creep deformations (b) over time. The mean contact pressures of the filled materials are slightly lower than the mean contact pressure of the PMMA ba. The normalized indentation creep deformations are equal within experimental errors. Thus the filler addition in small amount reduces the mechanical properties without changing the creeping.

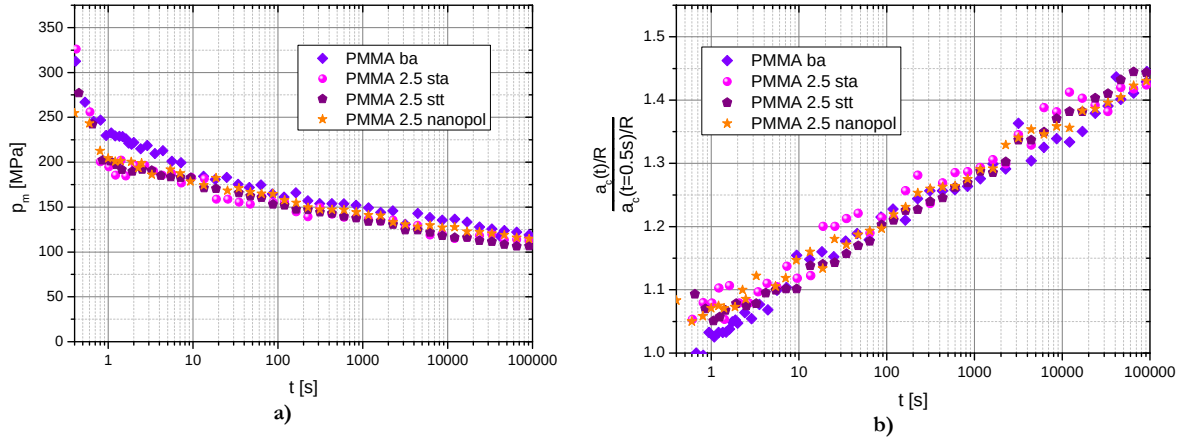

Figure VI-36 Mean contact pressure (a) and Normalized indentation creep deformation (b) versus creep time for PMMA filled with stober acrylate, stober thiol or nanopol particles at 30°C

VI.4.3. Conclusion

The addition of AlO(OH) and nanopox were conducted. In both cases the particles were macroscopically well dispersed in the samples. Nonetheless on the micro and nano scales agglomerates are observed thus making material translucent (nanopox) or matt (AlO(OH)). The bulk properties are almost identical for 10% filler addition but a plasticizer effect (T_α diminution) is observed. By increasing further the quantity of nanopox the bulk properties increase without further influencing the transition temperatures. The mean contact pressure follows the expected trend, the higher the filler content the higher the necessary mean contact pressure to obtain an initial Tabor deformation of 4%. As the best dispersion is observed for nanopox, other SiO_2 based particles were tested. The addition of a small amount of SiO_2 was macroscopically successfully conducted. Yet the dispersion is still not perfect. Thus the samples have a low transparency. The addition of 2.5% of filler neither increased the Young's modulus nor slowed down the creep of PMMA. Consequently SiO_2 can probably be added in a PMMA matrix. To improve material mechanical properties a large filler quantity is necessary. This important addition has a very small effect on the indentation creeping properties.

VI.5. CHAPTER CONCLUSION

This chapter was dedicated to the understanding of polymer mechanical behavior. In particular we studied the viscoelasticity in the bulk. Deformation-time master curves were constructed out of compression relaxation experiment. The indentation creep and recovery analysis allowed us to observe the apparition of plasticity in PMMA CN for long indentation time or high temperature. CR39 presented, like PMMA CN, thermoplastic behavior below its glass transition and elastomeric behavior above T_α. In the whole tested range CR39 showed only viscoelastic behavior. Furthermore the mean contact pressure enabled the creation of deformation-time-temperature master curves in almost perfect adequacy with the previous one. Thus demonstrating a non-influence of plasticity on viscoelasticity and an absence of viscoplasticity in polymer behavior. The immediate scratch recovery was presented in this chapter for the first time. Finally reinforced materials were tested. Their creeping capacities are the same as for standard PMMA, the only improvement is the increase in mean contact pressure.

VI.6. BIBLIOGRAPHY

[1] T. Chatel, Fluage et recouvrance d'empreintes et de sillons sur suface de polymère, in, Université de Strasbourg, Strasbourg, 2010.

[2] H.H. Kausch, N. Heyman, C.J. Plumer, P. Decroly, Traité des matériaux, numéro 14 - Matériaux polymères : Propriétés mécaniques et physiques, (juin 2001) ed., Presses Polytechniques et Universitaires Romandes (PPUR) 2001.

[3] G. Hochstetter, A. Jimenez, J.P. Cano, E. Felder, An attempt to determine the true stress-strain curves of amorphous polymers by nanoindentation, Tribology International, 36 (2003) 973-985.

[4] J.J. Martinez-Vega, H. Trumel, J.L. Gacougnolle, Plastic deformation and physical ageing in PMMA, Polymer, 43 (2002) 4979-4987.

[5] H.-G. Elias, Makromoleküle, wiley-vch, Neustadt, 2001.

[6] L.C.E. Struick, Physical Aging in Amorphous Polymers and Other Materials, Elsevier, Amsterdam, , 1978.

[7] M.L. Williams, R.F. Landel, J.D. Ferry, The temperature dependence of relaxation mechanisms in amorphous polymers and other glass-forming liquids, Journal of the American Chemical Society, 77 (1955) 3701-3707.

[8] J. Kolařík, Tensile creep of thermoplastics: Time-strain superposition of non-iso free-volume data, Journal of Polymer Science, Part B: Polymer Physics, 41 (2003) 736-748.

[9] M. Software, Volume A: Theory and User Information, in, 2012, pp. 813.

[10] V. Jardret, P. Morel, Viscoelastic effects on the scratch resistance of polymers: Relationship between mechanical properties and scratch properties at various temperatures, Progress in Organic Coatings, 48 (2003) 322-331.

[11] F. Quadrini, E.A. Squeo, A. Guglielmotti, Indentation creep of polymers. I. Experimental, Polymer Engineering and Science, 50 (2010) 2431-2439.

[12] J. Kolařík, A. Pegoretti, Non-linear tensile creep of polypropylene: Time-strain superposition and creep prediction, Polymer, 47 (2006) 346-356.

[13] S. Jazouli, W. Luo, F. Bremand, T. Vu-Khanh, Application of time-stress equivalence to nonlinear creep of polycarbonate, Polym. Test, 24 (2005) 463-467.

[14] P.A. O'Connell, G.B. McKenna, Large deformation response of polycarbonate: Time-temperature, time-aging time, and time-strain superposition, Polymer Engineering and Science, 37 (1997) 1485-1495.

[15] J. Zhao, G.B. McKenna, Temperature divergence of the dynamics of a poly(vinyl acetate) glass: Dielectric vs. mechanical behaviors, Journal of Chemical Physics, 136 (2012).

[16] H. Lu, X. Zhang, W.G. Knauss, Uniaxial, shear, and poisson relaxation and their conversion to bulk relaxation: Studies on poly(methyl methacrylate), Polymer Composites, 18 (1997) 211-222.

[17] S.B. Sane, W.G. Knauss, The time-dependent bulk response of Poly (Methyl Methacrylate), Mechanics Time-Dependent Materials, 5 (2001) 293-324.

[18] W.G. Knauss, V.H. Kenner, On the hygrothermomechanical characterization of polyvinyl acetate, Journal of Applied Physics, 51 (1980) 5131-5136.

[19] L. Cheng, X. Xia, L.E. Scriven, W.W. Gerberich, Spherical-tip indentation of viscoelastic material, Mechanics of Materials, 37 (2005) 213-226.

[20] P. Bertrand-Lambotte, J.L. Loubet, C. Verpy, S. Pavan, Understanding of automotive clearcoats scratch resistance, Thin Solid Films, 420-421 (2002) 281-286.

[21] P. Bertrand-Lambotte, J.L. Loubet, C. Verpy, S. Pavan, Nano-indentation, scratching and atomic force microscopy for evaluating the mar resistance of automotive clearcoats: Study of the ductile scratches, Thin Solid Films, 398-399 (2001) 306-312.

[22] B.J. Briscoe, E. Pelillo, S.K. Sinha, Scratch hardness and deformation maps for polycarbonate and polyethylene, Polymer Engineering and Science, 36 (1996) 2996-3005.

[23] I.C. Choi, B.G. Yoo, Y.J. Kim, J.I. Jang, Indentation creep revisited, J. Mater. Res., 27 (2012) 3-11.

[24] K. Sakaue, S. Okazaki, T. Ogawa, Indentation technique for evaluation of master curve of creep compliance, Experimental Techniques, 35 (2011) 16-22.

[25] J.L. Halary, F. Lauprêtre, L. Monnerie, Mécanique des matériaux polymères, Paris, 2008.

[26] I. Karapanagiotis, D.F. Evans, W.W. Gerberich, Dynamics of the leveling process of nanoindentation induced defects on thin polystyrene films, Polymer, 43 (2002) 1343-1348.

[27] Z.Y. Zhang, H.N. Dhakal, S.N. Surip, I. Popov, N. Bennett, Characterisation of roof tile coating degradation using nano-indentation test and surface profilometry, Polymer Degradation and Stability, 96 (2011) 833-838.

[28] W. Brostow, W. Chonkaew, L. Rapoport, Y. Soifer, A. Verdyan, Grooves in scratch testing, J. Mater. Res., 22 (2007) 2483-2487.

[29] J.S.S. Wong, H.J. Sue, K.Y. Zeng, R.K.Y. Li, Y.W. Mai, Scratch damage of polymers in nanoscale, Acta Materialia, 52 (2004) 431-443.

[30] W. Shen, S.M. Smith, H. Ye, F. Jones, P.B. Jacobs, Real time observation of viscoelastic creep of a polymer coating by scanning probe microscope, Tribology Letters, 5 (1998) 75-79.

[31] M. Wong, G.T. Lim, A. Moyse, J.N. Reddy, H.J. Sue, A new test methodology for evaluating scratch resistance of polymers, Wear, 256 (2004) 1214-1227.

[32] W. Brostow, B. Bujard, P.E. Cassidy, H.E. Hagg, P.E. Montemartini, Effects of fluoropolymer addition to an epoxy on scratch depth and recovery, Materials Research Innovations, 6 (2002) 7-12.

[33] S.C. Tjong, Structural and mechanical properties of polymer nanocomposites, Materials Science and Engineering R: Reports, 53 (2006) 73-197.

[34] S. Kim, C.A. Wilkie, Transparent and flame retardant PMMA nanocomposites, Polymers for Advanced Technologies, 19 (2008) 496-506.

[35] E.J.A. Pope, M. Asami, J.D. Mackenzie, Transparent silica gel-PMMA composites, J. Mater. Res., 4 (1989) 1018-1026.

CHAPTER VII. NUMERICAL RESULTS

CHAPTER VII. NUMERICAL RESULTS 172

VII.1. MODEL PRESENTATION 173
VII.1.1. Uni-axial 173
VII.1.2. Indentation 174
VII.2. CONSTITUTIVE LAWS 177
VII.2.1. Young's moduli and Poisson coefficients 177
VII.2.2. Elasto Plastic G'sell Jonas 177
VII.2.3. Viscoelastic Generalized Maxwell model 179
VII.2.4. Viscoplastic Norton's law 183
VII.3. UNI-AXIAL RELAXATION 186
VII.3.1. Relaxation at 4.88% 186
VII.3.2. Relaxation at 17.69% 187
VII.3.3. Conclusion 188
VII.4. INDENTATION CREEP 188
VII.4.1. CR39 188
VII.4.2. PMMA CN 189
VII.4.3. PMMA 10 AlO(OH) 190
VII.4.4. Law comparison 191
VII.4.5. Conclusion 191
VII.5. INDENTATION RECOVERY 191
VII.5.1. CR39 192
VII.5.2. PMMA CN 192
VII.5.3. Law comparison 193
VII.5.4. Conclusion 194
VII.6. CHAPTER CONCLUSION 194
VII.7. BIBLIOGRAPHY 195

VII.1. MODEL PRESENTATION

VII.1.1. Uni-axial

A schematic representation of the model is drawn in Figure VII-1. To limit the number of elements a 2D plane is used to represent a 3D cylinder. Therefore the model has a vertical symmetry axis (left side) and a horizontal mirror plane (at the bottom). It is constituted of 700 quad(4) elements. In order to be closer to the experimental set up a load bearing beam was implemented (red line at the top). This beam is in contact with the sample (touching) and the experimentally measured displacement is applied on the beam. The right scheme presents the von Mises stress once the sample is loaded. One can observe high stress concentration at the top right side. For this reason the element number is higher on the sample exterior to enable a good representation of the side's phenomenon. As the beam-sample contact is "only" touching and not gluing, the element can move horizontally without constraints. If the contact was glued, the element could not move horizontally. The reality is somewhere between these two extreme cases. This touching contact nonetheless explains why the sample can difficultly form the barrel shape, which is sometime experimentally observed. Finally there is a logarithmic discretization of the increment. There are roughly 100 increments per time decades.

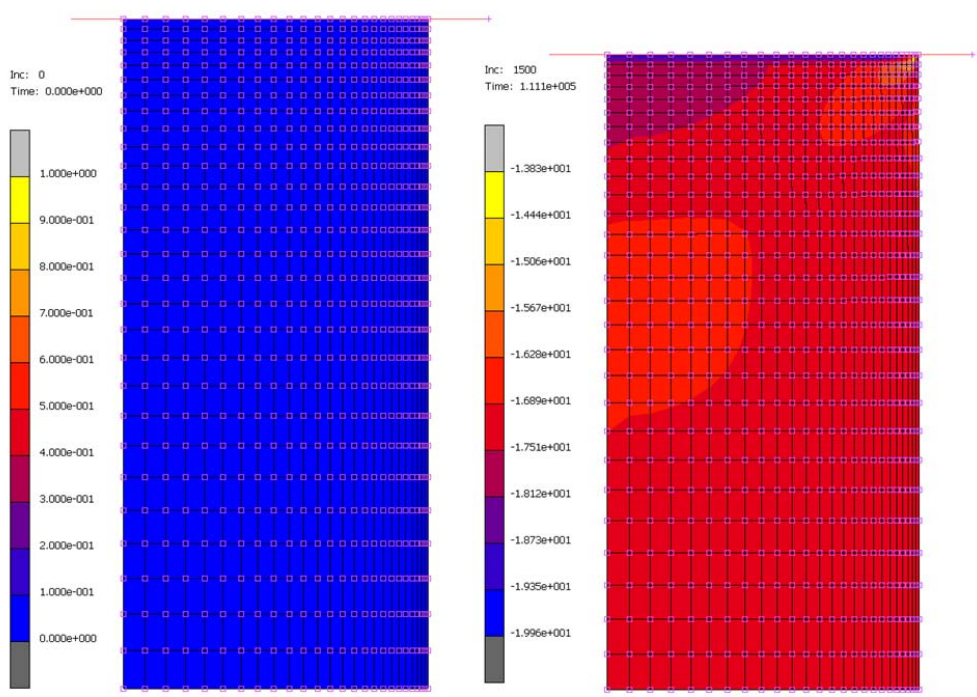

Figure VII-1 Used uni axial model, left without load, right loaded (von Mises stress)

Figure VII-2 presents the traverse displacement and calculated stress versus time. They respectively are the input and output of the uni axial simulation. The traverse displacement comes from experiments and is imposed on the beam thus on the sample. The stress is picked up at the sample center thus at the bottom left of the shown model (Figure VII-1). The stress values are compared with experimentally measured data.

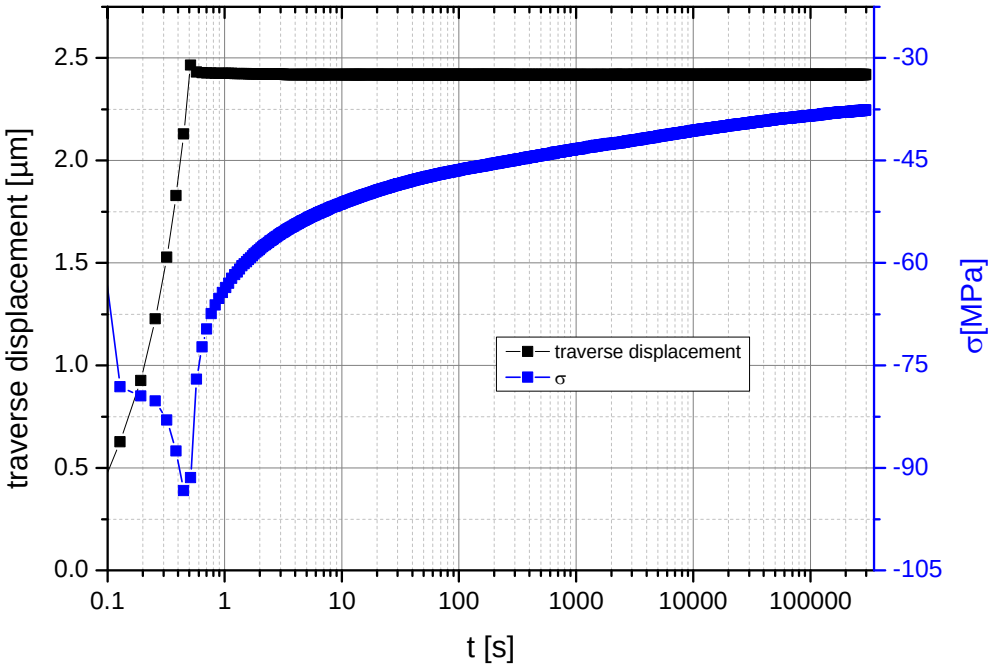

Figure VII-2 The experimental beam displacement and the calculated, by FEM, stress versus time input and output respectively of the uni axial simulation

VII.1.2. Indentation

Figure VII-3 a) presents a schematic representation of the used indentation model [1]. The considered problem displays an infinitely rigid sphere (rigid) in contact with a soft plane (deformable) (case of a spherical glass indenter in contact with a polymer) [2]. As the modeled indenter is spherical, a symmetry axis exists in the loading axis. The bottom nodes can not move vertically. In the same manner the node on the symmetry axis can not move horizontally. In Figure VII-3 b) the element disposition is presented. The model is constituted of 3332 Quad(4) elements. In order to avoid border effects the model width is 10 times higher than the maximum contact radius, whereas the height is 2 times longer than the width. In the contact region the element density is increased as it can be observed in Figure VII-3 c). Moreover, Figure VII-3 c) shows the Von Mises stress in the bulk for different indentation creep times. The major observation is the stress or strain gradient beneath the indenter [3, 4]. Thus the experimental stress and strain are not measurable (we measure only average value) and the computed one are hard to follow (which point is relevant). Therefore the numerical contact status is used to determine the contact radius. Afterwards the computed deformations can be compared to the experimentally measured deformations. Finally in order to improve the simulation quality and decrease the simulation size the used load cases follow a logarithmic rule. There is an average of 100 increments per time decade. Thus the 100 first increments duration is 1 s whereas the 99 next last 10 s.

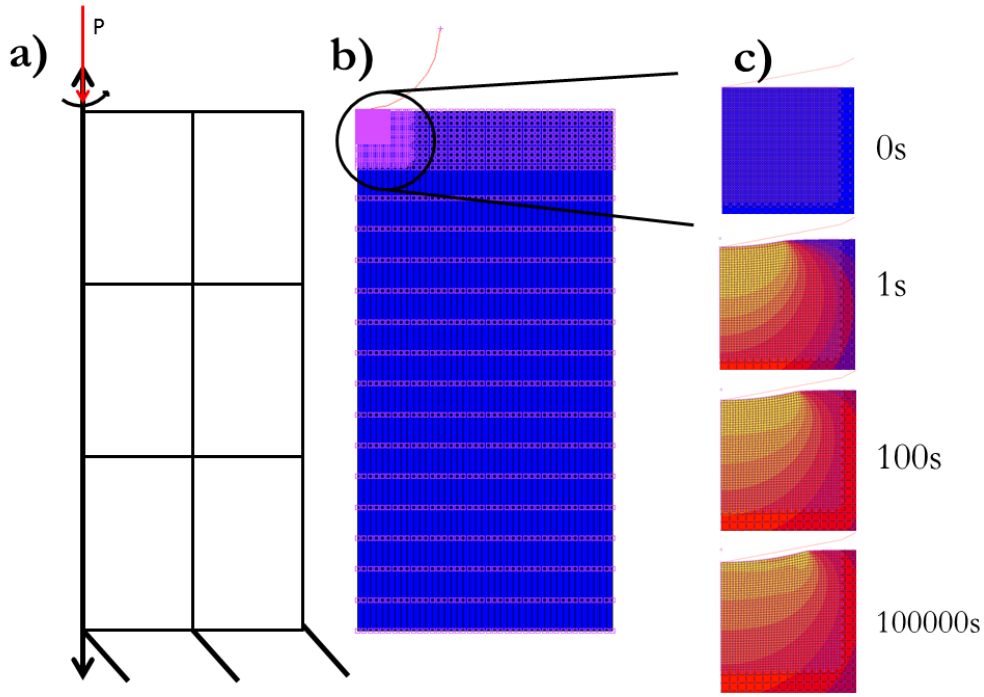

Figure VII-3 a) Shematic representation of the indentation model b) Indentation model used in MSC Marc c) Zoom on the volume below the contact during experiment

As in the uni-axial problem, the real constraints are inserted in the calculation. Figure VII-4 presents the introduced force and the calculated contact radius versus time. As previously mentioned in the Material and methods part (V.4.1.4) there is a load overshoot in the experiment. This load is reproduced in the finite element code. As in the experiment, the load is adjusted to obtain a 4% Tabor deformation at 0.5 s after the experiment starts. So the numerical and real experiments start with the same deformation but not necessarily the same mean contact pressure. Later on the mean contact pressure and normalized Tabor indentation creep deformation are shown versus time for experimental and numerical tests.

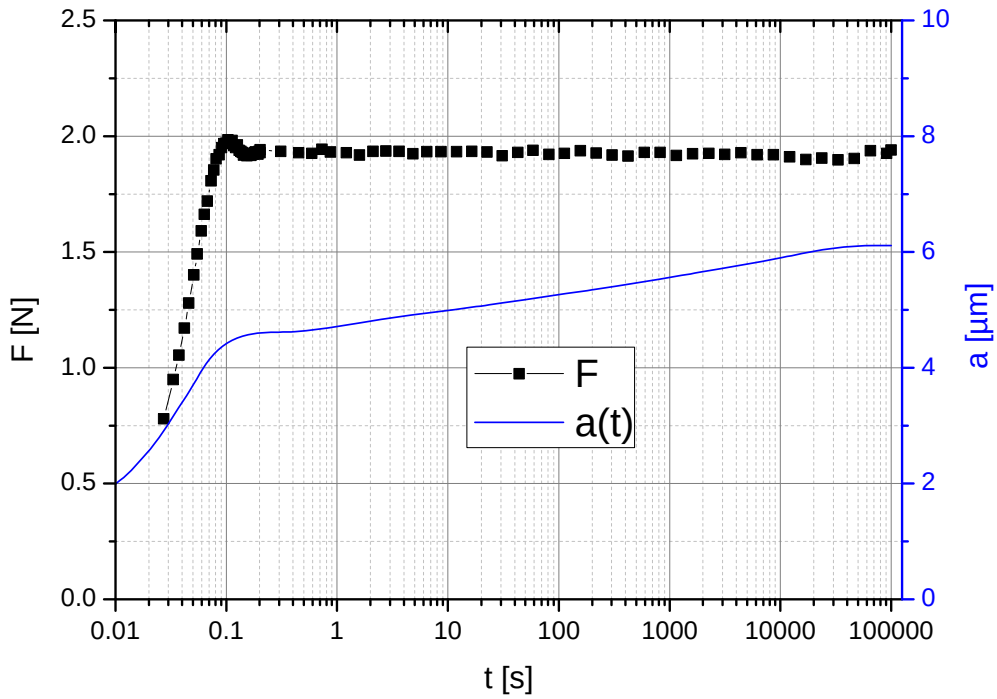

Figure VII-4 Load and contact radii versus experimental time, respectively input and output of the FEM indentation model

For the indentation recovery characterization, there is no longer contact between indenter and surfaces. Thus the contact status cannot be used. Instead the position of every surface node over time is known. One of these profiles is presented in Figure VII-5 a). The horizontal drift of the profile is also presented in this graphic. The drift increases versus axis distance until roughly 7 µm. Then the drift drastically decreases, corresponding to the annulation of the second derivative and to the limit of the "contact" recovery imprint. This position is highlighted on the graph by the vertical black line. The distance to the symmetry axis gives us $a_R(t)$, the computation of the profile ensues the R(t). They are shown versus recovery time in Figure VII-5. Thus one can calculate the normalized Tabor recovery deformation (Equation V-21).

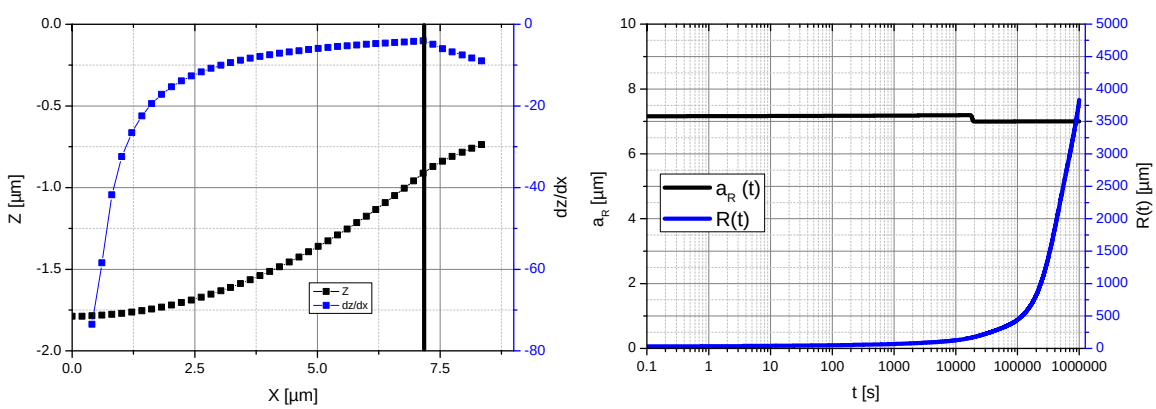

Figure VII-5 a) Indentation recovery half profile and its drift versus distance from symmetry axis b) Recovery contact radius and recovery curvature radius versus recovery time

VII.2. CONSTITUTIVE LAWS

In this part we will present the different constitutive laws used for the bulk materials. All the used laws are implemented in MSC Marc. This chapter will explain how the laws are identified and used. First the ELASTIC PLASTIC ISOTROPIC material (standard material in MSC Marc) is used as our materials are isotropic. This material requires at least one Young's modulus and one Poisson ratio. The used values are presented in the first part. Then the different used versions of the constitutive law are illustrated in one part for each: Elasto plastic G'Sell Jonas, Viscoelastic Generalized Maxwell [5] and Viscoplastic Norton's Law.

VII.2.1. Young's moduli and Poisson coefficients

Figure VII-6 presents the results of Dynamic Mechanical Thermal Analysis. There are the same as those observed in part VI.2.1. The graph illustrates the evolution of Young's moduli and Poisson coefficient versus temperature for CR39, PMMA CN and PMMA 10 AlO(OH) at 0.05 Hz. In the numerical code generally the injected mechanical properties correspond to the material behavior at 30°C. Thus the Young's moduli and Poisson coefficient at those temperatures are used except in the case of Maxwell viscoelastic law. More precisions are given for this special case in VII.2.3.

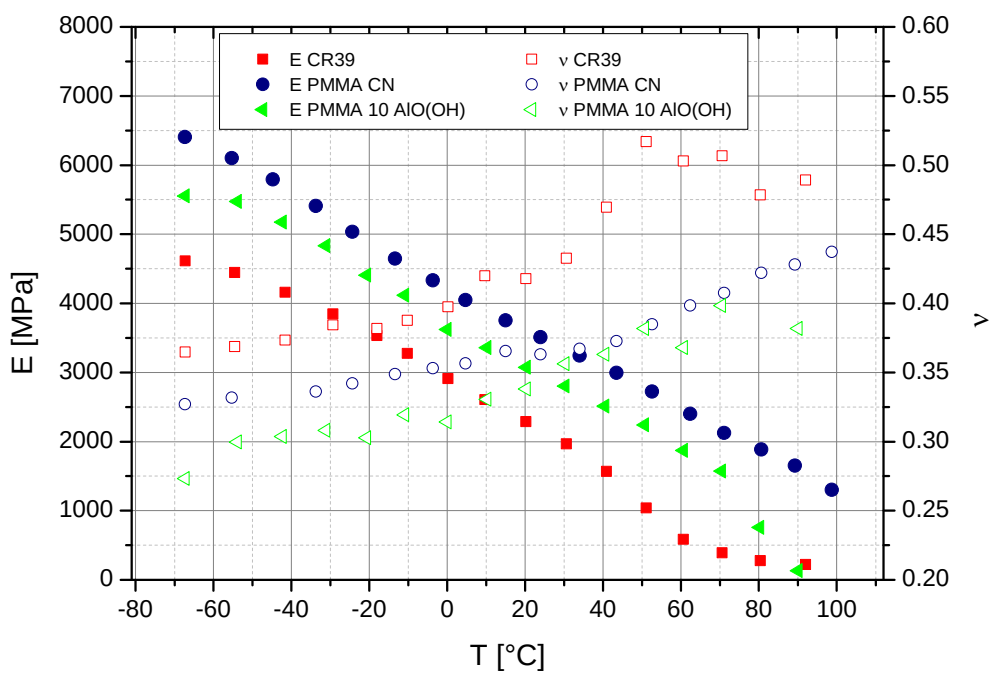

Figure VII-6 Young's moduli and Poisson coefficient for CR39 PMMA and PMMA 10 AlO(OH) versus temperature

VII.2.2. Elasto Plastic G'sell Jonas

The inserted elasto-plastic (EP) law is based on a G'Sell Jonas model [6]. G'Sell and Jonas proposed the Equation VII-1:

G'Sell Jonas plasticity law	$\sigma_{\text{true}}(\varepsilon_{\text{true}}, \dot{\varepsilon_{\text{true}}}, T) = K.e^{\frac{a}{T}}.(1-e^{-\omega\varepsilon_{\text{true}}}).e^{h_g\,\varepsilon_{\text{true}}^2}.\dot{\varepsilon}_{\text{true}}^{m}$	Equation VII-1

Where σ_{true} is the true stress, $\varepsilon_{\text{true}}$ the true deformation, $\dot{\varepsilon}_{\text{true}}$ the true strain rate and T the temperature. K, a, ω and m are material dependent constants respectively called the consistency, thermal coefficient, viscoelasticity parameter and the strain sensitivity. Finally the hardening modulus hg is used. A detailed explanation on the relative influence of each parameter is presented by Bucaille et al. [7]. During his PhD thesis [8], he developed a new method to identify these coefficients based on indentation creep and residual imprint experiments. The coefficients, used by Bucaille, [8, 9] are shown in Table 2. With G'Sell Jonas equation and Bucaille coefficient, one obtain Figure VII-7 graph for stress versus strain. It was cut to 40 % because it is the maximum observed deformation. This is the in MSC Marc implemented material comportment law under the entry plasticity/ Von Mises/ isotropic / table.

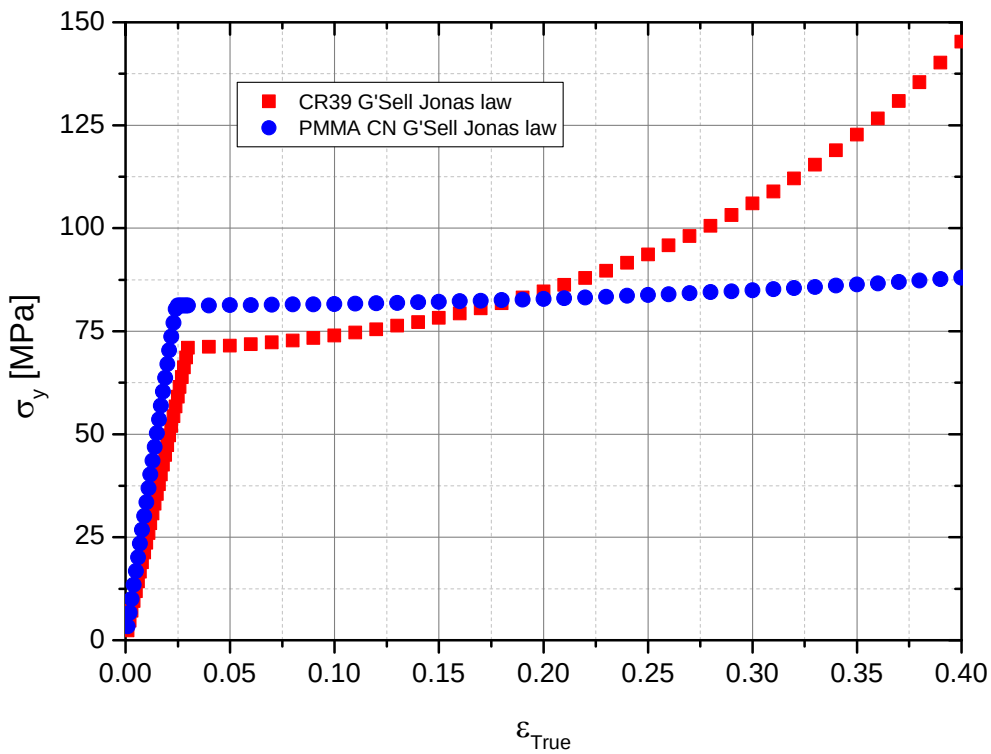

Figure VII-7 Introduced G'Sell Jonas law in Marc Mentat for CR39 and PMMA CN

	CR39	PMMA
K	145	81.2
m	0.078	0.1
hg	4.5	0.5

Table 2 Used coefficient for the G'Sell Jonas law in Marc&Mentat [8]

VII.2.3. Viscoelastic Generalized Maxwell model

A Maxwell model consists in a spring and a dashpot in series [10-13]. The spring is displaying the immediate elasticity, whereas the dashpot introduces the viscosity. This model enables only the elastic recovery therefore a more complex model is required: the generalized Maxwell model (VE). This consists in adding in parallel a spring and several Maxwell models (see Figure VII-8). Thus for each spring-dashpot pair a different time constant exists. The theoretical formula for uniaxial relaxation experiment is known. The demonstration can be found the book of Oudet [14].In our case experience and observation leaded us to add 1 Maxwell model per experimental time decade. Thus the time constants are 0.1, 1, 10, 100, 1000, 10 000, 100 000 and 1 000 000 s. The Equation VII-2 and Equation VII-3 were then fitted on the experiment, on which the loading part was removed.

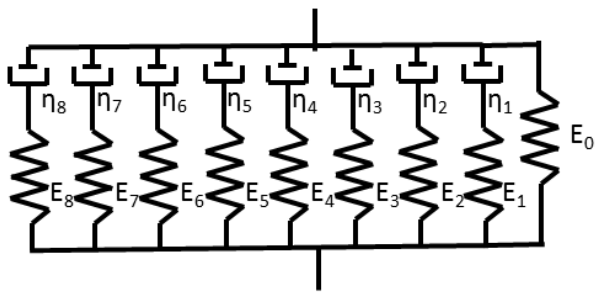

Figure VII-8 Generalized Maxwell model with 8 time constants

Generalized Maxwell shear modulus equation in relaxation [15]	$G(t) = G(\infty) + \sum_{1}^{i} G_i \times \exp(-t/\tau_i)$	Equation VII-2
Generalized Maxwell bulk modulus equation in relaxation	$K(t) = K(\infty) + \sum_{1}^{i} K_i \times \exp(-t/\tau_i)$	Equation VII-3

MSC Marc software picks up the viscoelasticity through these equations. Thus the τ_i and corresponding G_i K_i are implemented in the code. The G(∞) and K(∞) are introduced through the Young's modulus and the Poisson coefficient.

Calculus of the Young's modulus with Maxwell model	$E(0) = G(0) \times 2 \times (1 + \upsilon)$ $E(0) = \left(G(\infty) + \sum_{1}^{i} G_i \right) \times 2 \times (1 + \upsilon)$	Equation VII-4

For reasons related to the software, the Poisson coefficient is considered constant over the experiment. This is a commonly used approximation [16, 17]. Nonetheless, some studies [18-20] and our observation demonstrated a time and solicitation dependent Poisson's ratio.

An example of fit is shown in Figure VII-9. The relaxation shear and bulk modulus were calculated through Equation V-11 and Equation V-12. The graph shows the shear modulus the

fitted curves and the standard error for CR39 versus time. The fit accuracy is relatively high; the error is less than 1%. For each relaxation experiment a set of parameters is available.

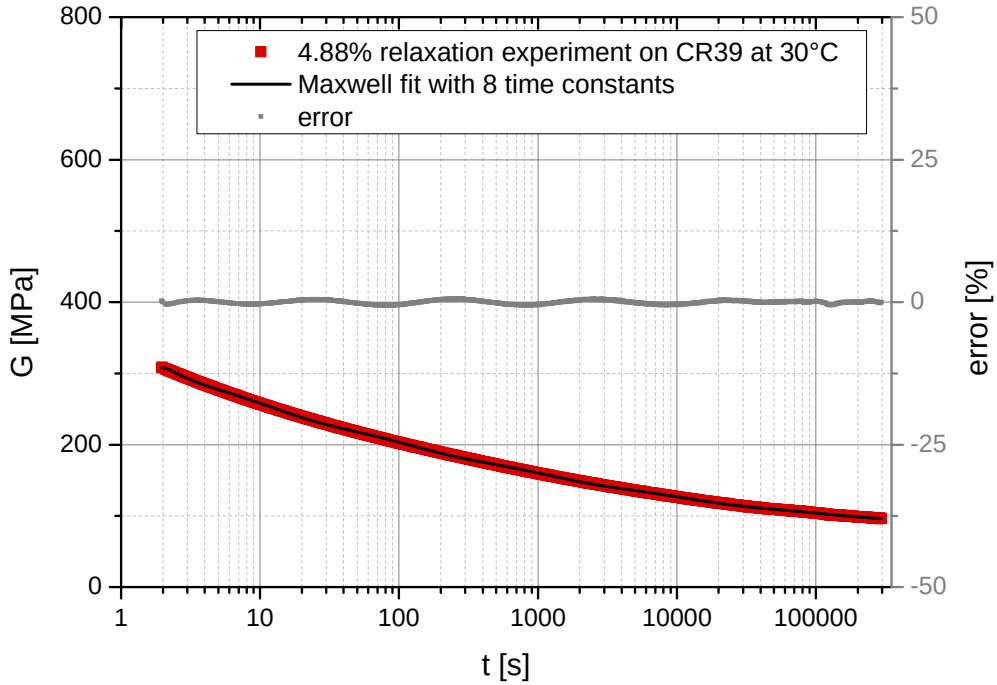

Figure VII-9 CR39 4.88% relaxation shear modulus versus time at 30°Cand its fit with generalized Maxwell formula and fit error

Furthermore we observed previously (VI.2.3) that it was possible to build master curves with the relaxation experiments. Thus one can fit a generalized Maxwell model on the master curve (MC VE) [17]. In this case the master curve is centered on the chosen relaxation. This means that, in Figure VII-10, which presents a master curve of shear modulus on CR39 centered at the 4.88% deformation relaxation, the values for this experiment (4.88%) are not shifted. The shear moduli coming from smaller deformation are shifted horizontally to the left whereas those coming from higher deformation are shifted to the right. The presented fit on this graph is a generalized Maxwell model with 18 time constants to cover the whole available time. The fit quality is lower than previously; this is probably due to the large amount of data, the discrepancy between experimental data, and the non-perfect shifting of the experimental curves.

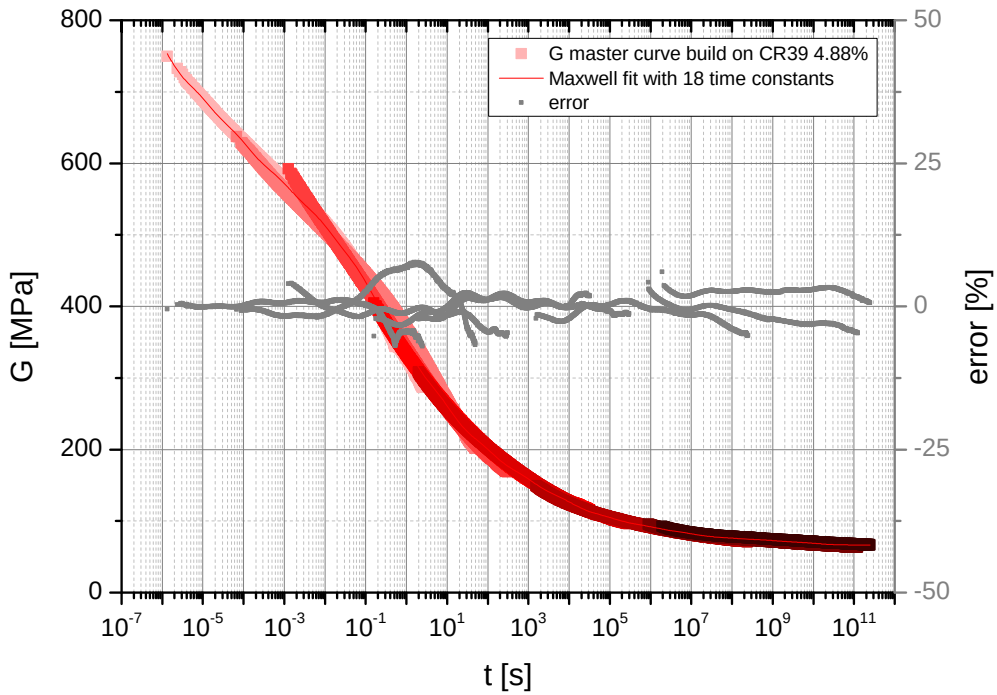

Figure VII-10 CR39 master curves shifted to 4.88% deformation, fitted with a generalized Maxwell equation (reproduction of Figure I-15)

As explained before each relaxation experiment enables a set of viscoelastic parameters and so does each master curve. The study on the viscoelastic parameter will be done with the most studied material, CR39. The generalized Maxwell model is a mathematical operator which fits well on viscous phenomena due to its high parameterization [21].

For comparison, four Maxwell based viscoelastic laws were analyzed. They were identified as previously shown at different strains. The chosen strains were 4.88% and 17.69%. These strains correspond to the true strain of relaxation experiment conducted at 5% and 19.4% engineering strain. For both relaxation master curves were constructed. Thus one has two "simple" viscoelastic constitutive laws and two viscoelastic constitutive laws master curves. The fitted coefficients are shown in Table 3. The coefficients named "simple" and master curves coefficients are very close from one another when at the same deformation and the same time constant.

CR39 VE 4.88%			CR39 VE 17.68%			CR39 VE MC 4.88			CR39 MC 17.68%		
E=2815			E=4124			E=2359			E=2385		
1E-01	587.2	3066.4	1E-01	1288.5	6728.8	1E-06	102.3	534.4	1E-12	108.0	563.8
1E+00	99.7	520.6	1E+00	85.2	444.8	1E-05	58.5	305.6	1E-11	58.8	307.1
1E+01	69.4	362.4	1E+01	5.4	28.1	1E-04	64.4	336.3	1E-10	64.5	336.7

1E+02	50.5	263.6	1E+02	7.8	40.5	1E-03	52.5	274.1	1E-09	52.9	276.3
1E+03	42.2	220.5	1E+03	3.8	19.7	1E-02	57.7	301.2	1E-08	56.9	297.1
1E+04	31.5	164.5	1E+04	4.8	25.0	1E-01	91.2	476.1	1E-07	89.0	464.6
1E+05	21.2	110.6	1E+05	3.2	16.9	1E+00	92.0	480.4	1E-06	93.4	487.9
1E+06	6.9	36.3	1E+06	1.5	8.0	1E+01	81.8	427.0	1E-05	82.0	428.1
						1E+02	51.1	266.7	1E-04	53.5	279.1
						1E+03	37.1	193.7	1E-03	36.8	191.9
						1E+04	31.2	163.2	1E-02	32.1	167.8
						1E+05	17.3	90.2	1E-01	17.9	93.3
						1E+06	10.6	55.2	1E+00	10.7	55.7
						1E+07	10.3	53.9	1E+01	10.5	54.8
						1E+08	3.6	19.0	1E+02	4.0	21.0
						1E+09	3.2	16.5	1E+03	3.0	15.5
						1E+10	4.7	24.8	1E+04	4.8	25.2
						1E+11	1.1	5.7	1E+05	1.3	6.9

Table 3 Coefficients used for the different CR39 VE laws

Moreover later on in the chapter some master curves laws are used. They are fitted for three different materials CR39, PMMA CN and PMMA 10 AlO(OH). There parameters are presented in Table 4.

CR39			PMMA CN			PMMA 10 AlO(OH)		
t	Gi	Ki	t	Gi	Ki	t	Gi	Ki
E=2359			E=3425			E=3027		
1E-06	102.3	534.4	1E-06	110.1	287.2	1E-07	178.3	464.9
1E-05	58.5	305.6	1E-05	90.8	236.9	1E-06	61.9	161.5

1E-04	64.4	336.3	1E-04	63.4	165.3	1E-05	62.1	162.0
1E-03	52.5	274.1	1E-03	57.6	150.3	1E-04	62.5	163.0
1E-02	57.7	301.2	1E-02	68.3	178.0	1E-03	80.2	209.1
1E-01	91.2	476.1	1E-01	87.5	228.1	1E-02	87.4	227.8
1E+00	92.0	480.4	1E+00	96.4	251.5	1E-01	82.5	215.3
1E+01	81.8	427.0	1E+01	112.1	292.4	1E+00	94.0	245.1
1E+02	51.1	266.7	1E+02	89.7	234.0	1E+01	70.1	182.7
1E+03	37.1	193.7	1E+03	84.5	220.2	1E+02	73.2	190.9
1E+04	31.2	163.2	1E+04	58.5	152.6	1E+03	48.9	127.6
1E+05	17.3	90.2	1E+05	45.7	119.2	1E+04	61.5	160.4
1E+06	10.6	55.2	1E+06	74.6	194.5	1E+05	48.1	125.5
1E+07	10.3	53.9	1E+07	72.6	189.2	1E+06	22.6	58.9
1E+08	3.6	19.0	1E+09	53.1	138.4	1E+07	24.4	63.7
1E+09	3.2	16.5	1E+11	50.3	131.1	1E+08	16.6	43.3
1E+10	4.7	24.8	1E+13	18.5	48.3	1E+09	17.3	45.1
1E+11	1.1	5.7	1E+15	14.8	38.5	1E+10	0.0	0.0
			1E+17	22.7	59.2			

Table 4 Coefficients used for the generalized Maxwell Viscoelasticity in MSC Marc

The viscoelasticity coefficients are introduced in MSC Marc as the tables shown previously under the option viscoelasticity isotropic.

VII.2.4. Viscoplastic Norton's law

Several authors introduced a strain or strain rate dependent plasticity level [22, 23]. MSC Marc enables the introduction of viscoplastic constitutive law. We choose to introduce the law under the form explicit Maxwell. Then a piecewise linear method presenting the equivalent creep strain rate as a function of equivalent creep strain and stress. The introduced law is a Norton's law, the Equation VII-5 presents it.

Norton's law	$\dot{\varepsilon}_{vp} = \left(\frac{K \times \varepsilon_{vp}^{\frac{1}{M}}}{\sigma} \right)^{N}$ $\sigma = K \times \varepsilon_p^{1/M} \times \dot{\varepsilon}_p^{1/N}$	Equation VII-5

This law supposes that there is neither viscoelasticity nor plasticity. Therefore the strain can be decomposed in an elastic (ε_e) and a viscoplastic part (ε_{vp}), as shown in Equation VII-6. Furthermore, the Equation VII-8 shows the well-known Hooke's law for an elastic isotropic solid where E is the Young's modulus.

Norton's law assumption	$\varepsilon = \varepsilon_e + \varepsilon_{vp}$	Equation VII-6
Hooke's law	$\sigma = E \times \varepsilon$	Equation VII-7

The deformation can be derived as a function of time. Equation VII-8 presents the Equation VII-6 derived versus time in the special case of relaxation experiments. In a relaxation test the strain is kept constant thus the strain rate is null.

	$\dot{\varepsilon} = 0 = \frac{\dot{\sigma}}{E} + \dot{\varepsilon}_{vp}$	Equation VII-8

Therefore for a relaxation experiment the stress σ and the total strain ε are known. Furthermore we can calculate εvp with Equation VII-6 and Equation VII-7. The viscoplastic strain rate can also be computed through Equation VII-8. Thus the Equation VII-5 can be fitted on the data and this is what is presented in Figure VII-11 a), b) and c) respectively for CR39, PMMA CN and PMMA 10 AlO(OH). For CR39 the plane goes relatively well through the data. It is on top of the experiment at low strain and low strain rate (end of experiment) and above it at high strain and high strain rate (experiment start). On the contrary, PMMA CN and PMMA 10 AlO(OH) display another behavior at low strain the plane is above then at middle strain the plane is below. Finally, at high strain the plane is again above the data. The CR39 reticulation block the material flow at high deformation thus the stress increases again after a fall at a strain at 5%. For the PMMA there is no reticulation therefore the higher stress is obtained before the plasticity apparition at 5% strain after it the stress drops drastically down. As the plane equation does not allow the plane to twist the PMMA CN plasticity is hard to take in account. On the contrary CR39 fit is better, thanks to its reticulation which raises the stress value.

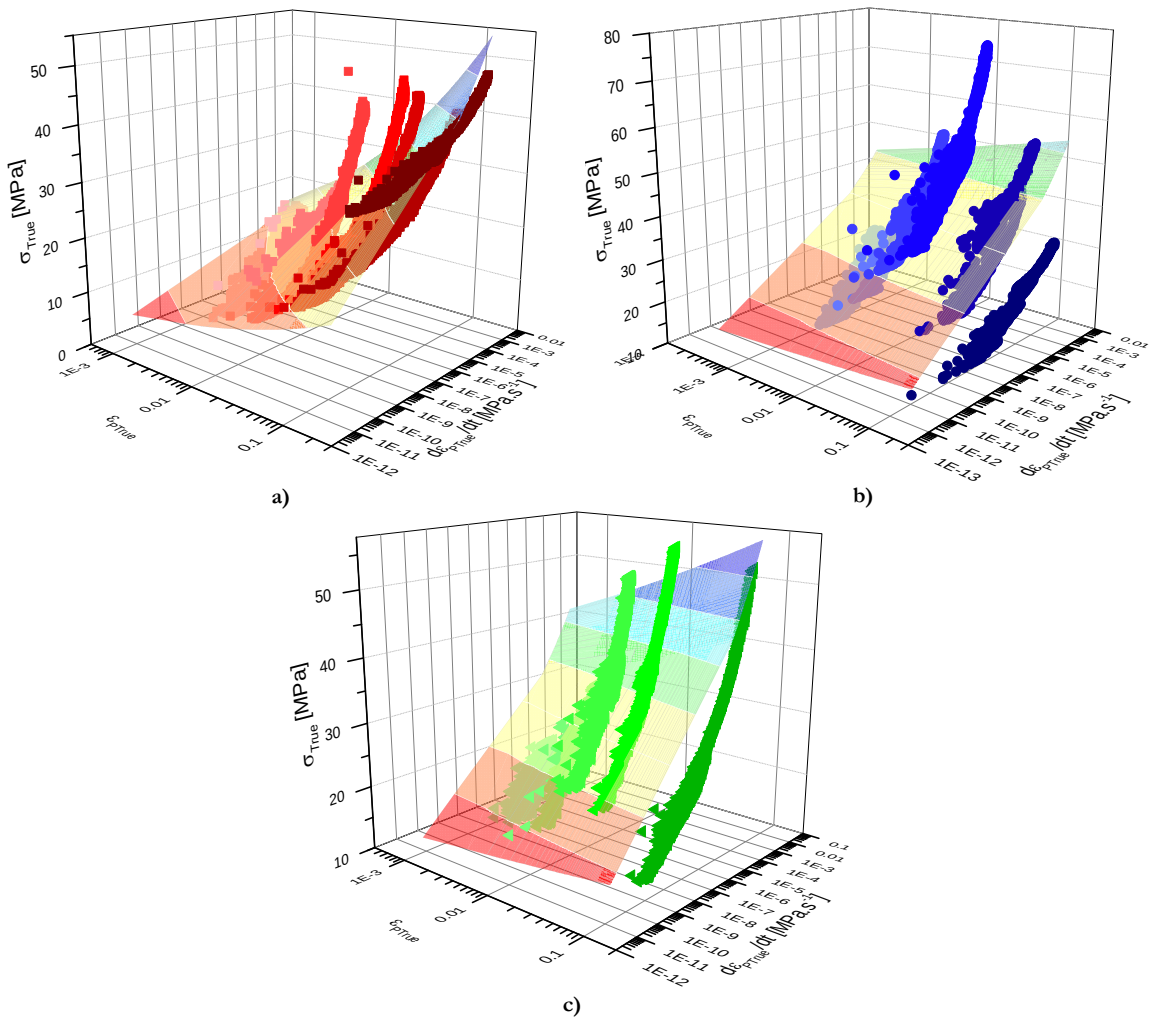

Figure VII-11 a) CR39, b) PMMA CN c) PMMA 10 AlO(OH) relaxation experimental set at 30°C (dots) and the fitted Norton's law surface

Finally Table 5 summarizes the calculated coefficient value for each material.

	CR39	PMMA	PMMA 10
K	131.6	93.7	100.1
M	4.5	29.9	16.0
N	14.4	16.8	13.7

Table 5 Coefficients used for Norton's law in MSC Marc

In MSC Marc a strongly discretized table (30 000 points) is introduced to imitate the equation results.

VII.3. UNI-AXIAL RELAXATION

The different constitutive laws are tested on a simple relaxation test. The advantage of the relaxation test is that the strain is almost uniforme in the material. Thus the quality of a constitutive law at a given deformation can be evaluated. The whole comparison is held on CR39 as it is the material for which the most data is available.

VII.3.1. Relaxation at 4.88%

Figure VII-12 presents the stress as a function of time for a relaxation test at 4.88%. The graph a) shows in addition the results of the numerical tests done with the viscoelastic laws identified at 4.88% deformation (VE and MC VE). Then the graph b) displays the results obtained with the viscoelastic laws identified at 17.69% relaxation (VE and MC VE). The last graph, c), presents the results obtained by numerical test with the viscoplastic and elasto-plastic law. It is remarkable that the VE laws identified at 4.88% are very accurate. The start of the simple VE is nonetheless of very poor quality. It is observable that the Master curve VE 4.88% fit is clearly better for shorter time. For longer time the fit is equal to the simple VE. This was expected as the coefficients are close for these time constants. The material described by this law is too stiff for this experiment (the stress is much smaller than the reality). The objective of this graph is to demonstrate the non-accuracy of a VE law identified on another deformation. The laws were not fitted for this strain but for a higher strain where the proportionality between stress and strain is different. Finally, the VP law gives a rough approximation of the obtained value whereas the EP law gives a good approximation of the instantaneous response but then does not evolve over time.

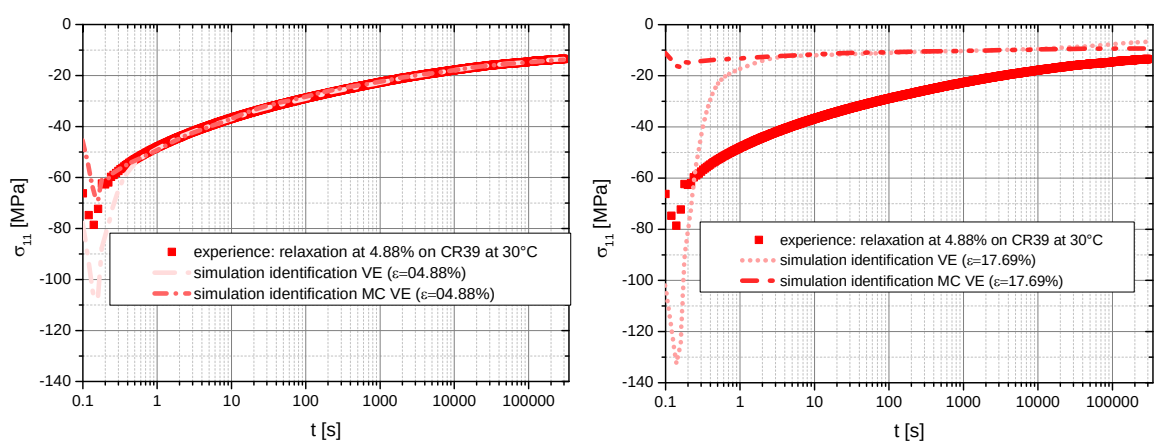

a) b)

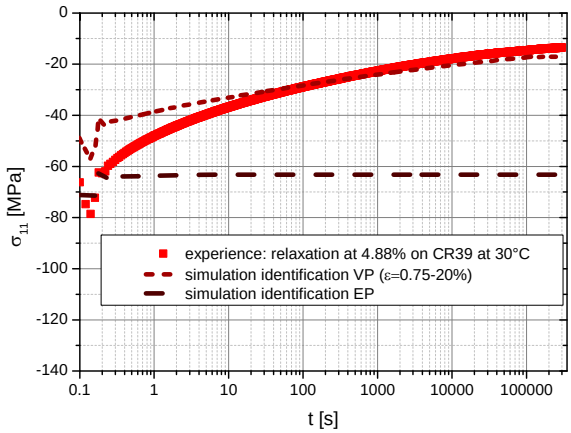

c)

Figure VII-12 Stress versus time for CR39 4.88% deformation relaxation experiment at 30°C for experiment and simulations a) VE laws identified at 4.88% b) VE laws identified at 17.69% c) EP and VP laws (reproduction of Figure I-16)

VII.3.2. Relaxation at 17.69%

In Figure VII-13 the stress versus time for a relaxation test at 17.69% is presented. As before the graph a) shows the experimental, VE 4.88% and MC VE 4.88% results, then the graph b) the experimental, VE 17.69% and MC VE 17.69% results, finally the graph c) the experimental, EP and VP results. The VE 4.88% laws stresses are much higher than those of the experiment thus the laws are too soft. The VE 17.69% laws demonstrate a very good accuracy after the loading, but the simple VE is too soft during loading whereas the MC VE is too stiff. Utterly the EP law gives a good approximation of the loading and the VP law is a little too stiff.

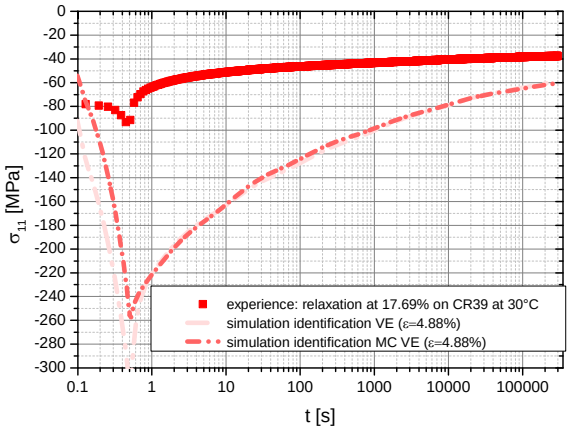

a)

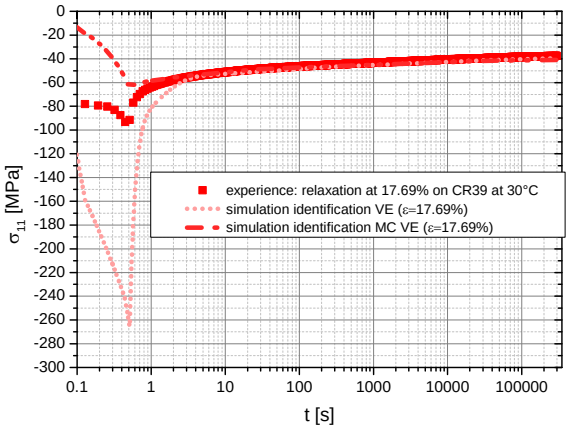

b)

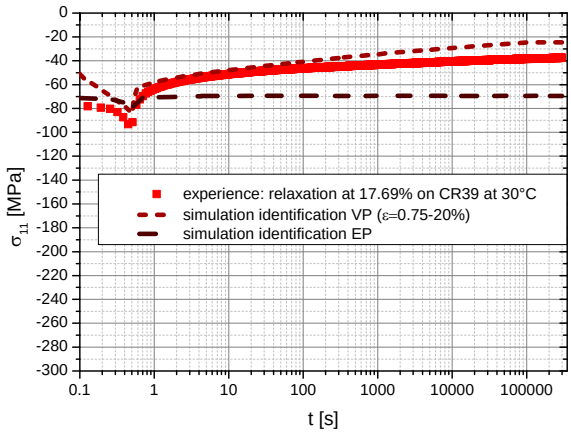

c)

Figure VII-13 Stress versus time for CR39 17.64% deformation relaxation experiment at 30°C for experiment and simulations a) VE laws identified at 4.88% b) VE laws identified at 17.69% c) EP and VP laws (reproduction of Figure I-17)

VII.3.3. Conclusion

The VE laws are very accurate when the strain is close to the strain for which there were identified. Furthermore the use of master curves improves the quality of the loading simulation. Indeed the MC VE improves the fit on the short times compared to the simple VE. The master curve laws are fitted for shorter and longer times. Moreover the EP law simulation gives an instantaneous accurate stress but no viscous phenomenon, crucial for accurate material description. In the end the VP law gives a rough, time evolving, approximation in all the cases. As our indentations have a mean contact Tabor deformation between 4 and 6% (begin and end of indentation on CR39 and PMMA CN) [4, 24], the viscoelastic constitutive law at 4.88% and the master curve viscoelastic law at 4.88% are used.

VII.4. INDENTATION CREEP

Indentation creep simulation has become of great interest for numerous applications in the recent years [25-27]. The indentation creep of the three studied materials is presented in this chapter part. The simulation are presented for each material CR39, PMMA CN, PMMA 10 AlO(OH) and finally a global comparison of the laws results is shown.

VII.4.1. CR39

The mean contact pressure versus time is drawn in Figure VII-14 a). The experimental data decreases versus logarithm of time. The G'Sell Jonas law does not decrease at all. The start value is nonetheless adequate. On the contrary the start value of the simple VE law is far too high thus it stays too high throughout the experiment. The VE master curve and the VP law are slightly below but decrease like the experiment over time. The non evolution of the plastic law was to be expected as the time is not taken into account in the equation. The high value of the VE law can be explained by the fact that the first milliseconds of the relaxation experiment are not taken into account thus inducing an error that is present during the whole experiment. The master curve corrects this shortcoming; indeed the start value is much closer to the experiment. The relative accuracy of the VP law comes from a wide deformation domain. Therefore all stressed material

has an averaged appropriate deformation. Figure VII-14 b) presents the normalized Tabor creep deformation for the experiment and the numerical tests versus time. As previously observed, the EP law does not evolve thus proving the absence of modification after loading. The master curve deformation is slightly above the experimental values. On the contrary, the VE and VP laws are below the experiment. The VP law is the closest to the experiment. Indeed the average response for each deformation seems to produce a good compromise.

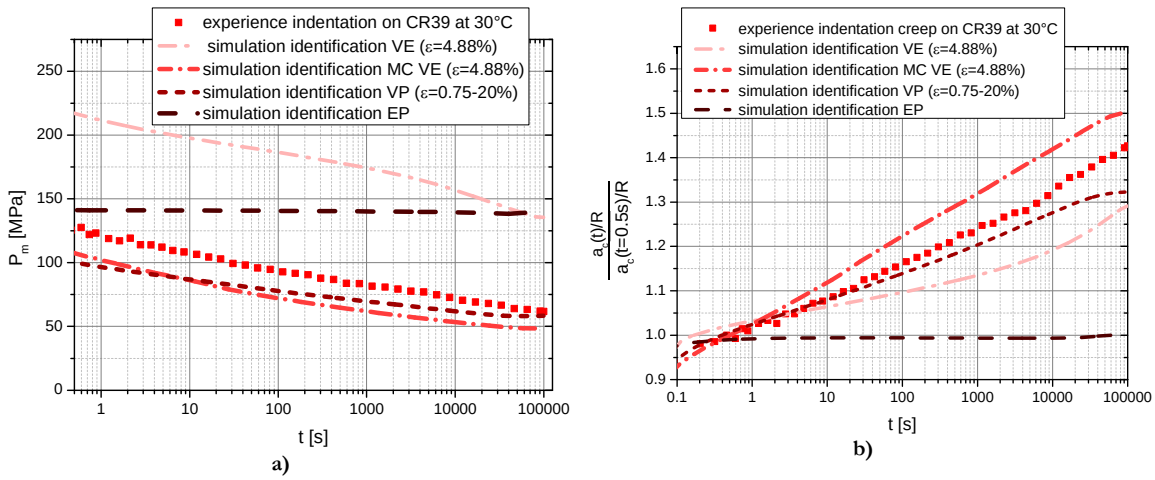

Figure VII-14 a) Mean contact pressure and b) normalized Tabor indentation creep during indentation creep experiment at 30°C for experience and simulation on CR39 (reproduction of Figure I-18)

As a conclusion the CR39 behavior can be simulated with more accuracy either by a Master Curve Viscoelastic 4.88% law or by a viscoplastic law. Both laws show a mean contact pressure slightly lower than the experiment but the numerical deformations frame the experimental deformation.

VII.4.2. PMMA CN

Figure VII-15 a) displays the mean contact pressure versus time for PMMA CN experimental and numerical tests. The experimental mean contact pressure decreases versus time, whereas the curve for EP numerical results is horizontal. The VP law is below and decreases slower than the experiment. Finally, the MC VE 4.88% starts with a lower mean contact pressure than the experiment but as its decreasing rate is lower it ends in the same point. Figure VII-15 b) presents the normalized creep deformation versus time. The EP law is not creeping. The MC VE 4.88% and the VP law does not induce enough creeping.

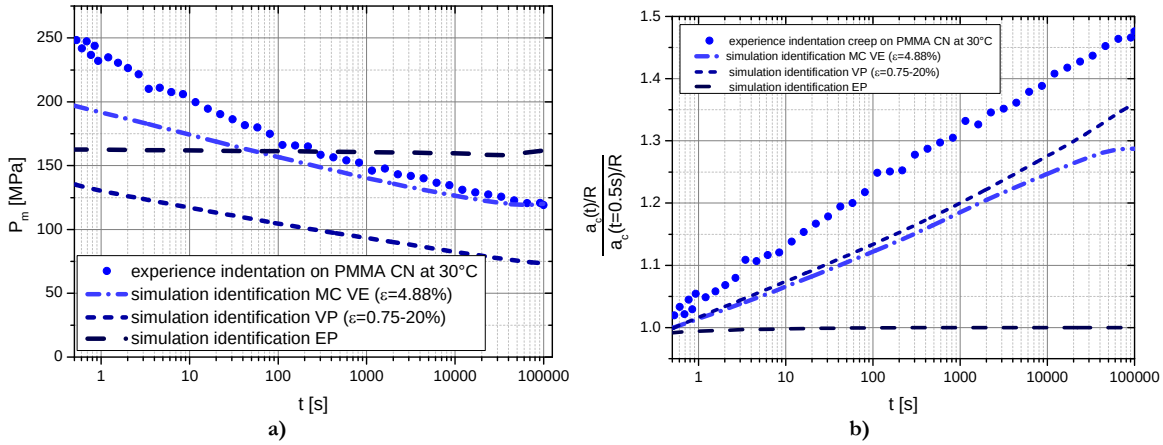

a) b)

Figure VII-15) Mean contact pressure and b) normalized Tabor indentation creep during indentation creep experiment at 30°C for experience and simulation on PMMA CN

The analysis in the experimental part (VI.3.2) demonstrated the presence of plasticity in the PMMA CN indentation after long indentation time. The plasticity appears during loading for the relaxation experiment. During the relaxation holding part there is no plasticity creation. So for the constitutive laws the stress decrease due to plasticity is always seen even for short times. As the plasticity occurs progressively in PMMA CN indentation the start mean contact pressure is higher and the decreasing slope is more pronounced experimentally than numerically.

VII.4.3. PMMA 10 AlO(OH)

Figure VII-16 a) introduces the mean contact pressure for PMMA 10 AlO(OH) indentation versus time. Both available constitutive laws are MC VE 4.88% and VP. They have the same decreasing slope as the experiment but the average value is half of the one observed experimentally. Figure VII-16 b) displays the normalized Tabor indentation creep deformation versus time. The simulation and experiment lead to the same deformation. The start mean contact pressure value comes probably, like for PMMA CN, from the plasticity. Then, why are the decreasing mean contact slopes identical? A possible answer is that the fillers influence the bulk creeping, thus making the normalized creep deformation close to the experimental measurements.

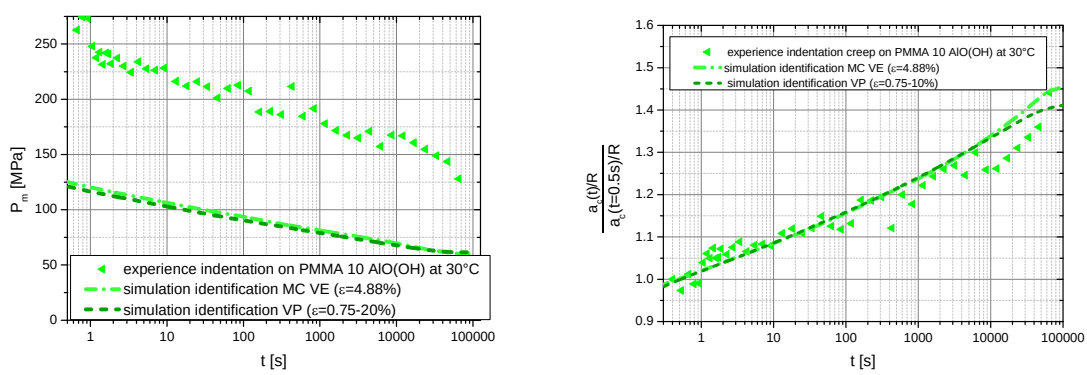

a) b)

Figure VII-16) Mean contact pressure and b) normalized Tabor indentation creep during indentation creep experiment at 30°C for experience and simulation on PMMA 10 AlO(OH)

VII.4.4. Law comparison

The objective of Figure VII-17 is to compare the different laws. The a) part illustrates the mean contact pressure versus indentation time whereas the b) part shows the normalized indentation creep deformation as a function of time. The experimentally observed ranking in mean contact pressure absolute start value PMMA CN, PMMA 10 AlO(OH) and CR39 is followed in the numerical tests. There is nonetheless a large difference in the mean contact pressure value coming from the two PMMA CN laws. It may come from the poor Norton's fit quality. On the other hand the normalized indentation creep Tabor deformations are close for the two laws coming from PMMA but not for the CR39.

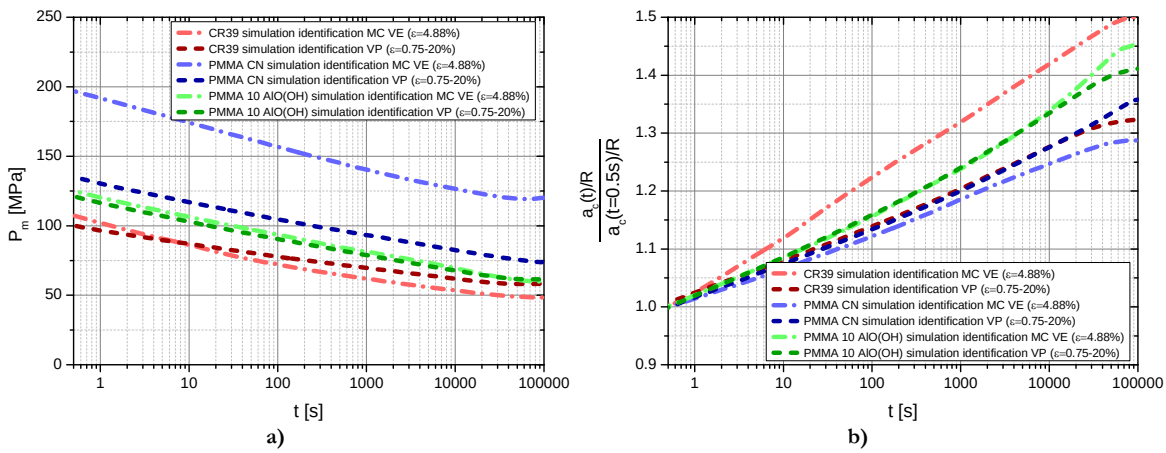

Figure VII-17 Comparison between the simulation resulting from the different laws

VII.4.5. Conclusion

The indentation creep recovery was simulated through VE 4.88%, MC VE 4.88%, VP and EP laws. The EP law gives generally a good initial value for the mean contact pressure. Then the deformation is not evolving and thus not following the mean contact pressure decrease. The VP law produces reasonable mean contact pressure value and creep according to the experiment. The VE 4.88% law illustrates the need for a good parameterization at short times. Indeed the high error value in mean contact pressure is due to the imprecise stress strain relation during the loading. This is improved by the use of master curves. As a summary, the constitutive laws displaying the more accurately the experimental behaviors are the master curves and the viscoplastic laws.

VII.5. INDENTATION RECOVERY

As for the experimental part, the recovery is measured immediately after the creep experiment. Thus the recovery starting imprints are not the same. So, one has to keep in mind the b) graphs from the previous section.

VII.5.1. CR39

The results of the experimental and numerical test recovery are presented in Figure VII-18. The normalized deformation in these graphics is equal to 1 at the end of indentation and to 0 for a full recovery. The EP and VP law curves are horizontal as expected. They respectively recovered 45% and 20% of the indentation imprints. In both cases, they recover immediately from the elastic part of the imprint and then no more. The EP law led to a smaller imprint (see Figure VII-14 b)) therefore the share of elastically deformed material is higher and so is the percentage of recovered material. The two other laws fully recover. The immediate recovery of the VE 4.88% law is roughly 45%, 20% more than the experiment. This higher immediate recovery comes from the smaller final indentation deformation. On the contrary the final deformation observed with MC VE 4.88% law is 5% higher than the experiment. The immediate recovery of the simulation with the MC VE 4.88% is therefore much closer to the experiment. The MC VE 4.88% presents a very accurate representation of the experiment thus supporting our assumption that CR39 is viscoelastic on the whole tested range.

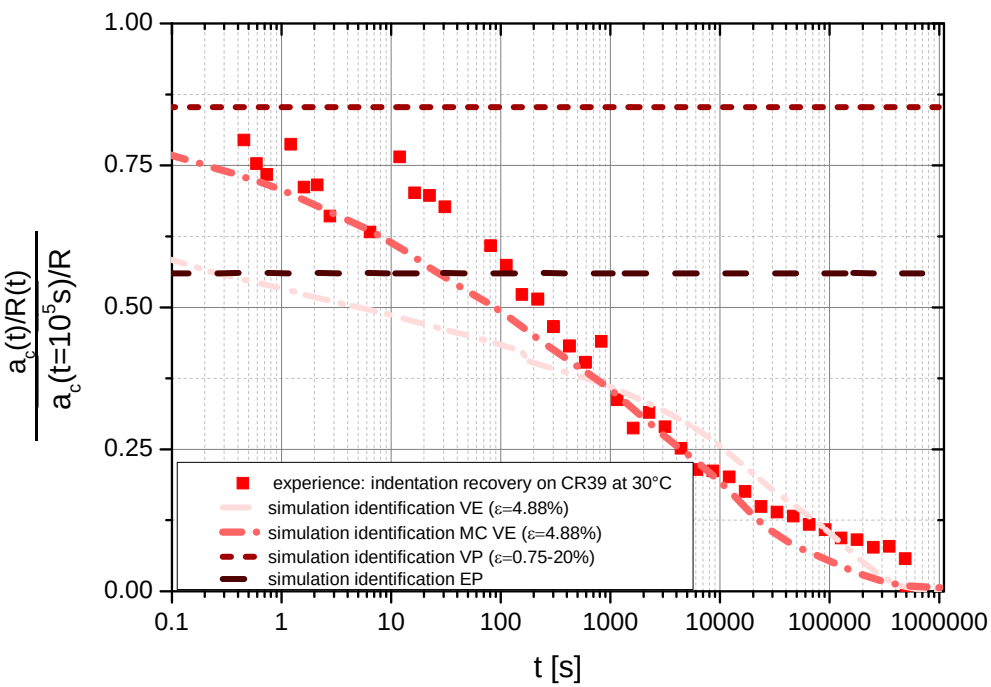

Figure VII-18 CR39 experimental and simulation indentation creep recovery (reproduction of Figure I-19)

VII.5.2. PMMA CN

Figure VII-19 shows the normalized indentation Tabor recovery versus time. As before the EP and VP laws are horizontal. The EP law recovers proportionally more than the VP law for the same reasons as previously (VP law simulation evoluated whereas EP law stayed stationary thus the elastic part of the recovery has a higher proportion for the EP law than for the VP law). The MC VE 4.88% law curve is below the experiment. The MC VE 4.88% simulation undergoes a full imprint recovery. The experiment presents some remaining imprints. In the simulation the plasticity is not taken into account; it leads probably to the smaller deformation at the end of

creep. Thus the immediate recovery is higher than the one observed experimentally and the full recovery is possible.

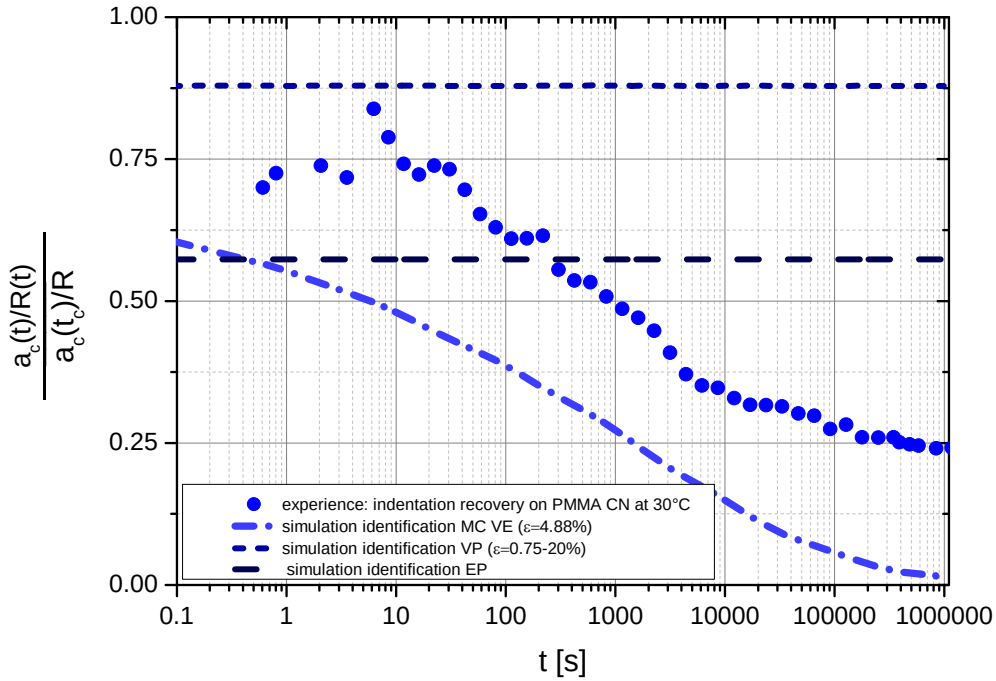

Figure VII-19 PMMA experimental and simulation indentation creep recovery

VII.5.3. Law comparison

Figure VII-20 displays the recovery of the six different simulations. The recoveries of the VP laws are always horizontal and represent a low percentage of the possible recovery. The MC VE 4.88% laws always recover entirely in 10 times the indentation time. This was expected as the influence of one coefficient (see Equation VII-2) is inferior to one per 10 000 after a 10 times its time constant.

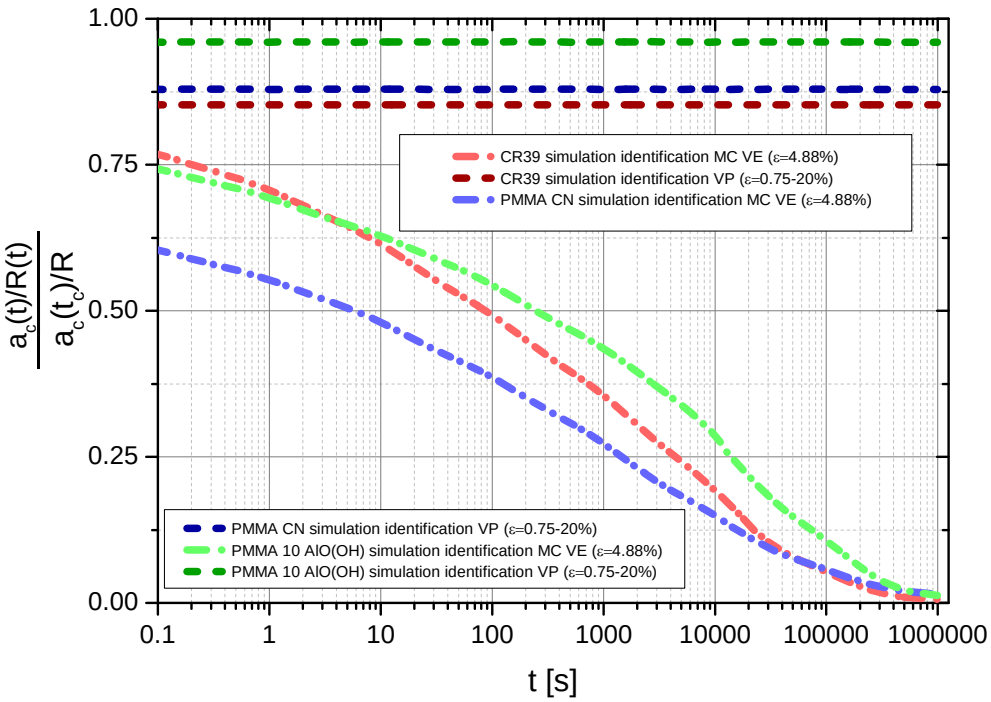

Figure VII-20 CR39, PMMA CN and PMMA 10 AlO(OH) simulation indentation creep recovery

VII.5.4. Conclusion

The indentation recovery of three materials was studied successfully in this chapter part. The EP and VP law did not give any useful information. But the MC VE 4.88% produces very accurate results for a viscoelastic material like CR39. When using it on a viscoelastic plastic material, like PMMA CN, the accuracy is poor. Indeed there is a time shift in the response and a flawed final deformation.

VII.6. CHAPTER CONCLUSION

Three types of constitutive laws were introduced in MSC Marc software. The EP law enables a good prediction of the immediate stress-strain relation on the tested polymers. There is no evolution due to creeping effects. The VP law gives a relatively good representation of the mean contact pressure evolution.

Finally the master curve law demonstrates a very good precision if it is used for the deformation on which it was fitted. In the case of indentation creep, it gives an accurate idea of the normalized creep deformation. The recovery of the master curves is appropriate and accurate as long as there is no plasticity involved in the deformation.

In order to improve the simulation quality, one should use the VE law on which a plasticity threshold is added. The next step towards constitutive law improvement would be to differentiate the compression, the pulling and the shear response. Ultimately the introduction of mechanic fracture and/or a strain dependent viscoelastic law would be of great interest.

VII.7. BIBLIOGRAPHY

[1] T. Chatel, H. Pelletier, V. Le Houérou, C. Gauthier, D. Favier, R. Schirrer, Original in situ observations of creep during indentation and recovery of the residual imprint on amorphous polymer, J. Mater. Res., 27 (2012) 12-19.

[2] H. Pelletier, J. Krier, C. Gauthier, Influence of local friction coefficient and strain hardening on the scratch resistance of polymeric surfaces investigated by finite element modeling, in, Como, 2011, pp. 1772-1778.

[3] G. Hochstetter, A. Jimenez, J.P. Cano, E. Felder, An attempt to determine the true stress-strain curves of amorphous polymers by nanoindentation, Tribology International, 36 (2003) 973-985.

[4] H. Pelletier, C. Gauthier, R. Schirrer, Experimental measurement and numerical simulation of the plastic strain during indentation and scratch tests on polymeric surfaces, J. Mater. Res., 24 (2009) 1184-1196.

[5] T. Chatel, V. Le Houérou, H. Pelletier, C. Gauthier, Numerical analysis of the creep of the contact and recovery of the imprint on amorphous polymer surfaces, Mech. Time-Depend. Mater., 17 (2013) 581-595.

[6] C. G'Sell, J.J. Jonas, Determination of the plastic behaviour of solid polymers at constant true strain rate, Journal of Materials Science, 14 (1979) 583-591.

[7] J.L. Bucaille, E. Felder, G. Hochstetter, Identification of the viscoplastic behavior of a polycarbonate based on experiments and numerical modeling of the nano-indentation test, Journal of Materials Science, 37 (2002) 3999-4011.

[8] J.L. Bucaille, Simulation numérique de l'indentation et de la rayure des verres Organiques, in, École Nationale Supérieure des Mines de Paris, Paris, 2001, pp. 239.

[9] E. Felder, J.L. Bucaille, G. Hochstetter, Influence of the rheology of polymers on their scratch resistance: Experimental and numerical simulation studies, Influence de la rheologie des polymeres sur leur resistance a la rayure: Etude experimentale et par simulation numerique, 28 (2003) 15-28.

[10] J.L. Halary, F. Lauprêtre, L. Monnerie, Mécanique des matériaux polymères, Paris, 2008.

[11] J. Lemaitre, J.-L. Chaboche, Mécanique des matériaux solides, Bordas, 1988.

[12] I.M. Ward, Mechanical properties of solid polymers, Bristol, 1979.

[13] M.D.G. Lechner, K. ; Nordmeier, E. H., Makromolekulare Chemie, Germany, 2010.

[14] C. Oudet, Polymères Structure et propriétés Introduction, Masson, Paris, 1994.

[15] P.J. Dooling, C.P. Buckley, S. Hinduja, The onset of nonlinear viscoelasticity in multiaxial creep of glassy polymers: A constitutive model and its application to PMMA, Polymer Engineering and Science, 38 (1998) 892-904.

[16] S.B. Sane, W.G. Knauss, The time-dependent bulk response of Poly (Methyl Methacrylate), Mechanics Time-Dependent Materials, 5 (2001) 293-324.

[17] L.C.A. Van Breemen, E.T.J. Klompen, L.E. Govaert, H.E.H. Meijer, Extending the EGP constitutive model for polymer glasses to multiple relaxation times, Journal of the Mechanics and Physics of Solids, 59 (2011) 2191-2207.

[18] M. Kästner, M. Obst, J. Brummund, K. Thielsch, V. Ulbricht, Inelastic material behavior of polymers - Experimental characterization, formulation and implementation of a material model, Mechanics of Materials, 52 (2012) 40-57.

[19] N.W. Tschoegl, W.G. Knauss, I. Emri, The effect of temperature and pressure on the mechanical properties of thermo- and/or piezorheologically simple polymeric materials in thermodynamic equilibrium - a critical review, Mechanics Time-Dependent Materials, 6 (2002) 53-99.

[20] H. Lu, X. Zhang, W.G. Knauss, Uniaxial, shear, and poisson relaxation and their conversion to bulk relaxation: Studies on poly(methyl methacrylate), Polymer Composites, 18 (1997) 211-222.

[21] P.E. Combette, Isabelle Physique des polymères propriété mécaniques, 6 rue de la sorbonne, paris, 2005.

[22] E.T.J. Klompen, T.A.P. Engels, L.E. Govaert, H.E.H. Meijer, Modeling of the postyield response of glassy polymers: Influence of thermomechanical history, Macromolecules, 38 (2005) 6997-7008.

[23] J. Wang, T.C. Ovaert, Computational mechanical property determination of viscoelastic/plastic materials from nanoindentation creep test data, J. Mater. Res., 24 (2009) 1245-1257.

[24] D. Tabor, The hardness of solids, Review of Physics in Technology, 1 (1970) 145.

[25] J. Krier, J. Breuils, L. Jacomine, H. Pelletier, Introduction of the real tip defect of Berkovich indenter to reproduce with FEM nanoindentation test at shallow penetration depth, J. Mater. Res., 27 (2012) 28-38.

[26] H. Jiang, R. Browning, H.J. Sue, Understanding of scratch-induced damage mechanisms in polymers, Polymer, 50 (2009) 4056-4065.

[27] F.L. Li, F.L. Peng, Y. Tan, W. Kongkitkul, M.S.A. Siddiquee, FE simulation of viscous behavior of geogrid-reinforced sand under laboratory-scale plane-strain-compression testing, Geotextiles and Geomembranes, 31 (2012) 72-80.

THESIS CONCLUSION

This thesis presents time dependent mechanical behavior of polymeric materials. In particular we studied the viscoelasticity in the bulk. Deformation-time master curves were constructed out of compression relaxation experiments. The indentation creep and recovery analysis permitted us to observe the apparition of plasticity in PMMA CN for long indentation time. CR39 presented, like PMMA CN, thermoplastic behavior below its glass transition and elastomeric behavior above. In the whole tested range CR39 showed only viscoelastic behavior. We determined whether a material is viscoelastic or elastic plastic by the analysis of the material recovery. Furthermore, through creep under indentation experiments, the mean contact pressure enabled the creation of deformation-time-temperature master curves in almost perfect adequacy with the classical time-temperature, thus demonstrating a non-influence of plasticity on viscoelasticity and an absence of viscoplasticity in polymer behavior. We demonstrated the equivalence of the contact and bulk master curves thus proving that one can predict the one master curve knowing the other. The immediate scratch recovery analysis is presented in this thesis for the first time.

Then the polymeric mechanical behavior is simulated by three types of constitutive laws in MSC Marc software. The elasto-plastic law enables a good prediction of the immediate stress-strain relation on the tested polymers. There is no evolution due to creeping effects. The viscoplastic law gives a relatively good representation of the mean contact pressure evolution. The viscoelastic master curve law demonstrates a very good precision if it is used for the deformation on which it was fitted. In the case of indentation creep, it gives an accurate idea of the normalized creep deformation. The recovery of the master curves is appropriate and accurate as long as there is no plasticity involved in the deformation.

To improve the simulation quality, the master curve viscoelastic law could receive a plasticity threshold. Indeed CR39 and PMMA CN can undergo plasticity that is absolutely not taken into account in actual model. More improvement would be obtained by differentiating compression, traction and shear in particular for scratch simulation. In fact the compression and traction comportment of polymers is different thus differentiating it in the simulation of scratch is one of the next steps toward a better constitutive law. There is place for improvement in the simulation of the indentation recovery. The combination of a plastically, a viscoelastically and an elastically deformed material remains to be done.

In order to improve the understanding of polymeric material, one should improve the time-temperature-deformation observed relationship by adding a molecular dynamic and a fracture mechanics understanding.

Joseph LEJEUNE

Surface recovery and reconstruction after deformation

Résumé

Les propriétés des polymères sont intéressantes pour des applications pneumatiques, de verres organiques, de joints, … Leurs propriétés mécaniques sont néanmoins mal comprises. Dans ce manuscrit, le comportement mécanique du PMMA et du CR39 est étudié en fonction du temps. Il en résulte des courbes maîtresses à partir d'expérience de relaxation de contrainte et de fluage d'indentation. D'autre part, le comportement mécanique au contact est analysé sur des expériences de fluage et recouvrance d'indentation et de rayures analysées pour la première fois dans cette thèse. Finalement, des lois de comportements sont construites, leurs précisions sont comparées grâce à des calculs par éléments finis aux expériences en contact.

Mots clefs : Viscoélasticité, WLF, courbes maîtresses, FEM, lois de comportement, indentation, fluage, relaxation, recouvrance d'indentation, recouvrance en rayure, PMMA, CR39

Summary

Polymer's low weight, deformability and easy manufacturing make them attractive materials for tire, organic glasses, sealing applications … Their mechanical properties are nonetheless poorly understood. In particular, two fields are searched over this thesis: time dependency and contact behavior for two transparent polymer: PMMA and CR39. The mechanical behavior time dependency is observed by the construction of stress relaxation and contact master curves. The mechanical contact behavior is analyzed by indentation creep and recovery experiments. Moreover the immediate scratch recovery is measured in the thesis. Finally, the uniaxial data is used to build constitutive laws, which accuracy is compared by Finite Element Modeling to contact tests.

Key word: Viscoelasticity, WLF, master curves, FEM, constitutive laws, indentation, creep, relaxation, indentation recovery, scratch recovery, PMMA, CR39